

Development of Radiochromic Film for Spatially Quantitative Dosimetric Analysis of
Indirect Ionizing Radiation Fields

by

Samuel Loren Brady

Program of Medical Physics
Duke University

Date: _____

Approved:

Terry Yoshizumi, Ph.D., Supervisor

Ehsan Samei, Ph.D.

Rathnayaka Gunasingha, Ph.D.

Donald Frush, M.D.

Robert Reiman, M.D.

Dissertation submitted in partial fulfillment of
the requirements for the degree of Doctor of Philosophy in the
Medical Physics graduate program in the Graduate School
of Duke University

2010

ABSTRACT

Development of Radiochromic Film for Spatially Quantitative Dosimetric Analysis of
Indirect Ionizing Radiation Fields

by

Samuel Loren Brady

Program of Medical Physics
Duke University

Date: _____

Approved:

Terry Yoshizumi, Ph.D., Supervisor

Ehsan Samei, Ph.D.

Rathnayaka Gunasingha, Ph.D.

Donald Frush, M.D.

Robert Reiman, M.D.

An abstract submitted in partial fulfillment of
the requirements for the degree of Doctor of Philosophy in the
Medical Physics graduate program in the Graduate School
of Duke University

2010

Copyright by
Samuel Loren Brady
2010

Abstract

Traditional dosimetric devices are inherently point dose dosimeters (PDDs) and can only measure the magnitude of the radiation exposure; hence, they are one-dimensional (1D). To measure the magnitude and spatial location of dose within a volume either several PDDs must be used at one time, or one PDD must be translated from point-to-point. Using PDDs for spatially distributed, two-dimensional (2D), dosimetry is laborious, time consuming, limited in spatial resolution, susceptible to positioning errors, and the currently accepted approach to measuring dose distribution in 2D. This work seeks to expand the current limits of indirectly ionizing radiation dosimetry by using radiochromic film (RCF) for a high-resolution, accurate dosimetry system. Using RCF will extend the current field of radiation dosimetry to spatially quantitative 2D and three-dimensional (3D) measurements.

This work was generalized into two aims. The first aim was the development of the RCF dosimetry system; it was accomplished by characterizing the film and the readout devices and developing a method to calibrate film response for absolute dose measurements. The second aim was to apply the RCF dosimetry system to three areas of dosimetry that were inherently volumetric and could benefit from multiple dimensional (2D or 3D) dose analysis. These areas were representative of a broad range of radiation energy levels and were: low-mammography, intermediate-computed tomography (CT), and high-radiobiological small animal irradiation and cancer patient

treatment verification. The application of a single dosimeter over a broad range of energy levels is currently unavailable for most traditional dosimeters, and thus, was used to demonstrate the robustness and flexibility of the RCF dosimetry system.

Two types of RCF were characterized for this work: EBT and XRQA film. Both films were investigated for: radiation interaction with film structure; light interaction with film structure for optimal film readout (densitometry) sensitivity; range of absorbed dose measurements; dependence of film dose measurement response as a function of changing radiation energy; fractionation and dose rate effects on film measurement response; film response sensitivity to ambient factors; and stability of measured film response with time. EBT film was shown to have the following properties: near water equivalent atomic weight (Z_{eff}); dynamic dose range of 10^{-1} - 10^2 Gy; 3% change in optical density (OD) response for a single exposure level when exposed to radiation energies from (75-18,000) kV; and best digitized using transmission densitometry. XRQA film was shown to have: a Z_{eff} of ~ 25 ; a 12 fold increase in sensitivity at lower photon energies for a dynamic dose range of 10^{-3} - 10^0 Gy, a difference of 25% in OD response when comparing 120 kV to 320 kV, and best digitized using reflective densitometry. Both XRQA and EBT films were shown to have: a temporal stability (ΔOD) of $\sim 1\%$ for $t > 24$ hr post film exposure for up to ~ 20 days; a change in dose response of ~ 0.03 mGy hr^{-1} when exposed to fluorescent room lighting at standard room temperature and humidity levels; a negligible dose rate and fractionation effect

when operated within the optimal dose ranges; and a light wavelength dependence with dose for film readout.

The flat bed scanner was chosen as the primary film digitizer due to its availability, cost, OD range, functionality (transmission and reflection scanning), and digitization speed. As a cost versus functionality comparison, the intrinsic and operational limitations were determined for two flat bed scanners. The EPSON V700 and 10000XL exhibited equal spatial and OD accuracy. The combined precision of both the scanner light sources and CCD sensors measured $< 2\%$ and $< 7\%$ deviation in pixel light intensities for 50 consecutive scans, respectively. Both scanner light sources were shown to be uniform in transmission and reflection scan modes along the center axis of light source translation. Additionally, RCFs demonstrated a larger dynamic range in pixel light intensities, and to be less sensitive to off axis light inhomogeneity, when scanned in landscape mode (long axis of film parallel with axis of light source translation). The EPSON 10000XL demonstrated slightly better light source/CCD temporal stability and provided a capacity to scan larger film formats at the center of the scanner in landscape mode. However, the EPSON V700 only measured an overall difference in accuracy and precision by 2%, and though smaller in size, at the time of this work, was one sixth the cost of the 10000XL. A scan protocol was developed to maximize RCF digitization accuracy and precision, and a calibration fitting function was developed for RCF absolute dosimetry. The fitting function demonstrated a superior

goodness of fit for both RCF types over a large range of absorbed dose levels as compared to the currently accepted function found in literature.

The RCF dosimetry system was applied to three novel areas from which a benefit could be derived for 2D or 3D dosimetric information. The first area was for a 3D dosimetry of a pendant breast in 3D-CT mammography. The novel method of developing a volumetric image of the breast from a CT acquisition technique was empirically measured for its dosimetry and compared to standard dual field digital mammography. The second area was dose reduction in CT for pediatric and adult scan protocols. In this application, novel methodologies were developed to measure 3D organ dosimetry and characterize a dose reduction scan protocol for pediatric and adult body habitus. The third area was in the field of small animal irradiation for radiobiology purposes and cancer patient treatment verification. Two methods for small animal irradiation were analyzed for their dosimetry. The first technique was within a gamma irradiator environment using a ^{137}Cs source (663 keV), and the second, a novel approach to mouse irradiation, was developed for fast neutron (10 MeV) irradiated by a Tandem Van de Graff accelerator in a $^2\text{H}(d,n)^3\text{He}$ reaction. For the patient cancer treatment, RCF was used to verify a 3D radiochromic plastic, PRESAGETM, using multi-leaf collimation (MLC) on a medical linear accelerator (LINAC) with 6 MV x-rays. The RCF and PRESAGETM dosimeters were employed to verify a simple respiratory-gated lung treatment for a small nodule; the film was considered the gold standard. In every

case, the RCF dosimetry system was verified for accuracy using a traditional PDD as the golden standard. When considering all areas of radiation energy applications, the RCF dosimetry system agreed to better than 7% of the golden standard, and in some cases within better than 1%. In many instances, this work provided vital dosimetric information that otherwise was not captured using the PDD in similar geometry. This work demonstrates the need for RCF to more accurately measure volumetric dose.

Dedication

This work, and all subsequent work, is dedicated to my loving, beautiful, patient wife Natalie, and to the two best sons a guy could ever hope for: Nicholas and Christian. This work is also dedicated to my parents, Loren and Susan, whom instilled in me the capacity and desire to be the person I have become. My family has enriched and blessed my life and without their dedication to me and this dream this work would not have come to pass; I am eternally thankful!

Contents

Abstract	iv
List of Tables	xiv
List of Figures	xv
1 Introduction.....	1
1.1 Motivation	1
1.2 Hypothesis.....	2
1.3 Background	2
1.4 Chapter Summary	4
2 Characterization of Radiochromic Film	6
2.1 Radiation Interactions with Film Structure	7
2.2 Optimal Film Readout (Densitometry) Sensitivity	12
2.3 Range of Absorbed Dose Measurements	12
2.4 Film Response Dependence on Changing Photon Energies	15
2.5 Fractionation and Dose Rate Effects	19
2.6 Film Response Sensitivity to Ambient Factors.....	19
2.7 Stability of Measured Film Response with Time	22
2.8 Conclusion	22
3 Radiochromic Film Digitization and Densitometry	24
3.1 Scanner Accuracy and Precision.....	26
3.2 Digitization Procedures and Post-Processing Techniques	30

3.3	Image Post Processing.....	35
3.3.1	Conversion of Film Digital Response to Optical Density	36
3.3.2	Light Non-uniformity Correction	38
3.3.3	Film Response Calibration to Absorbed Dose	41
3.3.4	Measured Total Uncertainty for Radiochromic Film Digitization	51
3.4	Discussion.....	52
3.5	Radiochromic Film Scanning Protocol using a Flat Bed Scanner	55
3.6	Conclusion.....	56
4	Low Energy Dosimetry.....	58
4.1	Applications to Uncompressed Breast Computed Mammotomography Dosimetry	58
4.1.1	Materials and Methods.....	60
4.1.2	Results and Discussion.....	69
4.1.3	Conclusions.....	80
5	Intermediate Energy Dosimetry	81
5.1	Application into an Investigation of a Dose Reduction Technique for CT	83
5.1.1	Materials and Method	84
5.1.2	Results.....	87
5.1.3	Discussion.....	95
5.1.4	Conclusion.....	100
5.2	Application into the Development of a Novel 3D Organ Dosimetry for CT ..	102
5.2.1	Materials and Methods.....	104

5.2.2	Results.....	114
5.2.3	Discussion.....	119
5.2.4	Conclusion.....	123
6	High Energy Dosimetry.....	125
6.1	Applications to ¹³⁷ Cs Irradiator Dosimetry	125
6.1.1	Materials and Methods.....	127
6.1.2	Results and Discussion.....	134
6.1.3	Conclusion.....	143
6.2	Applications to Respiratory-Gated Cancer Patient Treatment Verification ...	144
6.2.1	Materials and Methods.....	147
6.2.2	Results.....	158
6.2.3	Discussion.....	162
6.2.4	Conclusion.....	166
6.3	Applications to fast Neutron Dosimetry	166
6.3.1	Materials and Methods.....	168
6.3.2	Results.....	178
6.3.3	Discussion.....	185
6.3.4	Conclusion.....	189
7	Conclusion.....	191
8	Future work.....	193
A	Appendix-Traditional Dosimeters.....	195
A.1	Ion Chamber.....	195

A.2	Thermoluminescent Dosimeter (TLD).....	197
A.3	Metal-Oxide-Semiconductor Field-Effect Transistor (MOSFET).....	201
B	Appendix-Film Post Processing & Analysis Software.....	205
	References	235
	Biography.....	247

List of Tables

Table 2-1. Summary of attributes and characteristics for modern RCF types.....	8
Table 3-1 Calibration fitting parameters.....	47
Table 6-1 RCF response to changing neutron energies.....	179
Table 6-2 RCF calibration data and % γ -ray contamination from $^1\text{H}(n,\gamma)^2\text{H}$ reaction.....	180

List of Figures

Figure 1.1 Radiochromic film timeline.....	3
Figure 2.1 RCF construction.	7
Figure 2.2 RCF mass energy attenuation coefficient plots	9
Figure 2.3 XRQA absorption spectrum.....	13
Figure 2.4 Absorbed dose range and light wavelength digitization	14
Figure 2.5 XRQA beam energy response.....	16
Figure 2.6 Ambient light contamination.....	20
Figure 2.7 XRQA OD growth with time after post exposure digitization	21
Figure 3.1 Densitometers	25
Figure 3.2 Spatial and intrinsic accuracy for EPSON V700 and 10000XL scanners.....	27
Figure 3.3 Light source stability for EPSON V700 and 10000XL scanners	28
Figure 3.4 CCD element stability for EPSON V700 and 10000XL scanners.....	30
Figure 3.5 Film readout due to the effects of rotation in the setup	31
Figure 3.6 Readout effects due to anisotropic scatter	33
Figure 3.7 Light non-uniformity for transmission and reflection scan modes.....	34
Figure 3.8 Relative light intensity on CCD detector elements.....	36
Figure 3.9 EPSON 10000XL flat field response	39
Figure 3.10 Calibration fitting function comparisons	48
Figure 3.11 Exponential fitting function	49
Figure 3.12 Exponential fitting curve error	50

Figure 3.13 Total dose uncertainty associated with RCF	51
Figure 3.14 Calibration setup geometry: ion chamber scatter measurement.....	53
Figure 3.15 Film registration	54
Figure 4.1 SPECT-CT mammotomography system	61
Figure 4.2 Breast phantom geometrical shapes	63
Figure 4.3 TLD experimental setup	65
Figure 4.4 Excised cadaver breast.....	67
Figure 4.5 Dosimeter calibration fitting functions for CmT exposures.....	68
Figure 4.6 Conical phantom.....	70
Figure 4.7 TLD and RCF response comparison	72
Figure 4.8 Cylindrical breast phantom	73
Figure 4.9 Anthropomorphic phantom.....	76
Figure 4.10 Cadaver breast	78
Figure 4.11 Tissue specific dose histograms.....	79
Figure 5.1 CTDI head and body phantom.....	85
Figure 5.2 Anthropomorphic pediatric and adult female phantoms with MOSFETs.....	86
Figure 5.3 CTDI head phantom with RCF wrap and Xcare enabled.....	88
Figure 5.4 CTDI body phantom with RCF wrap and Xcare enabled.....	89
Figure 5.5 CTDI head phantom with RCF wrap and Xcare disabled.....	90
Figure 5.6 RCF inserts placed between two CTDI head phantoms	91
Figure 5.7 2D RCF dose distribution of a CTDI body phantom with Xcare enabled.....	92
Figure 5.8 Pediatric 5-yr old whole body dose	93

Figure 5.9 Adult whole body dose	94
Figure 5.10 Adult anthropomorphic phantom breast and lung dose.....	96
Figure 5.11 Adult anthropomorphic phantom skin and bone marrow dose	97
Figure 5.12 2D RCF dosimetry of a modified CTDI head phantom	103
Figure 5.13 RCF and TLD dosimetry compared within a modified CTDI head phantom	105
Figure 5.14 5-yr old pediatric anthropomorphic phantom with RCF inserts.....	107
Figure 5.15 TLD and RCF calibration.....	108
Figure 5.16 2D RCF dose distributions for lung volume in a 5-yr old phantom	116
Figure 5.17 2D RCF dose distributions of the liver and kidneys for a 5-yr old phantom	117
Figure 5.18 TLD and RCF responses compared	119
Figure 6.1 ¹³⁷ Cs irradiator Mark I-68A.....	127
Figure 6.2 Dosimetry experimental setup	130
Figure 6.3 Calibration experimental setup	133
Figure 6.4 EBT film and manufacturer’s overall data compared	135
Figure 6.5 EBT film and manufacturer’s vertical data compared	136
Figure 6.6 EBT film and manufacturer’s horizontal data compared	138
Figure 6.7 Dose rate correction.....	141
Figure 6.8 Dynamic thorax phantom and PRESAGE™ dosimeter	148
Figure 6.9 Optical-CT scanner configuration.....	149
Figure 6.10 Lung AP/PA ECLIPSE® treatment plan	153
Figure 6.11 Independent dosimetry verification using EBT film	156

Figure 6.12 Improved Optical-CT scan readout	158
Figure 6.13 Contour plots of PRESAGE™, EBT film, and ECLIPSE®	159
Figure 6.14 Gamma Maps of PRESAGE™, EBT Film, and ECLIPSE® inter comparison	161
Figure 6.15 Line profile comparison of PRESAGE™, EBT film, and ECLIPSE®	162
Figure 6.16 Absolute dose comparison between EBT film and ECLIPSE®	164
Figure 6.17 Neutron source gas cell.....	169
Figure 6.18 RCF calibration experimental setup.....	171
Figure 6.19 Neutron small animal irradiation setup.....	175
Figure 6.20 XRQA and EBT film sensitivity to 10 MeV neutrons	177
Figure 6.21 RCF response to changing neutron energies from (6-10) MeV	178
Figure 6.22 Calibration Curve	179
Figure 6.23 Internal to water target neutron dose distribution	181
Figure 6.24 XRQA and Monte Carlo absolute dose comparison.....	183
Figure 6.25 External dose distribution of live mouse exposure	184
Figure A.1 TLD energy level diagram	198
Figure A.2 P-Channel MOSFET diagram	202

Acknowledgements

No acknowledgement would be right if it didn't start with my wonderful mentor and advisor Dr. Terry Yoshizumi. He has worked with me since the beginning, when I started at Duke with my Masters degree, and was instrumental in helping me stay to finish my PhD. I have learned so very much from him, and I am honored to call him my advisor and my friend. I am also grateful for the mentorship that came from my Ph.D. committee, Drs Samei, Frush, Gunasingha, and Reimen. The many hours of council I received at their hands has been deeply appreciated.

I would also like to thank Dr. Mark Oldham my Masters' committee advisor. Even after finishing my Masters degree at Duke he made his time available to council me on a project that was included in my PhD dissertation.

Sincere thanks is owed to Greta Toncheva, the lab manager for Dr. Yoshizumi's research lab, who patiently taught me dosimetry and helped me at 5:30 am every time we had to make the long journey to Duke South for another early morning CT experiment. Also thanks is owed to: Giao Ngyuen, Colin Evan-Anderson, Mats Fredrickson, Brent Falin, Dr. Calvin Howell and TUNL staff, and finally for Dr. Martin Tornai and Dominic Crotty in the MMIL lab. All of their assistance and many questions that helped flesh out the weakest aspects of my dissertation. I am grateful for every one of the many co-authors and fellow students that with me slogged through the deep and

hard work of research these many years. I learn so much from my peers; each one is a mentor to me in their own way.

I am grateful for the faculty and staff of Utah Valley University my undergraduate alma mater. Their personal love of physics rubbed off on me and has shaped my future for the better. They persevered with me and taught me to love physics.

Finally, I am grateful for Mr Rutger, my High school English teacher. He befriended me and showed me how to think big. He told me before I walked out onto the stage at my High School graduation that he expected big things of me. His admonition has stuck with me all these 12 years.

1 Introduction

1.1 Motivation

This work seeks to expand the current limits of indirectly ionizing radiation dosimetry by using radiochromic film (RCF) as a dosimetric tool. Dosimetry is defined as a technique for measuring absorbed dose in a medium of a particular radiation field. A dosimeter is a device used for the quantification of the absorbed dose of a radiation field. Traditional dosimetric devices are: ion chambers, thermoluminescent dosimeters (TLDs), metal-oxide-semiconductor field-effect transistors (MOSFETs), diodes, etc. These devices are inherently point dose dosimeters (PDDs) and can only measure the amount or magnitude of the radiation exposure; hence, they are one-dimensional (1D). Several PDDs can be used at one time, or one PDD can be translated from point-to-point, to measure spatially distributed absorbed dose magnitudes. This two-dimensional (2D) approach to dosimetry is laborious, time expensive, limited in spatial resolution, susceptible to positioning errors, and the currently accepted approach to measuring dose distribution in 2D.

The primary motivation for this research is to develop a fast, high resolution, and accurate 2D dosimetry system that can be used to extend the current field of radiation dosimetry from traditional 1D quantitative measurements to spatially quantitative 2D and three-dimensional (3D) measurements. In this work, RCF is investigated for: its

inherent two-dimensionality; durability within experimental and clinical laboratory settings; and its general radiation detection properties.

1.2 Hypothesis

If RCF can provide an accurate dosimetric analysis of a radiation field then RCF dosimetry will offer a more accurate, time efficient means for spatially quantitative measurements of ionizing radiation.

1.3 Background

To establish RCF as an accurate 2D dosimeter, the film characteristics and limitations, relating to radiation detection, must be understood. But first what is RCF? RCF derives its name from the kinetic effect of electromagnetic energy (radio) induced color change (chromic) to a film medium. A RCF consists of several protective layers of polyester around one or more “active” layers. The active layer of a RCF comprises of radiosensitive organic microcrystals of double substituted diacetylene monomers that are evenly dispersed within a gelatin matrix¹. RCF, unlike its radiographic film counterpart, is a processor-less film that does not require latent-chemical or thermal processes for development². Instead, RCF undergoes a topotactic solid-state polymerization reaction to the kinetic energy released per unit mass (KERMA) of the incident ionizing radiation¹. The polymerization reaction creates a polymer dye complex that appears darker in color-intensity to the eye compared to unexposed portions of the film. The polymerization reaction occurs near instantaneously¹.

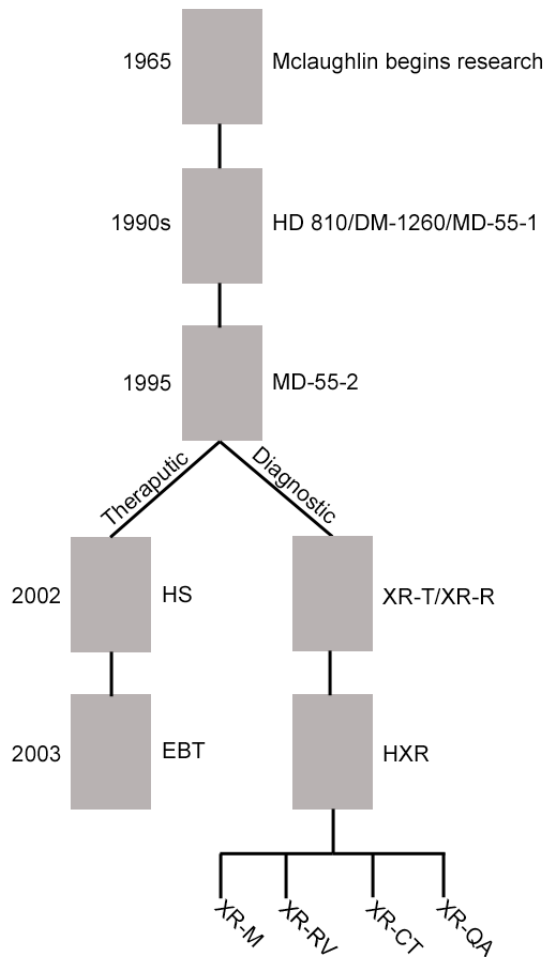


Figure 1.1 Radiochromic film timeline

Several types of radiochromic film have been developed since the initial research into radiochromic effects in 1965. Pre-MD-55 film was used for industrial use only due to the film insensitivity to medically relevant absorbed dose levels. EBT and XRQA are the current films predominately used for clinical use, however, older models like MD-55-2 and HD 810 are still available from the manufacturers for high dose measurements.

The field of RCF research has been developed over roughly four decades, where each decade of research has shown improvements to radiation response in energy and sensitivity to increasingly lower doses. See Figure 1.1 for a graphical representation of

the timeline for radiochromic film development. Most films prior to the 1990s were sensitive to absorbed doses on the order of $\sim 10^3$ - 10^4 Gy and were used for industrial purposes³⁻⁵. By the mid-1990s a film called MD-55 broke the clinical barrier and found use as a medical grade dosimeter due to improved sensitivity to lower doses, $\sim 10^1$ - 10^4 Gy^{2, 6-10}. At the turn of the 21st century, MD-55 went through several manufacturing iterations¹¹⁻¹⁹, each iteration made the film more robust and sensitive to lower doses. The two recently commercialized RCFs, XRQA and EBT film, are the subject of this thesis investigation as 2D quantitative dosimeters. Of the two types of film, EBT has had the most extensive scientific review as a 2D dosimeter; to date there are ~ 80 peer reviewed articles. However, it has been almost exclusively applied to external beam therapy (EBT), as its name so indicates, in cancer treatment verification. XRQA, though in existence for approximately the same amount of time as EBT film, has seen almost no scientific review. What little review XRQA film has received has been almost exclusively applied to the field of computed tomography (CT) dosimetry. In addition to the development of RCF as a quantitative dosimeter, this work seeks to expand the dosimetric roles of each film in non-traditional fields of RCF dosimetry.

1.4 Chapter Summary

This work seeks to characterize RCF as a quantitative dosimeter. To this end, chapter 2 will provide an extensive investigation into the characteristics and parameters necessary for quantitative RCF dosimetry for EBT and XRQA films. Chapter 3 will

provide a similarly extensive investigation of several types of film digitizers. Once characterized, the digitizers will be used to develop an accurate film digitization methodology and a means for film response to be calibrated for absolute dosimetry. As a fully defined and characterized RCF dosimetry system, the films will be applied to several dosimetric specific tasks that will range from relatively low to high radiation energy levels. The task of using RCF for quantitative dosimetry over a wide range of energy levels is meant to challenge the dosimetry system and will be used as a means to validate the RCF dosimetry system for robustness and accuracy. Few traditional dosimeters can provide accurate dosimetry at both very low and very high energy levels. Chapter 4 will investigate XRQA film at its lower limit of detection by measuring 2D dose distributions within a pendent breast for a novel 3D dose volume analysis of a computed mammotomography (CmT) system. Chapter 5 will investigate XRQA film within the mid range, optimal sensitivity, of the film. RCF will be applied to the task of validating a novel dose reduction technique for CT scans, and developing a novel organ volume dosimetry technique. Chapter 6 will investigate the potential for XRQA and EBT film to provide independent dose analysis of small animal γ -ray and neutron irradiation. Also in chapter 6 EBT film will be used for patient treatment verification in respiratory-gated lung treatment in radiation oncology.

2 Characterization of Radiochromic Film

In this work two current models of RCF, EBT, and XRQA film, were characterized through extensive experimentation and review of the scientific literature. The goal of the characterization phase was to define the working parameters and dosimetric limitations of the films to more accurately develop the films into quantitative dosimeters. The following characteristics of EBT and XRQA RCFs were investigated: radiation interaction with film structure; light interaction with film structure for optimal film readout (densitometry) sensitivity; range of absorbed dose measurements; dependence of film dose measurement response as a function of changing radiation energy; fractionation and dose rate effects on film measurement response; film response sensitivity to ambient factors; and stability of measured film response with time. Since each category was most often a separate and fully contained set of experiments, all methodology and results will be subdivided by the categories previously listed. A summary of the results for the characterization of EBT and XRQA can be found in Table 2.1. XRQA and EBT film results were compared to MD-55-2 film to compare the change in film characteristics from its original clinical inception till present.

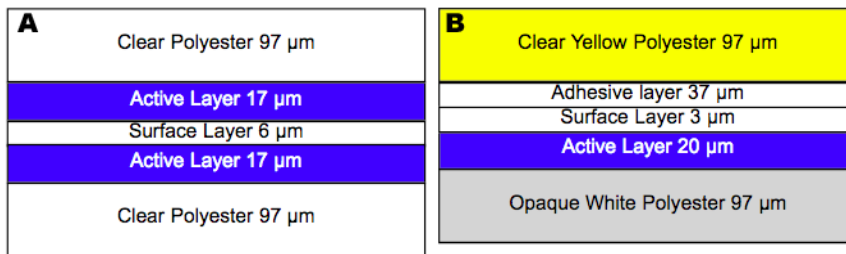


Figure 2.1 RCF construction.

RCF structure consists of protective polyester layers surrounding a radiosensitive active layer(s). Regions of the active layer exposed by the kinetic effects of indirectly ionizing radiation undergo a visible change in color. The amount of change is dependent on the amount of radiation exposure. EBT (A) and XRQA (B) film introduced a reformulated active layer that is 10 times as dense as the original MD-55 film making both films more efficient at measuring less dose.

2.1 Radiation Interactions with Film Structure

To ascertain the structure of EBT and XRQA films, the manufacturers were contacted directly^{19,20}. The film structure for EBT, Figure 2.1(A), consisted of a double active layer with a reformatted chemical structure that was used to increase the films sensitivity to lower absorbed dose²¹. The elemental composition of EBT film¹⁹ is: H (40%), C (42%), O (17%), N (1%), Li (0.1%), and Cl (0.02%), which when calculated¹⁹ gives a Z_{eff} of 6.6 using the following expression:

$$Z_{eff} = \sum_i (\alpha_i \cdot Z_i^a)^a, \text{ and } \alpha_i = \frac{n_i Z_i}{\sum_j n_j Z_j} \quad (2-1)$$

where α_i is the percent abundance of the element with atomic number Z and a is explicitly assumed to be 2.94, an empirically derived value equating the dependence of Z on the photoelectric interaction²². The atomic composition of EBT is close to water,

Table 2-1. Summary of attributes and characteristics for modern RCF types.

EBT and XRQA were compared to MD-55-2 (information regarding MD-55-2 came from literature or manufacturer provided data). All experimentally measured data that was cross referenced with scientific literature is indicated by (superscript).

	MD-55-2	EBT	XRQA
Standard size	(5 x 5) in	(8 x 10) in	(14 x 17) in
Digitization mode	Transmission		Reflection
Active layer (number of layers)	16 μm (2)	17 μm (2)	20 μm (1)
Spatial resolution	> 1200 lp mm ⁶		
Z_{eff}	6.5	6.6 ²³	24.0
Readout light peak of absorption	675 nm ¹³	635 nm ²⁴	635 \pm 1 nm
Measured dose range	(3-10 ²) Gy ¹⁰	(10 ⁻² -10 ¹) Gy ²⁵	(10 ⁻³ -10 ⁰) Gy
Film response change to radiation energy	~30% (28-1710) keV ⁹ < 5% (1-18) MeV ^{2, 6}	< 3% (75-18,000) kV ²⁶	2% (80-120) kV 25% (60-320) kV
Fractionation	< 5% for 30 min/exp vs. 120 min exp ^{2, 27-28}	\leq 2% ²⁹	
Dose rate	< 5% (0.03-3.4) Gy min ^{-1 2, 30}	< 5%(16-520) cGy min ^{-1 31}	
Fluorescent light sensitivity	$\Delta\text{OD}^{32} \propto 18$ cGy h ⁻¹	$\Delta\text{OD}^{33} \propto 0.03$ mGy h ⁻¹	
Film response change with time post exposure	~ 4% > 24 hr ^{2, 27}	6% < 6 hr < 1% ³⁴	3% < 24 hr < 1% ³³

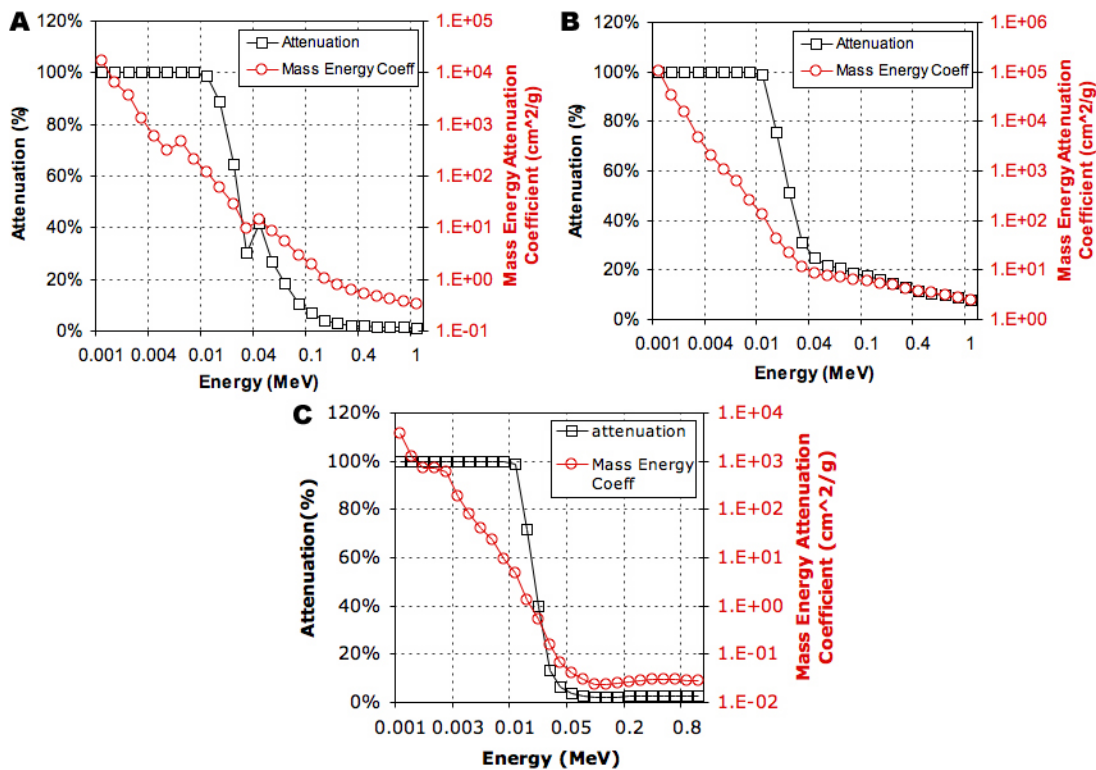


Figure 2.2 RCF mass energy attenuation coefficient plots

XRQA (A), EBT (B), and 0.18cc ion chamber (C) interaction probabilities are plotted as a function of changing photon energies.

Z_{eff} of 7.4, giving it a near soft tissue equivalence, but with a weighted density of 1.4 g cm^{-3} . The XRQA film structure, Figure 2.1(B), is similar in dimensions and material as EBT film, however, with a single active layer with dimensions of 20 μm . Additionally, the film layers were doped with higher Z elements to increase the film's sensitivity to lower photon energy exposures. The elemental composition²⁰ of XRQA film is: H (40%), C (41%), O (17%), N (0.4%), Li (0.1%), Cl (0.1%), Cs (0.2%), Br (0.2%), Ba (0.4%), and S (0.4%). The composition of XRQA gives a calculated Z_{eff} of 24.0, using equation (2-1), and a calculated weighted density of 1.4 g cm^{-3} . Both film types are ~ 0.3 mm thick.

The interaction efficiency of the XRQA, Figure 2.2(A), and EBT film, Figure 2.2(B), were determined by using the National Institute for Standards and Technology (NIST)³⁵ calculated mass energy attenuation coefficients for the known atomic composition of the films previously defined. The elemental mass energy attenuation coefficients were summed up and plotted verses energy. Knowing the mass energy attenuation coefficient and the densities of the film, attenuation was calculate using Beer’s law:

$$Attenuation(\%) = 1 - e^{\left(-\frac{\mu_{en}}{\rho} \cdot \rho \cdot T_0\right)} \quad (2-2)$$

where μ_{en}/ρ is the mass energy attenuation coefficient, ρ is the density, and T_0 is the thickness of the dosimeters. As a comparison, a 0.18 cc ion chamber’s detection efficiency is also shown, see Figure 2.2(C). The interaction efficiency is defined by the percentage of the incident fluence absorbed in the film such that the electrons from the interaction can then be absorbed in the active layer and induce coloration in the film. The films measured the best attenuation probability as radiation energies decreased. Although the film is able to capture a high percentage of the radiation beam fluence at very low energies, so to decreases the probability that the electrons from the KERMA interactions will be able to transverse the protective polyester covers to arrive at the active layer for coloration induction. The predominate interaction at the film interface is Compton scatter. Therefore, the primary photon will scatter with the “loosely” bound

electrons in the valance bands within the film's polyster layer. These electrons will gain energy from the incident photons due to the laws of conservation of momentum and energy. The range of the scattered electrons can be calculated considering the continuously slowing down approximation (CSDA)³⁶ for an electron in a medium:

$$R_{CSDA} = \int_0^{E_0} \left(\frac{dT}{\rho dx} \right)^{-1} dT \quad (2-3)$$

Where $dT/\rho dx$ is the mass stopping power for an electron within a medium and E_0 is the starting energy of the electron. The R_{CSDA} for a 0.001 MeV, assuming a $\theta = \pi$ photon scatter interaction, is ~98 μm and even if you add an additional distance equal to the mean free path ($1/\mu$) of the incident photon, a minor ~1 mm, then the incident radiation of 0.001 MeV isn't sufficient for signal induction in the film's active layer. However, when considering the interaction efficiency for CT exposures, then XRQA is ~20% compared to the ion chamber which is ~40%. Thus, XRQA film will absorb incident radiation for signal formation, but does not create a large perturbation in the fluence field due to its thin profile. The film maintains comparable detection efficiency to that of an ion chamber with its increased photoelectric cross-section due to a higher Z_{eff} composition. To provide dose measurements, films are cross calibrated with an ion chamber. Ion chambers themselves are not true absolute dosimeters, but require periodic calibration by a free in air ion chamber. Ion chambers are, however, very stable

and have a reputation of consistence and are, therefore, considered the golden standard in almost every cross calibration application.

2.2 Optimal Film Readout (Densitometry) Sensitivity

The polymerization of the monomers within the active layer of RCF creates an absorption spectrum with a peak of maximum absorption. Scanning the RCF at the maximum absorption wavelength allows for the greatest sensitivity to measurements of change in color intensity or OD. EBT film's maximum absorption peak was measured at 635 nm and did not undergo a shift in wavelength^{21, 24, 37}. In older versions of RCF, the absorption peak would shift towards shorter wavelengths with increasing exposure intensity due to a more unstable diacetylene monomer configuration²⁴. The absorption spectrum of XRQA was measured by using a photospectrometer that scanned a range of wavelengths, (560-700) nm, for films exposed to (0-38) mGy. The maximum peak of absorption was measured at a wavelength of (635 ± 1) nm, see Figure 2.3. For all dose levels investigated, the measured values are in good agreement with reported values from an XRQA equivalent film (XRCT)³⁸. Since EBT and XRQA absorption spectra maximums are at 635 nm, readout is optimized using red light for film digitization.

2.3 Range of Absorbed Dose Measurements

Previous models of RCF were insensitive to clinically relevant dose levels, i.e., mGy for diagnostic and cGy for therapeutic. The active layer(s) in EBT and XRQA RCF where increased in density allowing for a greater sensitivity to lower levels of absorbed

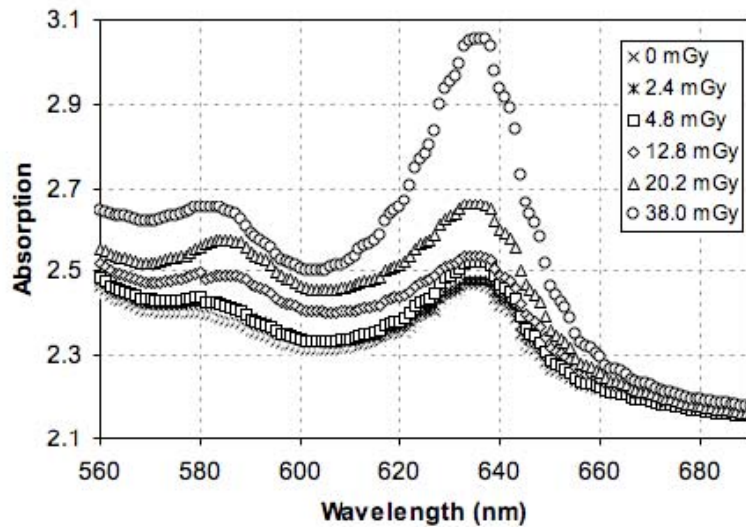


Figure 2.3 XRQA absorption spectrum

Absorption spectrum for XRQA measured a global maximum peak of absorption at (635 ± 1) nm and a secondary local maximum peak of (584 ± 1) nm. Film exposure was at 120 kVp over a dose range of (0-38) mGy.

dose measurements (mGy to cGy). The manufacturer defined optimal range for EBT film was quoted as $(0.1-8)$ Gy^{19, 39}, and for XRQA it was quoted as $(0.1-20)$ cGy. To ascertain a true range of doses over which the films could be used, the films were incrementally exposed to dose levels up to $(180-190)\%$ greater than their max optimal dose. EBT film was exposed up to a dose of 100 Gy at 663 keV using an ¹³⁷Cs irradiator, see Figure 2.4(A). XRQA film was exposed up to a dose of 1000 mGy at three x-ray energy levels (80, 120, and 300) kVp in an orthovoltage x-ray machine, see Figure 2.4(B-D), respectively. For each of the plots represented in Figure 2.4 the film response was plotted as a function of dose as it was measured using three different light wavelengths centered in the red, green, and blue regions of the visible light spectrum. Previously it

was demonstrated that RCF exhibited a maximum sensitivity to changes in OD when measured using a red light, see section 2.2. The RCF measurements for section 2.2 were

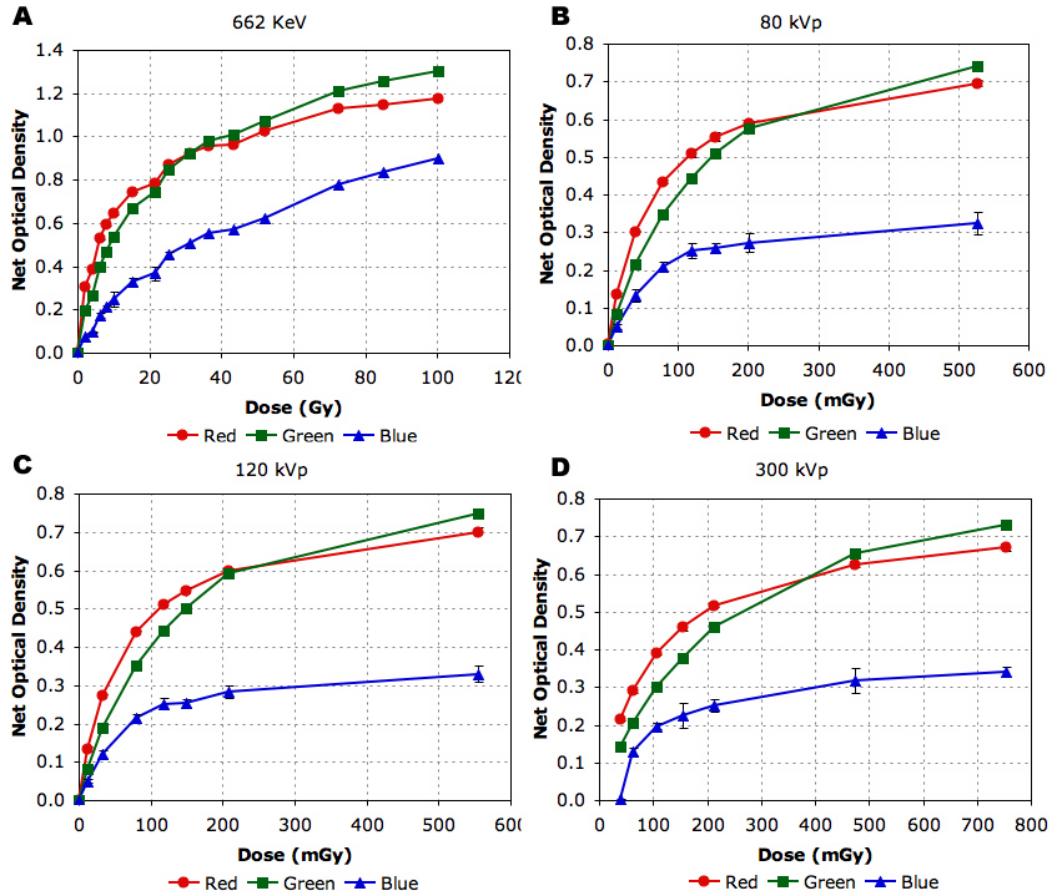


Figure 2.4 Absorbed dose range and light wavelength digitization

EBT (A) and XRQA (B-D) films measure a maximum sensitivity to changes of OD in the red channel of a RGB scan when exposed within their manufacturer defined optimal dose range. However, as the films are exposed to increasing dose levels, the OD of the films increases logarithmically. At a certain point the films digitized with a shorter light wavelength become more sensitive to changes in OD due to their increased penetration power. Light wavelengths centered in the green spectrum were optimal for doses that ranged up to (180-190)% greater than the optimal max dose. A further decrease in light wavelength, to the blue spectrum, measured suboptimal sensitivity to changes in OD.

exposed within the manufacturer specified optimal dose measurement range. The results of Figure 2.4 demonstrate a need for shorter light wavelengths, optimally a light centered in the green spectrum, to penetrate the increasingly optically denser film as a function of dose. Further decreasing the light wavelength to the blue spectrum, however, does not continue to increase the film read-out sensitivity to changes in OD. This is possibly due to the increased likelihood of light scatter and reflection at the film construction boundaries with shorter light wavelengths; thus, minimizing the overall light detection on the digitizer. Longer light wavelengths are less susceptible to light scatter and reflection at film boundaries. These results are in good agreement with other published work²⁵.

2.4 Film Response Dependence on Changing Photon Energies

When measuring dose within a standard x-ray beam (x-ray radiograph, CT, LINAC, etc), the measurement is within a polyenergetic spectrum. Thus, film response should be relatively independent to small changes in photon energy. Ideally, RCF would be able to measure 1 Gy worth of dose at low and high x-ray beam energies. With the addition of a moderately high-Z component, Cl, EBT film measures an increased response to photon energies $< 100 \text{ keV}$ ¹⁷ compared to MD-55-2 film, but the dose response remains near energy independent. The difference of dose response for EBT film was measured to be $< 3\%$ for photon energies between (75-18,000) kV²⁶, where

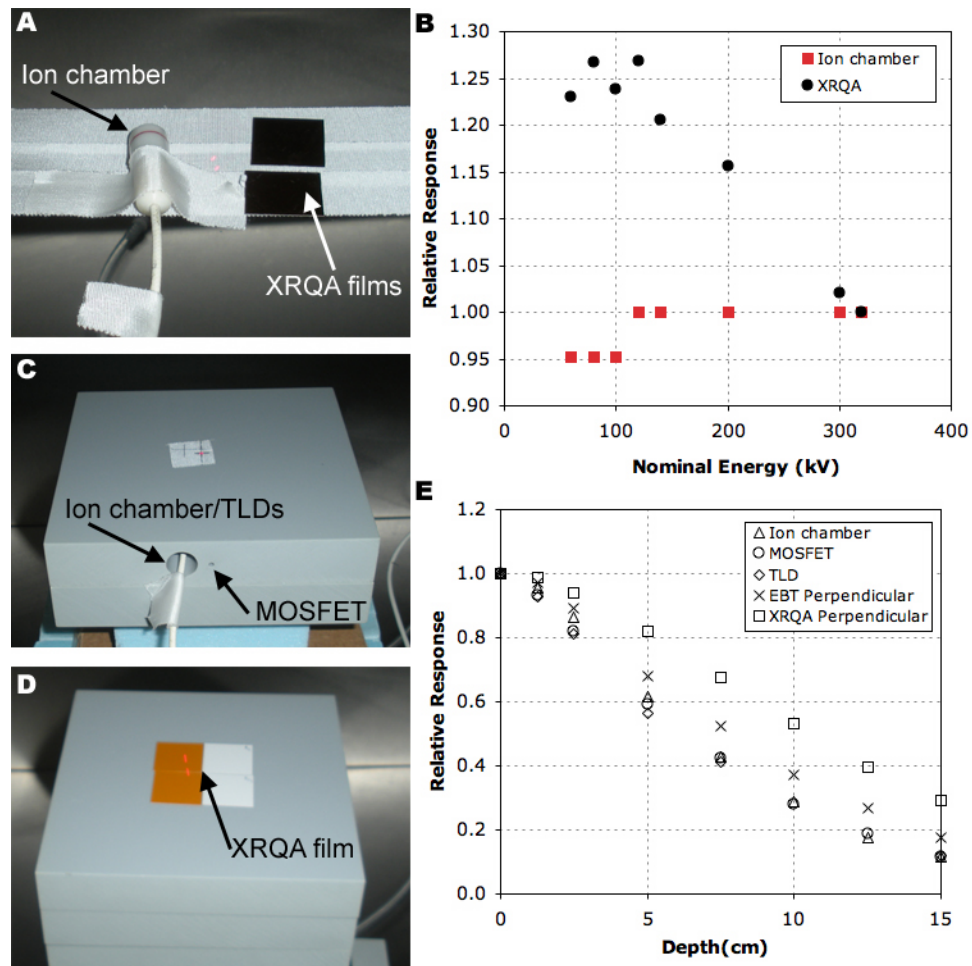


Figure 2.5 XRQA beam energy response

Several XRQA films were irradiated at 100 cGy by varying photon energies of (80-320) kVp and compared to an ion chamber (A-B). Five different dosimeters were exposed at eight depths within a soft tissue block while holding the exposure parameters (125 kV, 155 mA, and 0.3 min) constant (C-D). Dosimeter response was due to attenuation of primary beam with depth and dosimeter sensitivity to change in beam quality as a function of beam hardening with depth.

the maximal difference was seen in the lower energies and relatively no energy dependence ($\sim 0.7\%$) was measured for photon energies between (6-25) MV⁴⁰. XRQA, on the other hand, was produced with several high-Z elements to increase film response

sensitivity in the low energy and dose range through increased photoelectric effect involvement. The dependence on XRQA film response with photon energies was tested using an orthovoltage x-ray unit capable of exposures up to 320 kVp. The film was placed 50 cm source to object distance (SOD) on top of a strips of tape used to suspend the films in air, see Figure 2.5(A). The films and a 0.18 cc ion chamber were exposed simultaneously. XRQA film was shown to exhibit a greater dependence on photon energies at the low energy range, see Figure 2.5(B). The increase in dosimetric response at different energies was measured to be 25% for beam energies over the range of (60-320) kVp. However, a dosimetric difference of 2% in film response with changes in energy in the range of (100-150) kVp was measured. Results are in good agreement with previously reported values from an XRQA equivalent film (XRCT)⁴¹.

Results for Figure 2.5(B) were measured in air at a static SOD. Frequently, RCF is placed within phantoms as a means to measure dose to an object. When x-ray beams penetrate an object the beam becomes "hardened". Beam hardening is a filtration effect caused by the softer x-rays being absorbed superficially within an object and thus leaving more energetic, or "hardened", x-rays in the beam spectrum. Thus, beam hardening will cause the initial polyenergetic x-ray beam to change as a function of depth in an object and possibly introduce a dosimeter response dependence on beam energy. To ascertain the magnitude of this effect several XRQA, EBT, TLD, MOSFET, and ion chamber readings were measured as a function of depth within an object. The

SOD, as measured from the top of the phantom blocks, was held constant to maintain the same x-ray fluence at each beam exposure of 125 kV. A homogeneous soft tissue equivalent plastic phantom was used. The phantom consisted of multiple (15x15x2.5) cm slabs stacked upon one another. A block was customized to allow ion chamber, MOSFET, and TLD dosimeter placement within the block, see Figure 2.5(C). At the same depth as the previous dosimeters, but exposed separately, RCFs were placed between two slabs, see Figure 2.5(D). All dosimeter results were normalized by surface dose readings and are shown in Figure 2.5(E). For the first 2.5 cm the dosimeter responses varied in response, but at depths > 2.5 cm the TLD, MOSFET, and ion chamber relative responses were near identical. The XRQA response was identical in trend but ~25% more sensitive than the other dosimeters in response. This was most likely a cause of the increased photoelectric effect in the XRQA film compared to the other dosimeters due to its larger Z_{eff} . EBT film similarly measured a near identical trend and a response within ~10% of the other dosimeters. However, the EBT film required four times the radiation flux density to measure its response due to its relative insensitivity at low x-ray energies. The overall results of this experiment conclusively demonstrated that of the five dosimeters tested no significant dosimeter response dependence on beam hardening was found down to a depth of 15 cm.

2.5 Fractionation and Dose Rate Effects

EBT and XRQA film are comprised of the same active layer components. The new active layer structure was tested for dose rate effects using variously delivered dose rates of (0.16 to 5.71) Gy min⁻¹, and showed an 8-fold dose rate effect for post-irradiated scan times < 10 min; the measured values converged and were indistinguishable there after²¹. No dose rate effect is found for films scanned at times > 10 min post-irradiation⁴⁰. Additionally, fractionation effects were investigated using four different exposures to film at 30 min intervals compared to a single exposure to film; the ensuing results measured a fractionation effect $\leq 2\%$ ²⁹.

2.6 Film Response Sensitivity to Ambient Factors

Environmental factors such as temperature, humidity, and room lighting have been shown to affect the response of RCF during and after radiation exposure. The RCF chemical structure was shown to be temperature dependent during irradiation, ~5% increase in response with temperature increases from (20-40)°C, and ~2% per °C for temperature increases from (40-50)°C^{7, 42}. Temperatures > 60°C cause instability in the polymerization reaction and should be avoided². Changes in relative humidity in the range of (6-94)% can effect RCF dose response by $\pm 2\%$ ⁴³. Ambient lighting in most lab and clinical settings are comprised of a fluorescent spectrum with a luminance value measured to be ~500 cd m⁻². Two sets of films were exposed at two x-ray tube potentials over a range of doses. One set of films was left in the dark and the other set was placed

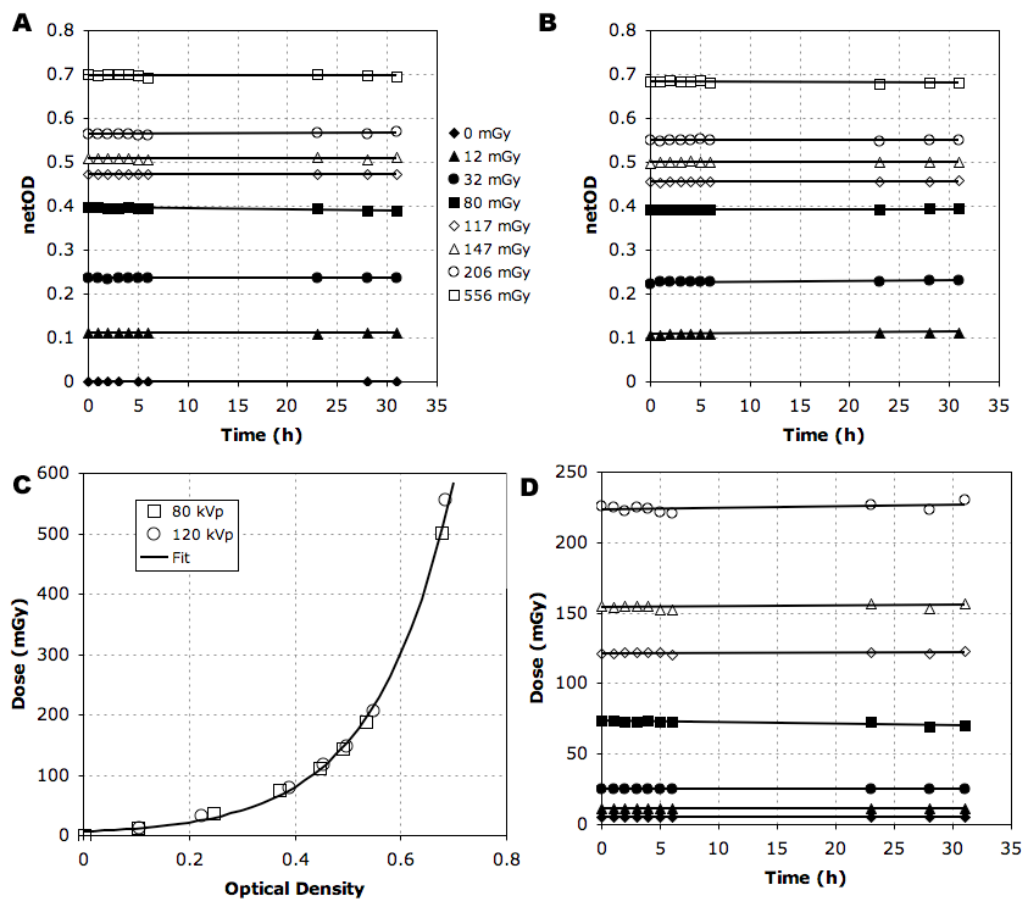


Figure 2.6 Ambient light contamination

XRQA film were exposed to (0-500) mGy and scanned 24 hours later. One set of film was exposed to continuous white light from a film view box (A). Another set was kept in the dark (B). A calibration curve was developed (C) and applied to the light exposed film for a calculated change of $9.9E-5 \text{ mGy hr}^{-1} \text{ m}^2 \text{ cd}^{-1}$ (D).

directly in front of a radiographic film view box, see Figure 2.6. An average view box luminance measurement is 1500 cd m^{-2} ⁴⁴. The maximum variation in light induced OD, as a function of dose, was calculated to be $9.9E-5 \text{ mGy hr}^{-1} \text{ m}^2 \text{ cd}^{-1}$, which was in good agreement with a previous report³³. RCF left in an average room would require $\geq 30 \text{ hr}$ for an OD induced change from ambient light to contribute $\sim 0.03 \text{ mGy}$ to the film's

overall signal after digitization. A digitization device's light source (with an average luminance of $22,000 \text{ cd m}^{-2}$) would require 1,400 sec of continuous exposure to contribute $\sim 0.03 \text{ mGy}$ to the film³³.

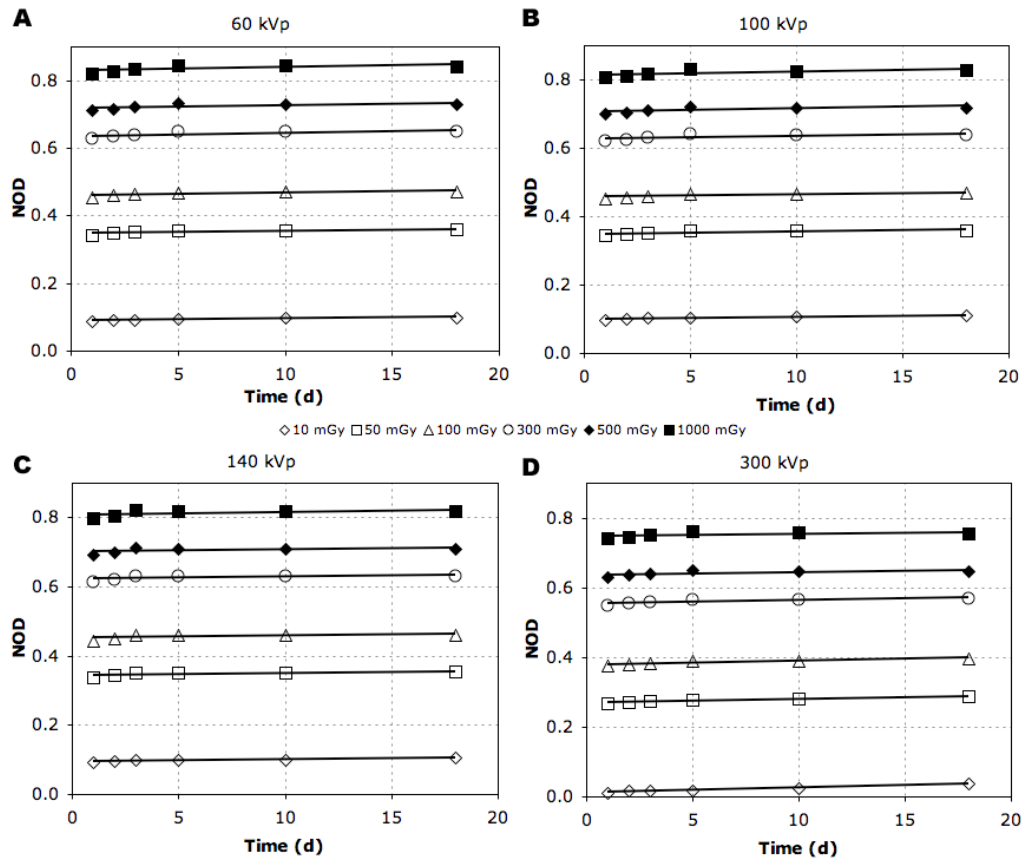


Figure 2.7 XRQA OD growth with time after post exposure digitization

XRQA film was tested for post exposure OD growth from the time of initial digitization ($t=0$). Films exposed at photon energies from (60-320) kVp were investigated (only 4 energy plots are shown for clarity). For times $> 24 \text{ hr}$ (which corresponds to $t=0$ on plots) $\Delta OD < 1\%$ for approximately 20 days.

2.7 Stability of Measured Film Response with Time

RCF is not processor-fixed like radiographic film, but is susceptible to ambient and latent-kinetic effects in the polymerization reaction. Of necessity, the films require time for the solid state kinetic effects to stabilize. The amount of latent kinetic effects, i.e., change in OD (ΔOD) post exposure, was tested. The films were given 24 hours to stabilize and were then scanned once a day, for the first five days, and approximately every five days thereafter. ΔOD was measured as the average difference between the final reading and the first reading. EBT film measured (6-8)% ΔOD for the first 24 hr post initial scan, where the majority of the ΔOD occurred for $t < 6$ hr and for $t > 6$ hr accounted for 1% ΔOD ^{34, 45}. XRQA film was investigated for ΔOD for (10-1000) mGy at (60-320) kVp, see Figure 2.7, and measured a $\Delta OD < 1\%$ for $t > 24$ hr³³.

2.8 Conclusion

EBT and XRQA film were tested for a full range of film characteristics to identify film limitations and optimal working parameters. The characteristics of EBT and XRQA RCFs were investigated: radiation interaction with film structure; light interaction with film structure for optimal film readout (densitometry) sensitivity; range of absorbed dose measurement; dependence of film dose measurement response as a function of changing radiation energy; fractionation and dose rate effects on film measurement response; film response sensitivity to ambient factors; and stability of measured film response with time were reported here. EBT film was shown to have $< 3\%$ difference in

OD response when exposed to energies ranging from (75 to 18,000) kV, a near water equivalent Z_{eff} , a dynamic dose range of (10^{-1} - 10^2) Gy, and best digitized using transmission densitometry. XRQA film was shown to have a 12 fold increase in sensitivity to lower photon energies compared to EBT film, a difference of 25% in OD response when comparing (120 to 320) kV, a larger Z_{eff} of ~ 25 , a dynamic range of (10^{-3} - 10^0) Gy, and is best digitized using reflective densitometry due to an opaque film layer on the back side of the film. Both XRQA and EBT films were shown to have a ΔOD of $\sim 1\%$ for $t > 24$ hr post film exposure; a ΔOD of ~ 0.03 mGy hr^{-1} when left exposed to fluorescent room lighting; a negligible dose rate and fractionation effect when operated within normal clinical ranges; and a film readout best tuned for red light (specifically 635 nm) when the films are exposed within optimal dose levels. With good experimental handling techniques, XRQA and EBT film are shown to be robust dosimeters that are well suited for clinical and experimental laboratory environments.

3 Radiochromic Film Digitization and Densitometry

Historically, two digitization methods have existed for film densitometry: point and line source light scanning. Point densitometry source light projects a small area of light (A_{light}) on a given area of film (A_{film}) such that $A_{light} \ll A_{film}$. Typical point densitometers in existence today are: manual single-read, see Figure 3.1(A), mechanized scanning single-read (experimental)⁴⁶, and lasers (e.g., HeNe). The primary advantage of the single-read system is a reduction of measured light from indirect light scattered off of the film's multiple layers. The limitations of point densitometers are: digitization speed²; resolution—as defined by the focal spot width and translational stepping size; and coherent light artifacts⁴⁷ that are specific to laser scanners only. An example of a mechanized single-read scanner's performance for RCF readout was shown to require 22 min for a 1 mm pixel scan resolution over a 15 cm² area of film⁴⁶. Lasers are not used for digitization of RCF because of a Moiré interference fringe patterns produced in the digitized film response from coherent light scatter off of the different layers of the film construction.

Line source scanners utilize a long light-tube that illuminates a full length of one dimension of the film at a time. Typical line scanners consist of medical grade film scanners, e.g., VXR (Vidar)⁴⁸ and MultiRad (Howtek)⁴⁷, or commercial flat bed document/photo scanners, see Figure 3.1(B-C). The primary advantage of the line source scanners is the digitization speed, e.g., a (15x15) cm² piece of film is scanned in ~3 sec at



Figure 3.1 Densitometers

Two types of densitometers are available for RCF OD readout: point and broad light source. Typical point source devices emit a very small spot of light on the film and read one OD value at a time (A). A broad light source device investigated in this work is a commercial flatbed photo scanner (B-C). Images shown here were taken from: www.xrite.com (A) and www.epson.com (B-C).

0.5 mm resolution. Disadvantages of the Howtek and Vidar scanners are price (~10-100 times greater in price than flat bed scanners) and they are limited to transmission scanning at red wavelengths only. The flat bed scanner was chosen as the primary film digitizer in this work owing to its: availability, cost, dynamic range, functionality, and speed. However, for quantitative RCF dosimetry using a flat bed scanner, several disadvantages have been reported⁴⁹⁻⁵⁰. First, lateral OD variations in film scans appear bowed due to light detection asymmetry. Second, the CCD detector has a narrow acceptance angle along the axis of source light translation causing the readout response to be rotationally inhomogeneous and suffer from anisotropic scatter. Several authors have published on the topic of accurate RCF digitization using flat bed scanners in transmission^{12, 49-56} and reflective^{18, 57-58} scan modes. The purpose of this investigation was

to determine the intrinsic and operational limitations of two flat bed scanners and define a standard operational protocol (SOP) to maximize RCF digitization accuracy and precision.

Two scanners of different size and cost were investigated: the EPSON Perfection Photo V700—a small photo scanner with maximum scanning capacity of (20.3x25.4) cm, see Figure 3.1(B), and the EPSON 10000XL—a large document/photo scanner with maximum scanning capacity of (31.0x43.7) cm, see Figure 3.1(C). Both scanners employed a white, cold-cathode fluorescent lamp as the light source, and an EPSON Color Matrix CCD™ line scanner photoelectric device for image digitization. The following factors were investigated to determine the scanners intrinsic limitations: OD readout accuracy; OD readout range; and scanner light source and CCD element temporal stability. The following factors were investigated to determine the operational limitation of the film dosimetry: variability in readout response to film rotation with respect to CCD acceptance angle; anisotropic scatter effects on film response with respect to CCD acceptance angle; and film response sensitivity to changes in positional setup.

3.1 Scanner Accuracy and Precision

Accuracy can be understood as a measurement of the systems spatial and OD fidelity to a known standard². Spatial accuracy was investigated by scanning a grid pattern of known size and spacing for both scanners in transmission and reflection

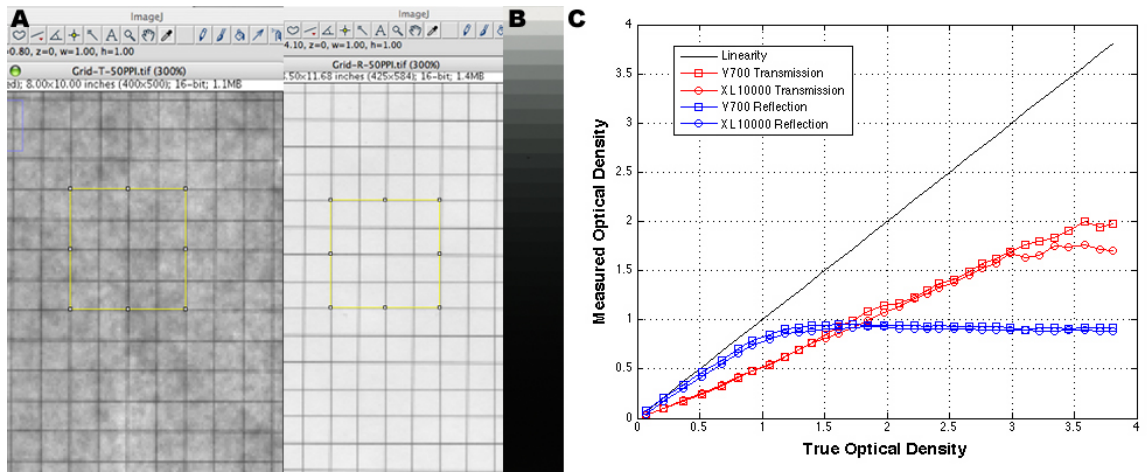


Figure 3.2 Spatial and intrinsic accuracy for EPSON V700 and 10000XL scanners

A grid pattern was scanned in transmission and reflection mode on the EPSON V700 and 10000XL scanners; only one scanner worth of data is shown (A). A 1 in² square (yellow) was compared in digital and true space for scanner spatial accuracy. Transmission and reflection OD measurements for both scanners were measured using an NIST calibrated OD step wedge (B) as a means to determine inherent scanner accuracy (C).

mode. The measured grid was checked for distortion in orthogonal directions and compared to physical measurements of the grids using a ruler, see Figure 3.2(A). The EPSON V700 and 10000XL digital measurements were both 1.0 cm² squares, and equal to the ruler measurements. OD accuracy is the scanners ability to reproduce true OD values and is a measurement of the upper and lower limits of digitization. The intrinsic accuracy of the scanners was investigated in both reflection and transmission mode by scanning a NIST calibrated OD step wedge that has an OD range of 0.07-3.81, see Figure 3.2(B). The scanned values were plotted versus the provided NIST values, see Figure 3.2(C). The reflection mode values measured a linear working range of OD up to values of ~0.9. For OD values > 0.9 the CCD detector became saturated. The transmission

mode measurements produced a larger linear working range of OD up to a value of ~ 1.7 but with an OD relationship defined as: $OD_{measured} \cong 1/2 \cdot OD_{true}$.

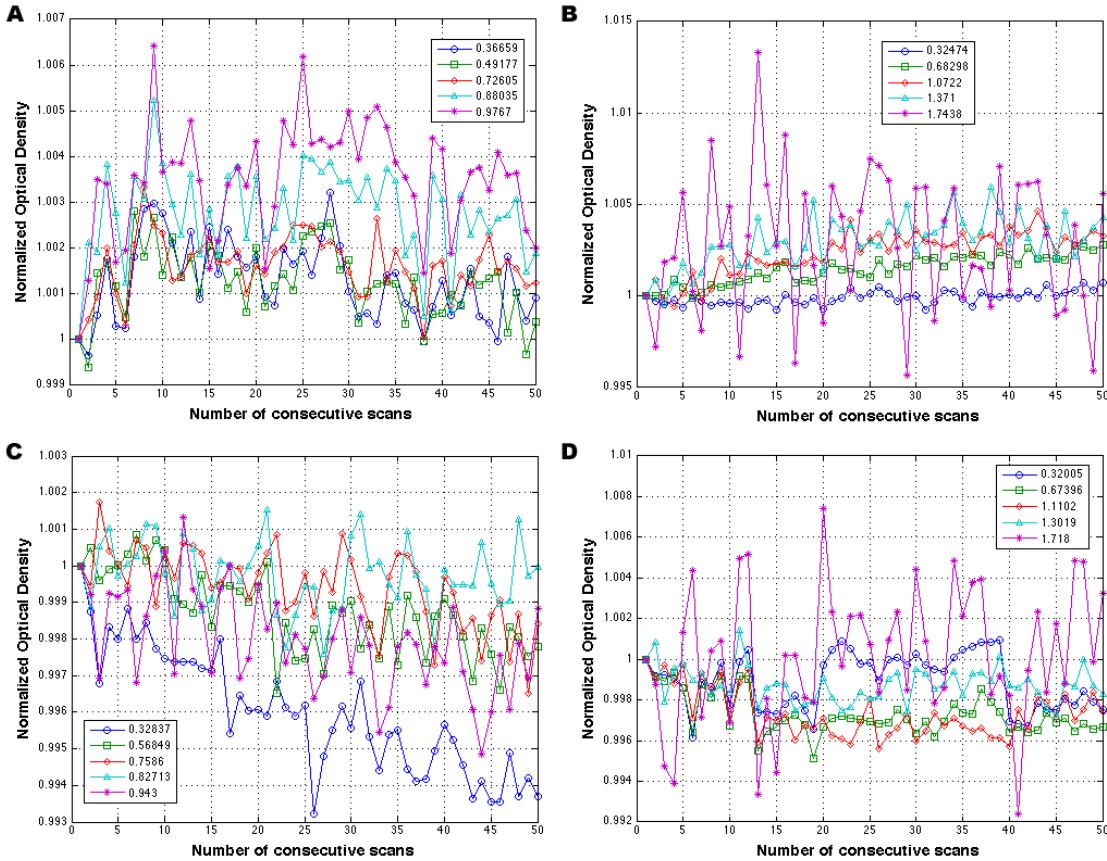


Figure 3.3 Light source stability for EPSON V700 and 10000XL scanners

EPSON V700 and 10000XL flatbed scanners were investigated for light source temporal stability. A NIST calibrated OD step wedge, Figure 3.2(B), was scanned 50 consecutive times. Reflection and transmission mode scanning for the EPSON V700 measured an overall percent deviation of 0.7% (A) and 2% (B), respectively, and for the EPSON 10000XL measured an overall percent deviation of 0.9% (C) and 1% (D), respectively.

The EPSON V700 and 10000XL were tested for light source stability using a NIST calibrated step wedge, see Figure 3.2(B), which was scanned 50 consecutive times in

both reflection and transmission scanning modes. Five averaged ROIs were used to sample the OD working range for each scanning mode, reflection—0.07-0.90 and transmission—0.07-1.70, and plotted versus scan number, see Figure 3.3. Each plot was normalized to the first scan. Reflection and transmission mode scanning for the EPSON V700 measured an overall percent deviation of 0.7% and 2.0%, see Figure 3.3 [(A) & (B)] respectively, and for the EPSON 10000XL measured an overall percent deviation of 0.9% and 1.0%, see Figure 3.3[(C) & (D)] respectively. Generally, after 5 consecutive scans, the scanner response is linear about its mean noise variation. The initial change in OD value is due to the fact that EPSON scanners do not illuminate their light sources until the scanner has been prompted to “Preview” or “Scan.” The first ~5 scans measure greater ΔOD as the light source approaches a stable temperature with time. Light source stability measurements and approximate “warm up” times reported here are in good agreement with previously reported values^{53, 55}.

The EPSON V700 and 10000XL scanners were tested for CCD sensor stability by measuring the change in dark current with scanning time. Inherent to all CCD elements is a thermally induced current from excitation of electrons in the material of the CCD elements. Dark current is a measurement of the baseline signal of the CCD sensors in the absence of light. CCD quality was investigated for the scanners by acquiring 50 consecutive scans in the absence of light at room temperature (25°C). The average of each scan was normalized to the average value of the first scan. CCD element stability

was determined from the normalized plotted response of the 50 consecutive scans, see Figure 3.4. The dark current signal measured variability in response of 7% for the V700 and 5% for the 10000XL. The average magnitude of the dark current on the CCD elements, for scans of ~15 min, was ~0.5 electrons s^{-1} at 25°C for V700 and for the 10000XL it was ~0.9 electrons s^{-1} at 25°C.

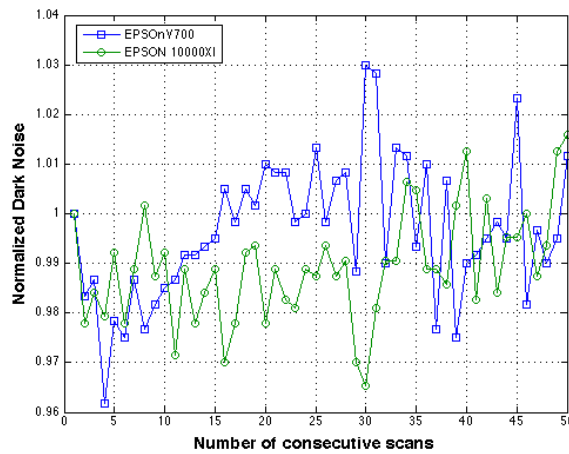


Figure 3.4 CCD element stability for EPSON V700 and 10000XL scanners

EPSON V700 and 10000XL flatbed scanners were investigated for CCD temporal stability. 50 consecutive dark field scans were performed. The EPSON V700 measured an overall variation of 7% and the EPSON 10000XL measured an overall variation of 5%.

3.2 Digitization Procedures and Post-Processing Techniques

The following is a review of the operational limitation of the scanning procedure and post-processing techniques for transmission and reflection scans. To maximize measurement accuracy, a digitization protocol must minimize film-positioning error by

establishing consistent setup guidelines and account for light non-uniformity post-processing corrections.

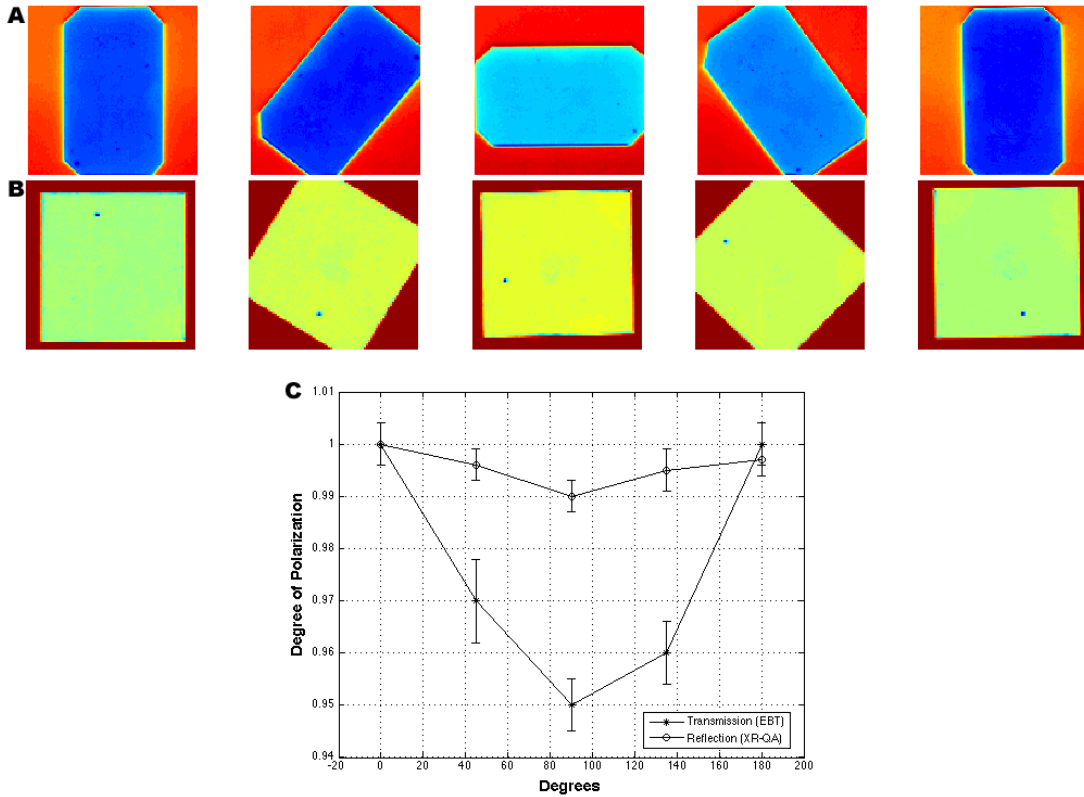


Figure 3.5 Film readout due to the effects of rotation in the setup

A piece of XRQA film (A) and EBT film (B) was rotated through 180°. ROIs were drawn in the center of both films and were plotted versus rotation degree as a measure of the magnitude of the polarization effect (C).

A change in film intensity output is measured when the film is rotated about an angle with respect to the acceptance aperture of the CCD device. The rotation of the film creates a polarization effect. The underlying cause of the polarization effect is presumed to be due to the needle-like-crystalline structure of the active layer, which lie parallel with the shorter length of the RCF size. In this regard, the film acts like a linear wire-

grid polarizer. Therefore when randomly polarized source light is incident upon the film the, light undergoes dichroism and the light emitted from the transmission axis of the film is perpendicular to the grid and physically anisotropic. The anisotropy creates a strong asymmetric light absorption in one axis of the propagating electric field of the light on the CCD detectors. This is shown to vary the light intensity output from the film scan through maximums, when the transmitted polarized light (P-state) is aligned with the CCD acceptance aperture opening, and minimums, when the P-state is normal to the aperture. The degree of polarization was investigated for EBT and XRQA film and is shown in Figure 3.5. Unexposed pieces of XRQA, see Figure 3.5(A), and EBT film, see Figure 3.5(B), were scanned from 0° to 180°. XRQA measured a 1% Δ OD per 90° rotation, see Figure 3.5(C), which amounts to an effect of 0.01% Δ OD per degree. EBT film measured a 1% Δ OD per 1° rotation, which is in agreement with a previous report⁵⁹.

Anisotropic scatter is also an effect of the orientation of the active layers crystalline structure with respect to the CCD detector. Light more predominantly scatters at an angle normal to the crystalline structure; thus, when the crystalline structure is aligned parallel with the axis of light source translation, i.e., when the film is scanned in landscape orientation, then a maximum light intensity is measured on the CCD detector, Figure 3.6(A). With greater light intensities comes greater OD resolution. Additionally, three EBT films, corresponding to (1, 4, and 8) Gy, were scanned at seven

locations from the center of the scanner bed, moving laterally off the scanner's central axis, to the edge of the scanning FOV. The responses of the films were normalized to the

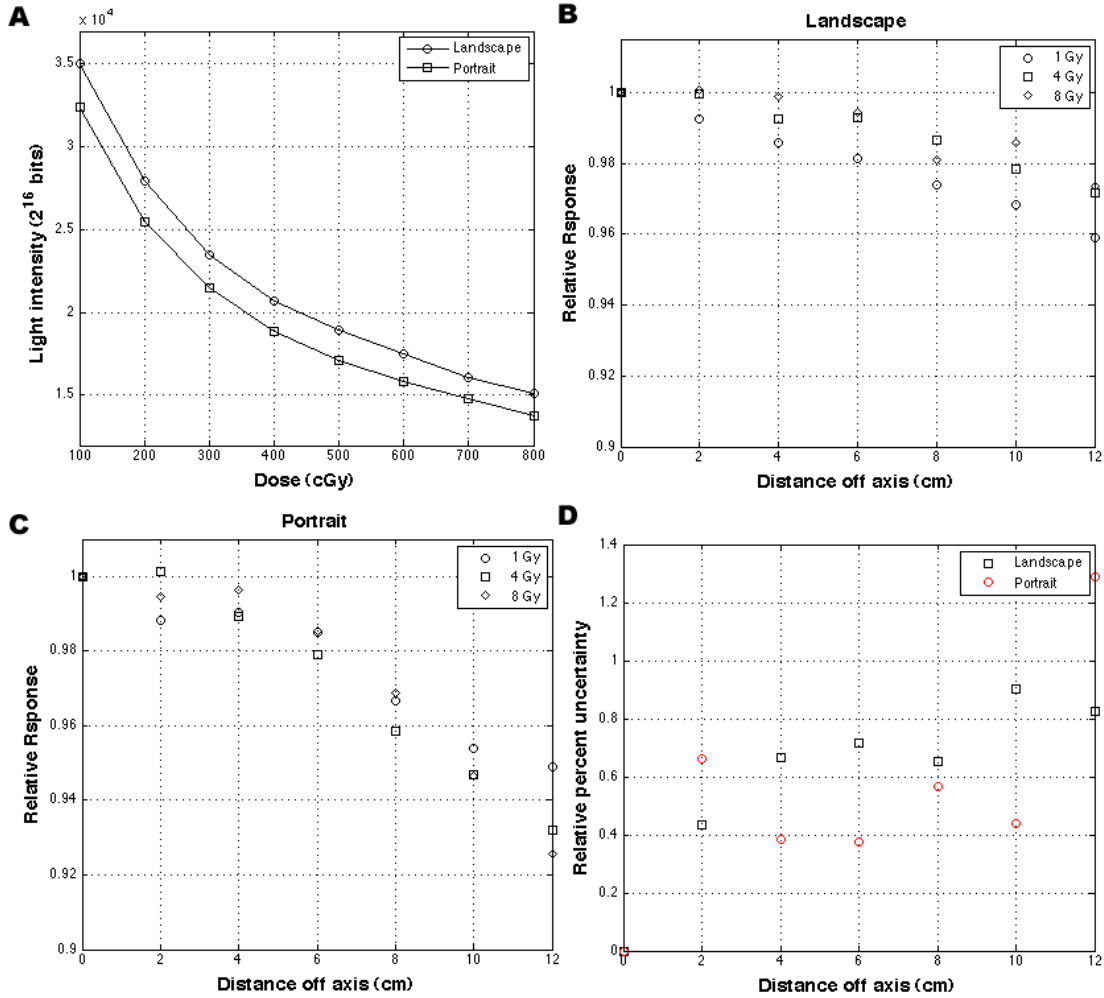


Figure 3.6 Readout effects due to anisotropic scatter

EBT film scanned on an EPSON V700 in landscape and portrait orientation (A). Three EBT films, corresponding to (1, 4, and 8) Gy, were scanned at seven locations from the center of the scanner bed moving laterally off the central axis. Each film was scanned in landscape (B) and portrait (C) orientation. The standard deviation (1σ) of each scan orientation at each distance off axis was measured and plotted in (D).

center film. Each film was scanned in landscape, see Figure 3.6(B), and portrait, see Figure 3.6(C), orientation. Films scanned in landscape mode measured less off-axis variability compare to the portrait mode, but generally the same amount of variability in scanner dose dependence, $\sim 1\%$, see Figure 3.6(D).

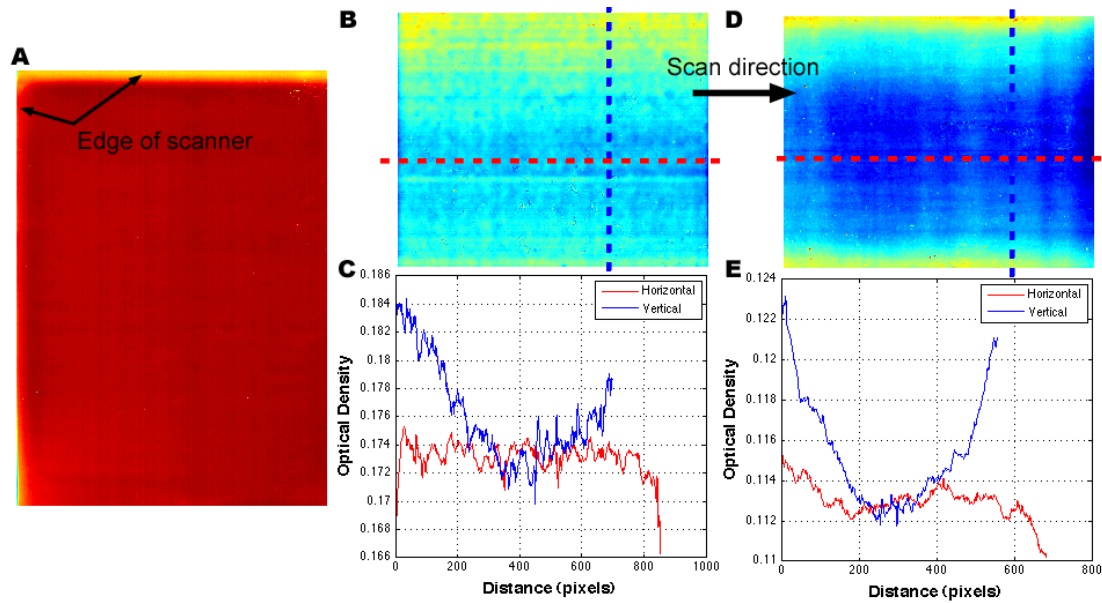


Figure 3.7 Light non-uniformity for transmission and reflection scan modes

Scanner light source non-uniformity was measured for both transmission and reflection scanning. Film should not be placed at edges of scanning field (A). An unexposed piece of XRQA was scanned on the EPSON 10000XL (B) and orthogonal profiles were plotted (C). Similarly, an unexposed piece of EBT film was scanned on the EPSON V700 (D) and orthogonal profiles were plotted (E).

Two types of light non-uniformity exist: (1) anisotropic light scatter normal to the direction of the active layer coating, which was previously discussed, and (2) Light source intensity variations that are measured at the edges of the scanning field of view along the axis of the light source and in the direction normal to the motion of the light

source^{53, 55, 60}, see Figure 3.7. The EPSON 10000XL and V700 scanners were measured for light intensity uniformity using an undeveloped XRQA film for a reflection scan, see Figure 3.7(B), and EBT film for a transmission scan, see Figure 3.7(D). Only one scan mode per scanner is shown for clarity. Similar reflection results for the V700 and transmission results for the 10000XL were measured. Orthogonal line profiles were measured parallel to the axis of light source translation (horizontal) and along the axis of the light source length (vertical), see Figure 3.7[(C)&(E)]. A minor fluctuation in scanner light uniformity of ~2%—for reflection scanning, and ~4%—for transmission scanning, was measured in the direction of the light source translation axis (horizontal). A greater ΔOD in scanner light uniformity of ~7%—for reflection scanning, and ~9%—for transmission scanning, was measured in the direction parallel to the axis of the light source length. Lower light intensity at the edge of the scanning field of view is due to the edges of the light sources not contributing similar light intensity as the middle portion, see Figure 3.8.

3.3 Image Post Processing

Once the film has been irradiated and digitized, the digital image requires post-processing for analysis. The processing of the films consists of converting the raw intensity values into OD, a recognized universal format for reporting film response change; correcting the film for scanner light inhomogeneities; and calibrating the film response to absorbed dose.

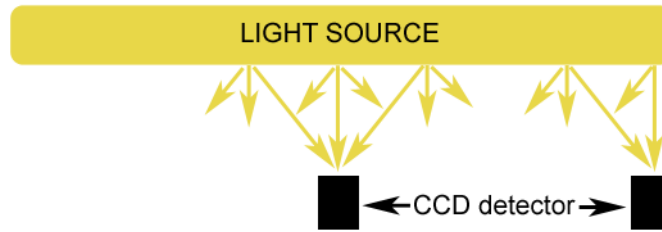


Figure 3.8 Relative light intensity on CCD detector elements

CCD detector elements at the periphery of the scanning field of view receive less light from the light source due to the geometry of the linear light source. The lower light output at the peripheries of the scanning field of view create an artificially darker area that will be perceived as a lower OD value. Film should not be placed at the edge of the scanning field of view with out corrections being applied.

3.3.1 Conversion of Film Digital Response to Optical Density

As a means to convert the raw intensity pixel values to OD and to account for the subtle differences in film manufacturing, each exposed film is normalized by its average pre-exposed response. This allows all films to be compared from an equal basis of zero. A report⁵² defined this response as the net OD (netOD). The mathematical calculation of netOD, with respect to the raw pixel value readout for pre-exposed (I_{unexp}), post-exposed (I_{exp}) films, and their accompanying dark field (I_{bckg}) scans, is shown here:

$$\begin{aligned}
 netOD &= OD_{exp} - OD_{unexp} \\
 &= \log_{10} \left(\frac{I_0}{I_{unexp} - I_{bckg}} \right) - \log_{10} \left(\frac{I_0}{I_{exp} - I_{bckg}} \right) \\
 &= \log_{10} \left(\frac{I_{unexp} - I_{bckg}}{I_{exp} - I_{bckg}} \right)
 \end{aligned} \tag{3-1}$$

There is no dependence on the original light source (I_0) for netOD. The accompanying error calculation for netOD is defined using propagation of error⁶¹ as established by expanding

$$\sigma_x^2 = \sum_i \left(\frac{\partial x}{\partial u_i} \right)^2 \sigma_{u_i}^2. \quad (3-2)$$

to form the following expression:

$$\sigma_{netOD} = \frac{1}{\ln 10} \sqrt{\frac{\sigma_{I_{unexp}}^2 + \sigma_{bckg}^2}{(I_{unexp} - I_{bckg})^2} + \frac{\sigma_{I_{exp}}^2 + \sigma_{bckg}^2}{(I_{exp} - I_{bckg})^2}}, \quad (3-3)$$

where $\sigma_{I_{unexp}}$, $\sigma_{I_{exp}}$, σ_{bckg} are the standard deviations of the measured quantities I_{unexp} , I_{exp} , and I_{bckg} respectively. The intensity quantities I_{unexp} , I_{exp} , and I_{bckg} are an average over multiple scans as defined by the weighted mean expression:

$$I_x = \frac{\sum_{i=1}^n \left(\frac{I_{x_i}}{\sigma_{x,1}^2} \right)}{\sum_{i=1}^n \left(\frac{1}{\sigma_{x,1}^2} \right)}, \quad (3-4)$$

where I_x is the intensity from either the unexposed, exposed, or background measurement, and $\sigma_{x,i}$ is the corresponding standard deviation of n scans of film with an I_x response. The accompanying statistical uncertainty of I_x is defined by:

$$\sigma_{I_x}^2 = \frac{1}{\sum_{i=1}^n \left(\frac{1}{\sigma_{x,1}^2} \right)}. \quad (3-5)$$

3.3.2 Light Non-uniformity Correction

The light non-uniformity parallel to the axis of source light length was shown to be a contributor of readout non-uniformity, see Figure 3.7 and Figure 3.8. When correcting for light non-uniformity, great care should be exercised to preserve the underlying non-uniformity being measured. The light non-uniformity has been shown to be temporally reproducible thus allowing for a correction factor matrix (CFM) to be established. One approach introduced by the film manufacturer was to develop the CFM utilizing the mean pixel value from a scanned unexposed film and divided pixel-by-pixel the unexposed scanned film to create a CFM:

$$CFM(i,j) = \left(\frac{x(i,j)}{\bar{x}(i,j)} \right), \quad (3-6)$$

where $x(i,j)$ is the pixel located at the i^{th} and j^{th} location on the scanner bed coordinates and $\bar{x}(i,j)$ is the average pixel value of the unexposed film. The CFM is developed using the pre-exposed film before the film is irradiated, and thus allows for a custom film-to-film correction. For the CFM to accurately account for the light source non-uniformity, the pre-exposed and post-exposed films must be: correctly registered and scanned in the same orientation and location on the scanner bed; the film properties must not change when exposed to radiation; and the CFM must not vary with changes in dose. To test CFM robustness for a variety of ODs, CFMs were created for netOD values ranging from 0.24–0.66 and investigated for inter-CFM variation. The CFM measured responses varied from (0.3–0.5)% (1σ). The results indicate that a CFM is dose

independent and can be created per film exposure and correctly account for spatial non-uniformities in light intensities⁶².

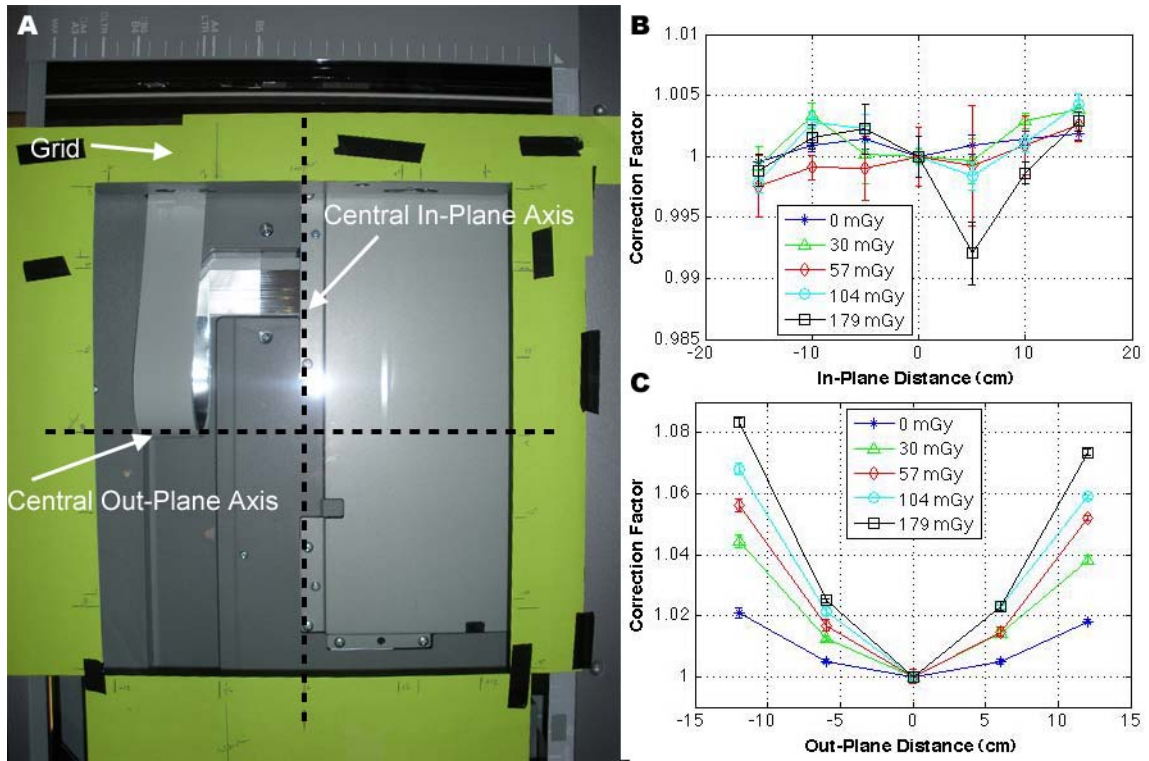


Figure 3.9 EPSON 10000XL flat field response

The EPSON 10000XL is shown from a top-view of the scanning bed (A). A paper grid was secured in place on the surface of the scanner for accurate placement of the RCFs. The light source (not shown) transverses the scanning bed from top of the figure to the bottom along the central in-plane axis. The scanned films were normalized along the central in-plane axis. The scanned film responses are shown for in-plane (B) and out-plane (C). In-plane results demonstrate a uniform light source scan time. Whereas the variations in the out-plane axis demonstrates the light non-uniformity of the long-diffuse light source. A dependence on scanner light non-uniformity with dose is also seen. With higher dose, i.e. the more optically dense film, less light is able to penetrate the film. With lower light signal on the CCD detector, the scanner becomes more sensitive to non-uniformities in the diffuse light source.

A second option to correct for light non-uniformity is not to correct for the non-uniformity. One advantage of using the EPSON 10000XL is that its scanning field of view is much larger than the V700 and therefore has a larger uniform light field of view. The light non-uniformity for the 10000XL was tested by using one 2 cm² piece of RCF and scanning the film at five locations along the axis of the light source length (out-plane) and seven positions along the axis of the light source translation (in-plane). A grid was established on the scanner bed, see Figure 3.9(A), and a large ruler was used to align each piece of film. Each location was scanned five times and averaged for a total of 175 scans over 35 locations using equations (3-4) and (3-5). Furthermore, the scanner was tested for light non-uniformity as a function of dose levels. Each set of 35 locations was scanned for XRQA films exposed to (0, 30, 57, 104, and 179) mGy. Each scan was normalized to the central axis indicated by the vertical dotted line in Figure 3.9(A). The normalized plots of all five dose levels are shown for in-plane, Figure 3.9(B), and out-plane, Figure 3.9(C). In-plane variability at all dose levels, except one point at 5 cm for the 179 mGy dose level, did not change more than 1% from the central axis value. Out-plane measured the greatest variability from the central plane over all dose levels. However, the central (11 to 12) cm measures only ~2% variation from the central axis for all dose levels tested. If lower dose levels are measured then the central uniform region grows and allows for bigger film dimensions scanned with a tolerance of 2% error due to light non-uniformity.

3.3.3 Film Response Calibration to Absorbed Dose

In order to calibrate RCFs of unknown doses for quantitative analysis, an absolute dose calibration curve is developed. The calibration curve consists of three essential components, (1) accurate absorbed dose measurements plotted as a function of (2) the measured film response and (3) an accurate fitting of the data using a least-squares regression method. To accurately measure absorbed dose, an independent dosimeter is used, e.g., an ion chamber; where absorbed dose (D) is calculated as a function of a raw ionization readout ($X(R)$):

$$D(\text{cGy}) = X(R) \cdot P_{TP} \cdot P_{ion} \cdot P_{pol} \cdot P_{elec} \cdot \kappa \cdot fFactor_{medium}^{energy} \left(\frac{\text{cGy}}{R} \right). \quad (3-7)$$

Here $X(R)$ must be corrected for read-out signal variations at the time of measurement due to: the temperature and pressure (P_{TP}), ion recombination (P_{ion}), polarity (P_{pol}) effects, and inherent bias due to electrometer (P_{elec}) and ion chamber (κ) dependence on radiation energy as established by an accredited dosimetry calibration laboratory (ADCL). An explanation of the ion chamber correction factors can be found in appendix A.1. The f -Factor ($f - Factor_{medium}^{energy}$) is used to correct for attenuation properties of a medium with respect to air and is calculated using the following expression:

$$f - Factor_{medium}^{energy} \left(\frac{cGy}{R} \right) = 0.869 \left(\frac{cGy}{R} \right) \cdot \left(\frac{\left(\frac{\mu_{en}}{\rho} \right)_{medium}^{energy}}{\left(\frac{\mu_{en}}{\rho} \right)_{air}^{energy}} \right), \quad (3-8)$$

where 0.869 cGy R⁻¹ is derived from the definition of the roentgen (R) and $\overline{W_{air}}/e^{63}$, and $\mu_{en} \rho^{-1}$ are mass energy attenuation coefficients found on the NIST website³⁵.

The resulting dose measurements are plotted as a function of film netOD and a proper fitting function is fit to the data. The response of RCF to dose is nonlinear and therefore requires a multivariate regression function. Many fitting function types have been reported in the scientific literature. However, of all the types, the fitting functions can be distilled into two broad classifications:

$$D_{fit}(netOD; a_n) = \sum_{n=0}^m a_n \cdot netOD^n, \quad (3-9)$$

$$D_{fit}(netOD; a_n) = a_1 \cdot (e^{a_2 \cdot netOD} - 1). \quad (3-10)$$

The first set are polynomial functions represented by equation (3-9), developed by Devic *et al*^{49,52}. The second set are exponential functions represented by equation (3-10). Equation (3-10) is a modified variation on an exponential function first reported by Rampado *et al*.³³; the equation was modified to include a second optimization parameter, a_2 , in the exponential, which allowed the exponential function to better adjust with the rate of change in OD for higher dose measurements; this was necessary to account for saturation effects of the RCFs at very high exposures not accounted for in the original

report by Rampado *et al.* To determine the best universal fitting function for XRQA and EBT films, the following criteria were explicitly assumed to test equation (3-9) and equation (3-10):

1. The fitting function will be linear in its parameters
2. The fitting function will pass through zero when dose = 0 and netOD = 0; thus, the coefficient a_0 from equation (3-9) will be held to zero and the exponential term in equation (3-10) must be subtracted by one.
3. The fitting function will be monotonically increasing (monotonicity is defined for two points that lie on a curve, x_1 and x_2 , such that $f(x_1) \leq f(x_2)$ thereby preserving the order)
4. The fitting function will provide a universal coverage over a range of absorbed dose levels that extend from the very low to (180-190)% of the maximum optimal dose.
5. The fitting function will minimize the fitting parameters such that the error in the fitting function will be $\leq 2\%$ of the known dose.

A Levenberg-Marquardt algorithm (LMA)⁶⁴⁻⁶⁵ was developed as an analytical method to optimize the a_n coefficients in equation (3-9) and equation (3-10). The following is a description of the implementation of the LMA and the development of the calibration curve for RCF.

The LMA is a hybridization between the Gradient Search method and the Gauss-Newton analytical algorithm used for regression fitting. The hybridization of the two methods was used to maximize the strengths of each technique and minimize their weaknesses. The Gauss-Newton algorithm is comparatively the fastest algorithm of the two, but it requires good initial heuristic controllers, or a good initial guess of the fitting parameters, to start the algorithm within the general area of the global minimum on the hypersurface in parameter space or it can get stuck in local minima. The Gradient Search is capable of starting far from the global minimum on the hypersurface, thus not requiring robust initial estimations of the fitting parameters, but it does not converge rapidly. The LMA utilizes the Gauss-Newton algorithm to compute a simple first order expansion of the fitting function to place the search within the local region of the global minimum then the Gradient Search method is employed to step along the steepest descent of the hypersurface, avoid local minima, and converge more rapidly on the global minimum. At the heart of the LMA is an optimization in the sum of squares of the deviations and an adaptive damping factor, λ , used to smoothly modify the algorithms incremental descent along a path of the hypersurface. The damping factor can also be seen as a fine/gross controller, i.e., the LMA will speed up in flat regions of the hypersurface and slow down in the gradient regions⁶⁵. The LMA is empirically defined as follows:

$$(J^T J + \lambda \cdot \text{diag}(J^T J)) \cdot \delta = J^T \cdot [D_{\text{measured}} - D_{\text{fit}}(\text{netOD}; a_n)]. \quad (3-11)$$

The LMA is executed in the following order:

- (1) A Jacobian (J) vector is formed:

$$\left[\frac{\partial D_{\text{fit}}}{\partial a_{n+1}}, \frac{\partial D_{\text{fit}}}{\partial a_{n+2}}, \dots, \frac{\partial D_{\text{fit}}}{\partial a_n} \right], \quad (3-12)$$

- (2) A Hessian (H) matrix is formed by computing the product of the transposed Jacobian

$$H = [J^T J], \quad (3-13)$$

- (3) Compute difference (ΔD) between the known doses and either equation (3-9) or equation (3-10) using initial estimates for the coefficients (a_n).

$$\Delta D = D_{\text{measured}} - D_{\text{fit}}(\text{netOD}; a_n), \quad (3-14)$$

- (4) Calculate the dose error (D_ε) between the fitting function and the known calibration points. This will be used to terminate the LMA when $D_\varepsilon < 10^{-5}$.

$$D_\varepsilon = [\Delta D \bullet \Delta D], \quad (3-15)$$

- (5) Increment the H matrix by λ

$$H_\lambda = H + (\lambda \cdot [\text{eye}] + \text{diag}(H)), \quad (3-16)$$

- (6) Update the $D_{\text{fit}}(\text{netOD}; a_n)$

$$\delta a_n = H_\lambda \cdot (J^T \cdot \Delta D) \quad (3-17)$$

- (7) Re-compute $\Delta D(a_n + \delta a_n)$ if $\Delta D(a_n + \delta a_n) > \Delta D(a_n)$ then increase λ by a factor of 10 else if $\Delta D(a_n + \delta a_n) < \Delta D(a_n)$ then decrease λ by a factor of 10. Repeat steps 1 through 7 but substituting the new $a_n' = a_n + \delta a_n$.

The minimization algorithm will run until the D_ϵ is $< 10^{-5}$ or an equivalent predetermined termination value is reached.

The best fitting function metric was determined by a combination of a coefficient of determination calculation and a point-by-point comparison between the known dose values and the fitting function estimated values. The coefficient of determination, or as it is colloquially known as the “R²”, is a global goodness-of-fit measurement and determines the best fitting function for the measured data by scoring the correlation of the fitted functions with the data. A scored curve would receive a value between 0-1, where 1 was the strongest measurement of correlation and 0 represented no correlation. The following is the common mathematical definition of R²:

$$R^2 = \frac{regSS}{regSS + resSS} \quad (3-18)$$

where the regression sum of squares (*regSS*) is the difference between the fitted dose value (D_{fit}) and the average value of the measured doses ($D_{measured}$) as determined by:

$$regSS = \sum_i \left(D_{fit,i} - \bar{D}_{measured} \right)^2, \quad (3-19)$$

and the residual sum of squares (*resSS*) is the difference between $D_{measured}$ and D_{fit} as determined by:

$$resSS = \sum_i \left(D_{measured,i} - D_{fit,i} \right)^2. \quad (3-20)$$

Five power series polynomials and one modified exponential fitting function are plotted, for XRQA and EBT film in Figure 3.10, and their fitted coefficients with coefficient of determination calculated scores are shown in Table 3-1. The modified exponential fitting function out scored the power series polynomials for both XRQA and

Table 3-1 Calibration fitting parameters

Five power series polynomials, $n = 1-3$, and a modified exponential were compared as calibration functions for both XRQA and EBT films. The fitting parameters (n) and coefficient of determination (R^2) calculations are shown.

n	XRQA				EBT
	Low	Medium	High	All	All
1	0.9768	0.8863	0.4136		0.8825
1.5	0.9986	0.9902	0.8515		0.9933
2	0.9992	0.9944	0.8910		0.9966
2.5	0.9997	0.9972	0.9210	0.9726	0.9987
3	0.9999	0.9946	0.7539		0.9865
Exp	0.9996	0.9992	0.9943	0.9941	0.9996

EBT films at all levels of dose; thus, satisfied criteria 4. However, on closer inspection, a global, one-size-fits-all fitting function did not satisfy criteria 5. When using equation (3-

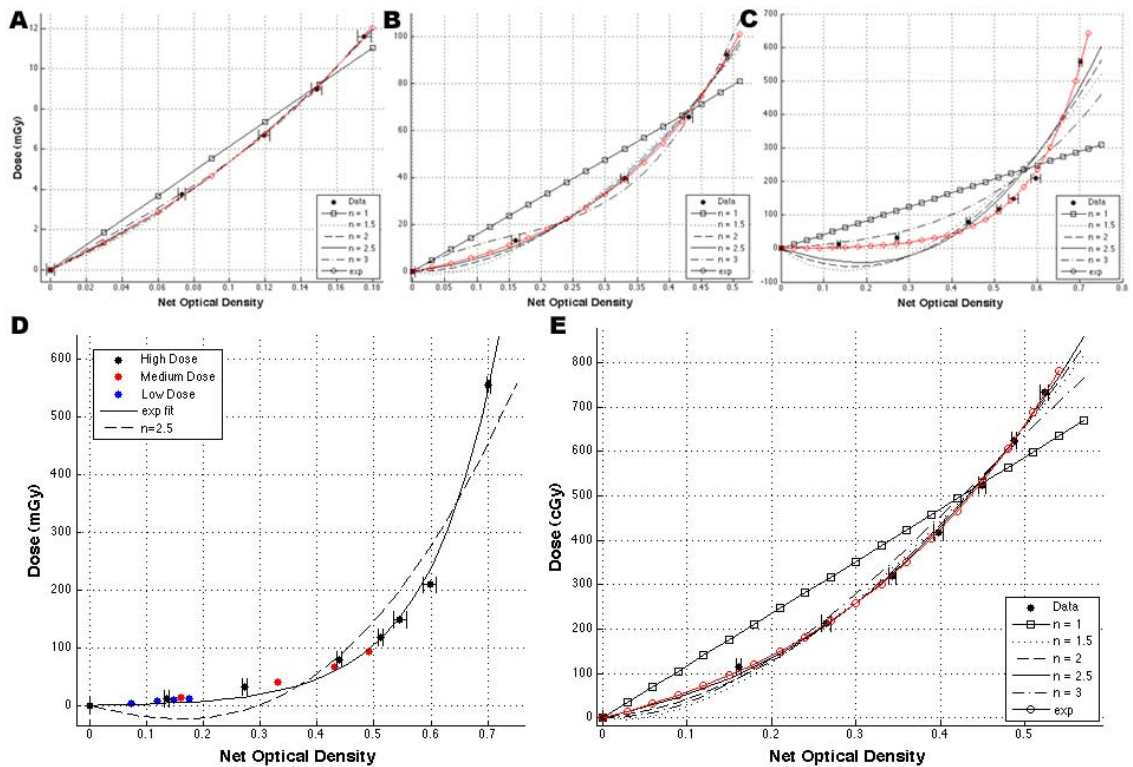


Figure 3.10 Calibration fitting function comparisons

Five power series and one exponential calibration curves were fit to the measured calibration data for XRQA (A-D) and EBT (E) film. The power series fitting functions varied from $n = 1$ to 3 by power increments of 0.5. Plots (A-C) represent three specific dose ranges for XRQA film fitting: (A) low-mamographic, (B) medium-CT, and (C) high-orthovoltage beam dose. Initially, the polynomials fit the measured data fairly well, but as the doses continued to rise, the curve becomes more exponential in the high dose range.

10) to fit dose values from (0 to 1000) mGy, the fitting function receives an R^2 score of 0.9980, see Figure 3.11(A). However, when comparing the dose uncertainty derived from the fitting function, see Figure 3.12 top pane, the low dose region of the fitting function shows an error in excess of 60% of the known dose levels. In fact, only the top four fitting function estimated doses values measure a dose within 2% of the known

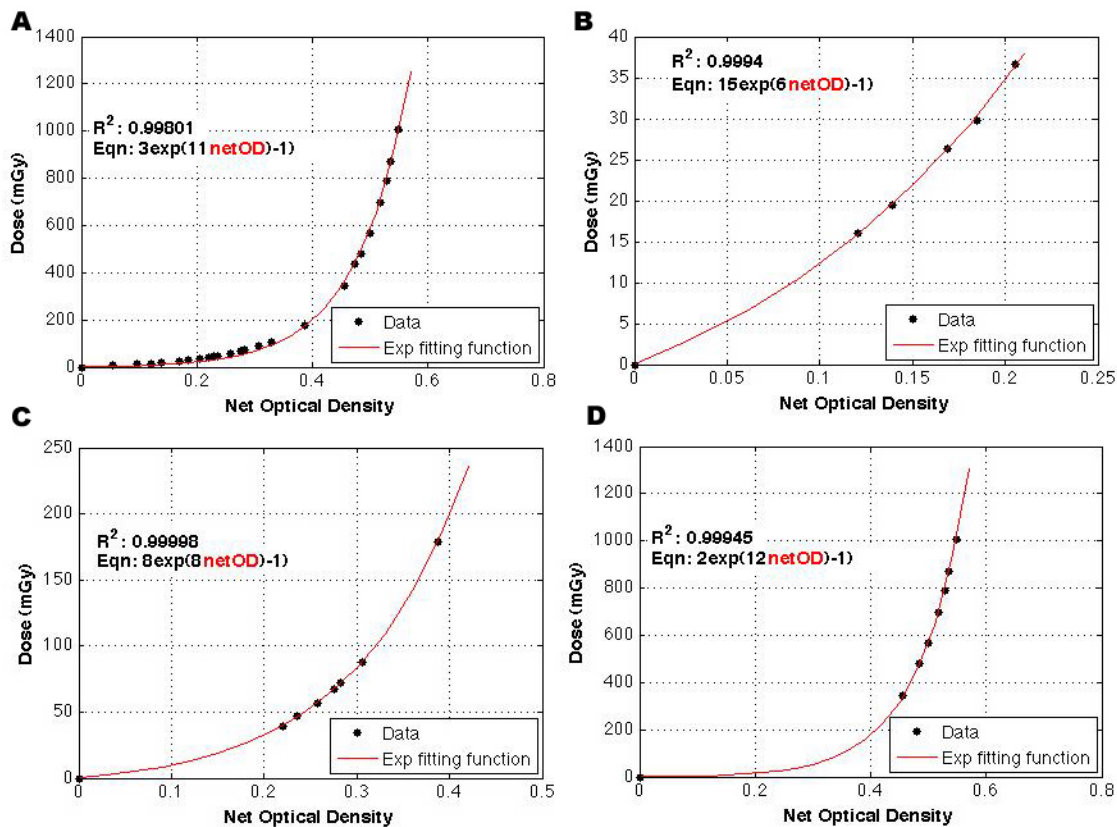


Figure 3.11 Exponential fitting function

A modified exponential fitting function, equation (3-10) was used to fit all measured dose data points over a range of (0-1000) mGy for XRQA (A). The R^2 score for (A) measured a great global goodness-of-fit (0.9980), however, the point-by-point dose uncertainty measured for the low to intermediate dose values was greater than permitted by criteria 5. The data in (A) was divided into three dose categories: low (B), medium (C), and high (D). Fitting functions were established for all categories.

dose values as stipulated by criteria 5. As the RCF measured dose levels approached the upper limits of the scanner's light source penetration ability, the subsequent fitting curvature of the data becomes less exponential as it approached a saturation asymptote. The exponential fitting function attempts to force the function's curvature to pass through the extremely high dose levels and through zero, which causes the intermediate

dose levels to be underestimated. In order to meet criteria 5, three general levels of dose were determined for XRQA film they were: low-mammography see Figure 3.11(B), medium-CT see Figure 3.11(C), and high orthovoltage see Figure 3.11(D); EBT film is not as sensitive in the low energy level and therefore was only considered for medium and high dose levels. When measured dose data was divided into the three categories and fit using equation (3-10) the dose uncertainty was measured to be better than 2% at all levels, see Figure 3.12 bottom pane.

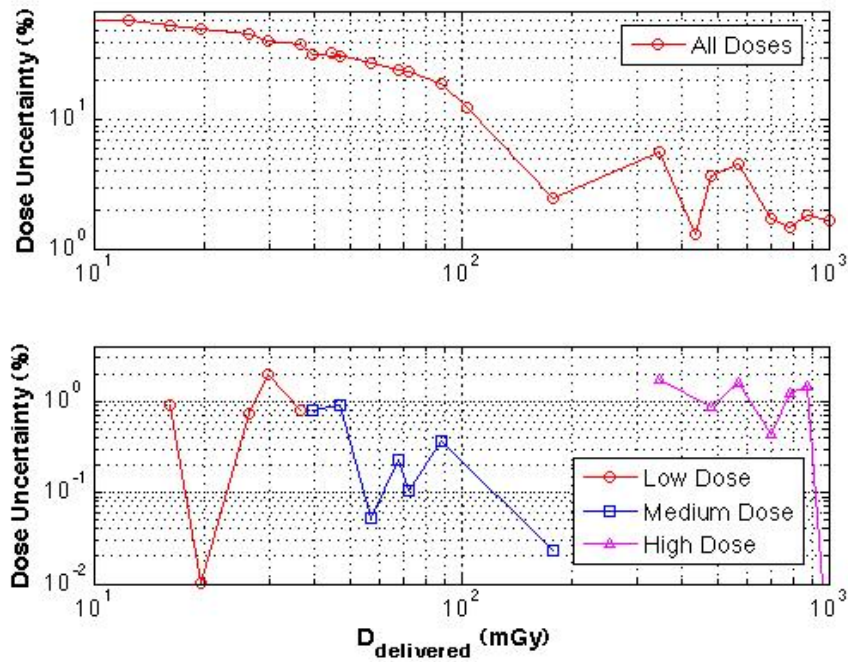


Figure 3.12 Exponential fitting curve error

Dose uncertainty is calculated by subtracting the fitting function estimated dose from the known dose values. The dose uncertainty for Figure 3.11(A) is plotted in the upper pane and demonstrates a general failure of criteria 5. The dose uncertainty for Figure 3.11(B-D) are plotted in the lower pane as indicated by the low, medium and high dose plots.

3.3.4 Measured Total Uncertainty for Radiochromic Film Digitization

To measure the total error associated with quantitative RCF measurements, the following error analyses were considered: fitting, experimental, and scanner bed position (dose-distance). As an example, a 12 cm² piece of XRQA film was exposed to an x-ray fluence that provided a range of doses from (0-200) mGy. The film was allowed to

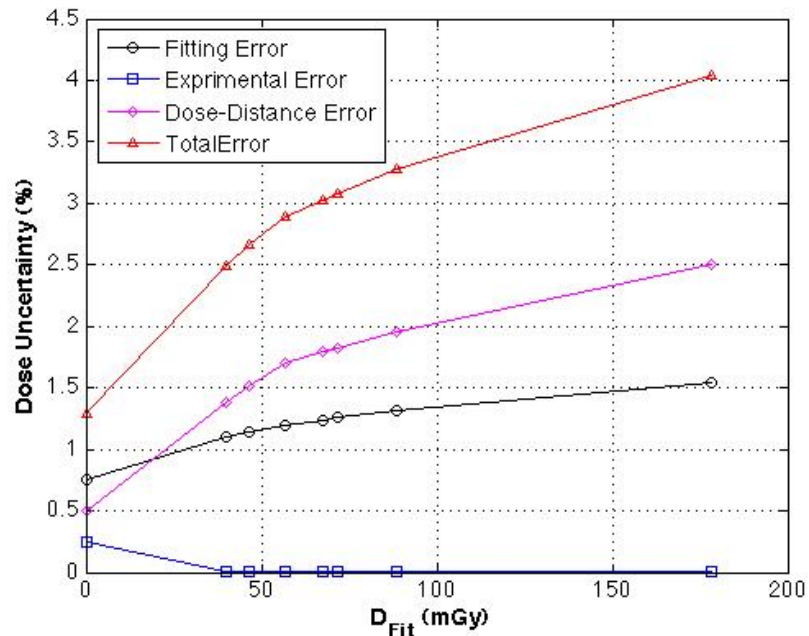


Figure 3.13 Total dose uncertainty associated with RCF

Total RCF error is a summation of experimental, calibration (fitting), and scanner bed positioning (dose-distance) error. The plotted errors are from a (12x12) cm piece of XRQA film that was exposed to a fluence pattern that provided dose readout results from (0-200) mGy. The film was scanned on the EPSON 10000XL scanner.

stabilize for 24 hours and was then centered on the EPSON 10000XL and scanned one time. The film was smoothed using a 2D Wiener filter to minimize the impulse noise

from the scanner's CCD detectors. The film response was converted to netOD using equation (3-1). The dose uncertainty associated with the dose levels in the film and the position and distance on the scanner bed was taken from Figure 3.9. The experimental uncertainty was calculated using a combination of equations (3-3) and (3-5). The film was calibrated using equation (3-10) to provide a netOD-to-dose calibration. The dose uncertainty of the calibration function was calculated as previously shown for Figure 3.12. The summation of these fitting errors gives a general "total" error for RCF experimental, digitization (dose-distance), and calibration fitting function as seen in Figure 3.13.

3.4 Discussion

To establish the known dose for calibration purposes, RCF is often placed alongside and exposed simultaneously with an ion chamber. The RCF and ion chamber must be in close proximity to measure the same photon fluence and calibrate to the same dose. The close proximity of the two dosimeters could induce spurious measurements from inter-dosimeter scatter. To measure the possible scatter contamination from a 6 cc ion chamber, MOSFET detectors were placed at varying distances from the ion chamber. The three positions are shown in Figure 3.14(A) with position one being the closest to the ion chamber and position three being the furthest away. Three separate exposures were measured with the MOSFETs and averaged for the three positions, see Figure 3.14(B). The MOSFETs did not measure statistically significant differences in the three

positions. The possibility for ion chamber scatter being measured by another dosimeter in proximity to the chamber is negligible. The most likely reason for this is that most ion chambers are made from air equivalent material like C552. Therefore the scatter probability from surrounding medium does not increase significantly when an ion chamber is placed next to RCF versus RCF place in air alone.

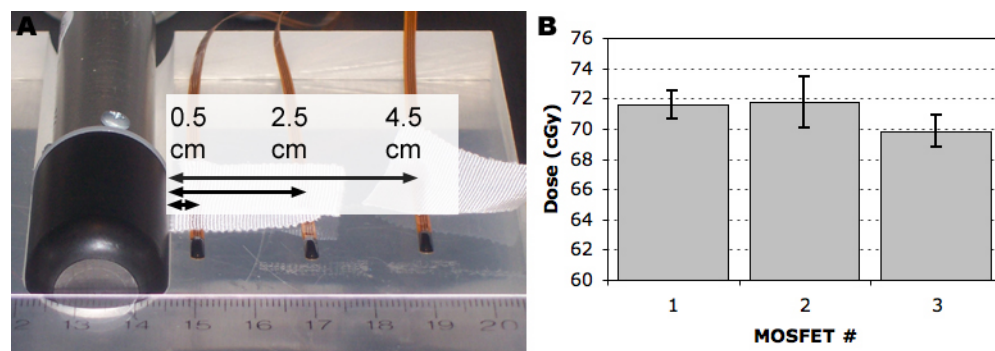


Figure 3.14 Calibration setup geometry: ion chamber scatter measurement

An assessment of scatter from an ion chamber on dose measurements when a dosimeter is calibrated adjacent to an ion chamber was performed. A 6 cc ion chamber was placed on an acrylic block that was customized to provide a recessed well which allowed for three MOSFET detectors to be placed in the same plane as the ion chamber's anode (A). The result of the MOSFET readings indicated that, within the bounds of the measured error, no difference in dose was found from 0 – 4.5 cm from the edge of an ion chamber (B).

In the proceeding sections several aspects of light source non-uniformity were reported. As a means to minimize setup inaccuracies registration guides should be used for consistent realignment of the film for both transmission and reflection modes, see Figure 3.15(A-C). However, care should be exercised to remove the alignment blocks from the scanning bed after each use or a shadowing effect will occur. Shadowing is not prominent in transmission mode scanning but can cause a noticeable effect during

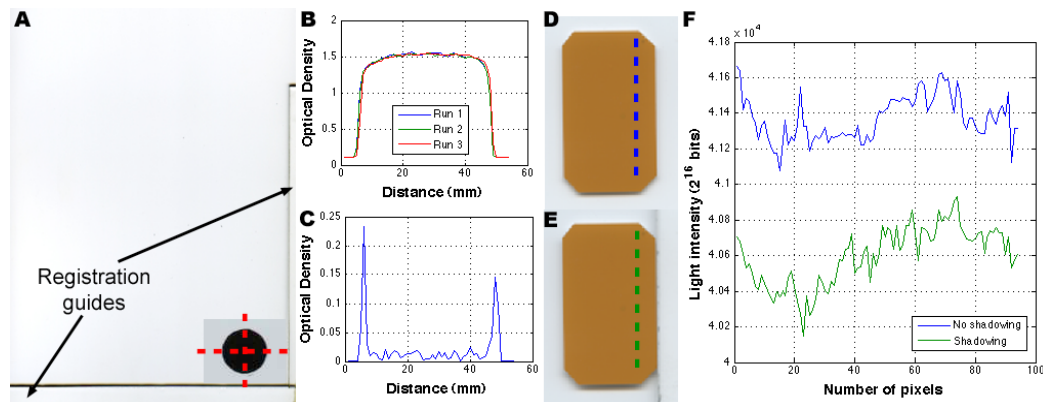


Figure 3.15 Film registration

Registration guides (A) were used to align a piece of RCF (black dot). The film was realigned three separate times and corresponding horizontal and vertical (B) line profiles were taken along the red dotted lines in (A). The average difference of the realigned profiles in (B) is plotted in (C). A piece of XRQA film is scanned without a registration guide in place (D) and with a registration guide left in place (E). Corresponding line profiles taken from (D-E) are shown in (F), which represents a relative error of 2%.

reflection scanning. Shadowing during reflection scanning occurs when the reflection mat on the scanner lid does not uniformly press down on the film because of the raised height of the registration guide(s). This causes the light to scatter differently off of the raised portion of the reflection mat and creates an artificially darker region in that corresponding area of film scanning. A piece of XRQA film was scanned in reflection mode without a registration guide left on the scanner, see Figure 3.15(D) and with the guide left on the scanner, see Figure 3.15(E). Two line profiles were taken at the same location on the film and plotted in Figure 3.15(F). The relative percent error caused by shadowing was measured to be 2%. Paper can be used as an alternative registration

guide to allow physical registration with out shadowing effects, see Figure 3.9(A) as an example.

3.5 Radiochromic Film Scanning Protocol using a Flat Bed Scanner

In light of the results of this section, the following scanning protocol as been developed:

1. Warm up scanner by initiating 5-10 consecutive scans of the empty scanner bed
2. Set up registration guides for pre-irradiation and post-irradiation scans
 - a. Position short axis of the film perpendicular with the motion of the light source (landscape mode)
3. Scan pre-irradiated film 1 time
4. Measure dark noise
5. Post-irradiation scanning is a repeat of steps 1-4. Allow up to 24 hours for the films to stabilize.
6. Post process films in Matlab
 - a. Filter the pre-irradiation film with a 2D Wiener filter using a (7x7) pixel kernel
 - b. (Optional) calculate correction factor matrix (CFM)
 - c. Filter the post-irradiation film with a 2D Wiener filter using a (3x3) pixel kernel

- d. (Optional) apply CFM to pre-irradiation and post-irradiation films. If using an EPSON 10000XL scanner, films placed in the central region of the scanner bed will be minimally affected by the light non-uniformity.
- e. Register pre- and post-irradiation films
- f. Calculate netOD and its uncertainty
- g. Apply netOD-to-dose calibration function

3.6 Conclusion

The flat bed scanner was chosen as the primary film digitizer due to its availability, cost, OD range, functionality (transmission and reflection scanning), and speed. The purpose of this investigation was to determine the intrinsic and operational limitations of two flat bed scanners and define an SOP to maximize RCF digitization accuracy and precision. The EPSON V700 and 10000XL exhibited equal spatial and OD accuracy. The precision of their light source and CCD sensors measured $< 2\%$ and $< 7\%$ deviation in pixel light intensities for 50 consecutive scans, respectively. Furthermore, the film was shown to be sensitive to positional and rotational setup. To maximize film accuracy care should be taken to position the RCFs in the same orientation and at the same location on the scanner for pre-exposure and post-exposure digitalization. The RCF demonstrated a larger dynamic range in pixel light intensities, and to be less sensitive to off axis light inhomogeneity, when scanned in landscape mode. The scanner light source is shown to be uniform in the center of the scanner bed for both scanners in

either transmission or reflection mode. In light of the results of these investigations, the EPSON 10000XL demonstrated slightly better light source/CCD sensor temporal stability and additionally provided a capacity to scan larger pieces of RCF in landscape mode due to its larger more uniform central region on the scan bed. However, the EPSON V700 only measured an overall difference in accuracy and precision by 2%, and though smaller in size, is one sixth the cost as the 10000XL.

An SOP for RCF digitization and post processing was introduced. An investigation into a universal RCF calibration fitting function, equation (3-10), demonstrated a superior goodness of fit for both RCF types over a large range of absorbed dose levels as compared to the previously accepted function shown in equation (3-9).

Overall RCF digitization error was calculated for sample exposure (12 cm² XRQA film exposed at (0-200) mGy). The calculated total error was ~4% for dose levels at 200 mGy, but between (2.7-3.0) mGy for CT dose exposures.

4 Low Energy Dosimetry

Low energy dosimetry has always been the more difficult of the dosimetry levels to measure. Traditional low energy radiation ranges from (40-60) kV. The low penetrating power of the radiation beam limits the exposure geometries and detector thickness available for dosimetry. However, in the field of low energy dosimetry, RCFs may prove to be very effective due to their thin construction and large area of detection. To demonstrate RCF dosimetry at low energies, XRQA films were employed to measure 3D breast dose for a novel 3D breast-CT exposure geometry. XRQA was specifically developed for lower energy dosimetry with its higher Z_{eff} material composition and therefore EBT was not investigated in the low mammographic energy exposure levels.

4.1 Applications to Uncompressed Breast Computed Mammotomography Dosimetry

In this work a prototype device dedicated to breast cancer imaging using cone beam computed tomography, CmT, was investigated for volumetric breast dosimetry. One advantage of this tomographic device over dual view mammography, the current standard of care for breast cancer screening, is the potential for improving contrast between tissues with similar attenuation coefficients in reconstructed images of the breast volume. This 3D volumetric imaging may: improve small lesion visibility that may otherwise remain occluded in conventional 2D planar imaging; improve the

diagnostic accuracy of breast imaging; increase the effectiveness of breast cancer screening; and have a beneficial impact on patient outcomes.

Since breast CT acquires many hundreds of individual 2D projection images, the cumulative dose absorbed by the breast during a tomographic scan is of paramount importance to imaging system design. Guidelines from the American College of Radiology (ACR) require that the average absorbed dose from dual view mammography to a 4.2 cm-thick compressed breast consisting of 50-50% adipose-glandular tissue not exceed 6 mGy⁶⁶. The ACR has not defined a specific dose level for CmT devices and so investigators using CmT devices for breast imaging aim to confine the cumulative absorbed dose for a breast CT scan to that of dual view.

Dosimetry for mammography has been performed using both empirical and simulation-based measurements⁶⁷⁻⁷¹; whereas, dosimetry for breast CT has generally been estimated using a combination of measurements in air, computer-modeling of x-ray tube spectra incident on the breast, and 3D Monte Carlo simulations⁷²⁻⁷⁴. This study attempts to quantify the dose imparted to uncompressed pendant breast geometry for a CmT system by way of empirical measurements. This work characterizes the absorbed dose to the uncompressed breast using a tomographic cone beam imaging protocol in conjunction with TLDs and XRQA RCFs. Oil and water, two distinct attenuating media, are separately employed in the breast phantom volume to characterize the variation in absorbed dose for what would be the expected boundary conditions of 100% fatty or

100% glandular breast tissue composition, respectively; though it is acknowledged that no such boundary may actually exist⁷⁵. Three different phantom shapes are tested to observe variations in absorbed breast dose as a function of the shape and effective radius of the breast phantoms, and the x-ray cone beam intersecting it. Ultimately, an excised breast cadaver is scanned using the dedicated breast CT imaging system; the cadaver results are compared to the geometric phantom experiments.

The following work represents the combined effort of two research groups at Duke University. I handled the radiation dosimetry aspects of these experiments, which include all handling, calibration, and post processing of the dosimeters. The experimental concept and design, data acquisition, and analysis of the dosimeter data, as presented in this chapter, are credited to Dominic Crotty, PhD, one of the original researchers that helped develop the CmT device.

4.1.1 Materials and Methods

4.1.1.1 Dedicated Breast CT Imaging Subsystem

Details of the prototype compact dual-modality CmT breast imaging system are described elsewhere⁷⁶. The following is a brief review of the CmT system. The SPECT and CT sub-systems are secured to a common rotation stage capable of 360° azimuthal rotations around the vertical chest to nipple axis of the pendant breast. The CT subsystem employs a rotating tungsten target cone-beam x-ray source (model Rad-94, 0.4 mm focal size, 14° anode angle, Varian Medical Systems, Salt Lake City, UT) and a

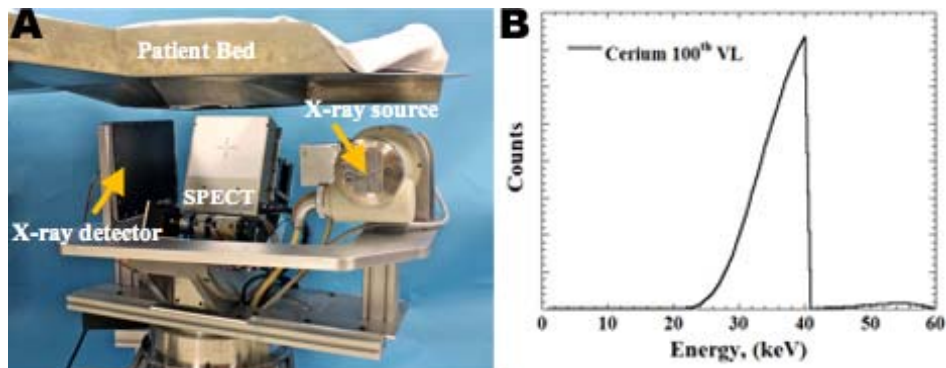


Figure 4.1 SPECT-CT mammotomography system

Photograph of the prototype integrated SPECT-CT system dedicated to breast cancer imaging seen below the Pb-shielded patient bed (A). The SPECT system gamma camera is visible in the center of the image. The x-ray source and detector are nominally tilted from the horizontal. The combined system rotates around a common vertical axis of rotation, with the CT subsystem restricted to purely circular orbits in this prototype. Breast-incident energy spectrum of the unconventional, ultra thick K-edge Ce-filtered beam at 60kVp (B).

CsI:Tl based amorphous silicon digital x-ray detector (model Paxscan 2520, Varian Medical Systems, Salt Lake City, UT) with a grid size of (1920x1536 and 127) μm pixel pitch. A cerium ($Z=58$, $\rho=6.77 \text{ g cm}^{-3}$, K-edge = 40.4 keV, Santoku America, Inc., Tolleson, AZ) 100th value attenuating filter (0.051 cm, evaluated at 60 kVp) is used to yield a mean x-ray beam energy of approximately 36 keV and a FWHM of 15%⁷⁷, see Figure 4.1(B). These non-conventional beam characteristics have been previously exploited to optimize the dose efficiency of the system for uncompressed breast imaging⁷⁶. For these studies, a 60 cm source-to-image distance (SID) is used with a magnification of 1.6 for an object located at the system's isocenter. The integrated CT sub-system is restricted to simple circular motion about a vertical axis at a nominal 3.11°

fixed source-detector tilt with respect to the horizontal. The typical tomographic data acquisition protocol consists of an x-ray exposure technique (60kVp, 100mA, 25msec) and 255 projection images collected about the breast; with 15 projection images used for system calibration and other technical reasons.

4.1.1.2 Dosimeter Preparation and Readout

The XRQA film used in the experiment was digitized using the EPSON 10000XL scanner. Each exposed film was scanned at a resolution of 72 pixels per inch (0.4 mm pixels), with no color corrections, and image files were saved in uncompressed format. All TLDs used in the experiment were Harshaw TLD-100 (LiF:MgTi) chips, Thermo Eberline, LLC, Franklin MA) and measured (3x3x1) mm in dimension; see Appendix A.2 for more details on TLD dosimetry.

4.1.1.2.1 Dosimeter Calibrations

The TLDs and XRQA film were cross-calibrated with a 6 cm³ ionization chamber (Mammochamber, Model 10x5-6M-3, RadCal, Monrovia, CA). Four separate sets of dosimeters including one piece of film, two TLDs, and the ion chamber were exposed in air to four separate exposure levels with the quasi-monochromatic x-ray beam, ranging from (0.660 to 1.915) R. The dosimeters were located approximately 38 cm from the x-ray focal spot (on the tomographic system's isocenter) and localized along a vertical line near the center of the x-ray cone beam field of view to eliminate variations associated with the heel effect due to the tube's orientation. One set of TLDs and one section of film were set aside for background measurements. TLD and film responses were

plotted as a function of the measured ion chamber exposure readings converted to absorbed dose. Absorbed dose was calculated using equation (3-7) with the energy dependent water and oil *f-factors* (0.88 and 0.58) cGy R⁻¹, respectively, calculated using equation (3-8). The ion chamber correction factor, κ in equation (3-7), was based on ADCL provided calibration factor for 60 kVp. Dosimeter calibration plots were fit using least-squares regression techniques discussed in section 3.3.3.

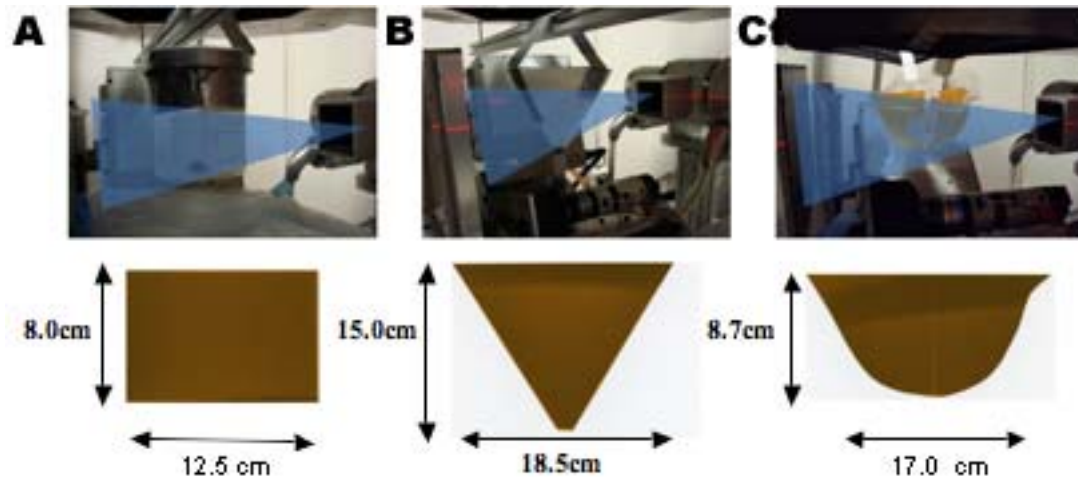


Figure 4.2 Breast phantom geometrical shapes

Photographs of the scanned (A) cylindrical, (B) conical and (C) anthropomorphic breast phantoms containing RCFs of the same cross-sectional shape (seen below their respective photograph). Dimensions of the RCF inserts are provided.

4.1.1.3 Dose Measurements of the Phantom Volumes using RCF

Three phantom volumes were used to measure the absorbed dose using the CT sub-system of the CmT scanner: two geometric phantoms in the shapes of a cylinder, see Figure 4.2(A) and a cone see Figure 4.2(B), and one anthropomorphically shaped breast phantom, see Figure 4.2(C). The regular cylindrical phantom presents a constant cross

section of attenuating material to the divergent x-ray cone beam, and mimics the setup often used in Monte Carlo dose simulation studies. The conical shape phantom more closely mimics the shape of a pendant breast, decreasing in radius from chest wall to nipple, but in a geometrically uniform fashion. Previous studies have demonstrated that approximately 15% of subjects have conically shaped pendant breasts⁷⁸. The anthropomorphic breast shape is modeled as an intermediary progression from the cylindrical and conical breast shapes and represents a 60% prevalent clinical geometric pendant breast shape, dimension, and volume⁷⁹.

Mid-axis cross-sectional templates of the phantom volumes were used to shape the RCF, see Figure 4.2. In general, the cone simulates a large diameter breast at the upper edge of the cone, tapering to a smaller diameter breast towards the nipple. Due to the asymmetry of the anthropomorphic breast phantom, templates of the sagittal and axial axes were created. The sagittal axis film was sliced vertically through its center to enable interlacing of the sagittal and axial films for a simultaneous exposure of both films within the anthropomorphic breast phantom. For each of the variously shaped phantoms, the RCF was attached with adhesive tape at several points to the inside surface of the phantom, ensuring minimal movement of the film during filling of the volumes with water or oil and subsequent scanning. The phantoms were positioned at the isocenter of the cone beam CT imaging system, see Figure 4.2, and scanned using the tomographic imaging protocol described previously. This enabled the absolute dose

and dose profiles to be measured across the 2D central plane of each of the 3D breast phantom volumes. The phantoms were initially filled with 1000 mL of water ($\rho = 1.0 \text{ g cm}^{-3}$) and scanned. The water was subsequently replaced by 1000 mL of mineral oil ($\rho = 0.84 \text{ g cm}^{-3}$) and the tomographic exposure process repeated using a new set of unexposed RCF. To ensure adequate exposure of the RCF using the low flux CT scanning technique, each film-phantom setup was exposed to two consecutive full tomographic scans and the dosimeter responses were scaled to represent a single scan measurement.

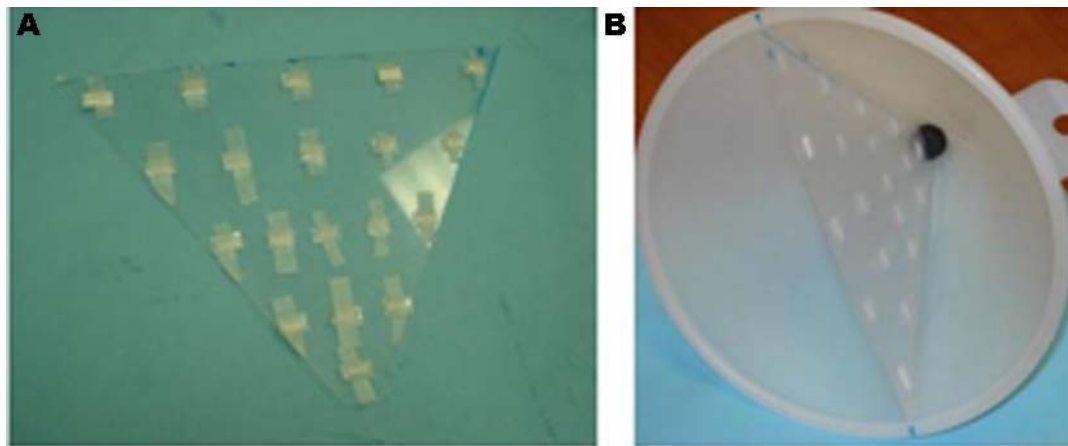


Figure 4.3 TLD experimental setup

TLDs were aligned and secured on a conical template for RCF cross-verification (A). The TLD template was aligned along the middle-axis of the cone breast phantom (B). The cone phantom was subsequently filled with water (not shown).

4.1.1.4 Validation of RCF Dose Measurements using TLDs

Results from the RCF measurements in the conical water breast phantom were cross-validated with dose measurements acquired using TLDs. Thirty seven TLDs (18 pairs and 1 single TLD, with pairs being used to ensure greater accuracy in the point

dose measurements) were located on a regular array of points across the triangular template of the conical phantom, see Figure 4.3. This template was used to measure the dose to the breast at varying distances from the breast surface to the center of the breast, and at different anterior distances from the “chest wall” towards the decreasing diameter at the nipple. Each pair of TLDs was secured to a 5 mm thin acrylic template of the conical phantom, see Figure 4.3(A). The acrylic template and TLDs were then additionally vacuum-sealed to isolate the TLDs from liquid contamination, and to further secure them in place to the template surface. The entire TLD validation experiment was repeated twice, separated by a number of days, using identically located pairs of TLDs on the template. Each TLD data set was separately calibrated to absolute dose and corrected for local background differences specific to the time of their exposures. The TLD exposure data were then combined for increased statistical power.

4.1.1.5 Measurements of Dose to an Uncompressed Breast using 3D Breast CT

A cadaver breast was used to investigate the dose to uncompressed human breast tissue using the tomographic protocol used with the breast CT system. The breast, obtained from a 48-year old woman who died of causes other than breast cancer, was secured inside the same plastic anthropomorphic breast phantom holder that was used in the geometric dose experiments described in the previous section, see Figure 4.4(A). The breast was cut initially along the medial-axial axis, from chest wall to nipple, see Figure 4.4(B). A sheet of RCF, cut to the contoured template of the breast phantom

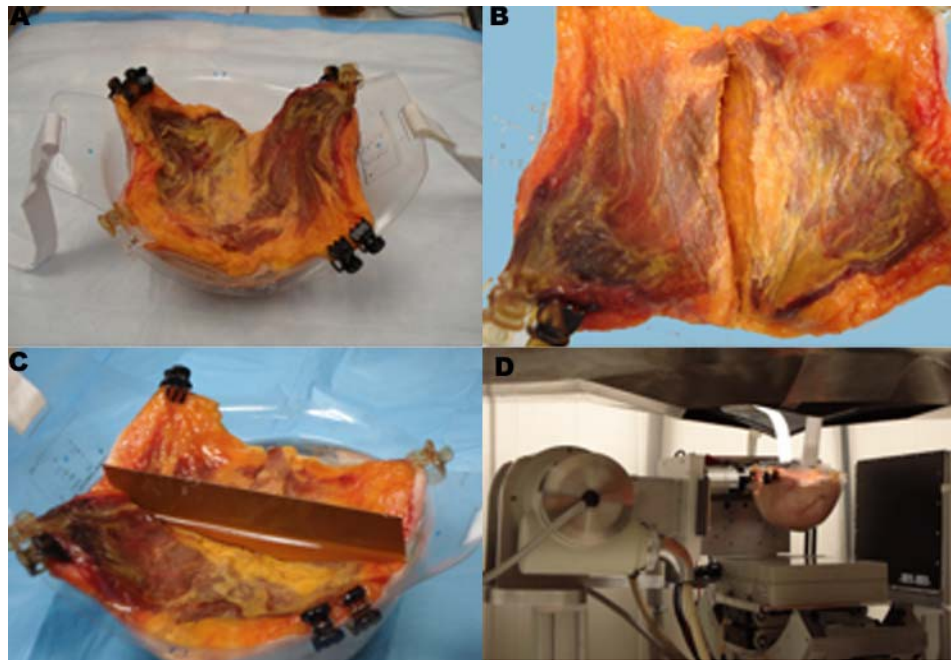


Figure 4.4 Excised cadaver breast

Photographs of the cadaver breast in the plastic breast phantom volume (A) with the incision made along the transverse axis of the breast (B). The oil back-filled breast with the visible RCF template inserted along the sagittal axis (C) and the breast suspended in the FOV of the breast CT system (D).

cross-section, was inserted between the two cut sections of breast tissue, see Figure 4.4(C). Due to the lack of an attached chest wall, the excised breast volume tended to sag in the middle of the phantom and so 175 mL of mineral oil was added to ensure a continuum of tissue equivalent medium above the “chest wall” of the suspended breast. The phantom was then suspended into the FOV of the CT system, see Figure 4.4(D). Two identical full tomographic scans using the same developed imaging protocol as was used for the geometrical phantoms were performed on the suspended cadaver breast. The experiment was subsequently repeated using a new sheet of RCF inserted into an

incision cut orthogonally into the suspended breast along the medial-sagittal axis, (not shown). Each film response was scaled to represent one tomographic scan.

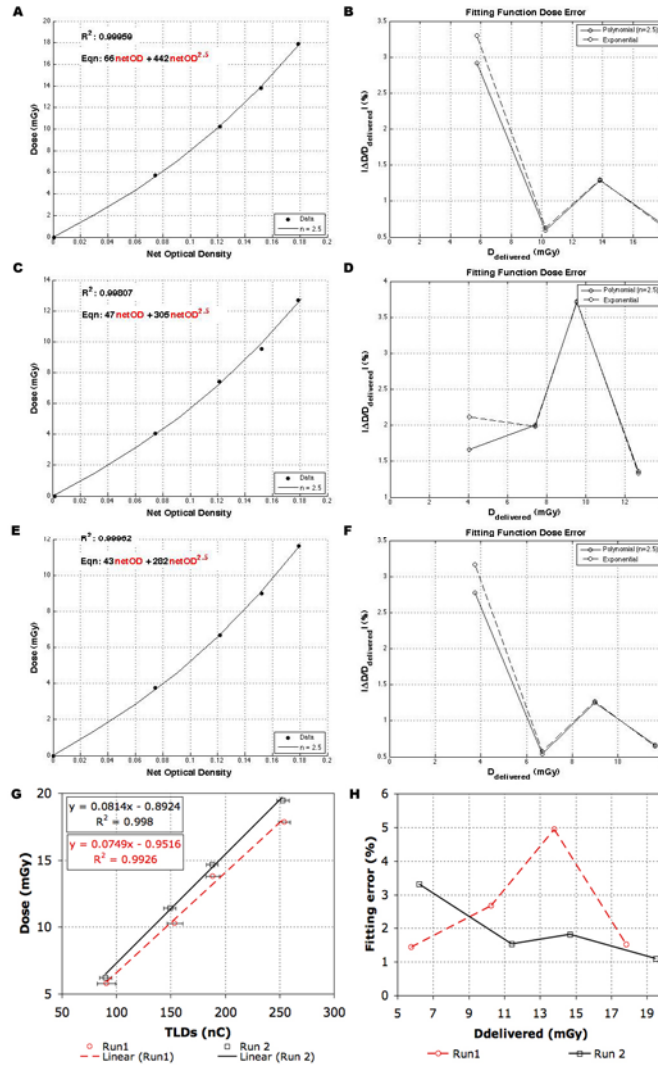


Figure 4.5 Dosimeter calibration fitting functions for CmT exposures

RCFs were separately calibrated for water (A), oil (C), and cadaver breast (E) mediums (cadaver breast calibration function used the same *f*-Factor as oil since no *f*-Factor for 50-50% tissue existed). The fitting function error is shown for RCF fitting functions for water (B), Oil (D), and cadaver breast (F). Two sets of TLDs were calibrated for water (G). The TLD fitting error is shown in (H).

4.1.2 Results and Discussion

4.1.2.1 Dosimeter Calibration

Shown in Figure 4.5 are the fitting functions obtained for the calibration of the RCF measurements in water, Figure 4.5(A), oil, Figure 4.5(C), and cadaver breast, Figure 4.5(E); a calculation of $R^2 > 0.99$ was seen for all three cases. The calculated fitting error for all three RCF calibrations is shown in Figure 4.5(B,D,&F) respectively. The linear fitting functions for both TLD calibration runs in water are shown in Figure 4.5(G); a calculation of $R^2 > 0.99$ was seen for both runs. The fitting function error for both TLD runs is shown in Figure 4.5(H). The fitting functions represented in Figure 4.5 were used to calibrate the XRQA film and TLDs measured *in situ* for the three phantoms and the cadaver breast.

4.1.2.2 Dose Measurements

4.1.2.2.1 Conical Phantom

The cone shaped 2D dose distributions for water is seen in Figure 4.6(A) and for oil is seen in Figure 4.6(B). Three axial and one sagittal (chest wall to nipple) dose profiles were taken along representative dashed lines in Figure 4.6(A) and are displaced by their respective profile number in Figure 4.6. The profiles generally indicate that the measured dose in water is consistently greater than that of the equivalent profile in oil. This can be attributed to the greater mass energy absorption coefficient of water compared to oil. Also, there is a pronounced concavity in the water dose profile at the thickest section of the chest wall (profile #1 in Figure 4.6) with an approximate 50%

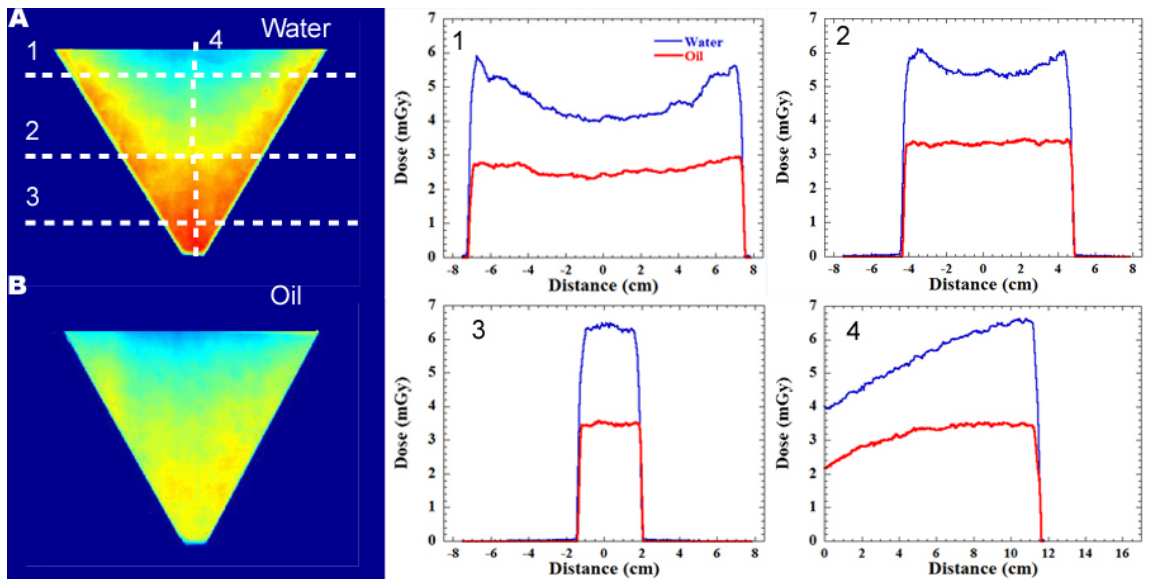


Figure 4.6 Conical phantom

Conical phantom RCF absorbed dose responses for water-filled (A) and oil-filled (B) experiments, with accompanying axial and sagittal line profiles. Note the pronounced concave dose profile across the thickest section (profile #1) of the cone, becoming less pronounced (profile #2) and turning convex as the effective diameter of the conical volume decreases near the nipple (profile #3). Note also that the mean dose level increases closer to the nipple (profile #4). The >50% increase in dose between the chest wall and nipple is evidence of the influence that the breast diameter has on absorbed dose. The dose profile for water (equivalent 100% glandular tissue) is again consistently higher than that of the oil (equivalent 100% fatty tissue).

difference between the peak periphery measured dose (~6 mGy) and the center of the phantom (~4 mGy). At this level the diameter of the cone is approximately 15 cm wide and represents the path of the greatest radiation attenuation. The peak peripheral dose in the equivalent oil dose profile is more uniform with only approximately 17% greater dose at the edges than that of the central section of the phantom (~2.9 vs. ~2.5) mGy. The cupping effect in the oil-filled phantom is less prominent compared to the water-filled

phantom in part due to the fact that the oil has a lower mass energy absorption coefficient (μ_{en}/ρ) and a lower material density (ρ) that allows for a longer mean free path along which the radiation can interact. Since the probability for energy deposition for an electron is constant along its path length, the axially sampled dose distributions in oil appear more constant or uniform through the breast phantom. However, as the breast diameter decreases, the cumulative absorbed dose in the center of the breast increasingly approaches that of the entrance dose. This is due to the short path length for the electrons released in the phantom to reach the film. Indeed, the convex appearance of Profile #3 in Figure 4.6, generated at a diameter of approximately 3 cm, indicates that very close to the nipple, the center of the phantom cumulatively absorbs more dose than the skin. The increasing nature of Profile #4 in going from the chest wall towards the nipple illustrates the increasing overall dose with decreasing phantom diameter. An option to reduce the dose to the nipple region in a conical breast shape would be to introduce compensation bolus on the breast itself, or aluminum wedged filtration at the exit portal of the x-ray tube. Each option would effectively create a dose environment similar to a cylindrical pendant breast described in the next section. The skin (edge) dose remains relatively constant (~6 mGy) as the breast diameter reduces, but the dose along the medial phantom increases from 4 mGy at the chest wall to approximately 6.5 mGy by the nipple region. The mean water dose measured in the conical phantom is (5.3 ± 0.6) mGy, and that of the oil is (3.1 ± 0.3) mGy.

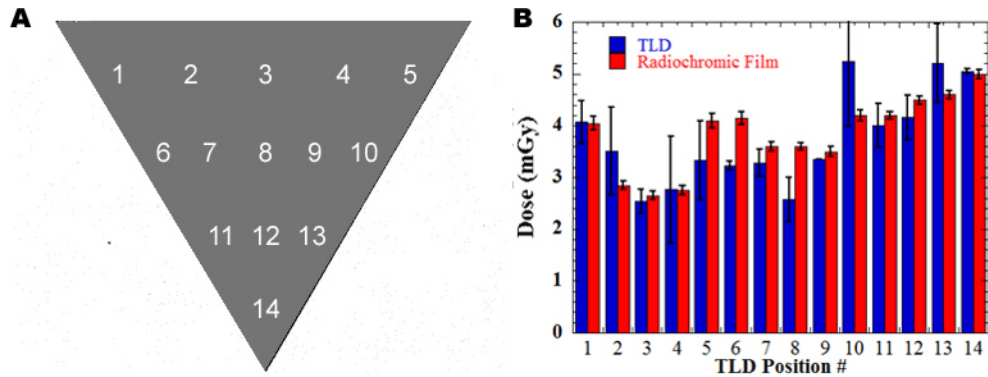


Figure 4.7 TLD and RCF response comparison

The conical template with the positions of the numbered TLD pairs (A). The average and standard deviation of the point dose measured from the TLDs in water compared to the dose at equivalent ROI locations in the RCF (B). Standard deviations for the RCF were determined as the variation from the mean of the ROI in the film.

Film absolute dose response was verified by comparing TLD point dose measurements in the conical water-filled phantom. The film dose response was extracted using ROIs of similar size as the TLDs and at locations that were spatially registered with the TLD positions, see Figure 4.7(A). Only 14 of the original 19 TLD pair locations were used for comparison; the top five TLDs (not shown in Figure 4.7(A)) were not covered by the 1000 mL of water that filled the phantom. Dose figures in Figure 4.7(B) range from (2.5-5.2) mGy with a TLD mean dose of (3.7 ± 0.9) mGy, and a RCF mean dose of (3.8 ± 0.7) mGy; the TLD and RCF responses agree to better than 10%. The greatest discrepancies between the dosimeter measurements are located along the periphery of the template. These discrepancies, however, are within the statistical uncertainty of the TLD and RCF measurements. While the calibration of the TLDs and

the film was performed using a perpendicular exposure technique in air, the angular dependence of the responses was not explicitly characterized in this study. The overall close agreement between TLD and RCF measurements serves to validate the RCF absolute dose measurements.

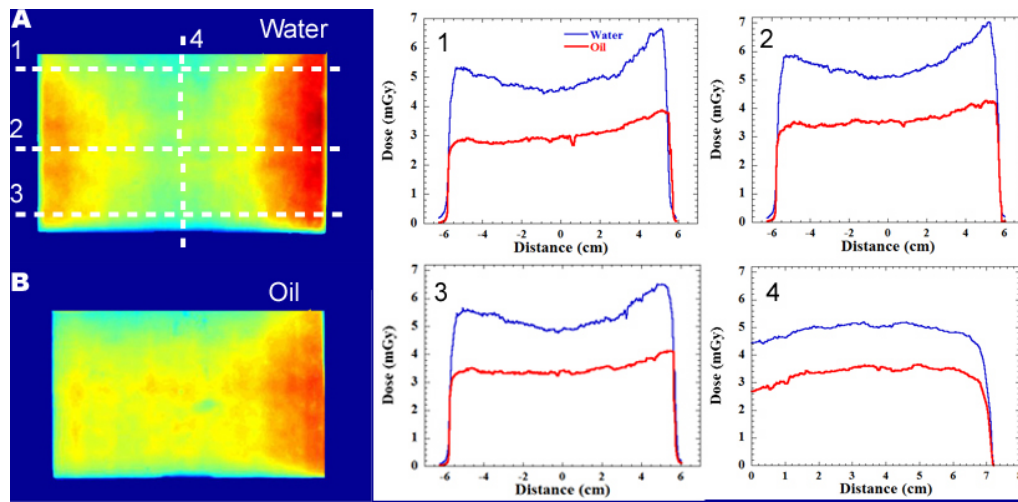


Figure 4.8 Cylindrical breast phantom

Cylindrical phantom film results (bluish color indicates areas of lowest absorbed dose and redish color indicate areas of higher absorbed dose) for water (A) and oil (B). Horizontal and vertical line profiles across the indicated locations accompanying the 2D dose images. Note, the water (mimicking 100% glandular tissue) is consistently higher than that of the oil (mimicking 100% fatty tissue).

4.1.2.2.2 Cylindrical Phantom

Figure 4.8 shows the absorbed dose to the cylindrical breast phantom for water and oil measurements using the RCF. Accompanying axial and sagittal dose profiles are shown in Figure 4.8. The measured cupping effect is similar to that demonstrated by the cone phantom and has also been demonstrated in other simulation studies employing

cylindrical phantoms at beam energies close to the mean beam energy of this CmT system⁷⁴.

For the water phantom, peak dose levels at the periphery of the rectangular film are approximately 13% and 34% greater than at the center of the phantom for the left and right peripheries, respectively. The slightly increased horizontal asymmetry seen in the profiles may be primarily due to an uncentered cylinder that received a higher x-ray dose while the CT system was on one side of the phantom. Other factors of the horizontal asymmetry were additionally investigated. The measured variation in flat field light exposure across the calibrated RCF scanner was approximately 1%, which effectively rules out bias in the scanning process. Some of the asymmetry may be caused by a larger number of calibration images, required for the CmT scanning protocol, occurring at one specific azimuthal location of the cylinder relative to the x-ray source during the scan; however the effect of the proportionally small number of calibration exposures (4% of the total number of exposures are for calibration) cannot explain the magnitude of the elevated dose levels. Nevertheless, careful patient breast centering is recommended given the close geometrical configuration the system and its potential to asymmetrically dose the patient breast.

The sagittal dose profile from chest wall to nipple demonstrates an approximate 5% change between maximum and minimum absorbed dose values. The greater uniformity in the sagittal dose profile may be due to the constant diameter that the

cylinder presents to the divergent CT cone beam. If positioned exactly at isocenter, the constant diameter equalizes the path length of the x-rays incident on the cylinder at all discrete tomographic angles and so photons tend to deposit the energy in a likewise consistent manner. There is a slight peak in the absorbed dose profile approximately where the central x-ray of the beam is located. This may be explained by two factors: the greater photon fluence along the central ray of the x-ray beam; more scattered photons contribute to the dose in this symmetric cylindrical phantom⁷⁹. The decrease in dose levels along the sagittal profile at the upper edge of the cylinder may be attributable to the air interface which is lacking in chest-wall radiation in-scatter. The mean dose measured by the RCF within the water filled cylindrical phantom for a single tomographic scan was measured to be (5.4 ± 0.4) mGy, ranging from (3.4 to 7.1) mGy. The equivalent measurement for oil had a mean dose of (3.5 ± 0.3) mGy with a range between (2.5 to 4.5) mGy.

4.1.2.2.3 *Anthropomorphic Breast Phantom*

Figure 4.9 illustrates the dose measured in the more clinically relevant anthropomorphic breast phantom, based on shape, size, and density content. The variation in dose distribution from the center of the thickest section of the breast highlights the spatial trends seen in the profiles for cylindrical, conical, and anthropomorphic phantom exposures. In these three exposure geometries the periphery of the breast receives between (30-40)% more dose than the central volume of the breast. Asymmetry is evident in the dose profile close to the chest wall of the breast phantom

with the peak peripheral dose being between (20-30)% greater than the mean dose in the center of the phantom. This trend in increased periphery dose to the skin corroborates previous simulated and measured dosimetry experiments for breast CT^{74, 80}.

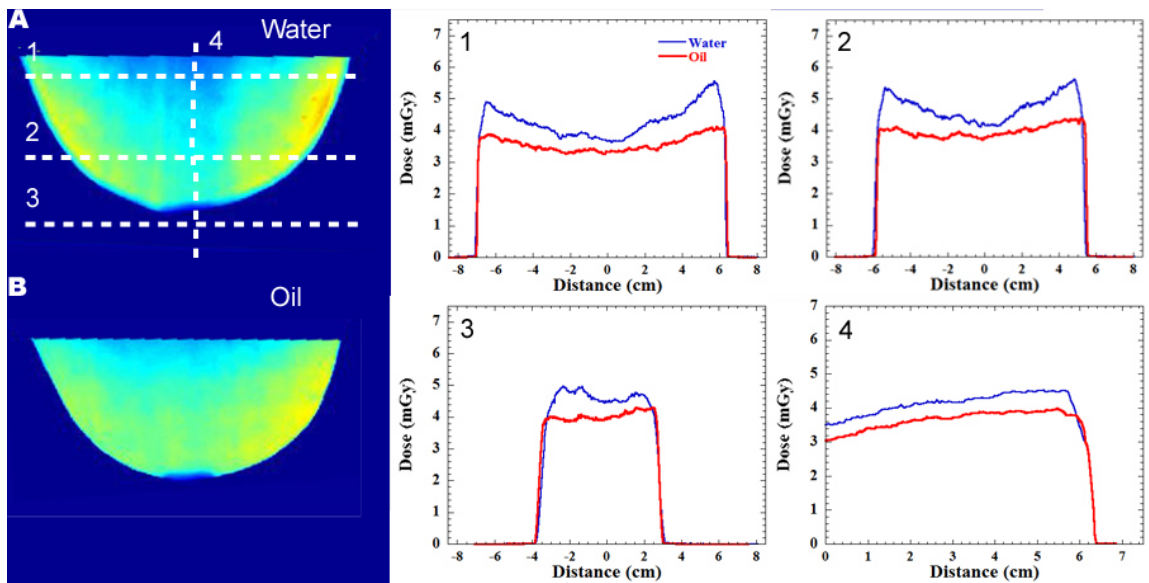


Figure 4.9 Anthropomorphic phantom

Anthropomorphic phantom RCF absorbed dose response for the water-filled (A) and oil-filled (B) with accompanying axial and sagittal line profiles. Similar to the responses observed in the other phantoms, the sagittal dose profiles progressively flatten and the mean dose level increases approaching the nipple. The more rounded shape of the breast indicates that, unlike the conical phantom, the dose profile is not markedly convex at the nipple. The sagittal dose profile indicates a 28% increase in dose along the center of the breast from the chest wall towards the nipple. The dose profile for water (equivalent 100% glandular tissue) is again consistently higher than that of the oil (equivalent 100% fatty tissue), but the difference is less pronounced compared to the geometric phantoms.

Evident in the profiles is the cupping close to the chest wall of the breast (profile #1 is generated at abreast diameter of 13.4 cm) and the gradual flattening of the profile as the nipple is approached. However, the anthropomorphic breast does not taper near the

nipple as sharply as the cone (the breast diameter for profile #3 is 6 cm) and so the convexly shaped profile that was present close to the nipple in the conical phantom is not present in the anthropomorphic breast phantom. Although not shown, overall measured dose levels for the sheet of RCF placed orthogonally in the breast phantom volume are identical to the one shown here. Furthermore, breast dose measured in oil is consistently higher than for the other geometric phantoms, and the reverse is true for the breast dose measured in water, making the point-wise differences between water and oil (glandular and adipose) smaller. The mean dose measured in the water-filled phantom was (4.5 ± 0.4) mGy and that of the oil-filled volume is (3.8 ± 0.2) mGy. The results in Figure 4.9 also illustrate an increase in mean dose levels closer to the nipple, similar to the other geometric shapes. All measurement procedures, RCF immersion in the fluids, calibration, and characterization procedures were identical to the earlier measurements. Thus, the greater similarity in the cumulative mean dose levels for both oil and water indicates that the breast geometry may play a larger role in overall absorbed dose than material content alone.

4.1.2.2.4 *Cadaver Breast Tissue*

Dose colorwash images of the orthogonally positioned RCF templates irradiated inside the cadaver breast volume are shown in Figure 4.10. The locations of axial dose profiles across various planes of the RCF templates are indicated in Figure 4.10(A). Generally good agreement exists in the absolute dose measurements and in the shape of the dose profile across the templates with a slight asymmetrical increase towards one

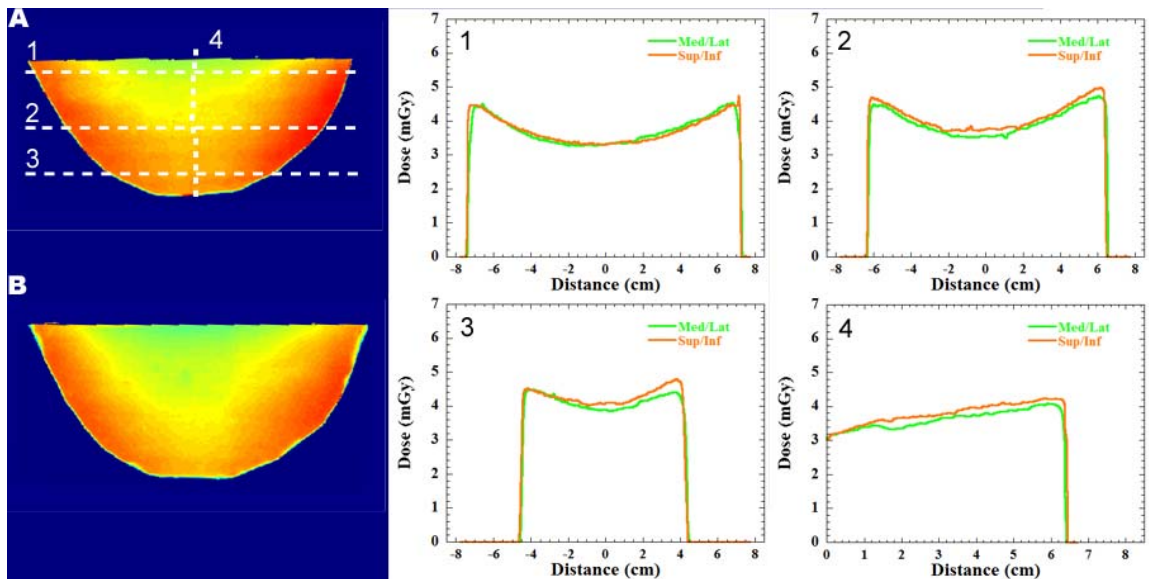


Figure 4.10 Cadaver breast

Dose color wash images of the absorbed dose in the cadaver breast for the medial-lateral (A) and superior-inferior film templates (B). The accompanying dose profiles indicate good agreement for the templates across dose profiles as the nipple is approached.

side in the superior inferior template, potentially caused by asymmetrical placement of the dose template across the center of the breast tissue volume in that orientation. The orthogonal cadaver tissue sagittal dose profiles agree with the anthropomorphic phantom sagittal dose trend, namely: the sagittal profile measures an increase in mean dose as it approaches the nipple with the dose at the nipple being approximately 33% greater than that at the level of the “chest wall”. The mean doses measured for the cadaver tissue, measured outside of the mineral oil-filled regions, were (4.3 ± 0.3) mGy and (4.2 ± 0.3) mGy in the medial-lateral (axial) and superior-inferior (sagittal) directions, respectively; for an overall cadaver breast tissue mean dose of (4.3 ± 0.4)

mGy. This mean breast tissue dose measurement is between the mean doses of (3.8 ± 0.2) mGy and (4.5 ± 0.4) mGy measured for the oil-filled and water-filled anthropomorphic phantoms, respectively. Figure 4.11 illustrates the composite histogram of the dose distribution of the cadaver breast tissue and those of the oil and water-filled anthropomorphic phantoms. This result both corroborates and validates the previous anthropomorphic data using the boundary materials of oil and water to simulate lower and upper material composition bounds.

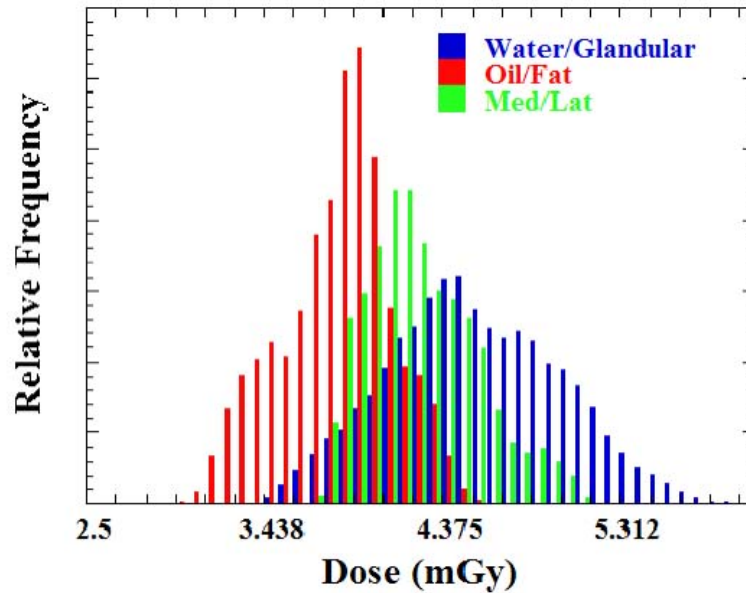


Figure 4.11 Tissue specific dose histograms

Histogram composed of the (blue) water and (red) oil-filled anthropomorphic breast phantom dose distribution along with the dose distribution of the combined cadaver breast tissue measurements (green).

4.1.3 Conclusions

In this study, RCF was used to measure the dose distribution in an uncompressed pendant breast geometry using a CmT tomographic scanner. The RCF dose measurements were validated using TLD results. Spatially registered RCF and TLD absolute dose measurements agreed to better than 10%. The 2D RCF dose measurements in oil and water served to describe the boundary conditions for a measurement of a breast of 100% adipose, (3.8 ± 0.2) mGy, and 100% glandular, (4.5 ± 0.4) mGy, tissue, respectively, and to validate the dose measurement using human breast tissue as the attenuation medium (4.3 ± 0.4) mGy. In each case, either the emulated boundary or nominal 50-50% breast types, the absorbed dose to an uncompressed pendant breast scanned using a CmT tomographic scanner was within the ACR specified 6 mGy limit.

This RCF measuring technique produced high-resolution 2D dose distributions in the uncompressed breast cadaver and in the geometric and breast shaped phantoms. These distributions can then be extended to a 3D dose distribution throughout the volume, assuming symmetry in the phantom shapes. However, it was shown that the wide angle x-ray CT cone beam affected the dose distribution given various geometrical configurations, shapes, and material contents of the 3D phantoms, so caution must be used when interpolating the dose distribution to 3D.

5 Intermediate Energy Dosimetry

Intermediate energy radiation is the proverbial bread-and-butter of most dosimetries. Traditional intermediate energy radiation ranges from (80-140) kV. The radiation energy levels are suitable for interactions with little or no modification to the dosimeter device for charged particle equilibrium (CPE). Also, intermediate energy emitting radiation devices are found in most medical departments in hospitals and free standing clinics. Because of the wide use of these devices, RCFs will potential improve large populations of patient care through multi-dimensional dosimetrical analysis.

The CT scanner is an intermediate energy emitting device that has revolutionized modern medicine. Typical CT scanners are equipped with the potential to deliver energies ranging from (80-140) kV and are a main source of radiation dose to the patient population. In fact, as of 2006, CT exams are reported to have increased by 10% per year, over the last 10-15 years, and now accounts for 49% of the total collective dose (person-Sv) to patients undergoing a radiological examination; this corresponds to a 120-fold increase in CT collective dose since the 1980s⁸¹. Accurate patient dose measurements are required to help mitigate the increasing trend of CT dose especially within pediatric patient populations.

Since the 1980s, the industry standard technique for scanner output determination has been the computed tomography dose index (CTDI)⁸²⁻⁸³. CTDI was developed for single slice axial CT technology primarily as a means to correlate CT

exposure for different CT manufacturers. The CTDI has also come to be accepted as an indicator of patient dose. The CTDI volume ($CTDI_{vol}$) and dose length product (DLP) calculations are displayed on CT consoles as a means to assess scan parameter impact to deliverable dose, and are archived as a “Dose Report” with the CT examination. Though accepted as a dose descriptor, the CTDI is incapable of directly measuring organ dose; it is only defined for two anatomical regions, the head and body, and any extrapolation to effective organ dose requires conversion factors such as those generated by Monte Carlo⁸³.

A more direct means of measuring organ dose for patients undergoing CT examinations utilizes an anthropomorphic phantom in conjunction with TLD or MOSFET dosimeters⁸⁴⁻⁸⁵; this is called a point dose method (PDM). Anthropomorphic phantoms are human like in size and weight and are designed with complex heterogeneous tissue types to emulate real patient attenuation and scatter properties. TLD and MOSFET dosimeters can be used to measure point doses in each organ throughout the phantom.

In the following chapter, XRQA RCF will be used in conjunction with anthropomorphic phantoms to introduce novel approaches 2D and 3D CT dosimetry. XRQA film, as previously discussed for low energy dosimetry, was developed specifically for the low to intermediate radiation energy ranges. EBT film has been shown to respond to radiation energies as low as 75 kV, see section 2.4; however, EBT

film readout response (OD) at these energies is lower compared to XRQA. MOSFET, TLD, and ion chamber dosimeters will be used as a means to validate the XRQA response.

5.1 Application into an Investigation of a Dose Reduction Technique for CT

Recently, a novel dose reduction technique became available on the Siemens SOMATOM Definition CT scanner at Duke University Hospital. The SOMATOM Definition is a state of the art multi detector-row CT scanner that has two CT tubes for single energy (SECT) or dual energy (DECT) CT scans. When the SOMATOM Definition operates in SECT mode the scan time can be reduced to 0.33 sec for a full rotation. With the availability of faster tube rotation, patient dose could be minimized via shorter exposure times by using high pitch scan protocols. In addition to this technologically inherent dose saving technique, Siemens is developing a protocol driven dose reduction technique called Xcare.

Xcare was developed for dose reduction for radiation sensitive breast tissue in thorax scan protocols. Xcare could be extended to other scan protocols for dose reduction to radio-sensitive tissues, e.g., lens of the eye for head CT angiography (CTA) exams. Conceptually, Xcare works by decreasing the CT beam output intensity over a predefined arterial area of the body. The tissues within this area will be presumably spared significant radiation dose. However, one aspect of Xcare feature is that the scan protocol with Xcare enabled will maintain the same noise level in the reconstructed

image and the same CTDI value as an unmodified scan. Presumably to maintain noise and CTDI levels would require an amplification of CT beam output in other regions of the x-ray beam coverage not reduced by Xcare.

In the following investigation, XRQA RCF and MOSFET detectors were used to determine the magnitude of dose reduction possible for breast tissue in a standard thorax exam using: (1) high pitch, (2) Xcare, (3) a standard Bismuth (Bi) shield, or a combination of any of the three methods. The magnitude of the dose reduction for these methodologies was quantified and compared to the measured absorbed dose in the standard thorax exam without dose reduction techniques enabled. Several types of phantoms were used to emulate different body habitus shape and dimensions.

5.1.1 Materials and Method

To measure the relative dose distribution through out the scan volume and the angle over which the Xcare dose reduction feature decreases x-ray beam output, XRQA film and CTDI phantoms were employed. CTDI phantoms are simple cylindrical phantoms made from uniform Acrylic material. The CTDI phantom provided uniform scatter within its volume when exposed to the CT beam. Two types of CTDI phantoms were used: (1) the head phantom, which measures 16 cm in diameter and 15 cm in length, and (2) the body phantom, which measures 32 cm in diameter and 15 cm in length; the CTDI head phantom served as the pediatric body phantom.

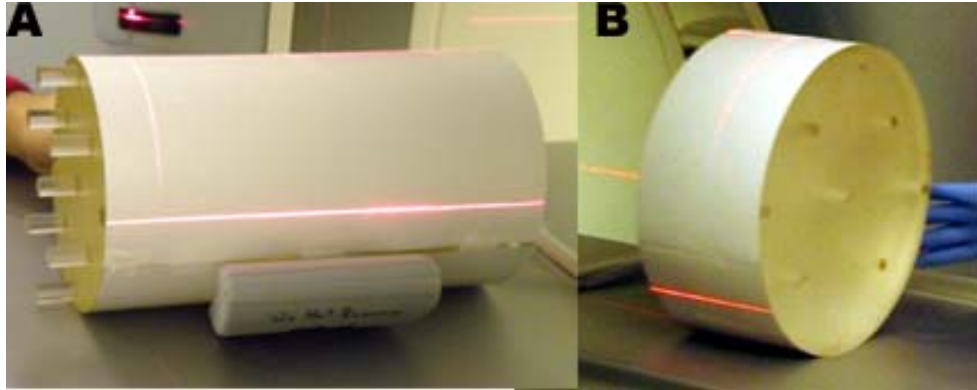


Figure 5.1 CTDI head and body phantom

The CTDI head (A) and body (B) phantoms are shown. Two CTDI head phantoms were combined to allow RCF to be placed between the phantom halves, not shown. The CTDI body phantom was cut into three 5 cm slabs and RCF was placed between one of the slabs, not shown. XRQA film was then wrapped around the circumference of the phantoms.

To measure the relative dose distribution for a pediatric and adult patient body, the head, Figure 5.1(A), and body, Figure 5.1(A), phantoms were respectively wrapped with RCF. Additionally, RCF was used to measure the 2D transaxial dose distribution within each CTDI phantom volume. The film was cut to match the cross-sectional area of the phantom and placed between two head phantoms. The two head phantoms were held together by tape and the probe holes from both ends of the phantom set were filled with acrylic rods. The acrylic rods were carefully placed in contact with the film to remove all air gaps within the phantom. The body CTDI phantom had been previously cut into three 5 cm slabs and therefore a RCF was placed between two of the three slabs and taped together. Two pieces of film were cut to shape the cross-sectional area of the

CTDI body phantom due to its large, 32 cm, diameter. Likewise, the probe holes were plugged using acrylic rods to remove the effects of radiation scatter in air.

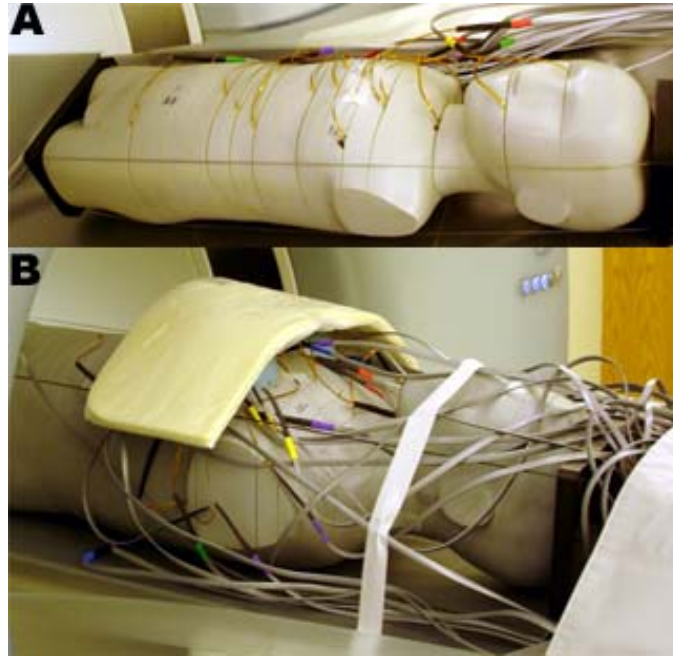


Figure 5.2 Anthropomorphic pediatric and adult female phantoms with MOSFETs

The 5-yr old pediatric (A) and adult female (B) anthropomorphic phantoms are shown. The phantoms were loaded with MOSFETs for direct organ measurement. The adult phantom is shown with a Bismuth breast shield in place.

For direct organ dosimetry, several sets of MOSFETs (BEST Medical, Canada) were placed within a 5-yr old pediatric and adult male with breast organs (used to emulate a female of larger body size) anthropomorphic phantom (CIRS, Norfolk VA), see Figure 5.2(A-B). For a discussion on the theory of MOSFET dosimetry see Appendix A.3. The anthropomorphic phantoms were used to emulate real patient scatter geometry. The phantoms included a number of transverse sections that were each 25 mm thick. Each slice had 5 mm diameter holes drilled within the various organs

through out the phantom volume. The MOSFETs were placed in select holes of 12 organs; the unfilled holes were filled with material equivalent plugs.

For each phantom size, i.e., pediatric and adult, a typical thorax scan protocol was chosen. The CTDI phantoms were scanned with Xcare enabled and with Xcare disabled. The anthropomorphic phantoms were scanned with a thorax protocol using high pitch ($Adult_{pitch} = 2.4$ and $Pediatric_{pitch} = 3.0$) with and without Xcare and normal pitch ($Adult_{pitch} = 0.8$ and $Pediatric_{pitch} = 1.4$) with and without Xcare. Additionally, the adult female phantom was scanned with at high pitch and a Bismuth (Bi) breast shield protocol.

5.1.2 Results

5.1.2.1 CTDI Phantoms with XRQA Films

Figure 5.3 and Figure 5.4 demonstrate the effects of a thorax scan with Xcare enabled for a pediatric and adult body habitus. The films from the head and body phantoms were removed, digitized, and plotted as one continuous film using Matlab. A clearly demarcated area of lower CT beam output intensity is seen in Figure 5.3(A) and Figure 5.4(A) when compared to the

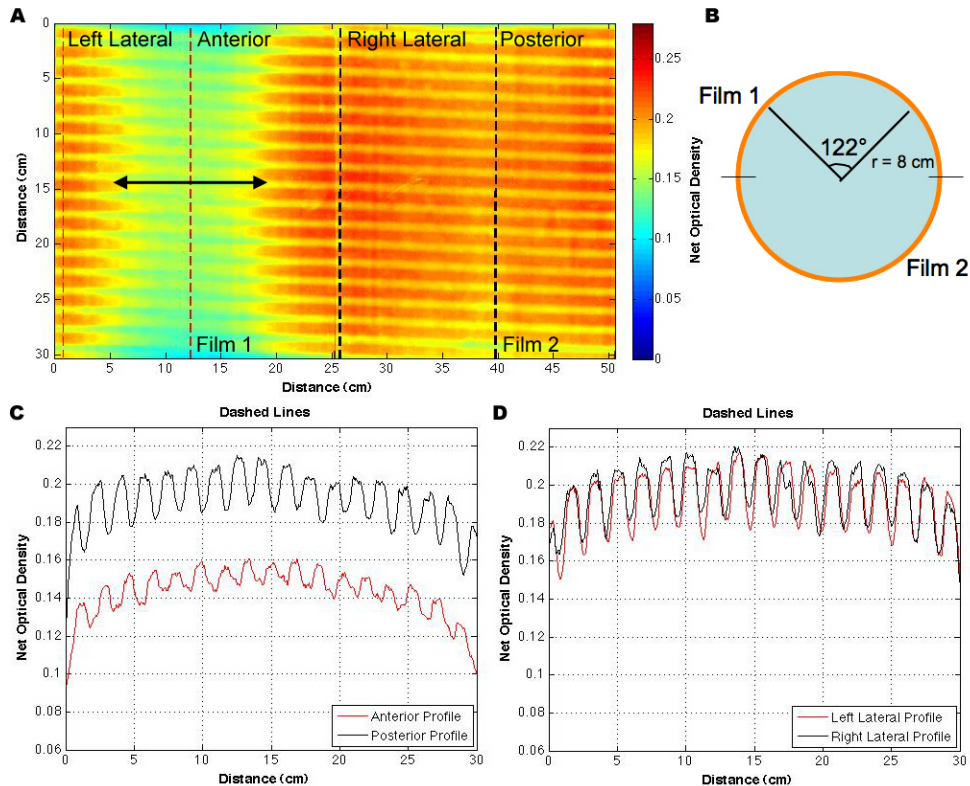


Figure 5.3 CTDI head phantom with RCF wrap and Xcare enabled

The RCFs around the circumference of the two head phantoms were scanned with Xcare enabled. The films were unwrapped (A) from their original positions as shown in (B). A line profile, shown in (A), through the anterior area of film was compared with a profile through posterior area (C). Similarly, line profiles for the right and left lateral sides of the phantom were compared (D).

posterior and lateral sides of the films. Striation is seen in the film response due to the scan with pitch < 1. The angle subtending the area of lower beam output intensity was measured using the following relation:

$$\theta = \frac{s}{r} \cdot \frac{180^\circ}{\pi}, \quad (5-1)$$

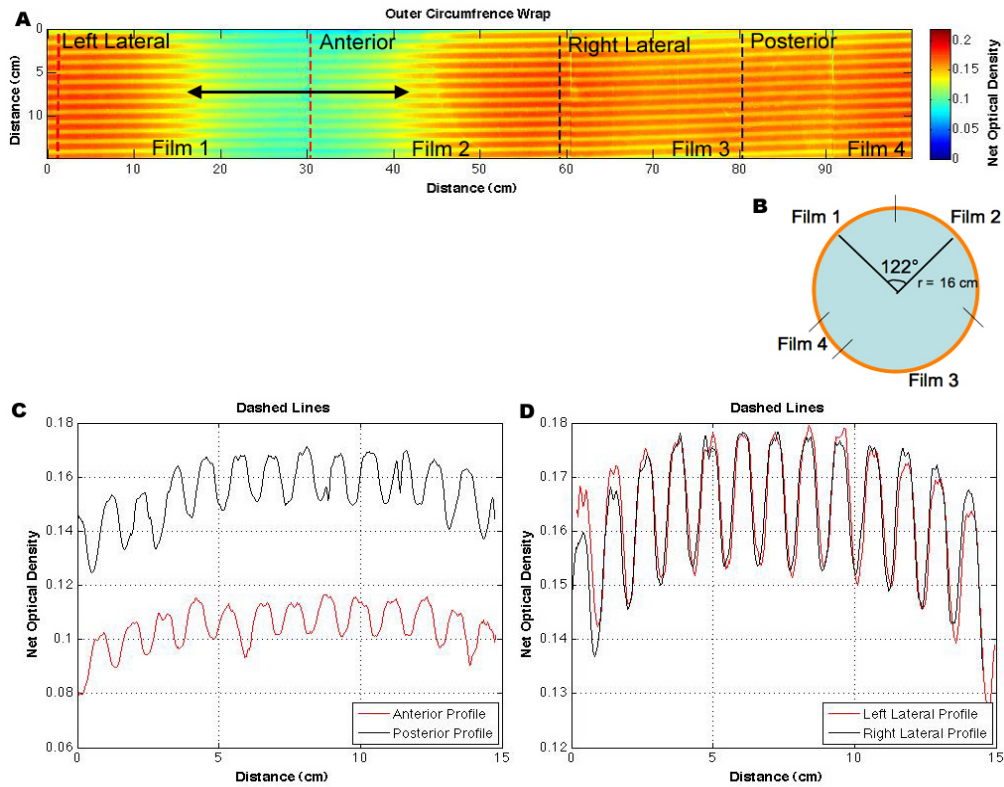


Figure 5.4 CTDI body phantom with RCF wrap and Xcare enabled

The RCFs around the circumference of the two head phantoms were scanned with Xcare enabled. The films were unwrapped (A) from their original positions as shown in (B). A line profile, shown in (A), through the anterior area of film was compared with a profile through posterior area (C). Similarly, line profiles for the right and left lateral sides of the phantom were compared (D).

where s is the arc length, r is the radius of the phantom, and the equation was converted from radians to degrees. The arc length was determined by measuring the distance on the film of the lower beam output intensity, as shown in by the double arrow in Figure 5.3(A) and Figure 5.4(A). To measure the distance of the low intensity, the film color range was set to be 82% of the scanners maximum light output. This normalized the color intensities in each plot. The boundaries of the measured low intensity were

defined at 90% of the maximum film response so the results from the different size CTDI phantoms could be compared. The angle subtending the area of low CT beam output intensity was calculated to be 122° for both the head and body phantom sizes, see Figure 5.3(B) and Figure 5.4(B), respectively.

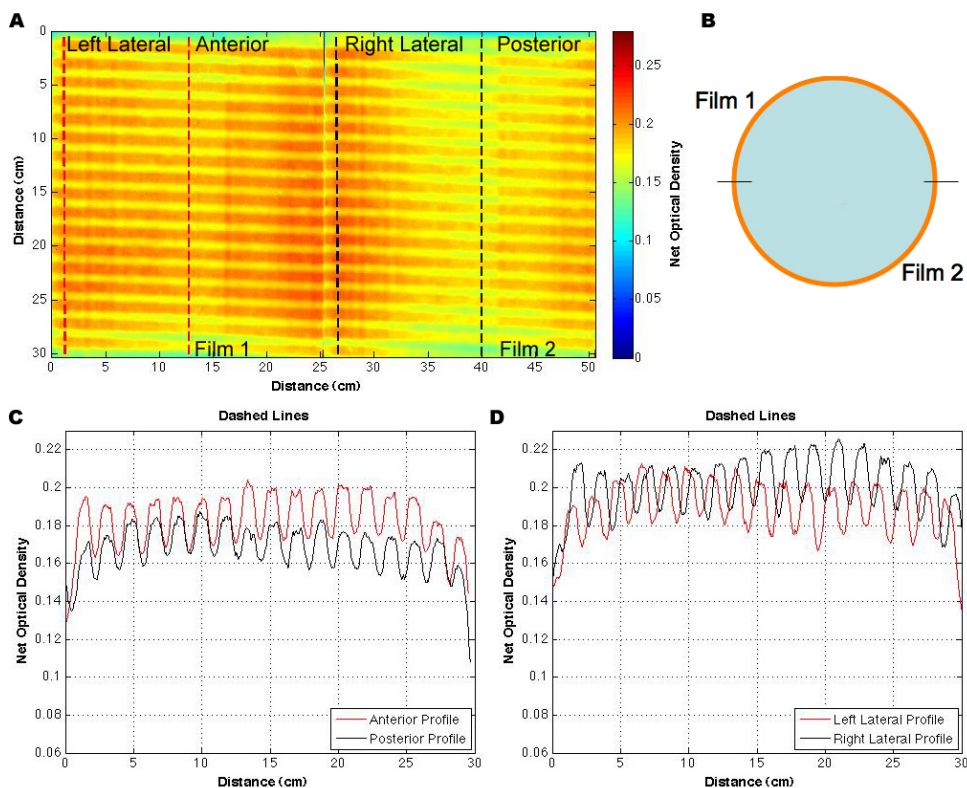


Figure 5.5 CTDI head phantom with RCF wrap and Xcare disabled

The RCFs around the circumference of the two head phantoms were scanned with Xcare disabled. The films were unwrapped (A) from their original positions as shown in (B). A line profile, shown in (A), through the anterior area of film was compared with a profile through posterior area (C). Similarly, line profiles for the right and left lateral sides of the phantom were compared (D).

The RCF wrapped around the head phantom measured an overall 29% reduction in beam intensity when comparing the anterior and posterior portions of the film, see

Figure 5.3(C), but measured identical relative responses for the right and left lateral sides of the film, see Figure 5.3(D). Likewise, the exposed film around the body phantom measured an overall reduction in relative response by 38%, see Figure 5.4(C) and identical relative responses for the right and left lateral sides of the film, see Figure 5.4(D).

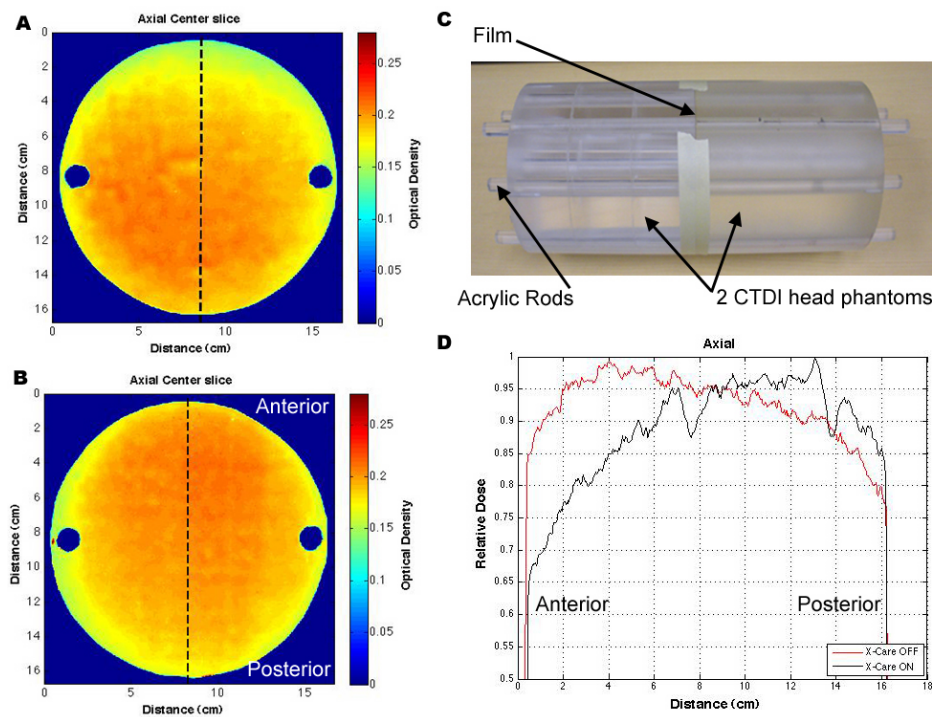


Figure 5.6 RCF inserts placed between two CTDI head phantoms

2D dose distribution readout results compare Xcare enabled (A) with Xcare disabled (B). The film inserts were placed between identical CTDI head phantoms (C). Anterior-to-posterior line profiles compare Xcare enabled with disabled (D).

As a control, the CTDI head phantom with RCF was scanned with the Xcare dose reduction technique disabled, see Figure 5.5. The outer RCF wrap did not display the same lower response in measurement along the anterior portion of the film, see Figure

5.5(A). However, when comparing the anterior and posterior portions of the film, an overall 15% reduction in dose was measured for the posterior side of the film, see Figure 5.5(C). The lateral left and right sides of the film were similar in response, Figure 5.5(D).

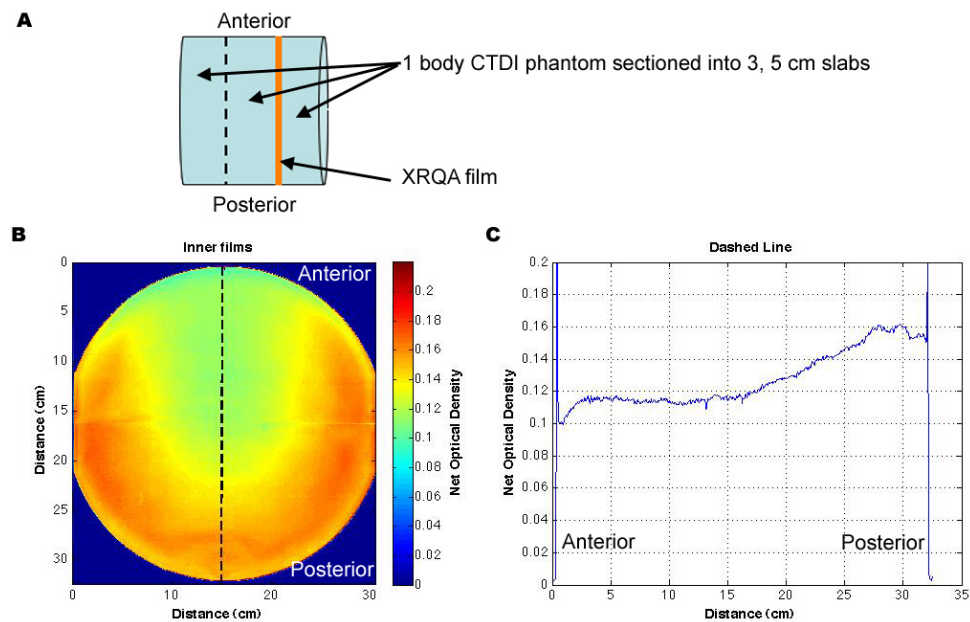


Figure 5.7 2D RCF dose distribution of a CTDI body phantom with Xcare enabled

The CTDI body phantom was sectioned into three 5 cm slabs. Two RCF sheets were placed between two of the three slabs (A). The 2D dose distribution was formed by combining the two RCF sheets in Matlab (B). An anterior-to-posterior line profile demonstrates the anterior dose reduction to an adult body phantom when Xcare is enabled (C).

2D dose distributions were measured by the films placed between the phantom slabs for the head phantom with and without Xcare enabled, see Figure 5.6(A) and Figure 5.6(B), respectively, and for the body phantom, see Figure 5.7(B). The films placed between the head phantoms, see Figure 5.6(C), and the body phantom slabs, see

Figure 5.7(A), were sampled using an anterior-to-posterior line profile, see Figure 5.6(D) and Figure 5.7(C). The profiles demonstrate a relative dose reduction from the Xcare enabled CT scan, but an increase in relative posterior dose compared to the Xcare disabled CT scan. Also, the Xcare disabled scan demonstrates a dose reduction along the posterior side of the film as compared to the anterior side.

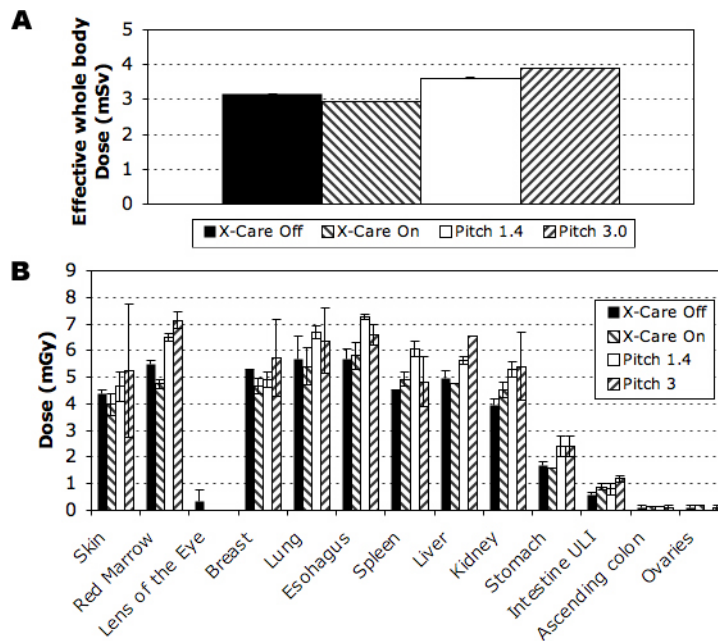


Figure 5.8 Pediatric 5-yr old whole body dose

The pediatric 5-yr old phantom was measured for a whole body dose with Xcare enabled and disabled and with a high and normal scan pitch (A). The organ dose breakdown is listed in (B).

5.1.2.2 Anthropomorphic Phantoms with MOSFET Dosimeters

Whole body dose for a 5-yr old pediatric phantom was measured using MOSFETs for a CT scan with Xcare enabled, (3.0 ± 0.05) mSv, and disabled, (3.2 ± 0.05)

mSv, see Figure 5.8(A). The measured whole body reduction in dose using Xcare was 6% compared to the standard thorax scan with Xcare disabled. However, the whole body dose measured for a pitch of 1.4, (3.6 ± 0.04) mSv, and for a pitch of 3.0,

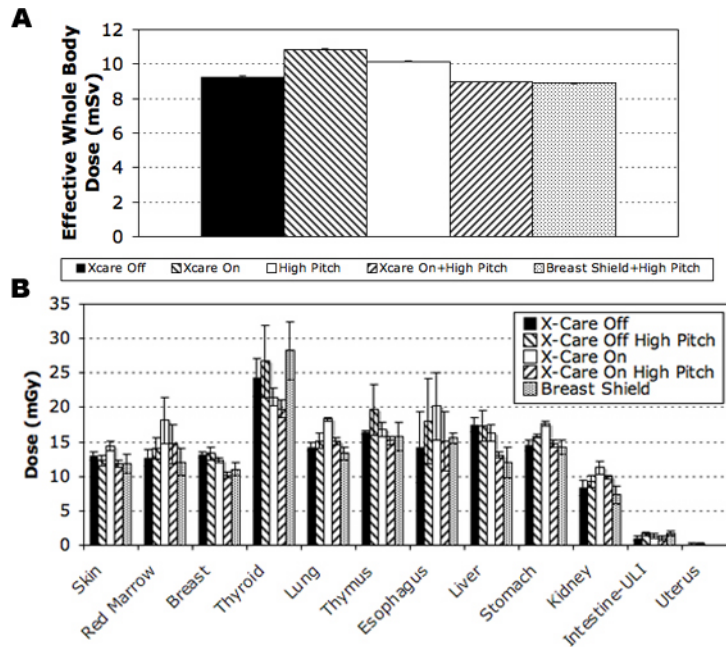


Figure 5.9 Adult whole body dose

The adult female phantom was measured for a whole body dose with Xcare enabled and disabled, and with a high and normal scan pitch (A). The organ dose breakdown is listed in (B) with an additional comparison with a Bismuth shield over the breasts, see Figure 5.2(B).

(3.9 ± 0.01) mSv, both measured an increased effective dose of 12% and 19%, respectively. The absorbed dose break down per organ measured is shown in Figure 5.8(B). The whole body dose for the adult female anthropomorphic phantom was measured using MOSFETs for a CT scan with Xcare enabled, (10.9 ± 0.01) mSv, and disabled, (9.3 ± 0.01) mSv, see Figure 5.9(A). The measured whole body dose for Xcare

enabled was shown to increase by 14% as compared to the standard thorax exam with Xcare disabled. The whole body dose measured for high pitch only was (10.2 ± 0.02) mSv; for a high pitch with Xcare enabled was (9.0 ± 0.01) mSv; and for high pitch with Bi breast shield was (8.9 ± 0.01) mSv. The high pitch exam measured a whole body dose increase of 10% as compared to the standard thorax exam where as the high pitch with Xcare enabled and the high pitch with Bi shield measured a whole body dose reduction of 3% and 4% respectively. The absorbed dose break down per organ measured is shown in Figure 5.9(B). Four tissue types of the twelve listed in Figure 5.9(B) were analyzed for trends in absorbed dose as a function of MOSFET dosimeter location within the phantom organs, see Figure 5.10 and Figure 5.11.

5.1.3 Discussion

The RCF demonstrated an anterior reduction in dose over an area that subtends 122° from the center of the patient phantom. However, the film also demonstrated, with Xcare enabled, an increased posterior dose, see Figure 5.6(D), as compared to the same scan geometry and protocol but with Xcare disabled. When comparing the relative response difference along the posterior side and the lateral left and right sides of the Xcare enabled and disabled films in Figure 5.3(D), Figure 5.5(D), and Figure 5.6(D), a consistent trend of ~5% increase in relative dose is measured. This same trend is verified when the individual tissue types are compared in Figure 5.10 and Figure 5.11. In the later figures, all MOSFETs positioned along the central medial axis of the adult female

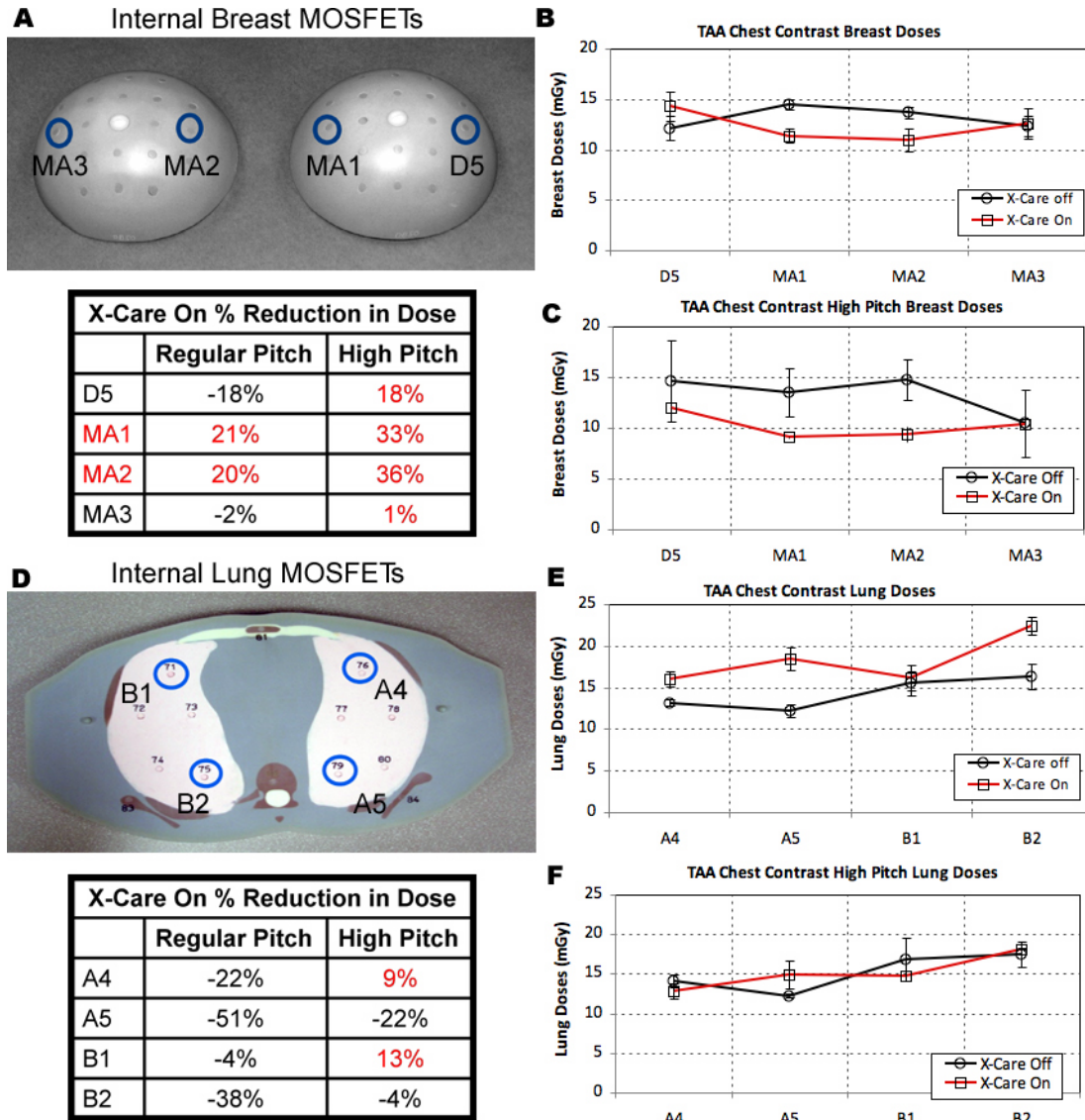


Figure 5.10 Adult anthropomorphic phantom breast and lung dose

MOSFETs results for specific locations in the adult female breasts (A) were compared for Xcare enabled and disabled at regular pitch (B) and high pitch (C). Similarly, MOSFETs results for specific locations in the lungs (D) were compared for Xcare enabled and disabled at regular pitch (E) and high pitch (F). The percent reduction in dose for both tissue types are listed in their respective tables in red font.

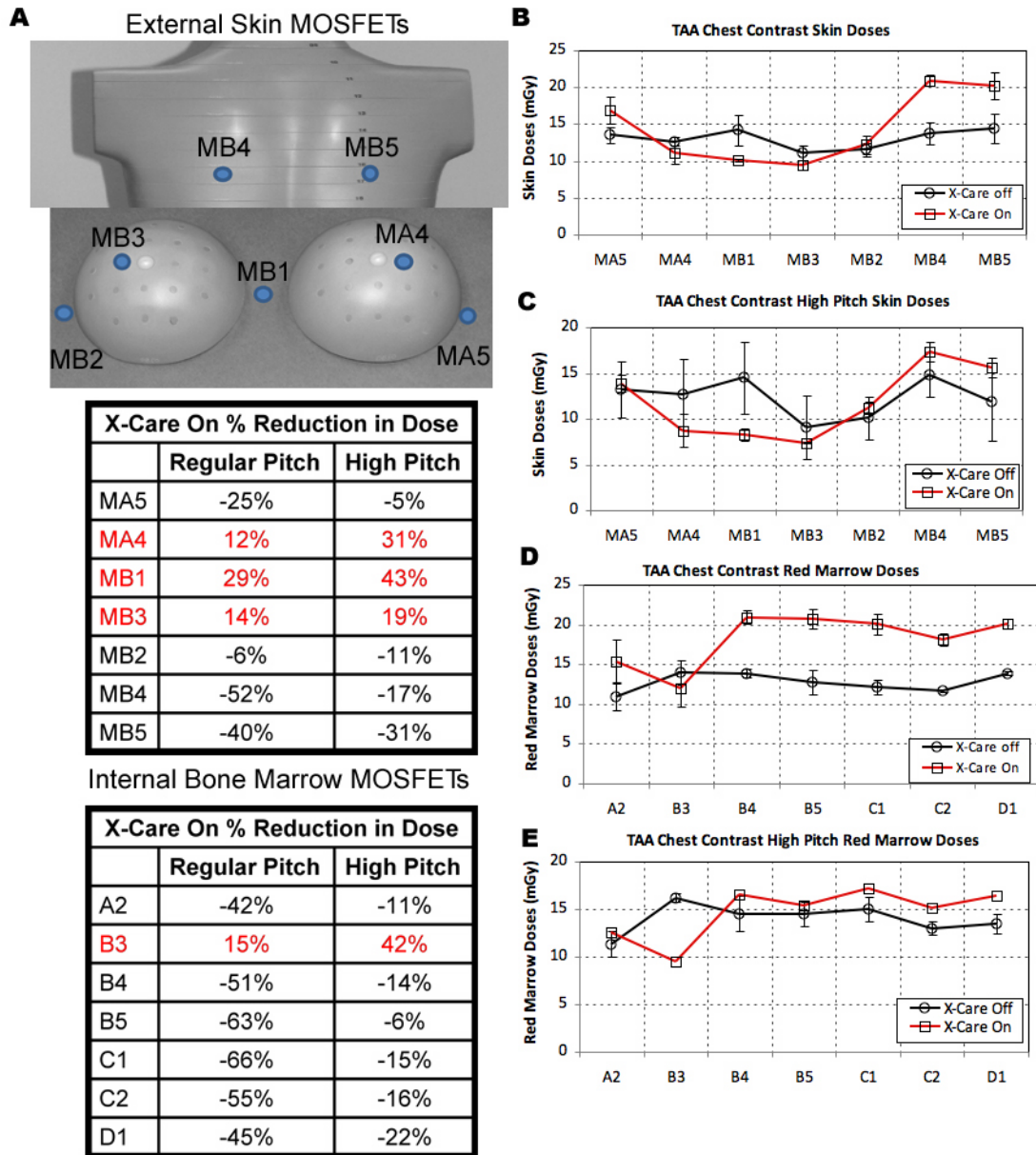


Figure 5.11 Adult anthropomorphic phantom skin and bone marrow dose

MOSFET results for specific locations on the adult female skin (A) were compared for Xcare enabled and disabled at regular pitch (B) and high pitch (C). Similarly, MOSFET results for specific locations through out the body for bone marrow were compared for Xcare enabled and disabled at regular pitch (E) and high pitch (F). The percent reduction in dose for both tissue types are listed in their respective tables in red font.

phantom measured a reduction in absorbed dose compared to the same scan geometry and protocol but with Xcare disabled. An example of this is seen in Figure 5.11(D). The only MOSFET result that measured a reduction in dose was B3, which was placed inside the sternum. The other MOSFETs were distributed through out the body: A2 upper spine, B4-B5 anterior lateral ribs, C1-C2 posterior lateral ribs, and D1 lower spine. This underscores the limitation of using a whole body effective dose measurement as a means to quantitatively score the effects of a scan protocol for dose reduction. In the case of Xcare, all measurement points outside of the anterior area subtended by the 122° angle saw an increase in dose with respect to the normal scan protocol and therefore skewed the whole body effective dose calculation and did not accurately account for the dose reduction measured in some organs, see Figure 5.9(B). However, it should be noted that the Xcare enabled breast tissue scan did not measure a statistically significant reduction in dose compared to the standard scan. Only when Xcare and high pitch or high pitch and Bi breast shield features were combined did the MOSFETs measure a statistically significant reduction in dose. As for the pediatric anthropomorphic phantom, there was a significant reduction in dose measured for the breast with Xcare enabled. A possible reason for the difference between pediatric and adult body habitus could be that part of the adult breast tissue laid outside the 122° angle of dose reduction and the lateral sides of the breast probably received an elevated dose compared to a scan without Xcare enabled. In general, the pediatric phantom did measure an overall

effective whole body dose reduction compared to the adult; this most likely emanated from the fact that the pediatric organs were more compactly situated and more direct organ measurements likely fell within the 122° angle.

In the case of the anthropomorphic phantoms, each phantom habitus was scanned at normal and high pitch. As of late, high pitch protocols for dual source CT have been investigated for their overall dose reduction possibilities. In the case of the Adult body habitus, an increase in scan pitch with Xcare enabled saw a whole body dose reduction of 3%; where the scan with high pitch and Xcare disabled measured an elevated effective whole body dose. For the pediatric body habitus, high pitch all around measured increases in effective whole body dose with the greatest increase in dose coming from the highest pitch (pitch of 3.0). In the case of these measurements, high pitch scan protocols did not demonstrate a dose reduction capacity.

One final note, was the standard dose thorax scan, with no dose reduction techniques enabled, measured a 15% reduction in posterior dose relative to the anterior portion of the scan. The most likely reason for this reduction in posterior dose is CT table attenuation. This finding brings to light the potential use of the CT scanner bed as a passive means for dose reduction. In fact, if the patient was placed in a prone position overall dose reduction to the breast tissue could be commensurate with the 15% reduction measured generally and would demonstrate a larger reduction to breast tissue than Xcare and High pitch alone, and nearly equivalent to high pitch combined with

either Bi shields or Xcare. Also, the passive shielding from the CT couch approach would minimize dose increases through out the remaining patient organs.

5.1.4 Conclusion

RCF and MOSFET dosimeters were employed to verify the potential dose reduction capacity of a novel scan protocol using a dual source CT introduced by Siemens. This scan protocol is called Xcare and claims to reduce CT beam output intensity over a predefined anterior area as a means to reduce dose to breast tissue. Along with the claim of dose reduction, Siemen's Xcare claims to maintain similar CTDI and noise index levels as compared to a similar scan protocol with Xcare disabled.

XRQA RCF 2D dose distributions measured, both around and within the CTDI phantom volumes, a relative anterior dose reduction over an anterior area subtended by an angle of 122° subtended from the center of the phantom. The films also measured a relative increase in dose along the lateral and posterior sides of the phantom as a possible means to compensate for the reduction in anterior CT beam output intensity to maintain the noise index and CTDI value. MOSFET measurements within a 5-yr old pediatric and an adult female anthropomorphic phantom demonstrated a similar dose reduction along the anterior portions of the phantom and an increased dose elsewhere as compared to a similar scan protocol with Xcare disabled. The MOSFET dosimeters within the pediatric phantom measured an effective whole body dose of (3.2 ± 0.005) mSv with Xcare disabled and (3.0 ± 0.005) mSv with Xcare enabled. The effective whole

body dose reduction was calculated to be 6%. The MOSFET dosimeters with the adult female measured an effective whole body dose of (9.3 ± 0.01) mSv with Xcare disabled and (10.9 ± 0.01) mSv with Xcare enabled. The effective whole body dose measured an increase in dose of 17%. The increase in effective whole body dose was attributed to the fact that when the Xcare feature is enable, to maintain identical CTDI and noise levels the photon flux through out the remainder of the scan must be increased to compensate for a reduction in anterior photon flux. When individual organs were compared for dose reduction, the anterior organs such as the breast, sternum bone marrow, and certain regions of the skin did measure a lower dose compared to similar scans with Xcare disabled.

A similar thorax scan protocol with high pitch was investigated as an attempt to mitigate the whole body effective dose increase. The MOSFET measurements with the adult female measured an effective whole body dose of (10.2 ± 0.02) mSv with Xcare disabled for a scan at high pitch. A similar high pitch scan protocol measured (9.0 ± 0.01) mSv with Xcare enabled and (8.9 ± 0.01) mSv with Bi breast shield in place. Only with the combination of high pitch and Xcare enabled or high pitch with Bi shield was a dose reduction of 3% or 4% measured as compared to the standard scan protocol.

A final note of interest, the RCF measured an approximate 15% reduction in relative posterior dose as compared to the anterior portion of a standard scan with Xcare disabled. This natural reduction in dose was attributed to CT table attenuation.

5.2 Application into the Development of a Novel 3D Organ Dosimetry for CT

In this work, a means for organ based volumetric 3D dosimetry is proposed using XRQA RCF. XRQA film is used to simultaneously measure high-resolution, slice-by-slice, spatial dose distributions within an organ volume. Volumetric CT dosimetry is investigated as a means to provide a more robust determination of radiation impact from a CT scan to an organ within a heterogeneous scatter environment as compared to the traditional PDM techniques. TLD and MOSFET PDM dosimetry can be used to measure point doses in each organ throughout the phantom. However, TLD measurements are labor intensive and time consuming to use, and MOSFET detectors have limited life spans. Furthermore, PDM measurements assume a homogeneous dose distribution within an organ volume when quoting an average response per organ. This assumption is intuitively incorrect especially for CT exposures to geometrically complex phantoms with tissues of heterogeneous attenuation coefficients. Assuming a homogeneous dose distribution could lead to an under or over estimation of radiation risk in effective dose calculations for large organs such as the liver or lung that may extend out of the primary coverage area of a CT scan.

The following study was comprised of two main investigations. (1) Measurements were compared between XRQA film and TLDs within a geometrically simple phantom of uniform scatter and attenuation material. The simple phantom was used to verify film response accuracy and sensitivity to CT exposure geometry, i.e., with

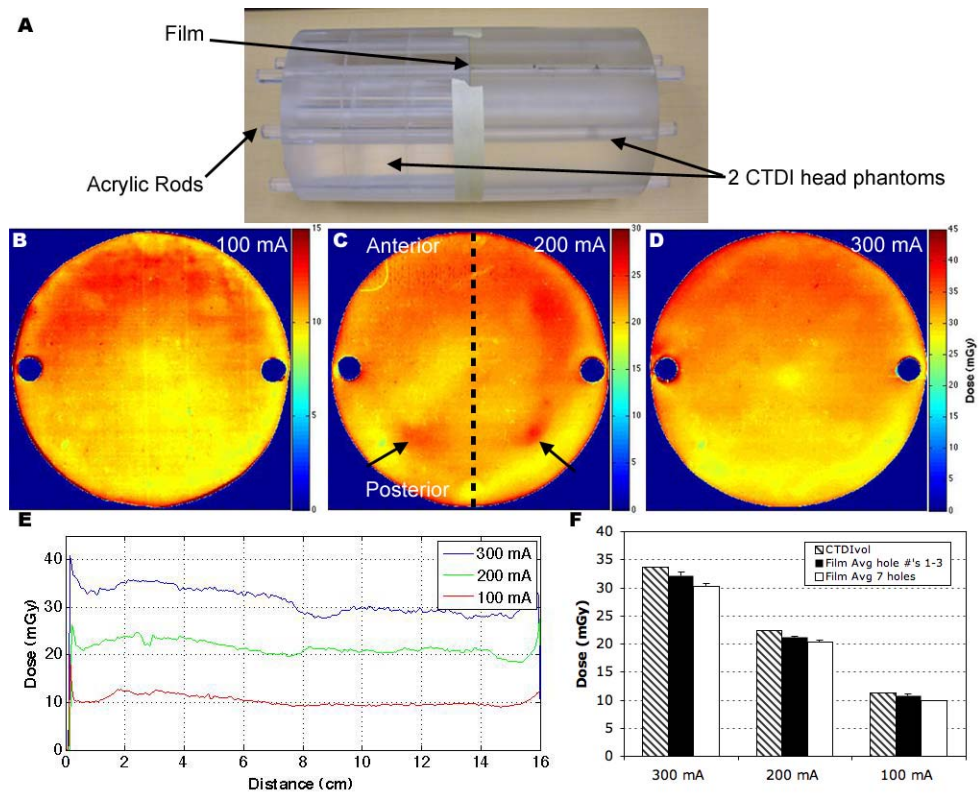


Figure 5.12 2D RCF dosimetry of a modified CTDI head phantom

XRQA films were situated between two CTDI head phantoms (A). The two CTDI phantoms provided a uniform scattering environment for film detection. Each film was exposed to identical scan parameters, but with varying tube currents (mA). The film was used to measure the overall dose distribution uniformity from an axial CT with varied tube currents: 100 mA (A), 200 mA (B), and 300 mA (C); note the dose color scale is different for each tube current plot. Arrows in plot (C) represent areas of higher dose due to air gaps in the CTDI phantom setup. Vertical line profiles were taken along each of the films exposed to the three different mA settings and showed an increase in dose levels from the anterior to posterior sides of the film. Dose levels over select areas of the films are compared to the calculated CTDIvol of the given scan parameters, i.e., (100-300) mA (F).

a geometry that orients the more sensitive, large surface area of the film, parallel to the CT beam. This phantom was created by combining two CTDI head phantoms into one with the dosimeters situated in between the overall phantom halves. (2) Measurements

between XRQA film and TLDs were compared within a 5-yr old pediatric anthropomorphic phantom as a means for organ dosimetry in the lungs, liver, and kidneys. For data analysis within the phantom volumes of aim one and two special software was written to: individually calibrate TLD and film dosimeter responses for different tissue attenuation *f-Factors*; to spatially register dosimeters with respect to phantom and CT coordinate systems; and extract dose responses from film for TLD comparison. As a comparison, TLDs were considered the gold standard and were used to measure dose in the same geometry as the XRQA films.

5.2.1 Materials and Methods

Two CTDI head phantoms were combined, end-to-end, to form one geometrically simple phantom that provided a uniform scatter environment, see Figure 5.12(A). The CTDI head phantoms, together, measured 16 cm in diameter by 30 cm in length. Each phantom had nine probe holes that ran the length of the phantom. The unused holes were plugged using acrylic rods to remove the effects of radiation scatter in air. The phantoms were aligned to create a grid pattern shown in Figure 5.13(A-B). The two most lateral holes each had an acrylic rod inserted between the two CTDI phantoms to act as an anchor to prevent either phantom from rotating with respect to the other. Once the phantoms were placed together they were held together by tape.

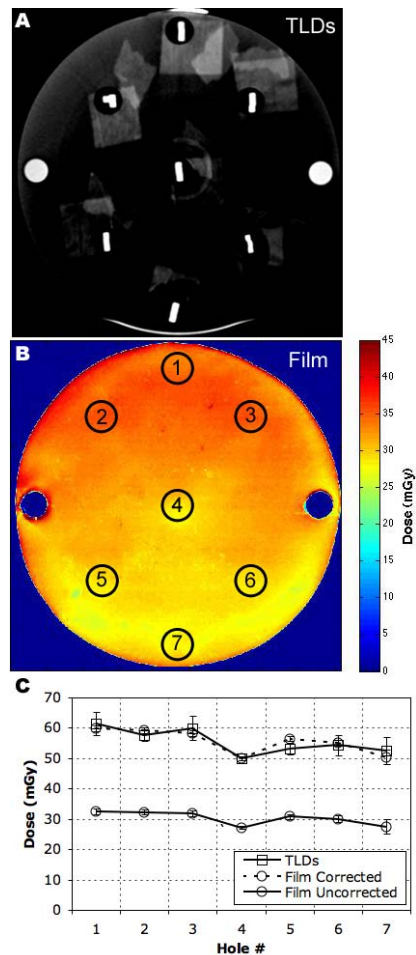


Figure 5.13 RCF and TLD dosimetry compared within a modified CTDI head phantom

TLD (A) and XRQA (B) measured dose levels are compared. TLD and film detectors were exposed with 300 mA tube current. Seven locations over the area of the CTDI phantom were used to compare dosimeter responses (C). Initial film response levels were 45% lower than the TLD responses. The difference in film and TLD responses was consistent among high and low dose regions, and therefore was correctable. The initial film response was corrected using the average percent difference calculated between the film and TLD values.

A 5-yr old anthropomorphic phantom (CIRS, Norfolk VA) was used in this study to emulate pediatric patient geometry. The phantom included 26 numbered transverse

sections, each 25 mm thick, see Figure 5.14(A-B). Each slice had 5 mm diameter holes placed in predefined grid patterns, see Figure 5.14(C). The holes were numbered on the phantom (not shown in Figure 5.14(C)) for convenience when correlating dosimeter position with organ selection. Each organ had a number of holes within its boundaries for TLD placement. Unused holes were filled with material equivalent plugs. The phantom consisted of 5 tissue types: soft tissue, lung, brain, spinal cord, and bone. The tissue types were engineered to produce photon attenuation values within 1% for bone and soft tissue substitute, and 3% for lung tissue substitute over the range of 30-20,000 keV (as quoted by CIRS); hence, the phantoms anthropomorphic likeness in reconstructed CT images, see Figure 5.14(D).

XRQA films were digitized using reflection densitometry on a flatbed scanner (Expression 10000XL, Epson America, Long Beach, CA)⁵³. All films were digitized using 48-bit color depth with RGB file format (16-bit per color channel) and the red (R) channel was extracted for analysis in Matlab (R2007a, Mathworks Inc., Natick, MA). For film verification, (3x3x1) mm Harshaw TLD-100 chips (LiF:MgTi, Thermo Eberline, LLC, Franklin MA) were used. See Appendix A.2 for a description of TLD dosimetry. A 0.18 cc ion chamber (10X5-0.18, Radcal, Monrovia, CA), with an ion chamber monitor (9015, Radcal), was used for TLD and film calibration purposes. The ion chamber's active volume had a diameter of 14 mm and a length of 19 mm. The overall length of the chamber was 45 mm (active volume plus stem). The ion chamber anode and active

volume wall material was made from graphite and was near air equivalent at the effective CT energies used in this study.

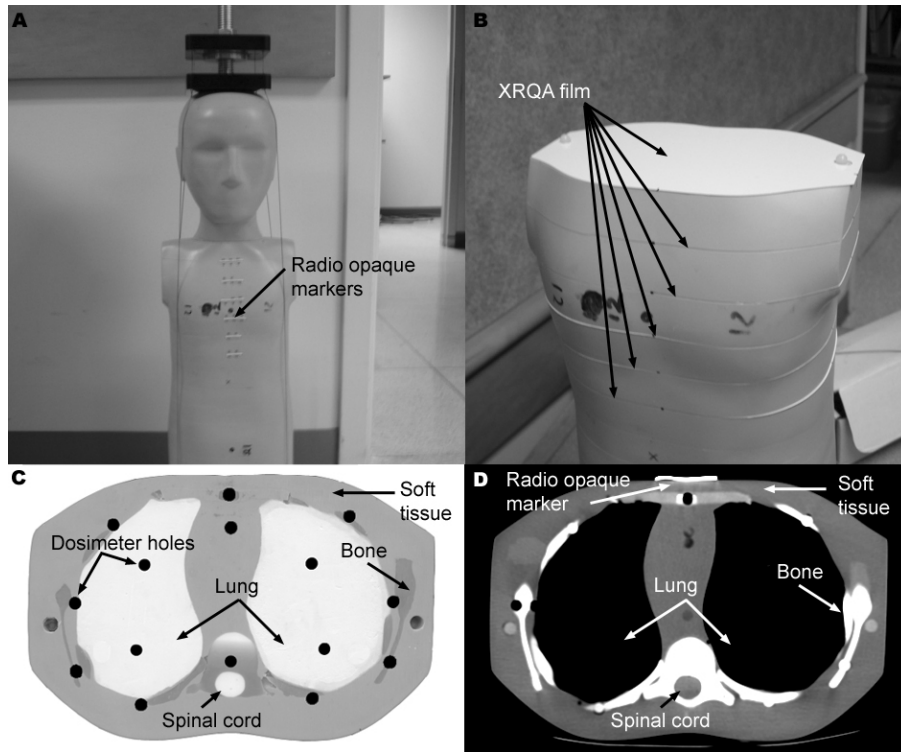


Figure 5.14 5-yr old pediatric anthropomorphic phantom with RCF inserts

A CIRS 5-year old anthropomorphic phantom with radio opaque markers is shown (A). Radio opaque markers indicate slice location of film and TLD dosimeters for dosimeter registration purposes. XRQA film is shown between phantom slices (B). An axial view of the phantom demonstrates tissue types as so indicated (C). The Black dots are predefined dosimeter holes where TLDs were inserted for *in situ* measurement. A corresponding axial view of the phantom in (C) is shown after CT reconstruction (D).

5.2.1.1 Dosimeter Dose Calibration

To correlate the in-situ TLD and XRQA film response to dose, dose calibration curves were developed. Two TLDs, one XRQA film, and an ion chamber were placed on

a Styrofoam block that was extended from the CT couch so that the dosimeters were placed at the CT scanner's isocenter in air, Figure 5.15(A). Four different sets of dosimeters were exposed at varying tube current settings, (150-350) mA, to provide a full range of calculated CT doses. An additional set of TLDs and film were left unirradiated for background subtraction. The calibration of the dosimeters occurred concurrently with the phantom study. To convert the exposure $X(R)$ measurements from the ion chamber to dose, specific for either lung or soft tissue (kidneys and liver) attenuation, the equations (3-7) and (3-8) were used. The effective CT energy (E) used

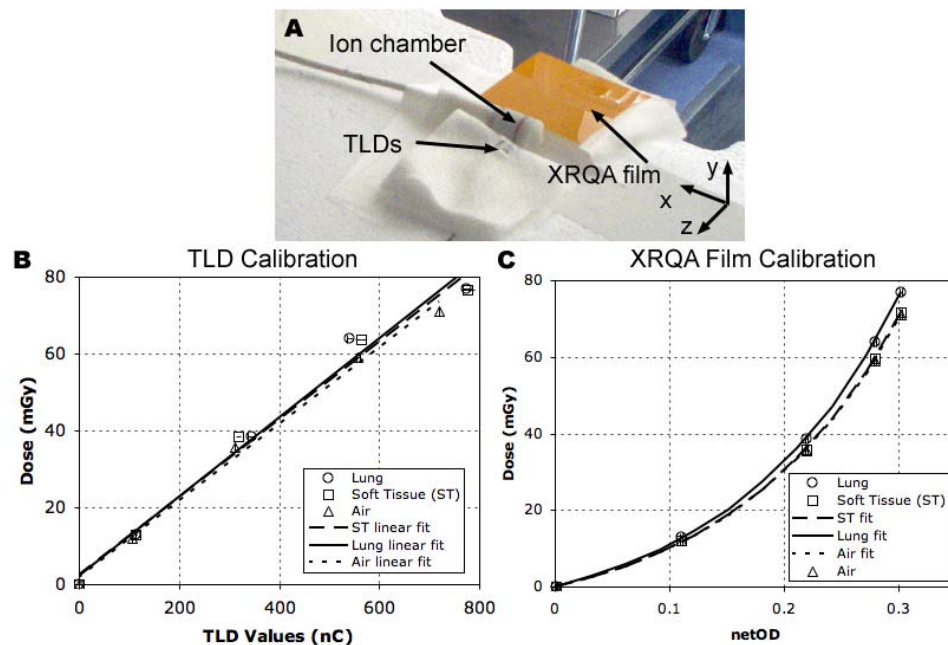


Figure 5.15 TLD and RCF calibration

XRQA and TLD dosimeters were placed on a Styrofoam block and placed next to an ion chamber at the CT isocenter for an in-air response-to-dose calibration (A). The TLD dosimeter response was plotted versus dose and fit using a linear-regression curve(B). The XRQA film was fit with a modified exponential function using a Levenberg-Marquardt algorithm for coefficient optimization (C).

for equation (3-8) was 74.4 keV derived from WinDose⁸⁶. To calculate the *f-Factor* for lung and soft tissue at 74.4 keV, the NIST attenuation coefficient tables for each tissue type, and for air, were plotted and fit using a Boltzmann Sigmoidal fitting function with Prism (Version 4, Graphpad Software, La Jolla, CA) a statistical software package.

Separate calibration curves were developed for both tissue types and for air (used in the case of the CTDI experiment) to calibrate the TLDs and film. The TLD detector response plots were fit using a linear-regression curve, see Figure 5.15(B). The average calculated coefficient of determination (R^2) for the TLD fitting functions was 0.9880. The XRQA film response plots were fit using the modified exponential function in equation (3-10). The fitted functions for XRQA film are shown in Figure 5.15(C); the average calculated R^2 value was 0.9999. The film and TLD fitting functions were created and applied to the experimentally measured data using software written in house using Matlab. The fitting function portion of the software code was benchmarked versus Prism software as a means to validate its accuracy.

5.2.1.2 Phantom Setup and Scan Parameters

For both CTDI and anthropomorphic phantom exposures, the phantom setup and exposure consisted of three phases: (1) the TLD exposure, (2) film exposure, and (3) a phantom only exposure. The TLD and film dosimeters were scanned separately so not to introduce possible spurious results from inter dosimeter scatter. A phantom only

scan was required for the analysis software to be used for organ contouring and segmentation as part of the film calibration process.

A 64 slice CT scanner (LightSpeed VCT, GE healthcare, Milwaukee, WI) was used for phantom scanning. The CT scan and reconstruction parameters used for all three scans consisted of: 120 kVp tube potential, pitch of one (axial scan), 40 mm detector width collimation, and 5 mm reconstructed slice thickness. Generally, most films were exposed to a tube current of 300 mA except for the CTDI phantom exposure where additional scans were performed at a tube current of 200 and 100 mA.

5.2.1.3 CTDI Phantom Exposure Experiment

XRQA film was cut to match the shape of the CTDI phantom profile and placed between two CTDI phantoms. Once the phantom halves were in place, the probe holes were filled with acrylic rods. The rods were placed in contact with the film from both ends of the phantom. Five separate films were exposed to three different tube currents: three scans at 300 mA, one scan at 200 mA, and one scan at 100 mA; each film was exposed separately. Seven sets of three TLDs were bagged and taped into place such that the TLDs were suspended within the seven probe holes, shown in Figure 5.13(A). Acrylic rods were then carefully placed in contact with the TLDs from both ends of the phantom. The TLDs were exposed to one scan with a tube current of 300 mA.

5.2.1.4 Anthropomorphic Phantom Exposure Experiment

Three organs were identified for dosimetry: lungs, liver, and kidneys. The lung region spanned six slices (slices 10-15), and the kidneys and liver spanned three and four slices, respectively, (slices 15-18). The lung, liver, and kidney regions were scanned in one contiguous scan, starting from the neck and ending in the pelvis region. Select locations within the phantom organs were filled with two TLDs each and the remaining holes were filled with tissue equivalent material. The TLDs in each hole were set to be flush with the top of the phantom slice, so when the phantom was assembled no pressure was placed on the TLDs. The phantom slices containing dosimeters were marked using radio opaque fiducial markers on the anterior surface of the phantom, see Figure 5.14(A). The fiducial markers were used for TLD and film spatial registration. The phantom, with TLDs *in situ*, was carefully aligned within the CT bore using the lasers and marked for subsequent repositioning for film and phantom only scans. After the TLD scan, the TLDs were removed and the holes that held TLDs were filled with tissue equivalent material. The XRQA film, which was previously cut to shape to match the different anthropomorphic phantom slices, was placed between the phantom slices, see Figure 5.14(B). The phantom was assembled with nine films between phantom slices and repositioned on the CT couch. The positional displacement between TLDs and film was ~1 mm. Two sets of films, each at a tube current setting of 300 mA, were separately exposed for a measurement of experimental precision. After the film exposure, the films

were removed and the phantom was reassembled, repositioned, and scanned without any dosimeters *in situ*. The scan of the phantom only was later used in the post processing procedure to extract contours of the lungs and register the TLD and film data together.

5.2.1.5 XRQA and TLD Data Reduction

No software existed that could perform the task of calibrating 2D films within a heterogeneous tissue environment, spatially register, and analyze multiple dosimeters at a time. Therefore, software was developed to perform these tasks in Matlab. The following data were acquired and loaded into the software: digitized pre-irradiated and post-irradiated films, TLD raw data, and the phantom only scans, which consisted of DICOM images. All scanned films and TLD readout results were categorized by slice location. Pre-irradiated and post-irradiated films were registered and converted from pixel intensity values to netOD using equation (1). DICOM images from the phantom only scan were used to differentiate and contour lung boundaries. To differentiate and contour the soft tissue organs, mathematical coordinates of the organ locations within the anthropomorphic phantom were used to develop geometrical masks, see Figure 5.17(A). This was because the anthropomorphic phantom emulated all its soft tissue organs as one material and, therefore, there was no contrast between the liver, kidneys, and surrounding organs in the abdomen. The mathematically generated masks were registered with the reconstructed images from the phantom only scan to indicate the

location of the organs within the coordinate system of the DICOM images. The phantom only DICOM scans were registered with the films and used to contour the lungs and soft tissue organ masks. Once registered, the film and DICOM images shared the same coordinate system. The information of the spatial locations of the organs was taken from the DICOM images and used to extract the dosimetric information from the films by overlaying the DICOM contours onto the films. The netOD from the extracted film data, corresponding to regions of lung and soft tissue, were then calibrated separately using equation (4) preserving the attenuation specific attributes of each organ. Since the CTDI phantom was of homogeneous material, a simple external contour around the phantom was used to calibrate the film. The results from the CTDI phantom were quoted with respect to air attenuation. To compare TLD readings with XRQA film measurements, for both the CTDI and anthropomorphic phantom experiments, the films were registered with digitized images of the phantom slices to match the location of TLDs with spatial locations in the film coordinate system. Once registered, regions of interest (ROIs) were extracted from the film at the locations that corresponded to the TLD positions and were plotted for comparison. See Appendix B for a technical guide of the film post processing and analysis software.

5.2.2 Results

5.2.2.1 Film/TLD Dose Comparison from CTDI Phantom Experiment

Five films were separately exposed when placed within the CTDI phantom; one film each was scanned at 100 mA and 200 mA, see Figure 5.12(B-C), respectively, and three films were scanned at 300 mA and averaged, see Figure 5.12(D). Generally, the films measured a greater dose along the anterior portion of the film than compared to the posterior portion. However, the film exposed at 200 mA exhibited a high dose region in the posterior portion of the film. These regions of high dose are located in the surrounding area of grid numbers 5 and 6, indicated by the arrows in Figure 5.12(C), and were due to the acrylic rods not being in contact with the film thus leaving an air gap between the film and the rods (which was evident from a review of the DICOM images, not shown). The air pocket created a low density region that allowed more radiation to strike the film in the regions surrounding grid numbers 5 and 6 and thus increase the dose. The difference in anterior and posterior dose levels was verified using line profiles taken from the anterior-to-posterior portions of the films, as taken along a representative dashed line in Figure 5.12(C). The line profiles measured a difference in anterior from posterior dose up to 16% for films exposed at 200 and 300 mA, and 13% for the film exposed at 100 mA, see Figure 5.12(E). An interesting point is that the $CTDI_{vol}$ values for (100-300) mA film exposures closely correlated with the film values see Figure 5.12(F); its correlation was calculated to be within 10%. A slightly better agreement between the three exposed films and the $CTDI_{vol}$ values was measured

when only considering the more uniform region of the film in the anterior portion of the film corresponding to grid hole numbers 1-3; its correlation was calculated to be within 4%.

As a measure of film accuracy, the film and TLD values were compared, see Figure 5.13(C). The average difference in magnitude of dose responses was calculated to be 45% (SD \pm 2%). The difference in film and TLD dose response was due to the lower response sensitivity of the film that arises when the film is oriented with its large surface area parallel to the main axis of the CT beam. The consistency of the response difference at both low and high doses allowed for a tissue specific correction to be applied. Once corrected, the average film response agreed to better than 3% (SD \pm 2%) of similarly located TLDs, see Figure 5.13(C).

5.2.2.2 Organ Dose Measurement using 5-yr Old Pediatric Anthropomorphic Phantom

The XRQA films were registered to the reconstructed CT images of the anthropomorphic phantom, see Figure 5.16(A) and Figure 5.17(A), and the area of the film corresponding to the organs of interest in the CT images was extracted and converted to dose using the film dose fitting functions plotted in Figure 5.15(C). The film measured lung dose response is plotted in Figure 5.16(B) and the dose responses corresponding to the liver and kidneys are plotted in Figure 5.17(B). The dose levels for both the thorax and abdomen regions are displayed in color wash and represented by the same dose scale measured in mGy. The magnitude of the dose reported here was

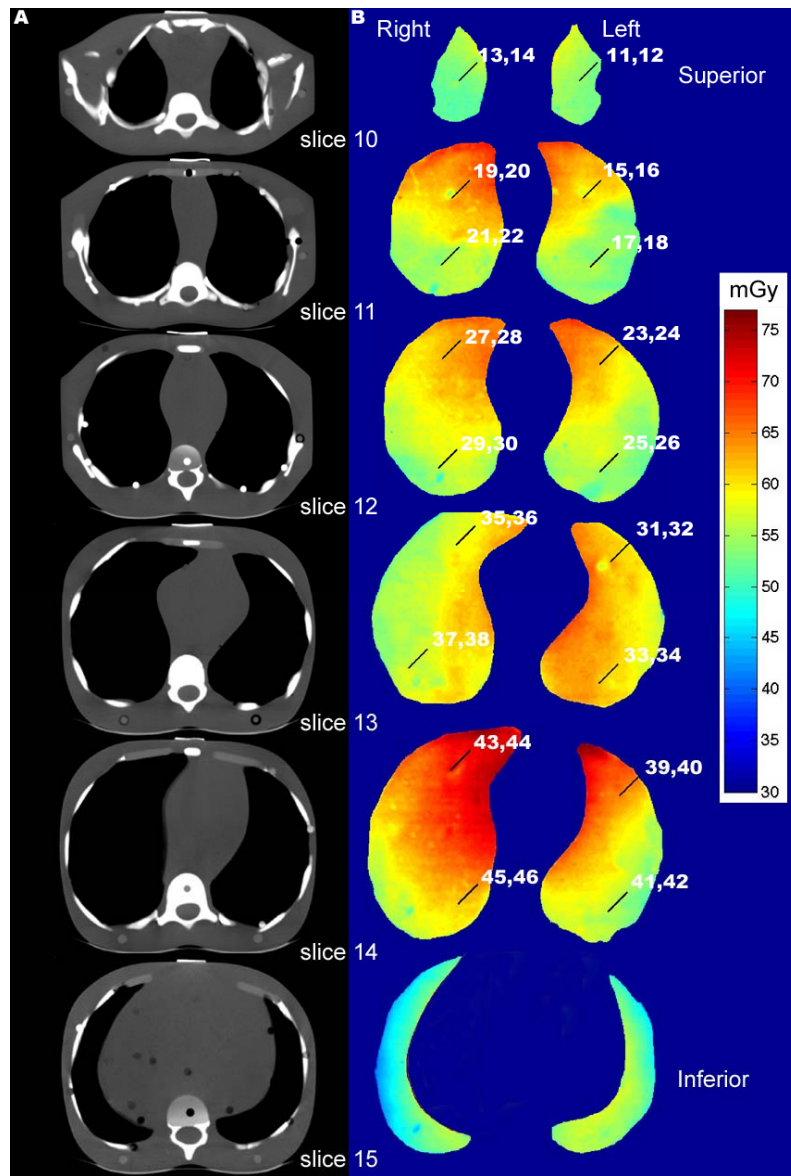


Figure 5.16 2D RCF dose distributions for lung volume in a 5-yr old phantom

XRQA film was placed in between six slices in the thorax region of a 5-yr old anthropomorphic phantom and CT scanned. The reconstructed CT slices of the phantom are shown in (A). The lung regions within the reconstructed CT images were contoured and spatially correlated to the XRQA film lung regions by film/phantom registration. The lung regions of the exposed XRQA films were extracted and are shown in (B). Film dose responses (mGy) are shown in color wash. Separately, TLDs were placed within the lung volume, as indicated in (B), and the phantom and TLDs were CT scanned.

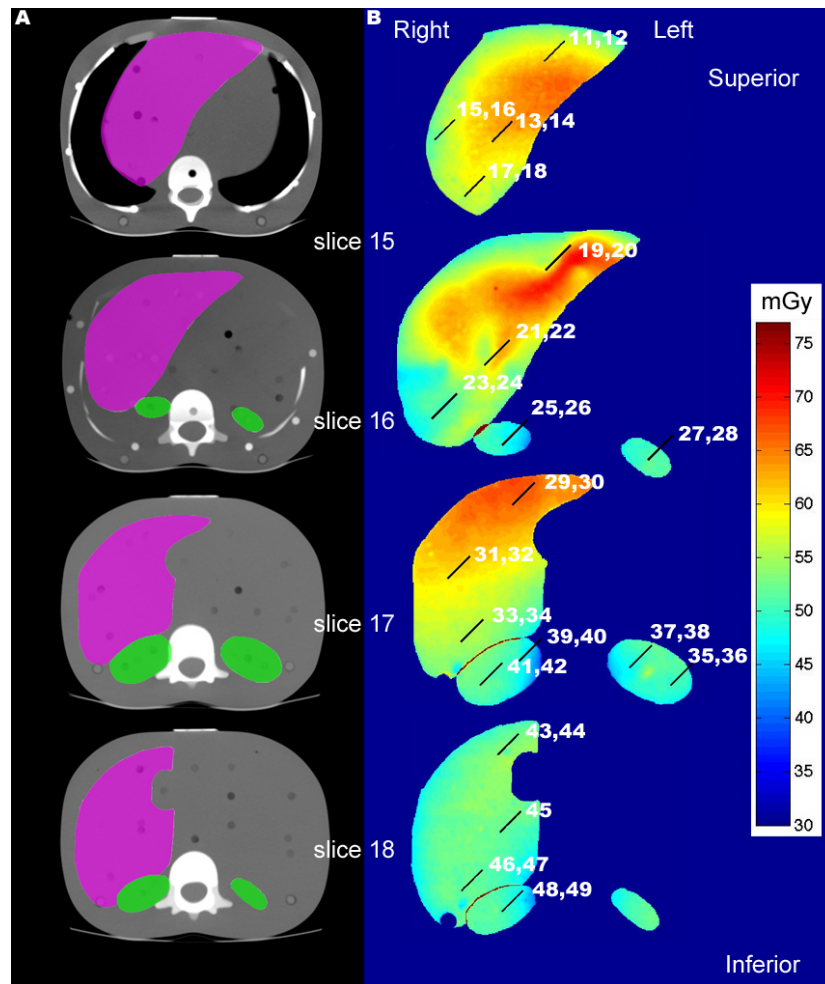


Figure 5.17 2D RCF dose distributions of the liver and kidneys for a 5-yr old phantom

XRQA film was placed in between three slices in the abdomen region of a 5-yr old phantom and CT scanned; slice 15 is a carry over from the thorax region but had liver involvement. The reconstructed CT slices of the phantom are shown in (A). Unlike the lung regions that were easily contoured, the liver and kidneys were not discernable in the reconstructed images. Because there was no contrast in the phantom for direct contouring, mathematical masks were created from digitized images of the actual phantom and overlaid with the DICOM images. The liver was represented in magenta and the kidneys in green. The films were spatially registered with the DICOM images and the areas within the film corresponding to the liver and kidneys were extracted and are shown in (B). Film dose responses (mGy) are shown in color wash and are on the same scale as lung dose responses shown in Figure 5.16. TLDs placed within the liver and kidney volumes are indicated in (B).

not meant to be clinically realistic for pediatric scan protocols. The tube current (mA) parameter was manually set high to provide large beam fluence on the film to maximize the precision of the film results.

In slices 10-14, pairs of TLDs were placed within the lung region to verify film lung response. The location and identification of the 36 TLDs are shown in Figure 5.16(B). For slice 15 the phantom slab did not have any holes within the lung region for TLD placement and, therefore, the film lung response was not verified. Similarly, in slices 15-18, 25 TLDs were placed within regions of the liver and 14 TLDs were placed within the kidneys, see Figure 5.17(B). The film and TLD dose responses for all three tissue types are plotted in Figure 5.18. The error bars on the TLD and film measurements represent the average of two TLDs and two films, respectively, at a confidence level of one standard deviation (1 SD). All film measurements correspond in space to the location of the TLD positions. A difference in film response and TLDs indicated a similar consistent difference in response for the lung, 28% (SD \pm 8%), and liver and kidneys, 15% (SD \pm 4%) as was seen by the CTDI phantom experiment; thus allowing for a tissue specific correction to be applied. Once corrected, the average film response in the lung tissue agreed to better than 3% (SD \pm 3%), for the liver 5% (SD \pm 3%), and for kidneys 4% (SD \pm 3%), see Figure 5.18.

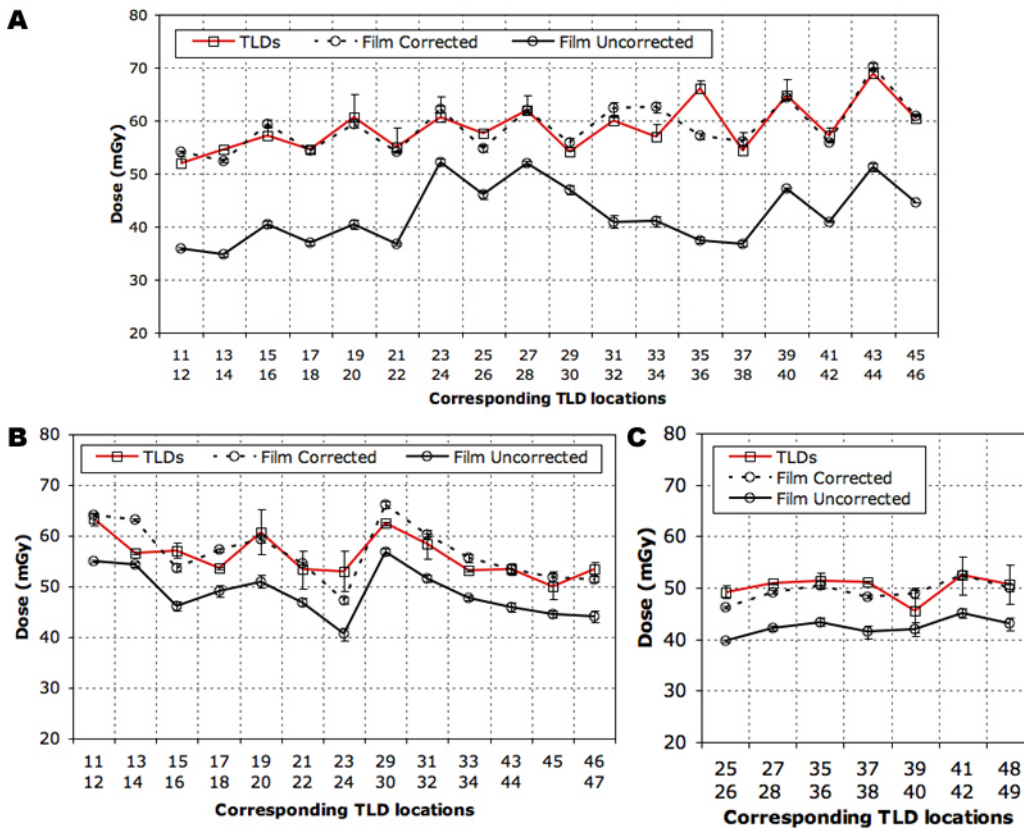


Figure 5.18 TLD and RCF responses compared

TLD and XRQA film dose responses are compared for the lung (A), liver (B), and kidneys (C). The XRQA film dose values were extracted using ROIs centered over the corresponding locations of the TLDs in the phantom, see Figure 5.16(B) and Figure 5.17(B) for TLD locations. Film and TLD values maintain a similar response pattern due to identical scan parameters and scatter geometries. Film values corrected using the tissue specific correction factors generally maintained similar dose response trends since film and TLD readings were consistently offset in both the high and low dose regions. Error bars for film and TLD are a measure of deviation for the two TLDs and two films measured per location (quoted at 1 SD).

5.2.3 Discussion

The lower film response, as indicated previously, was generally consistent in the low and high dose regions, as is seen by the similar trends in film and TLD responses,

see Figure 5.18. This allowed for tissue specific correction factors. The correction factors were calculated for each tissue type by measuring the average difference in response from all of the TLD and corresponding film values throughout the entire organ volume. The average difference of the two responses was used to globally correct the initial film dose values for all films located within the volume of the specific organ. This volumetric approach to correcting the film response was more consistent for the two soft tissue organs, liver and kidney. A possible reason was that within the abdomen region, the scatter conditions were more consistent from slice-to-slice because of the consistency in body habitus shape and homogeneity of the emulated abdomen tissue, see Figure 5.16(A). Within the thorax region the lung dose varied more, slice-to-slice, due to the change in scatter conditions from the varying difference in the ratio of lung and soft tissue area. The difference in scatter conditions from one slice of the lung to the next possibly caused the volume correction factor to under correct the film lung response in slice 12 (TLDs 23-30) in Figure 5.18. By considering this point a slice-by-slice correction method may be more appropriate. This is accomplished by averaging the difference of the film and TLDs per slice and using the percent difference in that slice only to correct the film. When considering the impact of radiation measurement techniques on risk assessment for organ based dosimetry, we propose that there is a clear need for 2D distributive dose information. With the introduction of RCF as a CT radiation dosimeter, CT dosimetry takes on another dimension of vital information. Instead of a

simple point dose measurement for the organ, CT film dosimetry now relates the amount, and 2D distribution of the dose in the organ volume. With dose distribution measurements, non-uniform dose deposition within an organ volume can be used to better provide a more complete dosimetric analysis for organ risk and CT scan protocol development as a means to mitigate increasing trends of CT dose. As a demonstration of the importance of RCF dosimetry, the dose to the lung, shown in Figure 5.16(B), is greater along the anterior medial portions of the bilateral lungs, which measurements are not captured by the placement of any TLDs. The increase in anterior dose measured by the film is supported by the CTDI phantom exposure results. Unfortunately, no predefined hole in this phantom grid configuration would have allowed for the TLDs to capture this spatial distributed dose information, see Figure 5.14 (C) as one example of the phantom dosimeter grid spacing within the lung. Thus, using a PDM technique will be intrinsically limited when measuring inhomogeneous dose distributions. This PDM limitation is also evident by the fact that the TLD measurements are shown to underestimate the maximum dose to the lung volume by 15%. TLD measured maximum dose was 70.0 mGy (TLDs 42 and 43 located in slice 14) and the measured minimum dose was 52.0 mGy (TLDs 11 and 12 located in slice 10), whereas the film measured maximum dose was 82.5 mGy (slice 14, anterior right lobe) and minimum dose was 52.7 mGy (slice 10, inferior middle right lobe). The TLD results were not inaccurate; they were just not located properly to measure the maximum dose in the lung volume.

The measured dose inhomogeneity to the organs is a function of the geometric complexity of the body and the different attenuating and scattering tissue types within that geometry. An argument can be made from the evidence on hand that to use a point dose dosimeter to measure dose within a volume, and assume that dose is indicative of the entire volume is incorrect. Therefore, it would be incorrect to alter CT protocols and develop scan protocols based on a limited measurement methodology.

Future considerations for this work may focus on reviewing the consistency of the tissue specific correction factors for different detector collimation configurations, i.e., varying the scan parameters to verify how the subsequent effects in changing scatter conditions might affect the use of one single correction factor per tissue type. Also, the eventual goal of this work will be to introduce helical scan parameters for more clinically relevant scatter geometries and dose distribution analysis. However, to incorporate film measurements into a helical scan geometry, the film response to angular dependence must be established. Figure 5.18 demonstrated a strong angular dependence on film response when orienting the large surface area of the film 90° from the rotational axis of the CT x-ray tube (i.e., placing the film perpendicular to the rotational axis of the x-ray tube). In this scan geometry, the CT tube was consistently held at an angle of 90° from the rotational axis, but with a helical scan geometry the scan rotation will vary in angle from the film. Finally, to develop a true 3D film dosimetry an increase in the dose resolution along the z-axis (body length direction) must be made. In

this initial work, serial 2D dose distributions were measured in an anthropomorphic phantom with 2.5 cm phantom sections. For a more accurate 3D measurement, a modified anthropomorphic phantom with slice thicknesses less than 2.5 cm thick will be required.

5.2.4 Conclusion

In this work we proposed a novel RCF dosimetry technique, using XRQA film, for organ dosimetry within a pediatric anthropomorphic phantom. XRQA film was used to measure a spatially high-resolution slice-by-slice dose distribution within an organ volume. First the film accuracy and sensitivity to a CT scan geometry was validated using TLDs within a modified CTDI phantom. The film measurements consistently under responded in the high and low dose regions, when compared to TLD results. This allowed for the film to have a correction factor applied. Once applied the film agreed to better than 3% ($SD \pm 2\%$) for the CTDI phantom. The under response of the film was attributed to the lower detection sensitivity of an x-ray beam when the film is oriented such that its large surface area is parallel to the x-ray beam's main axis. Measurements between XRQA film and TLDs were then compared within a 5-yr old pediatric anthropomorphic phantom in a similar methodology as the CTDI phantom. To analyze the data within the complex heterogeneous anthropomorphic phantom, software was developed: to individually calibrate TLD and film dosimeter responses for different tissue attenuation factors; to spatially register multiple dosimeters with respect

to phantom and CT coordinate systems; and extract dose responses from film for TLD comparison. The subsequent results of the dose measured for the lungs, liver, and kidneys also indicated a consistent geometrical sensitivity of the film detection within the anthropomorphic phantom. Once corrected, the film response agreed to better than 3% (SD \pm 3%) for lungs, 5% (SD \pm 3%) for liver, and 4% (SD \pm 3%) for kidneys. Additionally, high-resolution dose distributions were measured within the anthropomorphic phantom organ volumes. The film dosimetry measured a non-uniform deposition of dose to lung, liver, and kidney volumes, the extent of which, the TLD detectors were unable to measure. In fact, the film measured a 15% greater maximum dose than the TLD maximum. A 2D film measurement was essential in this instance to accurately locate the maximum dose and measure the extent of the dose distribution within the organ volumes. XRQA RCF has been shown to provide a novel and accurate organ dosimetry within a CT scan volume. Dose distributive CT dosimetry may provide a more robust means for determining radiation impact from a CT scan to an organ volume.

6 High Energy Dosimetry

Continuing with the application phase of this work, RCF dosimetry was applied to the upper limits of detection for XRQA and EBT film. In this chapter, RCF will be used for 2D dosimetry of three indirectly ionizing radiation energy levels: (1) ^{137}Cs exposures (663 KeV), (2) linear accelerator cancer patient exposures (6 MV), and (3) neutron exposures from a $^2\text{H}(d,n)^3\text{He}$ reaction (10 MeV). For these three exposures, the dose levels are on the order of (2-5) Gy.

6.1 Applications to ^{137}Cs Irradiator Dosimetry

The ^{137}Cs irradiator has been used as an irradiator for biological and clinical laboratories for many years due to its energy—662 keV gamma-ray (γ -ray), and its longevity—30 yr source half-life. The ^{137}Cs irradiator serves a diverse experimental population and is commercially available in two main configurations: a fixed source or a translatable source. With either type, once the source is located in the “on” position, the source is held stationary while exposing a sample to a flux density for a time interval of, dt . With a fixed irradiation geometry, a planar fluence field measurement is possible⁸⁷.

A high resolution dose distributive mapping is essential to localize the 100% region for accurate sample irradiation and dose rate measurements, else if samples are placed incorrectly and dose rates are improperly measured, spurious results will occur and a waste of time and resources will likely result. A common procedure for mapping dose distributions and determining regions of isodose is to use an ion chamber that is

physically translated around the irradiator cavity⁸⁸ or by using arrays of TLDs. Isodose curves are derived by interpolation of the PDD measurements. The use of a PDD technique results in a low-resolution mapping² of the radiation field, is laborious, time consuming, and is prone to dosimeter placement inaccuracies especially in regions of high-dose gradients. With RCF, a higher resolution isodose mapping can be created for analysis in a matter of hours, compared to what could be days using an ion chamber or TLD detectors.

A dose rate value is the second key piece of information necessary to accurately operate a ¹³⁷Cs irradiator. The dose rate is used for calculating irradiation exposure times, (“beam on” times), for the delivery of a prescribed dose. The following investigates dose rates measured during rotation and while stationary, exposure-to-dose correction factors for air and soft tissue as an assessment of delivered dose accuracy, and a proper timer error correction methodology.

In the following work, 2D RCF dosimetry is investigated as a more accurate means to establish dose distribution mappings for ¹³⁷Cs dosimetry. The RCF results will be compared to manufacturer-provided distribution mappings and independent PDDs using an ion chamber and TLD detectors. Once the dose distribution mappings are developed an improved dose rate measurement technique is proposed.

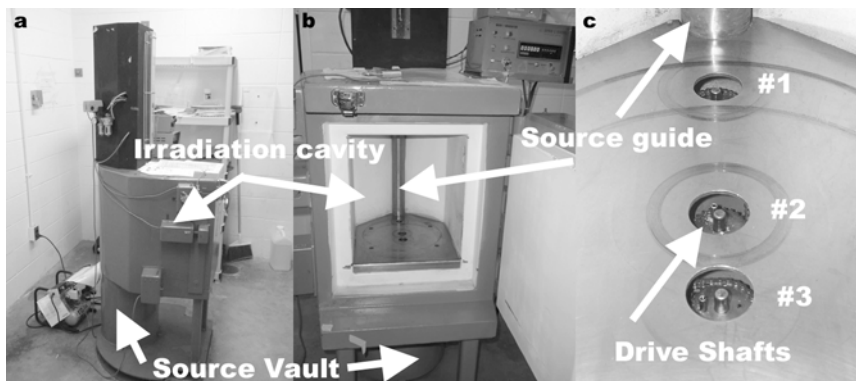


Figure 6.1 ^{137}Cs irradiator Mark I-68A

The Mark I-68A ^{137}Cs irradiator is shown from the side demonstrating the location of the source vault in relationship to the irradiation cavity, (a). The source resides in the source vault while in the “off” position and moves up along the source guide, (b), into the “on” position to expose the irradiation cavity with gamma radiation. The manufacturer provided dose distribution mappings are delineated at three specific cross-sectional planes that correspond with three drive shafts used to rotate sample turntables, (c).

6.1.1 Materials and Methods

The irradiator employed in these experiments was a Mark I-68A ^{137}Cs irradiator (JL Shepherd and Associates, San Fernando, CA). The irradiator was housed in a compact, self-shielded module (81 cm in diameter x 198 cm tall), Figure 6.1(a), with an interior irradiation cavity (31 cm wide x 36 cm tall x 15.5 cm deep), Figure 6.1(b). The source material is in the form of two Cesium Chloride (CsCl) sources, which have the consistency of a solid that are triply encapsulated in stainless steel containers and are welded to a translatable rod. The sources are stacked in a vertical column ~7 cm apart within a cylindrical source guide⁸⁹. The lowest source is ~0.3 cm from the irradiator cavity floor during “beam on”⁸⁹. The sources (referred to cumulatively as the source)

reside in a large vault at the base of the irradiator during times of “beam off”. The source moves into position by compressed air during “beam on” to expose the irradiation cavity with gamma radiation. The source transitions from the storage vault to the “beam on” position in (1.14 ± 0.05) sec negating any need for raise time dose corrections when calculating exposure time. Dose distribution and dose rates were measured in three locations. Each location corresponded to the location of a motor shaft used to rotate the sample turntables. The three motor shafts were labeled positions 1, 2, and 3 where position 1 is the closest to the source and position 3 the furthest, Figure 6.1(c).

EBT films irradiated at positions 1, 2, and 3 were from lot numbers 36076-002I, 36348-02I, and 35322-002I, respectively. All film samples were handled in accordance with the recommendations set forth in the American Association of Physicists in Medicine’s TG-55 report². All films were digitized pre-exposure and post-exposure using the EPSON V700 scanner. The digitized EBT film was analyzed using an in-house algorithm created in Matlab (7.0 Release 14, Mathworks, Natick, MA).

Due to ^{137}Cs ’s γ -ray energy of 662 keV, a 2 mm buildup plate of Polymethyl Methacrylate (Plexiglas) material was used for CPE. The buildup plate thickness was calculated using CSDA values for electrons with energies of 662 keV in Plexiglas³⁶.

A 0.18 cc ion chamber (10X5-0.18, Radcal, Monrovia, CA) with an ion chamber monitor (9015, Radcal) was used for calibration purposes, independent film distribution

verification, and dose rate measurements as was previously described in section 5.2.1. Harshaw TLD-100 (LiF:MgTi) chips (Thermo Scientific, Franklin, MA), that measured (3 x 3 x 1) mm, were also used for an independent comparison of the measured EBT film and manufacturer-provided dose distributions. See Appendix A.2 for a description of TLD dosimetry.

6.1.1.1 Comparison of Film, Manufacturer's Data, and Independent Dosimeters

The data provided by the manufacturer (provided at the time of irradiator installation September 16th, 1989) was compared with measured isodose plots using vertical and horizontal line profiles. Vertical profiles along the central axis of the manufacturer-provided and EBT-measured dose distributions were sampled from the top of the irradiator cavity to the cavity floor. The horizontal profiles consisted of seven points measured from left to right of the irradiator cavity at two heights: 11 and 19 cm from the cavity floor. The manufacturer's plots were sampled at the central point of each isodose region. TLD and ion chamber data were used to verify the EBT film dose response at position 2. The results of the ion chamber and TLD measured dose responses at position 2 represent a similar response to dose by EBT film at positions 1 and 3 since EBT film was established as dose rate independent, see section 2.5. The ion chamber and TLD detectors were placed inside empty (air filled) 50 ml plastic vials and were positioned on top of a Styrofoam block, Figure 6.2(a-b), allowing exposure

measurements in air. A beam attenuation of 0.6% was introduced by the vials and was accounted for in the calculation of dose.

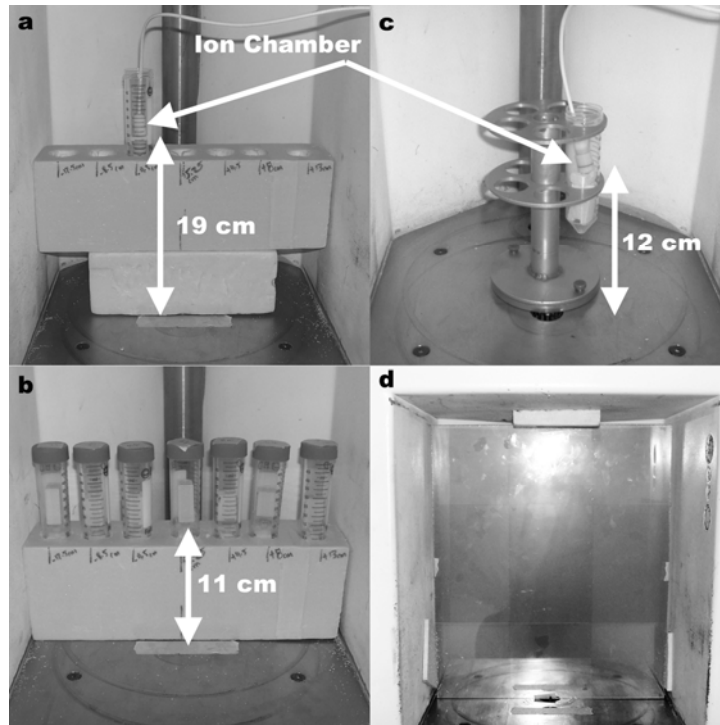


Figure 6.2 Dosimetry experimental setup

Two horizontal dose profiles were used to verify film results. Horizontal profiles were measured at 12 cm and 19 cm from the irradiator floor and centered over position 2. Each horizontal profile was independently measured with both an 0.18 cc ion chamber, (a), and TLD chips, (b), suspended in 50 ml plastic vials across seven locations. The dose rate measurements used a rotating vial platform and a 0.18 cc ion chamber suspended in a 50 ml plastic vial 12 cm above the irradiator floor, (c). Dose distribution mappings were measured at each position (position 2 shown) using a Plexiglas buildup plate and four EBT films, (d).

6.1.1.2 Dose Rate Calculations

Stationary dose rates were measured while the ion chamber was suspended in air, 12 cm above the irradiator cavity floor, and centered above the three positions.

Source-to-chamber distances (SCD) for the stationary setup were: position 1--5 cm, position 2--15 cm, and position 3--20 cm. Rotationally measured dose rates were measured with the ion chamber suspended in air using a platform (10 cm diameter x 15 cm tall) designed to hold 50 ml vials, Figure 6.2(c). The ion chamber was placed inside an air filled 50 ml vial at 12 cm above the irradiator cavity floor and rotated at a radial distance of 3.5 cm from the center of each position. Exposure readings were converted to dose using two dose-to-medium correction factors one for air and another for soft tissue. Air and soft tissue correction factors were calculated using equation (3-8): (1) air--0.869 cGy R⁻¹, and (2) soft tissue--0.9620 cGy R⁻¹ (E=662 keV). Dose was sampled over a range of (1-40) Gy, which corresponded to exposure times from (0.09-8.80) min. Actual exposure times, t_{actual} , were calculated to measure the presence of timer error using the following:

$$t_{actual}(\text{min}) = \frac{\dot{D}(t_{irradiator}) \cdot t_{irradiator}}{\dot{D}_{true}(t > d_{20Gy})}, \quad (6-1)$$

where \dot{D}_{true} is the mean dose rate calculated from exposure times greater than used to deliver a dose of 20 Gy (20 Gy represents a dose delivered for a long exposure time where timing error is minimal), and $\dot{D}(t_{irradiator})$ is the calculated dose rate from the irradiator timer's clock readout, $t_{irradiator}$, and the ion chamber measured dose.

The measured dose rate values were also corrected for ion chamber placement outside of the 100% isodose for positions 1 and 3. The ion chamber placed 12 cm from

the irradiator cavity floor for position 1 was located within the 103% isodose and for position 3 it was located within the 98% isodose.

6.1.1.3 Film Digitization

EBT film measures (20.3 x 25.4) cm. The irradiation cavity measured 31 x 36 cm, which required several films to provide coverage of the cross-sectional area of the irradiation cavity. A central (30 x 35) cm of the irradiator cavity was chosen for dose distribution measurements. Four films were placed at each corner of the cross-section overlapping in the central region, Figure 6.2(d). Each film was irradiated separately to avoid attenuation artifacts from overlapping films. The films were combined using Matlab for one continuous EBT film data set. Measured dose distributions were normalized to match the normalization patterns of the manufacturer-provided isodose plots. General points of normalization correlated to locations of maximum dose response. Each film was scanned in transmission mode at a resolution of 72 pixels per inch (0.4 mm pixels), with no color corrections, and saved in uncompressed Tagged Image File Format.

6.1.1.4 Dose Calibration

Calibration curves for film and TLD dose responses were created. The film and TLD responses to radiation were calibrated to dose to relate their respective responses to the manufacturer's data. Calibration curves for film and TLD chips were established using the following acquisition setups. For the film, an OD to dose calibration curve was created from seven pieces of EBT film. Each piece was irradiated at different

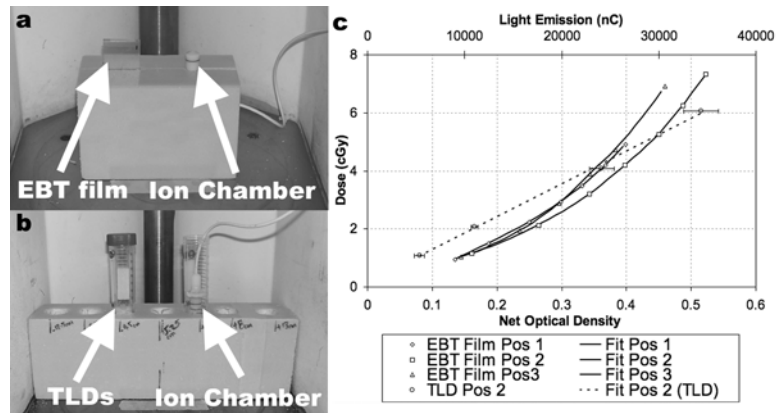


Figure 6.3 Calibration experimental setup

Calibration curve experimental setups: EBT film, (a), and TLDs, (b), required a Styrofoam block to place the dosimeters 12 cm above the irradiator floor to provide a free-in-air irradiation environment. Plexiglas buildup plates were used for film and TLD dosimeters, and dosimeters used in TLD calibration curve setup were corrected for beam attenuation due to the 50 ml plastic vials used to suspend dosimeters in air. Resulting calibration curves, (c), were developed at positions 1, 2, and 3 with net optical density to dose for films and light emission to dose for TLDs, (TLDs were only calibrated at position 2).

exposure levels along side an ion chamber. A Plexiglas buildup plate was used with the EBT films to provide proper CPE. The films were set atop a Styrofoam block so to be surrounded by air with the surface of the films set perpendicular to the main axis of the ^{137}Cs source, Figure 6.3(a). The films used for calibration were allowed the same amount of film stabilization time for equal OD growth as the dose distribution films. Similarly, two TLDs were placed next to an ion chamber atop a Styrofoam block within a custom built device, designed to hold the TLDs in air above the block and provide proper buildup for CPE, Figure 6.3(b). The average, of the three film positions' goodness of fit

was calculated to be 0.9934, Figure 6.3(c). TLD light emission values were plotted versus dose and the data were fit using a linear-regression curve:

$$Dose_{air}(cGy) = 0.0168 \left(\frac{cGy}{nC} \right) \cdot TLD(nC) + 16.52(cGy) \quad (6-2)$$

where $TLD(nC)$ is an average of two TLD light responses, as measured by the TLD reader. The goodness of fit for the TLD dose calibration curve was calculated to be 0.9975, Figure 6.3(c).

6.1.2 Results and Discussion

6.1.2.1 Film Dose Distribution Measurements

The resulting measured dose distributions are shown in, Figure 6.4(a-c), the film's dose distribution converted to isodose in, Figure 6.4(d-f), and the manufacturer-provided isodose distributions, Figure 6.4(g-i), for positions 1, 2, and 3. By qualitative inspection, the central-vertical 10 cm of the three measured isodose plots agree with the manufacturer-provided isodose plots. However, the surrounding gradient regions in the plots show a substantial difference between the measured and manufacture's data. The measured dose gradients were incrementally lower, in relative dose, compared to the manufacturer-provided values, which incrementally grew larger in the surrounding regions. Typically, samples are placed in the central 100% isodose region to fully deliver the desired prescription dose. An accurate spatial mapping of the 100% dose region is critical for proper sample placement. For position 2, the EBT film's 100% isodose region measured 10 cm (left to right) and 16 cm (top to bottom) compared to the manufacture's

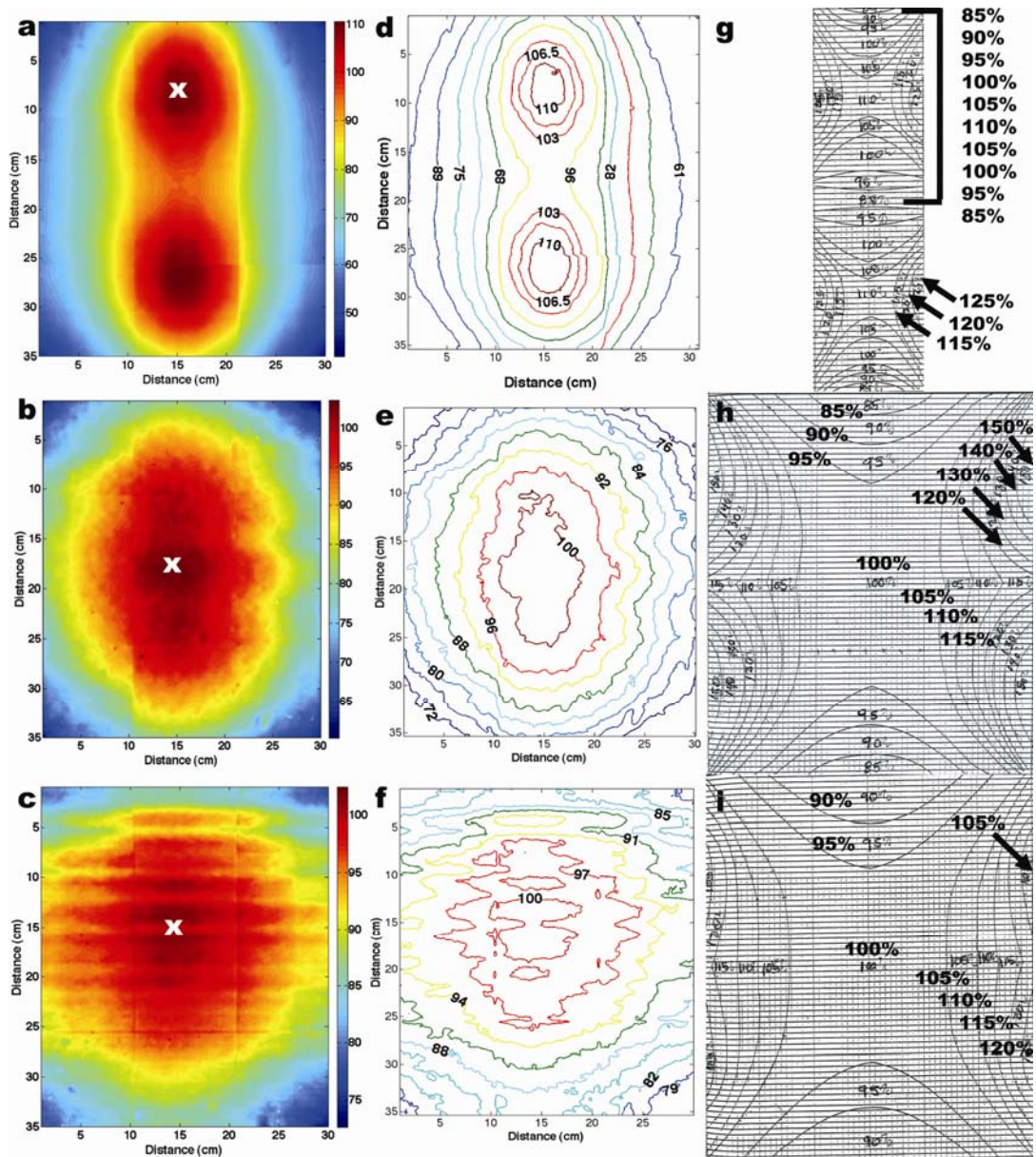


Figure 6.4 EBT film and manufacturer's overall data compared

Dose distributions measured with EBT films, (a-c), were converted to isodoses, (d-f), and compared with the manufacturer-provided isodose data, (g-i). Manufacturer's data at position 1 (g) was only established for the central 35 (vertical) x 10 cm (horizontal), however, positions 2 (h) and 3 (i) measured the full cross sectional area of the irradiator. The measured dose distributions were normalized at the location marked by the "x", in (a-c).

data which measured (14 x 18) cm, respectively. For position 3, EBT film's 100% isodose region measured (10 x 12) cm compared to the manufacturer's data, which measured (14 x 18) cm, respectively. Overall, the measured central 100% isodose area measured smaller than depicted by the manufacturer-provided plots, which information leads to the possibility of limiting the overall size of samples used in the irradiator.

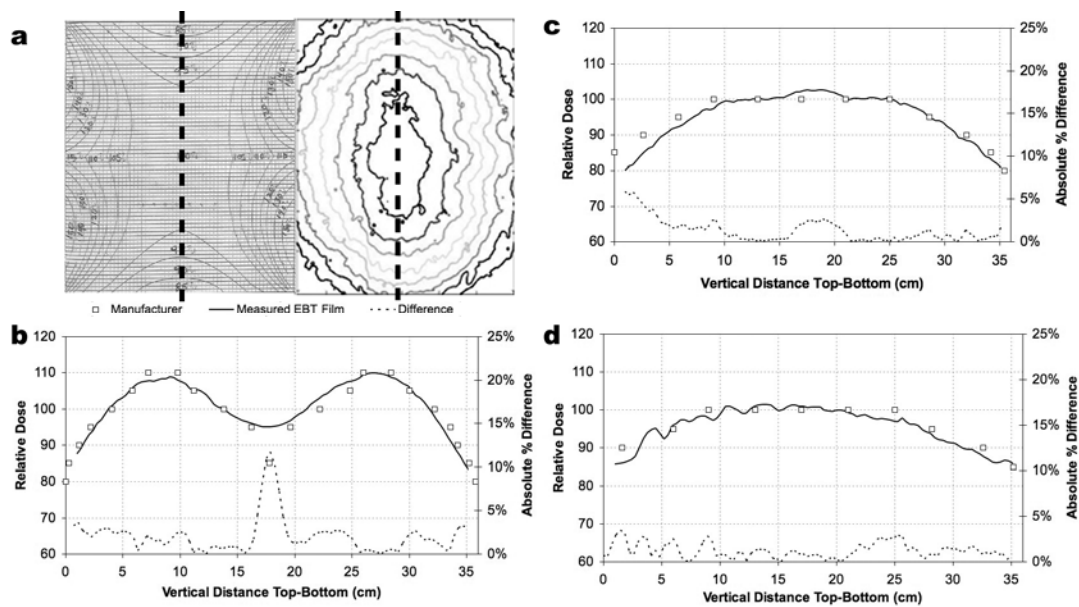


Figure 6.5 EBT film and manufacturer's vertical data compared

Vertical line profiles of the manufacturer-provided and EBT film measured data were compared along the central-vertical axis, (a), for positions 1, (b), 2 (c), and 3 (d). Relative dose difference plots showed general agreement within 95% between measured versus manufacturer data along the vertical central axis.

Some artifacts can be seen in the overall measured dose distribution mappings: horizontal and vertical lines. These lines are located at film boundary interfaces, and are due, predominantly, to intra-batch differences in film response. Film response artifacts had a negligible effect on the conversion from full dose distributions to isodose plots.

Recently, International Specialty Products introduced EBT films in sheets of (35.6 x 43.2) cm, which would allow one RCF to be cut to fit the full cross section of the irradiation cavity and remove film response artifacts altogether. However, the larger RCFs would require a larger scanner, at a significantly greater cost, to digitize the film.

Vertical profiles were used to quantify the agreement along the central-vertical axis where the measured EBT film and manufacturer-provided plots showed the greatest agreement, Figure 6.5(a). The high spatial resolution of the film allowed for one continuous sampling along the central-vertical axis whereas the manufacturer-provided data was discretely sampled in the central region of each isodose. The manufacturer-provided data was interpolated to allow a point-by-point absolute difference comparison with the measured EBT film data. A comparison of the measured to the manufacturer-provided profiles at position 1, Figure 6.5(b), differed by an average of 2%, with a point of maximum difference of 12%, position 2, Figure 6.5(c), differed by an average of 1%, with a point of maximum difference of 6%, and position 3, Figure 6.5(d), differed by an average of 1% with a point of maximum difference of 3%. EBT line profiles measured at positions 1 and 2 exhibited low noise (smooth) profile as was expected due to a high uniformity of construction of the film along its long-axis (1% variation as quoted by the film manufacturer). Position 3 showed greater variability in the top ~16 cm of the measured data. These undulations were investigated and were

reproduced over three separate experiments, and are shown to be a measured effect of the flux pattern at position 3.

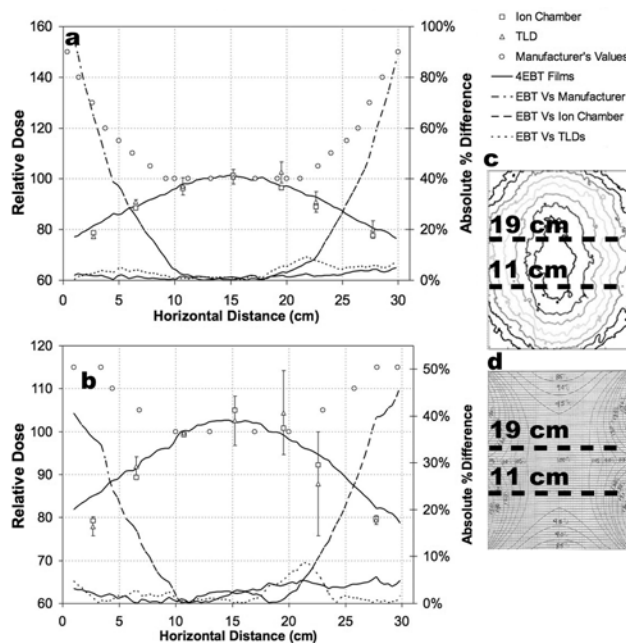


Figure 6.6 EBT film and manufacturer's horizontal data compared

Horizontal line profiles at 11 cm (a) and 19 cm (b) from the irradiator cavity floor sampled the measured distribution (c) and the manufacturer-provided distribution (d). Horizontal line profiles compared relative film dose distributions with manufacturer-provided dose distributions along with two independent dosimeters—TLDs and an ion chamber. Dashed lines depict absolute percent difference between EBT film and the other data sets.

Two horizontal profiles, one measured 11 cm and the other 19 cm from the irradiator floor, were used to compare EBT film with the manufacturer-provided data, and two independent dosimeters: an ion chamber, and TLD chips. Only two horizontal line profiles at position 2 were chosen for a comparison since the manufacturer-provided plots are quadrant-symmetrical, (i.e., symmetrical about the central axis, top to bottom and left to right), and EBT film does not exhibit differences in dose when delivered at

different dose rates. Therefore, films at position 1 and 3 will behave similarly to the film at position 2 making more than two line profiles sampled along the upper and lower horizontal quadrants and at different positions in the irradiator redundant for an independent measurement. EBT film, and manufacturer-provided data, agreed only in the central 10 cm of the dose distribution, which corresponded to the 100% isodose region, but not in the peripheral gradient regions. The 11 cm profile, Figure 6.6(a), measured an average difference between EBT film and the manufacturer-provided dose profiles of 24% with a point of maximum difference of 95%, a difference between EBT film and the TLD dose profiles of 4% with a point of maximum difference of 9%, and a difference between EBT film and ion chamber profiles of 2% with a point of maximum difference of 5%. The 19 cm profile, Figure 6.6(b), measured an average difference between EBT film and the manufacturer-provided dose profiles of 15% with a point of maximum difference of 46%, a difference between EBT film and TLD dose profiles of 2% with a point of maximum difference of 9%, and a difference between EBT film and ion chamber profiles of 3% with a point of maximum difference of 6%.

The results of this RCF dosimetry project have highlighted the necessity for irradiator quality assurance verification. Initial acceptance testing should be performed on all irradiators, when first installed, before scientific and clinical samples are exposed. Additionally, verification of dose distributions should be an ongoing procedure with the integration of RCF dosimetry as a quick and efficient process for measuring large areas

of dose distribution for isodose mapping. RCF dosimetry is a relatively low cost procedure that can be used to verify the mechanical movement of the ^{137}Cs source, and measure areas of isodose for correct sample placement. Specialized irradiation protocols requiring sample placement within dose gradient regions can facilitate a delivery of a lower dose to points surrounding the target by placing the points inside of the dose gradient region. To facilitate such protocols correct mappings of gradient regions are essential, but are difficult to map using conventional measuring systems, such as ion chamber and TLD chips, because they do not provide proper spatial resolution² whereas modern RCFs with spatial resolution quoted at > 1200 lines mm^{-1} ⁹ can make possible accurate measurements in gradient regions². Moreover, RCF dosimetry provides for archival imaging and data storage for long term quality assurance verification.

6.1.2.2 Dose Rate Measurements

Measured dose rates for positions 1, 2, and 3 are shown in Figure 6.7. Dose rates measured during rotation versus stationary exhibit differences of 18%, 10%, and 5% at positions 1, 2, and 3, respectively, Figure 6.7(a-c). Differences between rotated and stationary dose rate values represent the magnitude of error of a delivered dose when the delivery method, (e.g., sample is rotated), is inconsistently paired with the dose rate measurement methodology, (e.g., measured while stationary).

Larger fluctuations in measured dose rate values are seen in the rotated instead of the stationary dose rate values. Fluctuations in the rotated data were predominately

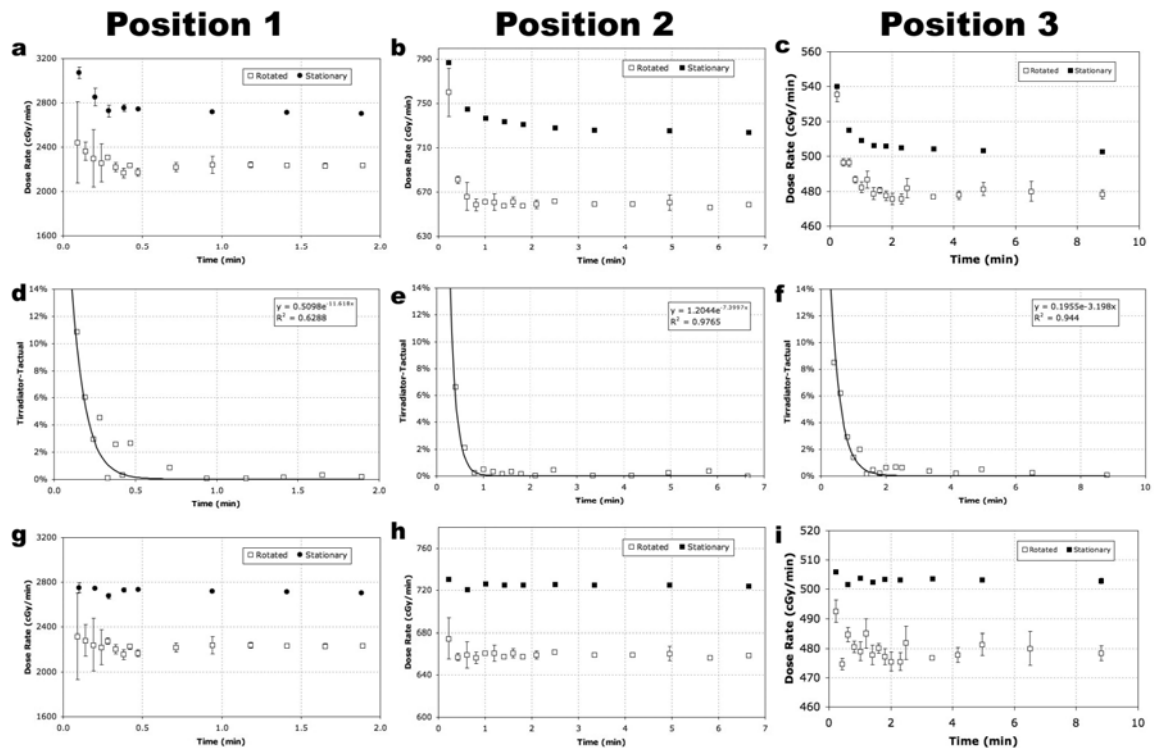


Figure 6.7 Dose rate correction

Measured dose rate values for positions 1, 2, and 3 measure an artificial rise in value do to timer error (a-c). Timer error was measured for a range of times of 0.09-8.80 min. Timer error measured the largest effect for short-time exposures (d-f). Dose rate values corrected for timer error (g-i) exhibit a consistent dose rate value over time with expected experimental fluctuation where greater experimental fluctuation is seen in the dose rate values measured during rotation. Dose rate plots represent values that have been corrected for soft tissue attenuation only.

measured for short-exposure times and are caused by the inconsistent pattern of rotation of the ion chamber used for consecutive measurements, namely: the ion chamber rotates at 10 rev min^{-1} , and starts and stops measuring exposure values at random positions. Fluctuation about the average dose rate is a natural stochastic effect where the larger error bars for short exposure time values, measured at exposure times of $\sim 0.1 \text{ min}$ (one

full revolution of the ion chamber), are due to insufficient sampling of the flux by the ion chamber. It is understood if many more measurements were taken at the shorter-time values a better-sampled measurement would show a lower deviation in value. However, under realistic experimental conditions, samples are not afforded the option for multiple exposures for a more accurate delivery of a prescribed dose using a short exposure time, and thus the values at ~0.1 min represents a lower-limit threshold for accurately delivering prescribed doses during rotation.

An artificial rise in dose rate was seen in Figure 6.7 (a-c) due to an irradiator timer error. To quantify the magnitude of the error, the true exposure time, t_{actual} , was calculated using the measured absorbed dose value divided by the measured true dose rate, \dot{D}_{true} , see equation (6-1). The \dot{D}_{true} was determined from the linear component of the dose rate plots in, Figure 6.7(a-c), which values corresponded to dose rates measured for long exposure times, (> doses of 20 Gy). The absolute percent difference between t_{actual} and the time the irradiator displayed, $t_{irradiator}$, was plotted in, Figure 6.7(d-f). Since the magnitude of the timer error is larger for short exposure times an exponential curve was fit to the data. By extracting fitted curves of the modeled timer error, over a large range of exposure times, future exposure times can be mathematically corrected, Figure 6.7(g-i), to produce the correct time for calculating a prescribed dose, (e.g., for position 2 an exposure time of 0.2 min should be delivered with a time of 0.23 min).

Dose rate values were separately corrected for dose to air and dose to soft tissue. Dose rate values corrected for air at positions 1, 2, and 3 were (2027.0 ± 36.9) cGy min⁻¹, (599.0 ± 1.6) cGy min⁻¹, and (434.7 ± 2.8) cGy min⁻¹, respectively, and dose rate values corrected for soft tissue at positions 1, 2, and 3 were (2233.6 ± 40.6) cGy min⁻¹, (660.1 ± 4.2) cGy min⁻¹, and (479.9 ± 3.0) cGy min⁻¹, respectively. Dose rate values for all three irradiator positions that were corrected for soft tissue attenuation were 10% higher than the same dose rate values corrected for air-attenuation. 10% represents the difference in the mass energy attenuation correction factors of soft tissue and air used to convert exposure-to-dose. Dose rate values are used to calculate irradiator "on time." If a soft tissue target is to be irradiated in a ¹³⁷Cs irradiator, but a dose rate corrected for air is used to calculate the irradiator "on time" a sample overdose on the order of ~10% will occur. It is important to consider the overall composition of the samples irradiated and which attenuation correction factor should be used in the exposure-to-dose conversion. The average sample composition should be used to choose the appropriate dose rate corrected values. Allowance can be made for mixed sample populations in the form of different dose rate tables for different sample types.

6.1.3 Conclusion

With the latest innovations in high-sensitivity RCF and in-beam ion chamber design, an accurate characterization of a ¹³⁷Cs irradiator is possible. The necessity to utilize modern dosimetric tools has been shown (1) in the measurement and comparison

of RCF isodose plots to manufacturer-provided isodose plots, and (2) in the proper measurement of dose rate values considering irradiator timer error, sample exposure method, (rotation versus stationary), and for the exposure-to-dose correction factors. The independent measurements of the ion chamber and TLD chips verified the sensitivity of the EBT film to the ^{137}Cs gamma-ray energy of 662 KeV, and validated the use of the RCF with a commercially available flatbed scanner for a modern dosimetry approach to provide accurate 2D dose distribution mappings. Furthermore, measuring the dose rate requires careful correction for timer error and dose-to-medium correction. Timer error must be corrected using independently modeled timer-error curves on a position-by-position basis since dose rate varies by $1/d^2$. Improper dose-to-medium correction can lead to irradiation discrepancies as was shown by the comparison of air and soft tissue correction factors. We conclude that initial irradiator acceptance testing and regular irradiator calibration protocols should include dose distribution verifications measured with modern, 2D high-resolution RCFs, and dose rates properly measured to correspond to irradiation protocol methodologies.

6.2 Applications to Respiratory-Gated Cancer Patient Treatment Verification

The necessity for quality assurance (QA) in gated radiation therapy treatments has been established^{2, 90}. However, the development of QA methods has not kept pace with the innovations in gating techniques. AAPM Task Group 76 outlined the necessity for a respiratory gating QA device to adequately simulate cyclical motion that is similar

to human respiration, and provide an adequate number of detectors for dose analysis. A variety of dynamic, high-resolution QA devices have surfaced over the years⁹¹⁻⁹⁶. However, each technology is inherently 2D and can only offer QA analysis in one plane of a 3D dose distribution. 3D QA analysis of a dose distribution is highly desirable since a 2D plane does not represent points through out the entire dose distribution in the presence of non-linear respiratory motion. Gel dosimetry has been shown to be a viable option for 3D gated therapy dosimetry QA⁹⁷⁻⁹⁹. Gel dosimeters however have been reported to have undesirable characteristics: PAG dosimeters are susceptible to atmospheric oxygen (O₂) that inhibits the polymerization reaction and MAGIC dosimeters are formulated with toxic chemicals¹⁰⁰. As an alternative to gel dosimetry, PRESAGETM dosimeters were investigated. Key advantages of PRESAGETM dosimeters include: (1) very low scatter due to absorption medium, (2) robustness to laboratory environment (i.e., no O₂ sensitivity), and (3) no need for external container which provides better dosimeter edge resolution through improved refractive index (RI) matching¹⁰¹. In this work we investigate the feasibility of PRESAGETM, a 3D plastic dosimeter, with much improved characteristics as a viable option for respiratory-gated 3D QA verification.

The PREASAGETM/optical-CT dosimetry system has previously been developed and tested for several applications of treatment verification namely: 3D conformal¹⁰², and IMRT¹⁰³⁻¹⁰⁵, this work represents the first attempt towards validating the use of

PRESAGE™ dosimetry for the verification of a gated treatment. The PRESAGE™/optical-CT dosimetry system consists of a radiochromic plastic dosimeter (PRESAGE™) and a novel fast, high-resolution, optical-computed tomography (optical-CT) scanner for dose readout. PRESAGE™ is a 3D leuco-dye doped dosimeter that is clear until irradiated, and once irradiated, it changes color proportionately to absorbed dose¹⁰⁶⁻¹⁰⁹. In a recent report¹¹⁰, PRESAGE™ was shown to be extremely robust with an intra-dosimeter radiochromic response variability of 2%, temporal stability for ~90 hr post-irradiation, and a reproducibility response of 2% was measured at all investigated dose levels. The optical-CT scanner is a dose readout system that utilizes parallel light and telecentric lens geometry for image readout as previously investigated¹⁰³. The scanner is capable of acquiring a complete 3D dataset in ~5 min. The scanner is based on telecentric optics to ensure accurate projection imaging that minimizes artifacts from scattered and stray-light sources as first demonstrated by¹¹¹⁻¹¹³ and allows isotropic high-resolution 3D dose readout.

This work presents results from the ongoing improvement of the fast, high-resolution optical-CT scanner and the results of three treatment scenarios: static, motion (free breathing), and gated were measured and compared to their respective calculated ECLIPSE® treatment plans. The PRESAGE™ measurements were benchmarked with EBT film. EBT film was considered the gold standard in light of prior studies demonstrating its accuracy^{49-50, 55, 101}.

6.2.1 Materials and Methods

6.2.1.1 PRESAGE™ 3D Dosimeter and Dynamic Thorax Phantom

PRESAGE™ dosimeters (Heuris Pharma LLC, Skillman, NJ) have been previously characterized for 3D dosimetry^{101, 110}. Specific to this study, the PRESAGE™ formulation had the following properties: Z_{eff} of 8.3, density of 1.1 g cm⁻³, and a CT number of ~170. Three identical homogenous cylindrical PRESAGE™ dosimeters (5 cm diameter x 5 cm length) were designed to fit into the Dynamic Thorax Phantom (CIRS Inc, Norfolk, VA). The PRESAGE™ dosimeters were maintained at a temperature of ~4°C before and after irradiation. The dosimeter was allowed to reacclimatize to room temperature, ~22°C, before irradiation and the optical-CT readout. Approximately 12 hrs were allowed for the post irradiation polymerization reaction to stabilize before optical-CT readout.

The Dynamic Thorax Phantom (referred to as the phantom) is a phantom that represents a heterogeneous human thorax in proportion and composition. The phantom consists of a tissue equivalent lung, cortical and trabecular bone, and water material, Figure 6.8(A-B). The phantom simulates motion by oscillating a rod made of lung-equivalent material. The rod was designed to hold 3D dosimeters with a diameter of ~5 cm. The rod was modified to accept a locking mechanism that was manufactured on the base of the PRESAGE™ dosimeter, Figure 6.8(C). The locking mechanism allowed for consistent realignment of the dosimeters within the lung-rod insert. All motion studies presented in this work utilized a customized sinusoidal motion profile with 4.5 sec cycle

time, and 15 mm superior to inferior motion that was created to simulate a simple, idealized patient respiration pattern with maximum target displacement in the coronal plane¹¹⁴⁻¹¹⁶.

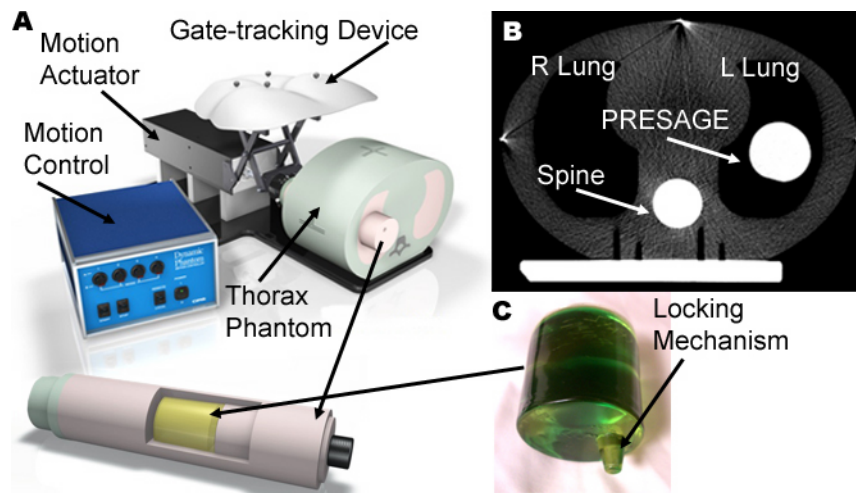


Figure 6.8 Dynamic thorax phantom and PRESAGE™ dosimeter

(A) A CIRS Dynamic Thorax Phantom is shown with a lung tissue-equivalent rod (image used from manufacturer's website). The cylindrical three-dimensional PRESAGE™ dosimeter is placed within the rod and oscillated to simulate respiration motion in the lung. (B) A central CT slice of the phantom shows prominent anatomy with the PRESAGE™ dosimeter in the lung. The PRESAGE™ dosimeter was manufactured with a docking mechanism (C) to allow for accurate repositioning within the lung rod.

6.2.1.2 Optical-CT Scanning of PRESAGE™ Dosimeter

6.2.1.2.1 Optical-CT Scanner Readout

PRESAGE™ dose readout was performed using an in-house fast, high-resolution optical-CT scanner that used a charge coupled device (CCD) area detector for signal digitization¹⁰³, Figure 6.9. In summary, the PRESAGE™ dosimeter is placed on a rotating stage inside an anti-reflection coated glass aquarium. The aquarium is filled

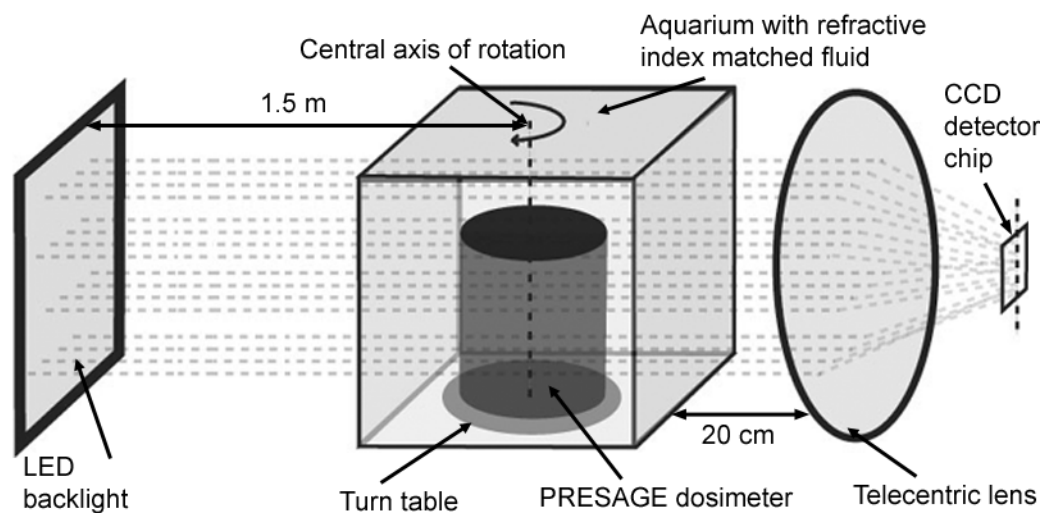


Figure 6.9 Optical-CT scanner configuration

A simplified schematic depicting light rays through the CCD based optical-CT scanner. Projection images through the PRESAGE™ dosimeter are focused onto the CCD camera chip using a tertiary telecentric lens system (acceptance angle < 0.1deg). A two-dimensional projection image was acquired at each rotation step.

with a RI matched fluid comprised of a mixture of octyl salicylate, methoxy octyl cinnamate, and a small amount (3-4 drops) of green oil-based dye. The dye was used to equalize the light attenuation between the dosimeter and the fluid. This optimized the dynamic range of the scanning system. Incident illumination was provided by a 633 nm LED array (Leutron Vision Inc., Burlington, MA). The light source was matched to the peak sensitivity of the PRESAGE™ dosimeters¹⁰¹⁻¹⁰². Projection images were acquired by an A-102f 12-bit monochrome CCD camera (Basler Vision Technologies, Ahrensburg, Germany) that digitized at a resolution of (1392x1040) pixel. The camera was coupled to a TECHSPEC 55-349 telecentric lens system (Edmund Optics Inc., Barrington, NJ). A LABVIEW (National Instruments Corp, Austin, TX) script controlled a step-and-image

acquisition scheme in which the stage made an incremental rotation after an image from the camera was written to disk. The optical-CT maximum field of view was $\sim 7 \text{ cm}^2$, which was limited by the physical size of the telecentric lens. Commercial telecentric lenses were available with a field of view up to 30 cm, though at a significantly increased price. Commercially available tomographic reconstruction software (COBRA, Exxim Corp, Pleasanton, CA), which used a filtered back projection reconstruction algorithm, was used for reconstructing the images readout by the optical-CT scanner. The projection images loaded into the COBRA software were down sampled from (1392x1040) pixel to (160x96) pixel using a bilinear interpolation with a (2x2) pixel kernel to achieve an isotropic spatial resolution of 0.4 mm.

6.2.1.2.2 *Improved Optical-CT Scanning Technique*

Sakhalkar et al.¹⁰³ demonstrated accurate 3D dosimetry in a novel bench top scanner incorporating telecentric optics. Three limiting artifacts were observed in the reconstructed optical-CT images: concentric rings, high noise-to-signal, and significant edge artifact. These three artifacts were minimized in the present work through the following improved scanning technique.

The concentric ring artifact was attributed to relatively stationary structures in all projection images due to particulates in the fluid and defects (e.g., scratches) on the aquarium wall. A 30 μm stainless steel wire mesh filter was used to improve the removal of fluid particulates. Increased fluid filtration was necessary to further remove microscopic debris from the fluid to improve the image signal-to-noise ratio (SNR). To

correct for aquarium wall defects, a series of 50 flood field images were taken. A flood field image consisted of a full aquarium or RI fluid without a dosimeter in place. One image was generated from a mean of the 50 flood field images and was subtracted from each projection image before 3D image reconstruction.

RI matching fluid filtration and flood and dark field subtraction improved the SNR by decreasing the high noise-to-signal ratio in the reconstructed images. Dark field images were generated and subtracted from the individual projection images prior to 3D image reconstruction. A dark field image measured the underlying signal generated by thermally induced electrons and captured in the non-cooled CCD camera's photosites. The acquisition of the 3D data set with a non-cooled CCD camera was limited in its dynamic range with increased acquisition time due to the thermal noise. To account for the thermal noise contribution of each projection image, the lens cap was placed over the lens and an identical number of dark fields were captured matching the number and time for the projection images. However, one mean image of only 100 consecutively acquired images, (acquired in ~1 min), was determined to be sufficient to account for the overall thermal noise contribution to a whole PRESAGE™ scan acquired in ~(5-10) min.

The edge enhancement artifact was attributed to imperfect RI matching between the fluid and dosimeter, and refracted light rays emerging from the dosimeter boundaries as accepted parallel light rays into the telecentric lens system. The RI of the fluid bath was adjusted adding a small amount of methoxy octyl cinnamate (RI value

1.542) to the octyl salicylate (RI value of 1.502) to match the RI of the PRESAGE™ dosimeter (RI value 1.503). Even with the fluid bath and dosimeter RI values matched, the edges of the dosimeter were visible due to non-parallel light, incident on the dosimeter boundaries, refracted such that the angle of refraction of the incident light was within the acceptance angle of the telecentric lens system and thus accepted for image formation. Telecentric lens systems are manufactured to allow only parallel light to be used for image formation. The acceptance angle, or tolerance of the telecentric lens system for non-parallel light, was considered double the angle from parallel which light was accepted for image formation¹¹². The acceptance angle for the telecentric lens system used in this investigation was < 0.1deg (as quoted by the manufacturer). It is possible that non-parallel light from the diffuse LED source could scatter into the parallel plane, and thus contribute to the image; this component is small due to the high transparency of PRESAGE™, but any component was further reduced by placing the LED source at the end of the bench (~150 cm from the PRESAGE™ dosimeter). A smaller scanner could be achieved by replacing the LED source with a telecentric light source.

6.2.1.3 Treatment Planning

Three treatment scenarios were planned and delivered: 1) static delivery where the PRESAGE™ dosimeter was stationary during treatment, 2) motion delivery ‘free breathing’ where the PRESAGE™ dosimeter was in motion during treatment, and 3)

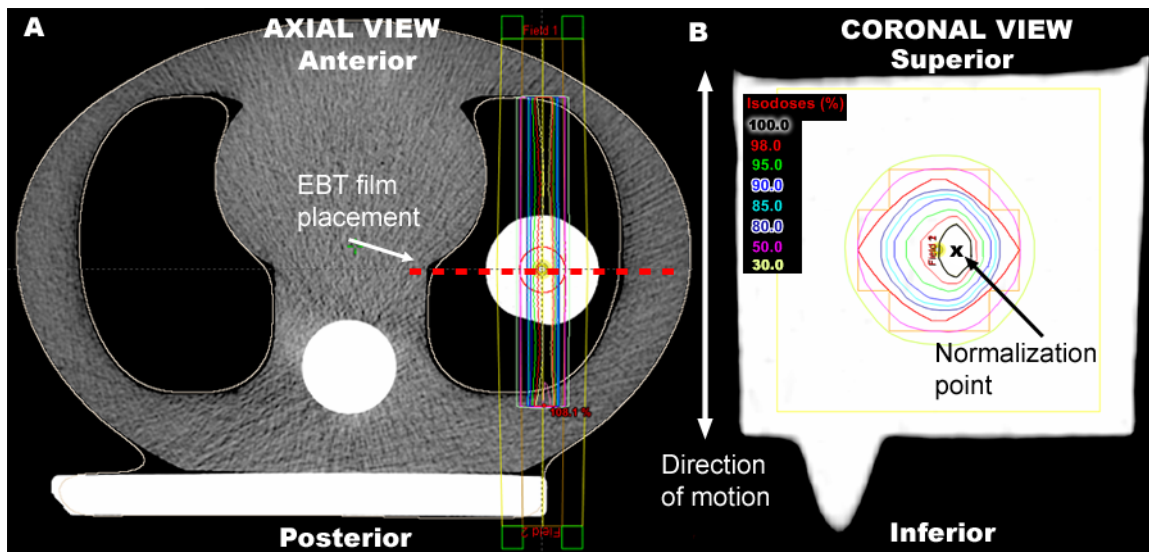


Figure 6.10 Lung AP/PA ECLIPSE® treatment plan

A central slice axial view of the Dynamic Thorax phantom with PRESAGE™ *in situ* (A) is shown with AP/PA beam configuration. EBT film was placed along the central axis of the PRESAGE™ dosimeter (dashed line in (A)) in the coronal plane (B). The approximate normalization point is shown in (B). Small radiosurgery type field sizes (~ 2 cm) were used to capture the full extent of the delivered dose distribution in the PRESAGE™ dosimeters while the phantom was in motion.

gated delivery where the PRESAGE™ dosimeter was irradiated while in motion, but gated to treat at a specific phase in the breathing cycle. For each of the three treatment scenarios small field parallel-opposed anterior-posterior (AP/PA) beams were planned using the ECLIPSE® treatment planning system (Varian Med. Systems, Palo Alto, CA). AP/PA beams allowed for a realistic lung treatment setup that maximized the accuracy for independent verification of EBT film by rendering film placement insensitive to positional differences in the AP direction, Figure 6.10(A). Small field sizes (~2 cm) were planned to capture the full extent of the delivered dose distribution in the PRESAGE™

dosimeter over the full range of displacement the dosimeter would undergo due to the phantom motion. Field sizes were on the order of sizes used for lung stereotactic radiosurgery (SRS).

6.2.1.3.1 CT Scanning Procedures

The phantom, including a PRESAGE™ dosimeter *in situ*, was CT scanned using a multislice CT scanner (Lightspeed, GE Healthcare, Waukesha, WI). The CT scan protocol for the static scenario consisted of a helical 4 slice mode with 5 mm collimation at 1.25 mm resolution per slice. The CT scan for the gated scenario (4DCT scan) consisted of an over-sampled CT acquisition at each slice¹⁷. This involved continuously scanning each slice in axial ciné 4 slice mode for 5.0 sec to scan during one full breathing cycle (4.5 sec). The slice collimation and resolution used were similar to the static scan protocol. Varian's Real-time Position Management software (RPM) recorded a breathing profile concurrent with the 4DCT scan. RPM tracked the motion of the phantom using an infrared (IR) camera and an external IR reflective marker mounted on top of the phantom. Advantage 4D software (GE Healthcare, Waukesha, WI), binned the acquired images retrospectively according to spatiotemporally recorded time signatures and table positions. Reconstructed images were assigned to one of ten specific respiratory phase bins, with a $\pm 5\%$ spatiotemporal tolerance for sorting. Each sorted bin was reconstructed into a 3D data set representing spatiotemporally similar images.

6.2.1.3.2 Treatment and Delivery

Two identical treatment plans were created using ECLIPSE® Figure 6.10. The calculation algorithm used in ECLIPSE® was AAA_8223 which consisted of a calculation matrix of 1.25 mm. The first plan was developed using the static CT scan and was used to deliver the static and motion treatment scenarios. The second plan was developed using the 4DCT scan where phases nine, zero, and one (9-0-1) of the ten respiratory phases were selected and used as the 'gate' for dose calculation and beam delivery of the gated treatment scenario. Phases 9-0-1 represent the point of maximum exhalation. For the delivery of the gated plan, the RPM software was used to track the motion of the externally mounted marker. This respiratory trace was matched with the trace acquired during the 4DCT scan and enabled 'beam on' for the LINAC when the phantom entered into phase nine of the 9-0-1 phases of the respiratory cycle.

6.2.1.4 Independent EBT Film Measurement

Independent verification of the dose distribution was achieved using EBT film. EBT film was chosen for its practical convenience as a self developing RCF, energy and directional independence, and temporal stability¹⁰¹. A PRESAGE™ dosimeter was cut at its central, long axis, which axis represented the coronal plane, and a piece of EBT film was placed between the two PRESAGE™ halves, Figure 6.11(A). The PRESAGE™ dosimeter, with EBT film *in situ*, was placed in the phantom and the treatment plans for the three scenarios were delivered to the EBT film inserts, Figure 6.11(C-E). A calibration curve was developed at the time of experimental irradiation Figure 6.11(B).

The films were digitized using an EPSON 4990 (an earlier model of the V700). Each film was scanned in transmission mode at a resolution of 72 pixels per inch (0.4 mm pixel) with no color corrections and saved as RGB uncompressed Tagged Image File Format. EBT film response was converted to dose using the fitting function of the film's calibration data. The EBT film dose responses were then normalized for inter dosimeter comparison.

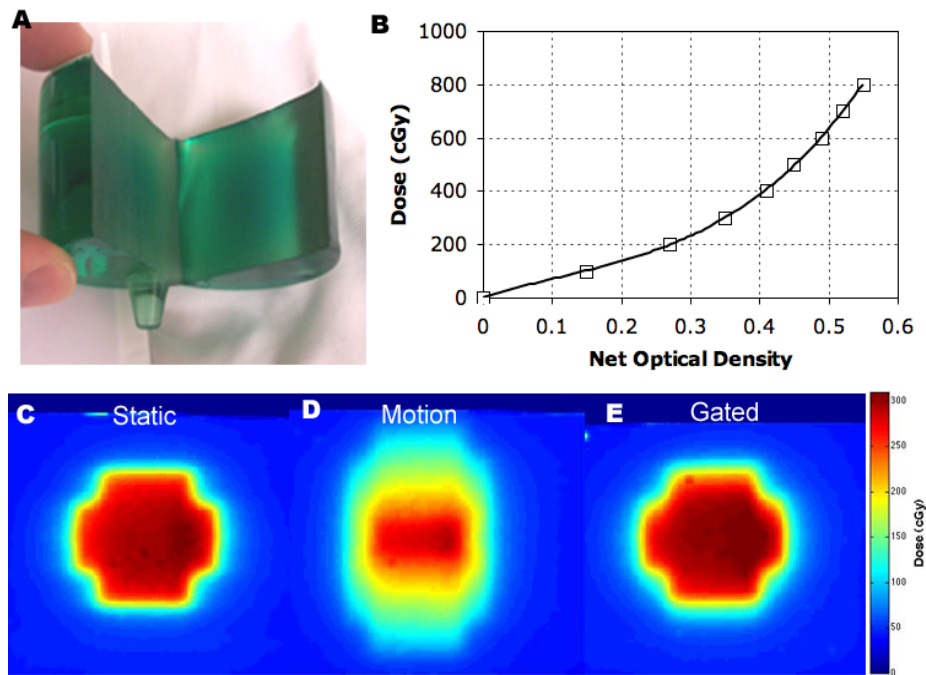


Figure 6.11 Independent dosimetry verification using EBT film

Independent measurement of dose was made with EBT film inside a PRESAGE™ dosimeter (A) in the coronal plane. EBT film calibration curve (B) showed a goodness of fit (R^2) of 0.9984. Distributions of the calibrated EBT film for the three treatment scenarios are shown: static (C), motion (D), and gated (E).

6.2.1.5 Data Analysis

Three types of data were available for analysis: 1) 3D static, motion, and gated PRESAGE™ dose distributions, 2) calculated 3D static and gated ECLIPSE® dose distributions, and 3) 2D static, motion, and gated EBT film coronal central axial plane dose distributions. The calculated static distribution from ECLIPSE® was compared to measured static and motion distributions from PRESAGE™ and EBT. The calculated gated distribution from ECLIPSE® was compared to the measured gated distributions from PRESAGE™ and EBT. Once all three data sets were spatially registered, an identical normalization point was chosen, see Figure 6.10(B) for inter-dosimeter comparison. Film post-processing, dosimeter registration, and data analysis were performed using CERR (Washington University, St. Louis, MO), a Matlab based software. Though, Babic et al.¹¹⁸ demonstrated a successful implementation of a 3D gamma analysis, at the time of this investigation, CERR software did not have a true 3D gamma calculation, so all quantitative analysis between datasets were restricted to a slice-by-slice analysis using line profiles and 2D gamma maps¹¹⁹⁻¹²⁰. The eventual use of 3D absolute dose analysis is currently being developed and will be the topic of future work. The analysis criteria for the gamma map were set at 3% dose difference and 1.2 mm distance-to-agreement (3%-1.2 mm). For the gamma maps, the dose difference acceptance criterion represents a more stringent criterion than currently used for the RTOG head and neck IMRT protocols (7%-4 mm)¹²¹. The distance-to-agreement

acceptance criterion of 1.2 mm was used as a match to the dose resolution of the calculated ECLIPSE® dose distribution and to more accurately reflect the differences in dose distribution over small distances as represented in this work. Comparisons with EBT film (gold standard) were used to establish PRESAGE™ feasibility where 3D comparisons with PRESAGETM and ECLIPSE® were used as a preliminary means to measure gating treatment efficacy.

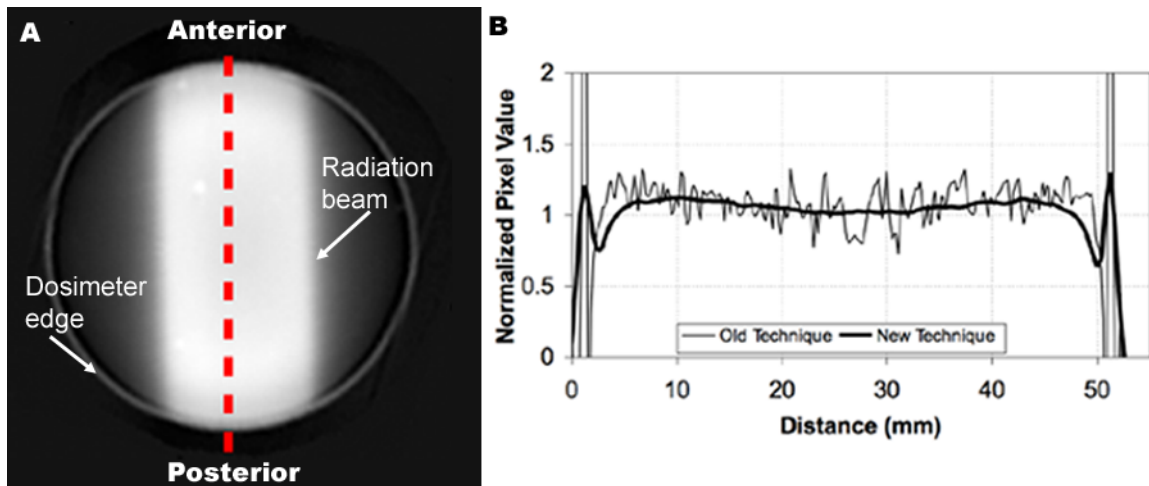


Figure 6.12 Improved Optical-CT scan readout

Reconstructed axial optical density map from PRESAGE™ dosimeter showing AP/PA beam configuration (A). Line profile (B) shows improved optical-CT dose readout technique ('New Technique') with noise reduction compared to 'Old Technique'.

6.2.2 Results

6.2.2.1 Improvements in Optical-CT Scanning Technique

A line profile through a reconstructed PRESAGE™ dosimeter, Figure 6.12(A), with and without the improved scanning technique is plotted in Figure 6.12(B). The line profile without the improved scanning technique measured 12% variability in the

normalized signal while the line profile with the improved scanning technique measured 4% variability. The improved scanning technique measured a factor of 3 increases in SNR. The edge artifact decreased from 5 mm to ~2 mm through improved scanning technique and setup geometry.

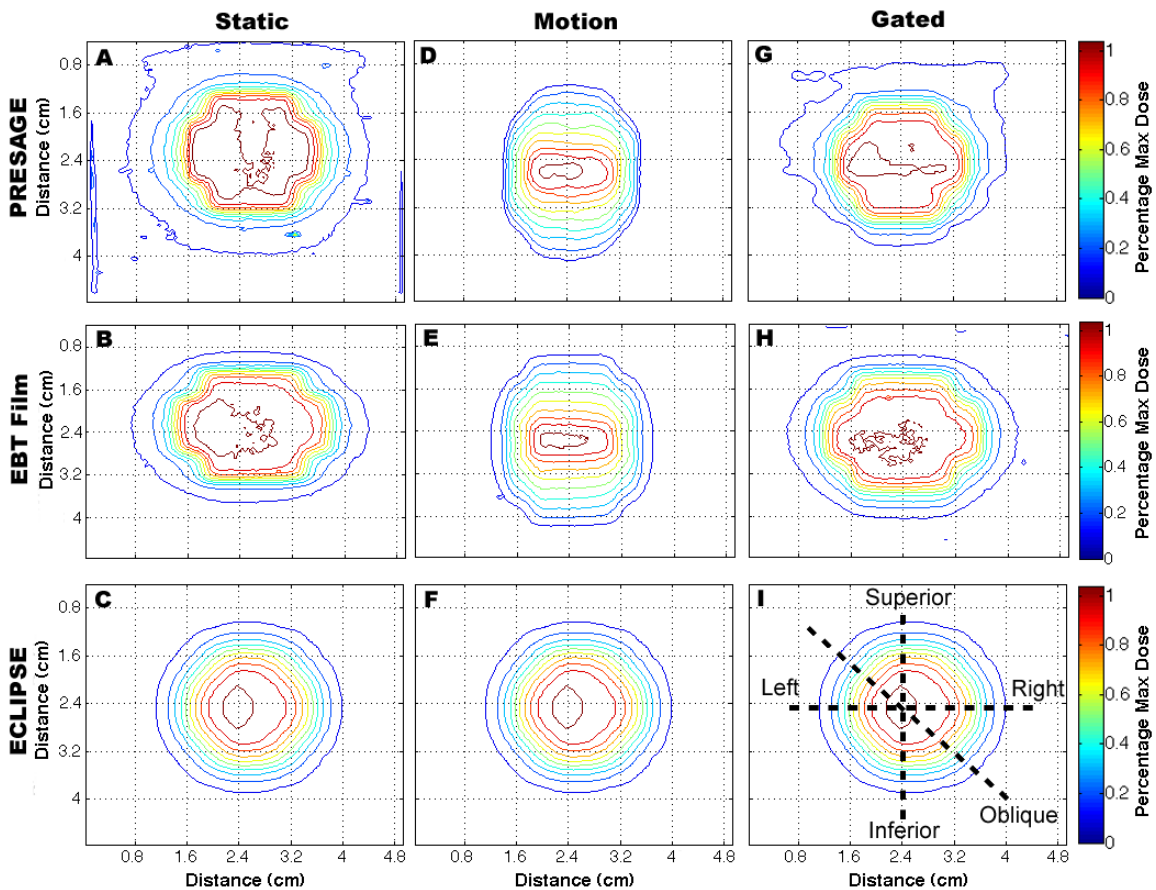


Figure 6.13 Contour plots of PRESAGE™, EBT film, and ECLIPSE®

Isodose lines in the central coronal plane (shown in Figure 3(A)) demonstrate maximum motion effect. Note, the ECLIPSE® distributions are unchanged since the distributions were calculated from static CT images for (C & F) and from one of the ten scanned respiratory image sets (I).

6.2.2.2 Dose Distributions in the Static, Motion, and Gated Treatment Scenarios

PRESAGE™, EBT film, and ECLIPSE® dose distributions are plotted as isodose contour mappings for the three treatment scenarios in Figure 6.13 with corresponding gamma map comparisons shown in Figure 6.14 and line profiles in Figure 6.15. Line profiles were taken along the representative dashed lines in Figure 6.13(I). An interdosimeter comparison between PRESAGE™ and EBT film distributions was compared for the static, motion, and gated treatment scenarios. Pass rates (3%–1.2 mm) of: 99.6%, 99.9%, and 99.4% were calculated for the static, motion, and gated treatments, respectively, as are shown in Figure 6.14(A-C).

Close examination of the dose distributions for the static and gated treatment scenarios reveal good agreement between PRESAGE™, EBT film, and ECLIPSE® as is evident by their similarly shaped and positioned isodose contour maps in Figure 6.13[(A-C) & (G-I)] and closely aligned profiles in Figure 6.15[(A-C) & (G-I)]. Whereas the motion dose distributions, Figure 6.13(D-E), exhibited broadening of the penumbral regions in both the superior to inferior, Figure 6.15(E), and left-right, Figure 6.15(D), directions as anticipated due to the phantom motion not modeled in the ECLIPSE® calculations, Figure 6.13(F). The measured dose distributions were compared versus the calculated ECLIPSE® distributions using the gamma map criteria. The pass rates for the ECLIPSE® and PRESAGE™ distributions were compared for the static, motion and

gated treatment scenarios: 84.7%, 84.5%, and 100.0%, respectively, and the ECLIPSE® and EBT pass rates are: 85.5%, 79.8%, and 86.0%, respectively.

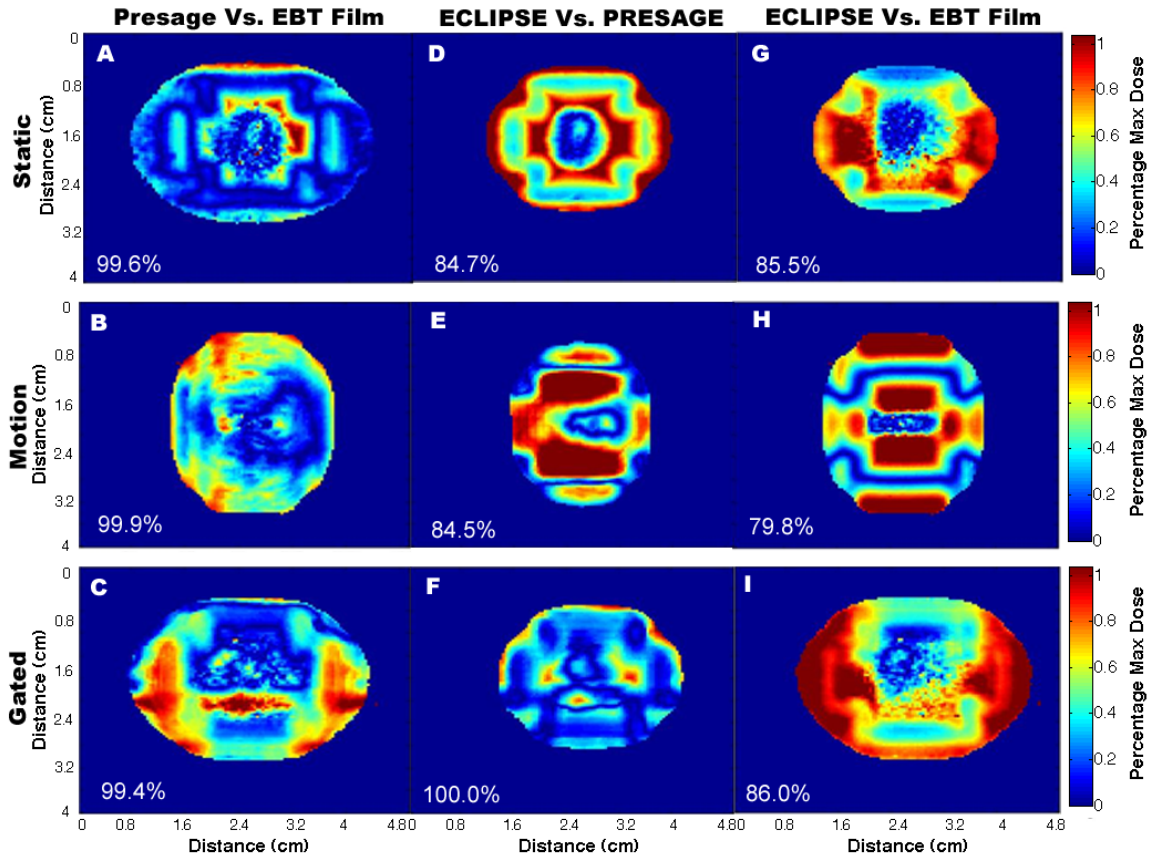


Figure 6.14 Gamma Maps of PRESAGE™, EBT Film, and ECLIPSE® inter comparison

Gamma maps (2%, 1.2mm) in the central coronal plane shown in Figure 3(A) indicating pass rates. Values of gamma > 1 indicates failure of one or both of the gamma criteria. Excellent agreement was observed between PRESAGE™ and EBT film (A-C) for all three treatment scenarios establishes feasibility of PRESAGE™/optical-CT dosimetry system. Good agreement between ECLIPSE® and PRESAGE™ and EBT film gated distributions demonstrates the effectiveness of the Varian’s gating system at delivering accurate dose distributions by reducing the motion induced errors (E & H).

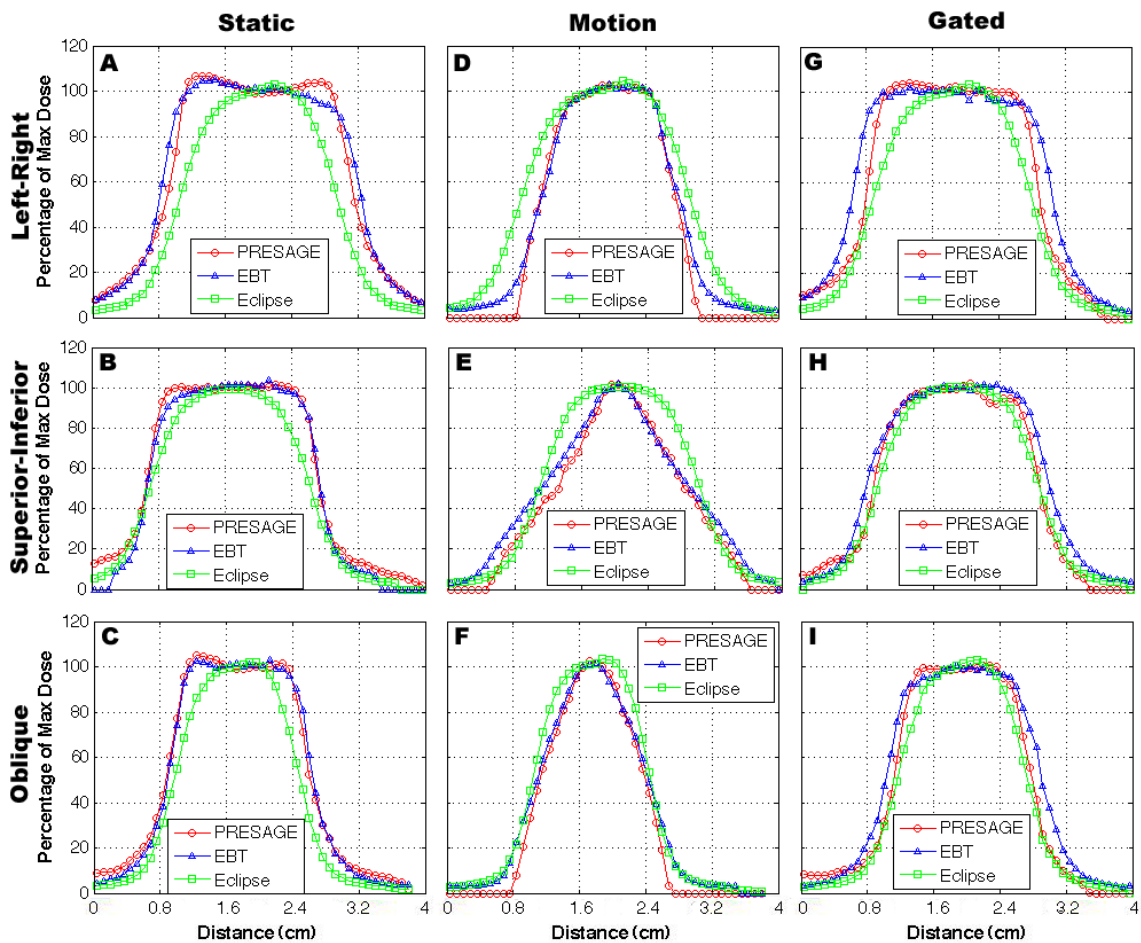


Figure 6.15 Line profile comparison of PRESAGE™, EBT film, and ECLIPSE®

Line profiles of the ECLIPSE®, PRESAGE™, and EBT dose distributions, along the dashed line shown in Figure 6(I) are shown for all three treatment scenarios. A left-right elongation of the dose distribution, measured by both PRESAGE™ and EBT film, is visible in the dose profiles (A,D,G). A possible explanation of the elongation effect is increased penumbral blurring when the radiation beam passes through the rounded ends of the Varian's MLC leaves, as reported in (Butson et al., 2003).

6.2.3 Discussion

An interesting point to note is that the pass rate is higher in the gated scenario than in the static scenario (compare Figure 6.14[(D) & (F)]). This is attributed to the fact

that the ECLIPSE® dose distribution incorporates effectively a convolution ‘blurring component’ due to the finite measurement volume of the ion chamber used to acquire the commissioning data. This slight blurring of the dose distribution is not observed in the static measurement of PRESAGE™, but a similar magnitude of blur is observed in the gated PRESAGE™ measurement, due to dosimeter motion during the finite time-width of the gating window.

The PRESAGE™ and EBT film distributions both measured an ~2 mm per side elongation in the left-right direction, seen in Figure 6.15(A-C), which is not consistent with the calculated ECLIPSE® distributions. The elongation is only measured in the direction parallel to the MLC leaves. Whereas the superior and inferior ends of the distribution, which are aligned perpendicular to the edges of the MLC leaves, do not measure the same dose elongation. The left-right elongation of the dose distributions may be attributed to the x-ray beam passing through the end of a rounded Varian MLC leaf which has been shown to increase penumbral blurring by ~2 mm compared to x-rays exposed to the edge of the same MLC leaf¹²².

One possible limitation of this work was the necessity to normalize the dose distributions for comparison. Normalization forces agreement at one dose level and may limit the value of subsequent analyses by masking possible dose differences where large discrepancies in dose magnitude exist. Therefore the analysis of data sets using absolute dose distributions is generally preferable when available. In the case of PRESAGE™,

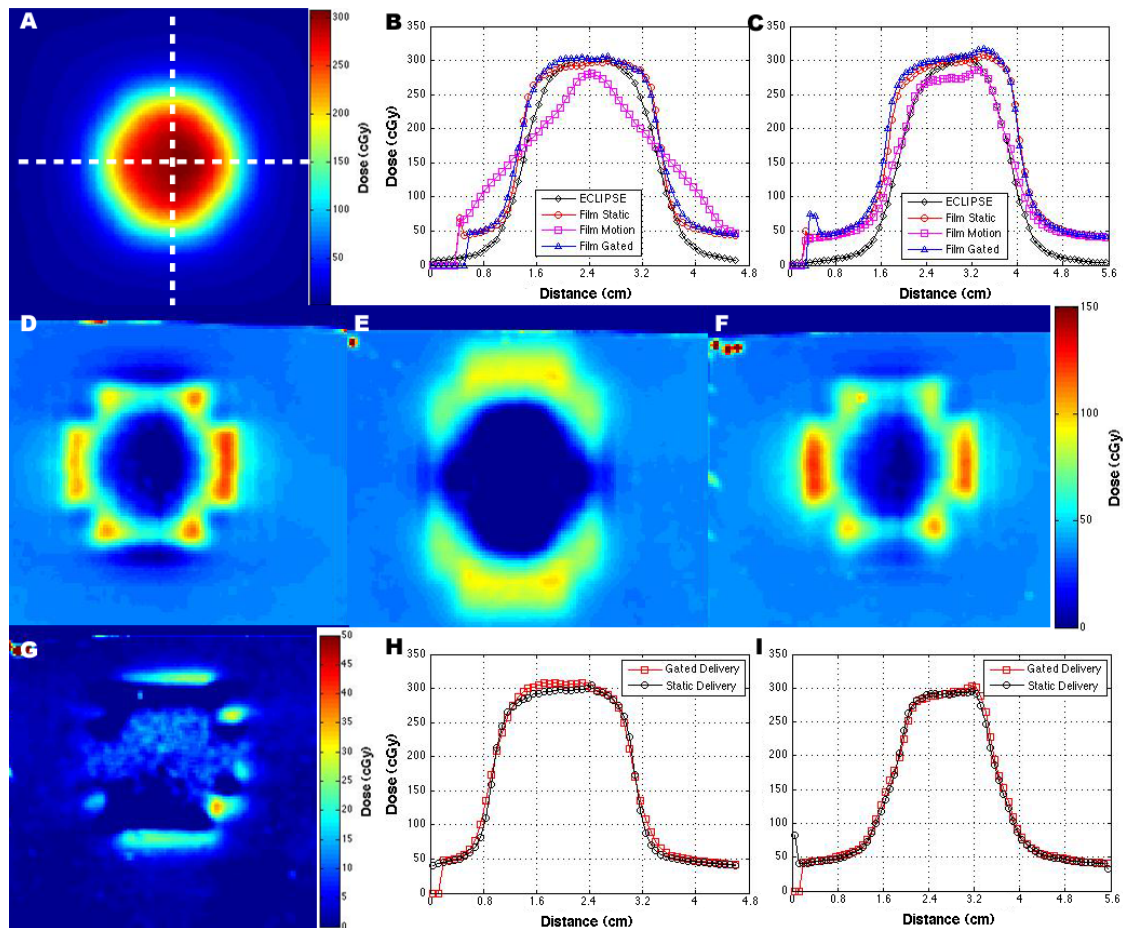


Figure 6.16 Absolute dose comparison between EBT film and ECLIPSE®

Absolute dose comparisons are presented between ECLIPSE® (A) and the calibrated EBT film for the three treatment scenarios (Figure 6.11(C-E)). Superior-inferior (B) and lateral (C) line profiles, taken along the dashed lines shown in (A), compare overall ECLIPSE and film absolute dose correlation. Generally, the calibrated film and calculated ECLIPSE dose line profiles demonstrate a similar magnitude of dose and profile shape (except for the film’s motion scenario). Eclipse and film dose difference mappings show, for the three treatment scenarios--static (D), motion (E), and gated (F), good agreement in dose delivery for the central, shallow dose gradient region, but poor correlation for the peripheral, steep dose gradients. The static and gated film dose difference map, shown in (G), demonstrates the ability of the gating technique to minimize motion induced dose blurring in surrounding regions of the planned target volume. Superior-inferior (H) and lateral (I) line profiles taken from the static and gated film treatment scenario dose distributions (figure 4 C & E) also show the high correlation of the gated treatment with the static scenario.

calibration to a given dose may be achieved from irradiation of small volumes of PRESAGE™ from the same batch. This method of establishing a calibration function using small volumes to calibrate a large 3D volume has been shown to introduce errors when comparing dose distributions¹²³. The extent of this volume effect for PRESAGE™ calibration has not yet been established in sufficient detail to know exactly how accurate the calibration is; a detailed study of the volume effect is part of an ongoing study. The uncertainty of the volume effect on the accuracy of the PRESAGE™ dosimeter analysis required the use of normalization as a means to compare PRESAGE™ with ECLIPSE® and EBT film dose distributions. However, the precise linearity of the PRESAGE™ dose-response has been extensively confirmed^{102, 110}. In the present paper, the given dose at the normalization point in the PRESAGE™ dosimeter was within the calibration uncertainty of the planned dose as determined from the film measurements, shown in Figure 6.16. We therefore conclude that the use of PRESAGE™ as a relative dosimeter, by normalizing to a point corresponding to the 100% isodose region of the planned dose distribution in the coronal plane and exploiting the strength of the linearity of PRESAGE™ response, will not introduce any limitation on the data analysis and will circumvent the demonstrated volume effect error.

This work presents the first application of PRESAGE™/optical-CT 3D dosimetry system to the verification of a simple gating treatment and lays the foundation for more advanced gating work. We envision a role for PRESAGE™ (and any of the other 3D

dosimetry approaches) as a final whole-system verification test during the commissioning stage. There may also be a future role in repeat or periodic QA of various techniques, i.e., respiratory gating, IMRT, RapidArc™, etc, but probably not on a per patient basis unless the costs and convenience for optical-CT readout improves.

6.2.4 Conclusion

Comparison between PRESAGE™ and EBT film showed excellent agreement for the three treatment scenarios. The average pass rate was > 99% with respect to a gamma map criteria of 3%-1.2 mm. Although the gated treatment plan was simple, this result establishes the feasibility of the PRESAGE™/optical-CT dosimetry system for verifying gating treatments, and lays the groundwork for future work to investigate more complex gated treatments. Significant differences were observed between the static planned dose distribution and the measured dose distribution in the presence of breathing motion. Varian's gating system was shown to correctly reduce this motion error through the implementation of a standard gating technique. Improvements in the optical-CT scanner design and acquisition techniques led to reduced edge artifacts and a factor of 3 increase in SNR while maintaining scanner readout times on the order of ~ (5-10) min.

6.3 Applications to fast Neutron Dosimetry

A report¹²⁴ in 2001 demonstrated the potential for slow and fast neutron dosimetry using RCF. Since that time, RCF has seen innovative changes in structure,

material, and sensitivity^{17, 40, 60}. The purpose of this work is to investigate the feasibility of using modern RCF as a passive neutron dosimeter for 2D neutron dosimetry. Current neutron dosimetry techniques can be performed using single-point measurements. Two examples of these techniques are direct ion chamber dose measurements or indirect neutron fluence-to-dose measurements using activation foils. However, 2D neutron dosimetry comparison is mostly restricted to time consuming Monte Carlo simulations. On the other hand, film dosimetry offers a potential passive measurement technique that exploits simultaneous multi-point direct dose measurements for quick experimental setup and target dose analysis. The film dosimetry technique can be fully analyzed within a few hours to a day after exposing the film; thus, giving the film the advantage for quicker 2D neutron comparison than Monte Carlo simulations.

Two types of modern RCF were chosen for analysis in this neutron film study. Both films have a number of features that make them attractive for use in neutron dosimetry, they have: a high-spatial resolution; a large fractional composition of hydrogen; an insensitivity to visible light and temperature changes that make it convenient for use in a normal laboratory environment; a resistance to water, thereby allowing the films to be submerged in a water bath^{62, 125} for use in direct dosimetry measurements in an imitation soft tissue environment; and they are mechanically pliable, allowing them to be shaped to the surface of the object being studied.

In this work (1) the sensitivity to 10 MeV neutrons was experimentally determined for two types of modern radiochromic films, (2) a technique for relating radiation dose to the film netOD was developed, and (3) a novel 2D film neutron dosimetry technique was investigated for measuring neutron dose distributions as a means to establish an experimental mouse irradiation setup and estimate the neutron dose to mouse.

6.3.1 Materials and Methods

XRQA and EBT films were digitized using the EPSON 10000XL flatbed scanner. Each film was scanned at a resolution of 72 pixels per inch (0.4 mm pixels), with no color corrections, and saved in uncompressed Tagged Image File Format. All films were digitized using 48-bit color depth with RGB file format (16-bit per color channel) and the red (R) channel was extracted for analysis in Matlab.

6.3.1.1 Neutron Beam Production

Film exposure to fast neutrons was studied at the Triangle Universities Nuclear Laboratory (TUNL) at Duke University. The neutron beam was produced via the ${}^2\text{H}(d,n){}^3\text{He}$ reaction, by bombarding a pressurized deuterium gas cell (7.8 atm), see Figure 6.17, with a deuteron beam from the tandem Van de Graaff accelerator¹²⁶⁻¹²⁸. The subsequent neutron beam had a monoenergetic peak of 10 MeV with a full width at half maximum (FWHM) of 1 MeV (at 7.8 atm), and a continuum of low energy neutrons due to the break-up of the incident deuteron beam (a major peak at 2.7 MeV) and the

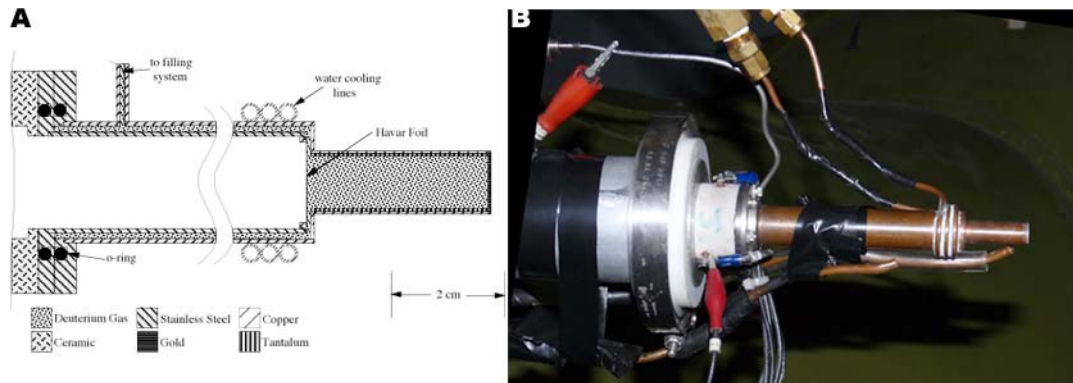


Figure 6.17 Neutron source gas cell

Gas cell for neutron production is shown. Side cut-away view is provided by reference Pedroni, 1986¹²⁷ (A). The gas cell is constructed of copper with an inner layer of tantalum used to shield copper from deuteron beam and shown in (B). The deuteron beam enters the gas cell from the beam line under vacuum and passes through a thin (6.4 μm) Havar foil (used to contain deuterium gas in cell under pressure) and stops in a 0.5 mm thick gold disk. The deuteron beam is collimated upstream of the gas cell to a diameter 4.8 mm. The cell is water cooled with additional cooling provided by air lines that are directed on the havar foil and gold disk. The maximum beam current allowed on the gas cell is $\sim 3.0 \mu\text{A}$.

deuterium gas threshold (a major peak at 4.4 MeV). The spectrum of low energy neutrons accounted for only $\sim 5\%$ (deuteron break up) and $\sim 1\%$ (deuterium threshold) of the overall beam flux, along the central axis of the neutron beam, compared to the major flux peak at 10 MeV; the break-up neutrons contributed much less to the overall neutron beam when measured 10° from the main beam axis¹²⁸. The cross section of the ${}^2\text{H}(d,n){}^3\text{He}$ reaction was sharply forward-angle peaked due to the forward momentum of the deuteron beam incident on the deuterium gas cell. The neutrons were emitted in a conical geometry, centered on the beam axis, with angular distributions with respect to energy. The kinematics of the reaction was such that the most energetic neutrons were

emitted at 0°, along the central beam axis, and the energies of the emitted neutrons decreased with increasing angle; e.g., the neutron energies decreased by ~10% (to 9 MeV) with a conical diameter of 20 cm when considering a 17 cm distance from the center of the 6 cm gas cell to the front of the film and mouse setups¹²⁸.

6.3.1.2 Characterization of RCF Response to Fast Neutrons

RCF response to fast neutrons was tested. The films were tested for (1) response sensitivity to neutron exposure, and (2) response dependence on changing neutron energies. First, XRQA and EBT film response sensitivity to a 10 MeV neutron beam was tested. XRQA and EBT film's sensitivity to a 10 MeV neutron beam was tested. The radiochromic films were mounted on a Plexiglas board (3 mm thick) and placed 17 cm from the neutron source. One XRQA film was mounted on the front side (closest to the neutron source) of the Plexiglas board, and one EBT film was mounted on the backside of the board. The films and board were set perpendicular to the main axis of the neutron beam and were exposed simultaneously. Films were digitized and then imported into Matlab for analysis. Both films were spatially registered and line profiles were taken from each film type. Film sensitivities were investigated by comparing FWHM measurements of the two line profiles, and by comparing max netOD values at the center of the measured neutron dose distribution for each film type.

Second, the dependence of RCF response to changing neutron energies was investigated. Changes in neutron energy will change their interaction cross section.

Three RCFs were separately exposed to neutron flux densities with energies of (6, 8, and 10) MeV.

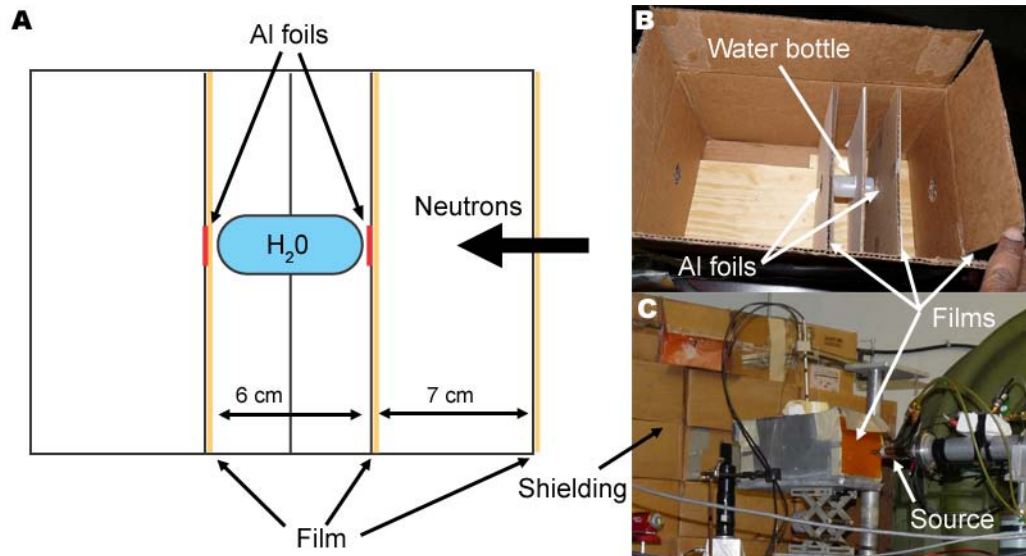


Figure 6.18 RCF calibration experimental setup

Diagram of a cross-sectional view of the calibration setup is shown in (A). A film and Al foil was placed in the neutron beam path on each end of the water bottle. Additionally, a piece of film was placed on the outside front of the target box. Three separate runs provided six data points. Each run consisted of a film and activation foil irradiation. The inside of the box that held the target (water bottle) and film is shown in (B), and the relative placement of the box with respect to the neutron source with a film placed on the outside is shown in (C).

6.3.1.3 RCF netOD-to-Dose Calibration

A netOD-to-soft tissue dose calibration technique was established using the following experimental setup. A water bottle (6 cm x 2.7 cm dia.) was mounted inside a box and the films were arranged at different distances with respect to the water bottle. Six XRQA films were exposed to three different neutron exposures. Each neutron exposure provided a different flux density and film distance configuration to vary film

netOD values and neutron doses. Two aluminum (^{27}Al) foils (1.3 cm dia. 0.03 cm thick) were placed at the front and backsides of the water target to estimate the neutron flux from Al foil activation ($^{27}\text{Al}(n,\alpha)$ where the alpha particle reaction creates a ^{24}Na atom that de-excites by a 1368 keV γ -ray). Film and foil exposures were generally performed simultaneously. A film exposure configuration is shown in Figure 6.18.

After each neutron irradiation, the films were digitized and film pixel values were converted to netOD using equation (3-10). The netOD used in the calibration curve analysis was the mean value of a region of interest (ROI) that measured ~13 mm in diameter and was taken from the center of the neutron OD distribution on the films. The dose used in the calibration curve analysis was considered for soft tissue and calculated using the FLUKA2008¹²⁹ Monte Carlo code. To calculate the neutron dose to a soft tissue target in the Monte Carlo simulations, the film material was replaced by A-150 material, a soft tissue equivalent plastic material. The accuracy of the Monte Carlo calculations were verified by comparing the neutron dose to the water in the bottle (D_{water}), as calculated from Monte Carlo simulations, to D_{water} determined from the neutron flux measured by Al foil activation spectroscopy. Monte Carlo simulations determined D_{water} over the entire volume of water within the bottle; however, the average D_{water} at the surface of the water bottle (i.e., the entrance dose) was compared with the Al foil dose results. The Al foil was located within ~1 mm of the front of the bottle of water, see Figure 6.18(A-B). After irradiation, the neutron-induced activity of

the Al foil was measured off-line in TUNL's low-background counting area. Each of the neutron-activated Al foils was measured using a High Purity Germanium (HPGe) detector (Canberra, Meriden, CT) to determine the neutron flux at the location of each foil. An energy window for the γ -ray spectroscopy was set at 1368 keV with an energy resolution of 1.8 keV FWHM. The $^{27}\text{Al}(n,\alpha)^{24}\text{Na}$ has an activation threshold of 3249 keV neutrons. Though, the neutron alpha threshold does allow for some deuterium breakup low energy neutrons to interact in the Al foil, the cross section of interaction is near zero for neutron energies < 6 MeV (0.001 barns) compared to neutron energies of 10 MeV (0.089 barns)¹³⁰. Hence the measured neutron flux from ^{24}Na atoms de-excitation by 1368 keV γ -ray were a measurement of the 10 MeV neutrons and not the lower energy neutron contamination. The majority of the measurement error from the HPGe detectors was determined to be detector efficiency for the 1368 keV γ -rays. The systemic error was measured to be $\sim\pm 5\%$ of measurement with an additional $\pm(1-2)\%$ being purely due to statistical uncertainty.

From the Al foil flux density measurements, the D_{water} was then calculated using the following relation:

$$D_{water}(cGy) = \phi_n \cdot F_{water}^{10MeV}, \quad (6-3)$$

where ϕ_n is the measured neutron flux and the neutron kerma factor, F_{water}^{10MeV} , for 10 MeV neutrons was obtained from the ICRU report 26¹³¹.

6.3.1.4 2D film Dosimetry Technique

As part of a small animal neutron dosimetry project, RCFs were used to measure the dose distribution of the neutron beam for each target setup and to estimate the dose to mice. The small animal dosimetry project utilized a hollow Plexiglas box (12.5 cm wide x 25.3 cm tall x 8 cm deep) that was constructed to hold seven 50 ml vials with one center hole and six peripheral holes each offset by 4.0 cm (measured center-to-center from central to peripheral slots), shown in Figure 6.19(A). The front of the Plexiglas box was positioned 17 cm away from the neutron source so that the peripheral holes were elevated 13° from the central neutron axis. The energy of the neutrons at 13° from the central axis measured an $E_{\text{neutron}} > 9.72$ MeV, or within 2.8% of the 10 MeV neutrons along the 0° axis¹²⁸. The mice were held within the 50 ml vials during the neutron irradiation. The Plexiglas box and 50 ml vials were attached 17 cm above a rotation stage, shown in Figure 6.19(B). The rotation stage was used to rotate the mice 180° half way through the irradiation to provide a more uniform exposure over the full length of each mouse; the neutron radiation was terminated while the stage rotated 180° , and was re-engaged once the mice and film were in position once again.

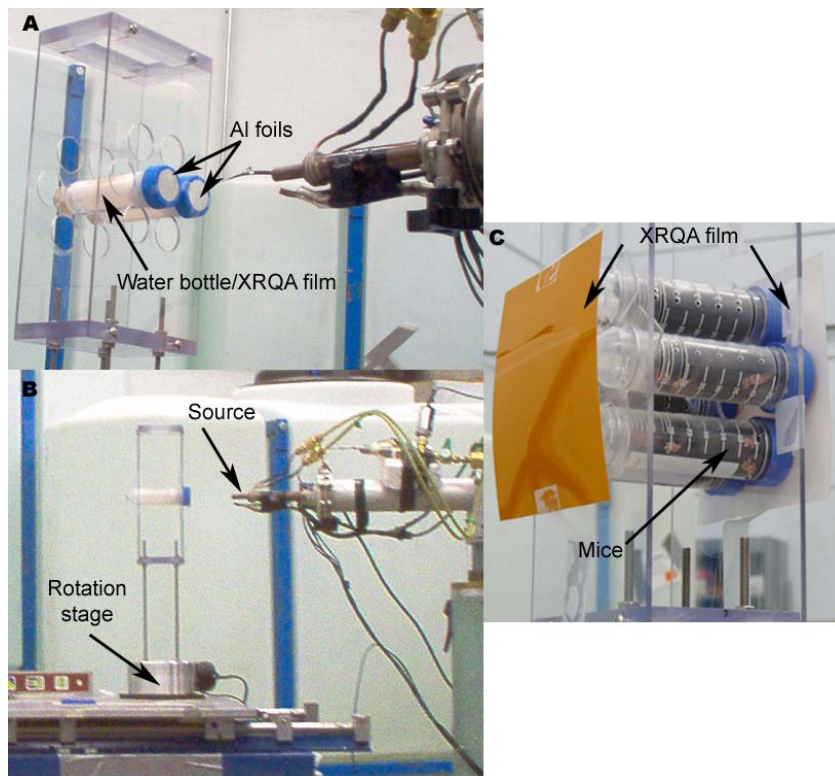


Figure 6.19 Neutron small animal irradiation setup

XRQA film was immersed in a water target, used to emulate mice, and loaded inside two 50 ml vials and placed on a Plexiglas box (A). The Plexiglas box and 50 ml vials were mounted on a rotation stage and placed 17 cm in front of the neutron source (B). Six mice were loaded onto the rotation stage with XRQA films placed in front and behind the vials containing mice for estimating the dose to each mouse; additionally, Al foils were placed on the cap and tip side of the vials containing mice (not visible) as a means to verify measured film doses (C).

6.3.1.4.1 Immersed Film Measurements

To measure the dose over the full length of the mouse volume, a 6 cm long (4.5 cm without the cap) x 2.7 cm diameter polyethylene bottle was filled with water and used to emulate a mouse target. XRQA film was cut to fit within the bottle and immersed in the water along the central-long axis of the bottle. The water-filled bottle and film were then placed within a 50 ml vial, see Figure 6.19(A). One vial was placed at

the center position of the Plexiglas box and another vial was placed at the 3 O'clock peripheral position; the center position of the Plexiglas box was aligned to the central axis of the neutron beam. Once positioned, the films within the bottle were exposed to half the calculated run time. The resulting longitudinal dose profile of the irradiated film was numerically "rotated" 180° and added to the original dose profile to generate an estimated dose to mouse volume to simulate the 180° rotation exposure pattern that the real mice underwent. Even though XRQA films have polyester layers that protect the radiosensitive active layers in the film (Figure 2.1), the sides of the film are not sealed and therefore water penetrated into the film from the edges. XRQA films were immersed in water for about 3 hr. The rate of water penetration (~7 pixels hr⁻¹) necessitated measurements to be 0.7 cm (~20 pixels), from the edge of the films.

6.3.1.4.2 *Externally Mounted Film Measurements*

Six mice were placed within the 50 ml vials and loaded onto the rotation stage in the six peripheral slots. XRQA films were placed on the front (cap) and backside (tip) of the 50 ml vials, see Figure 6.19(C). The films were used to estimate the entrance dose to the mice. Additionally, two Al foils were placed on top of the 50 ml vial caps (directly behind the film), and on the tips of the vials (directly in front of the film) for an independent measurement of the neutron flux incident on the mice. One set of Al foils were placed at 3 O'clock and the other set at 9 O'clock. The mice were rotated 180° half way through the irradiation for improved uniform exposure. The films were rotated along with the mice. Overall exposure time was 1.95 hr.

6.3.1.4.3 Analysis

Immersed film dose measurements were compared to externally mounted film dose measurements as a means to verify the accuracy of the external mounted film measured dose. The accuracy of the film in water was compared to independent Monte Carlo calculated doses over the length of the water bottle, and the accuracy of the externally mounted films was independently compared to Al foils located on the 50 ml vials.

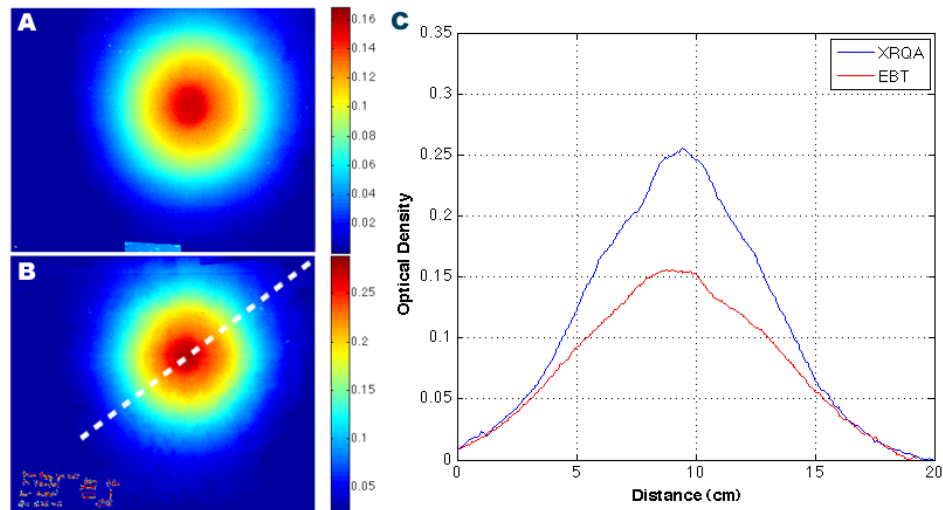


Figure 6.20 XRQA and EBT film sensitivity to 10 MeV neutrons

Intensity distribution of the 10-MeV neutron beam measured with EBT film (A) and XRQA film (B). Line profiles taken along dotted line in (B) are plotted for EBT film and XRQA film (C). Both films measured similar FWHM values (~9.5 cm). XRQA film measured a greater sensitivity to 10 MeV neutrons by a factor of 1.39; this is attributed to the larger hydrogen density and higher effective Z of XRQA film than EBT film.

6.3.2 Results

6.3.2.1 RCF Sensitivity to Neutron Exposure

Neutron fluence distribution was measured using XRQA and EBT as shown in Figure 6.20(A-B). FWHM and netOD values for each film type were calculated from line profiles, see Figure 6.20(C), taken along similarly positioned dotted lines represented in Figure 6.20(B). The measured FWHM of the netOD distribution of each film type was: $\text{FWHM}_{\text{XRQA}} = 9.5 \text{ cm}$ and $\text{FWHM}_{\text{EBT}} = 9.6 \text{ cm}$. netOD measurements of the two film types showed XRQA film ($\text{netOD}_{\text{XRQA}}$ measured 0.255) had a 39% greater sensitivity to 10 MeV neutrons than EBT film ($\text{netOD}_{\text{EBT}}$ measured 0.156) when exposed to a dose level of 165 cGy.

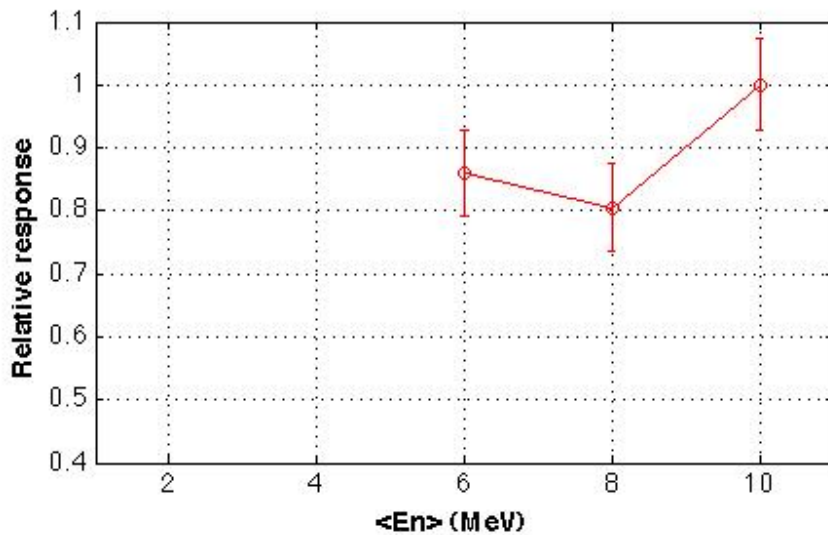


Figure 6.21 RCF response to changing neutron energies from (6-10) MeV

Three separate sheets of RCF were exposed to neutron beam energies of (6, 8, and 10) MeV. The average response was normalized to the 10 MeV response and plotted.

Table 6-1 RCF response to changing neutron energies

Three separate RCFs were exposed to varying neutron energies (<En>). The neutron fluence and RCF responses are listed.

<En> MeV	Fluence (n cm ⁻²)	Film response (avg netOD)
10	5.5E8	0.023 ± 0.002
8	3.9E8	0.019 ± 0.001
6	2.7E8	0.020 ± 0.001

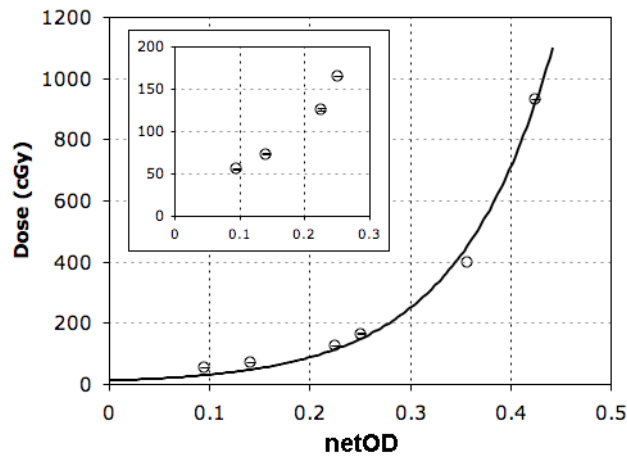


Figure 6.22 Calibration Curve

The dose to soft tissue simulated by Monte Carlo was plotted as a function of measured film OD. A non-linear regression curve was fit to the six data points with a coefficient of correlation (R^2) calculated to be 0.9926. Insert graph is a blow-up of data at low doses (0-200 cGy).

6.3.2.2 RCF Response to Changing Neutron Beam Energies

Three separate XRQA films were exposed to varying neutron energies, see Table 6-1. The RCF responses were normalized to the 10 MeV film netOD. The films normalized average netOD responses are plotted in Figure 6.21. A marginally

significant difference is measured for 6 MeV and 10 MeV. Otherwise, no true statistically significant difference is seen.

Table 6-2 RCF calibration data and % γ -ray contamination from $^1\text{H}(n,\gamma)^2\text{H}$ reaction

The XRQA film netOD values shown bellow were averages taken from the center of the exposed films and used along with the total dose calculated by Monte Carlo to generate the calibration curve shown in Figure 6.22. Monte Carlo was used to calculate the total dose to a soft tissue target, which included absorbed doses from neutron and γ -rays. The γ -ray dose quoted bellow was from the $^1\text{H}(n,\gamma)^2\text{H}$ reaction (+Q = 2.225 MeV). The percent dose contribution from γ -rays compared to the total dose is listed. Monte Carlo predicts that the dose contribution from $^1\text{H}(n,\gamma)^2\text{H}$ reaction γ -rays is negligible compared to 10 MeV neutrons.

XRQA Film netOD	Monte Carlo		
	Total Dose (cGy)	γ -ray Dose (cGy)	γ -ray Dose Contribution (%)
0.095 \pm 0.002	55.66 \pm 0.36	0.18 \pm 0.002	0.3
0.141 \pm 0.002	73.36 \pm 0.03	0.27 \pm 0.001	0.4
0.225 \pm 0.003	125.60 \pm 0.02	0.44 \pm 0.225	0.4
0.251 \pm 0.002	165.24 \pm 0.04	0.82 \pm 0.002	0.5
0.363 \pm 0.003	400.50 \pm 0.15	5.89 \pm 0.012	1.5
0.425 \pm 0.003	930.58 \pm 0.24	13.70 \pm 0.024	1.5

6.3.2.3 Film Calibration Technique

For the dose calibration technique, the highest neutron flux measured using the activation foil technique was $(8.5 \times 10^6 \pm 6.9 \times 10^4)$ n cm⁻² s⁻¹ at the front of the water bottle. Using equation (6-3) and from ICRU data tables, the calculated dose rate to the water target, from the location of the foil, was (189.0 ± 9.5) cGy hr⁻¹ and the calculated dose rate to the front end of the water target from the Monte Carlo calculation was (188.3 ± 0.001) cGy hr⁻¹, an agreement to better than 0.4%. Having established the accuracy of the

Monte Carlo calculations, the dose to soft tissue used for the calibration data was simulated using Monte Carlo with the results shown in Table 6-2, and plotted versus measured film netOD values in Figure 6.22.

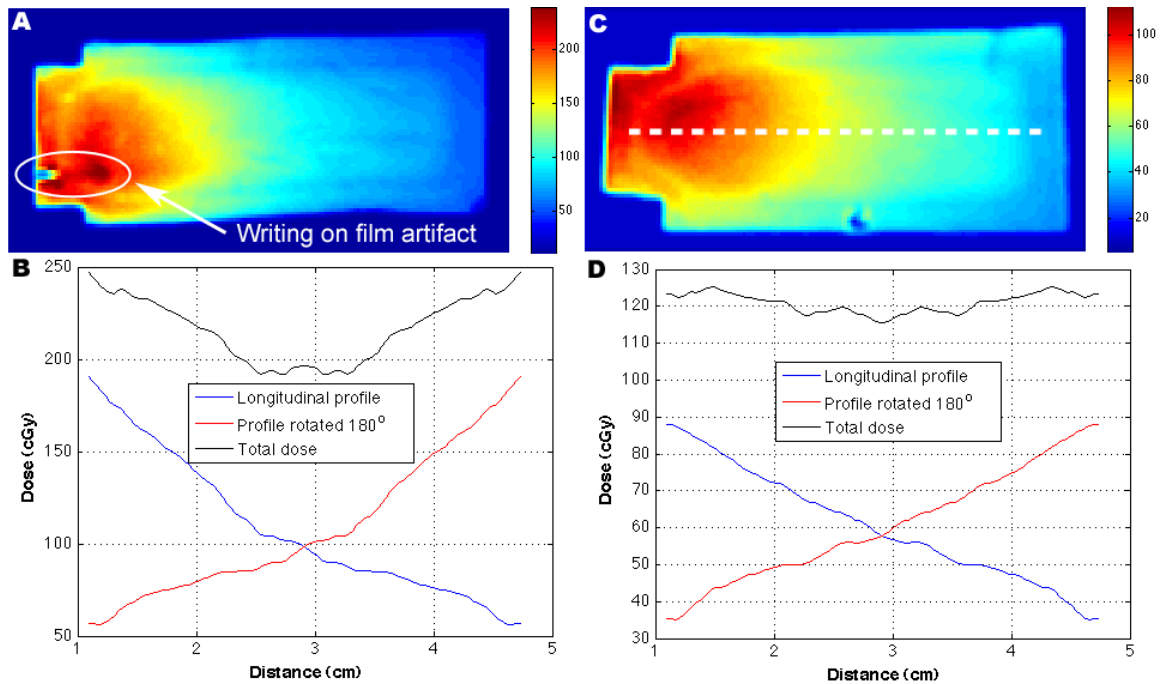


Figure 6.23 Internal to water target neutron dose distribution

XRQA film inserts were placed along the central-long axis of two water bottles, one centered about the neutron beam axis (A) and the other placed in a peripheral slot 4 cm from the central axis (C). Dose profiles, taken along the representative dotted white line (C), provide an estimated total dose to mouse target located at the center (B) and the peripheral (D) mouse locations. Dose to mouse volume was estimated using a single line profile from film inserts (blue lines) that was rotated 180° (red lines) and added to the original dose profile to create a total dose estimate for film targets (black lines) as if the film were physically rotated 180° as the mice were rotated during the actual mouse exposure.

6.3.2.4 2D Film Dosimetry Technique

6.3.2.4.1 *Immersed Film Dose Measurements*

Dose distributions and central axis dose profiles for films placed in water bottles located in the center slot and a peripheral slot are shown in Figure 6.23(A-B) and Figure 6.23(C-D), respectively. The entrance dose to the center film measured 190.6 cGy, and the dose at the entrance on the periphery film was 94.1 cGy. When the longitudinal dose profile was combined with the 180° rotated duplicate to create an estimation of the overall dose to the targets, the doses to the center film were 247.0 cGy at the entrance and exit and a minimum of 192.1 cGy at the center of the film. The overall change in dose along the length of the center filmstrip was 55.0 cGy. The doses to the combined peripheral profiles were 123.2 cGy at the entrance and exit and a minimum of 115.9 cGy at the center of the film. The overall change in dose along the length of the peripheral filmstrip was 7.3 cGy. To benchmark the film results, Monte Carlo was used to calculate the absorbed dose to the mouse phantom volume (bottle filled with water). A dose profile taken along the full length of the central axis of the mouse phantom in the peripheral location was compared to a dose profile taken along the full length of the central axis of the film, see Figure 6.24. A correlation calculation of the two profiles was performed as a means of quantitatively assessing the agreement in the Monte Carlo calculated and film dose responses. The correlation coefficient for curves in Figure 6.24 was 0.9982.

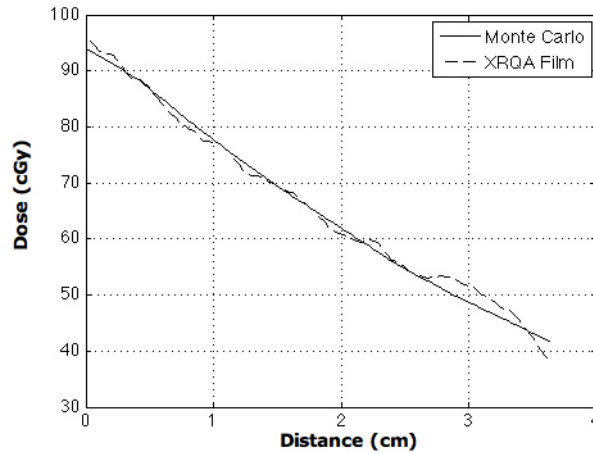


Figure 6.24 XRQA and Monte Carlo absolute dose comparison

Comparison of XRQA and Monte Carlo dose responses were taken from the water target located at the peripheral slot irradiation. The correlation coefficient for the two plots is 0.9982 lending confidence to the feasibility of using RCFs as accurate 2D neutron dosimeters.

6.3.2.4.2 Externally Mounted Film Dose Measurements

XRQA film was placed on each end of the mouse holder. The cap side film was closer to the neutron source than the mice during the first half of the mouse exposure, see Figure 6.25(A). The second film was placed on the tip side of the mouse holder and finished closer to the neutron source than the mice during the second half of the mouse exposure, see Figure 6.25(B). Orthogonal line profiles show symmetrical dose responses in the vertical and horizontal directions, see Figure 6.25(C-D). The dose profiles in Figure 6.25(C) did not overlap as well as the dose profiles in Figure 6.25(D) because the

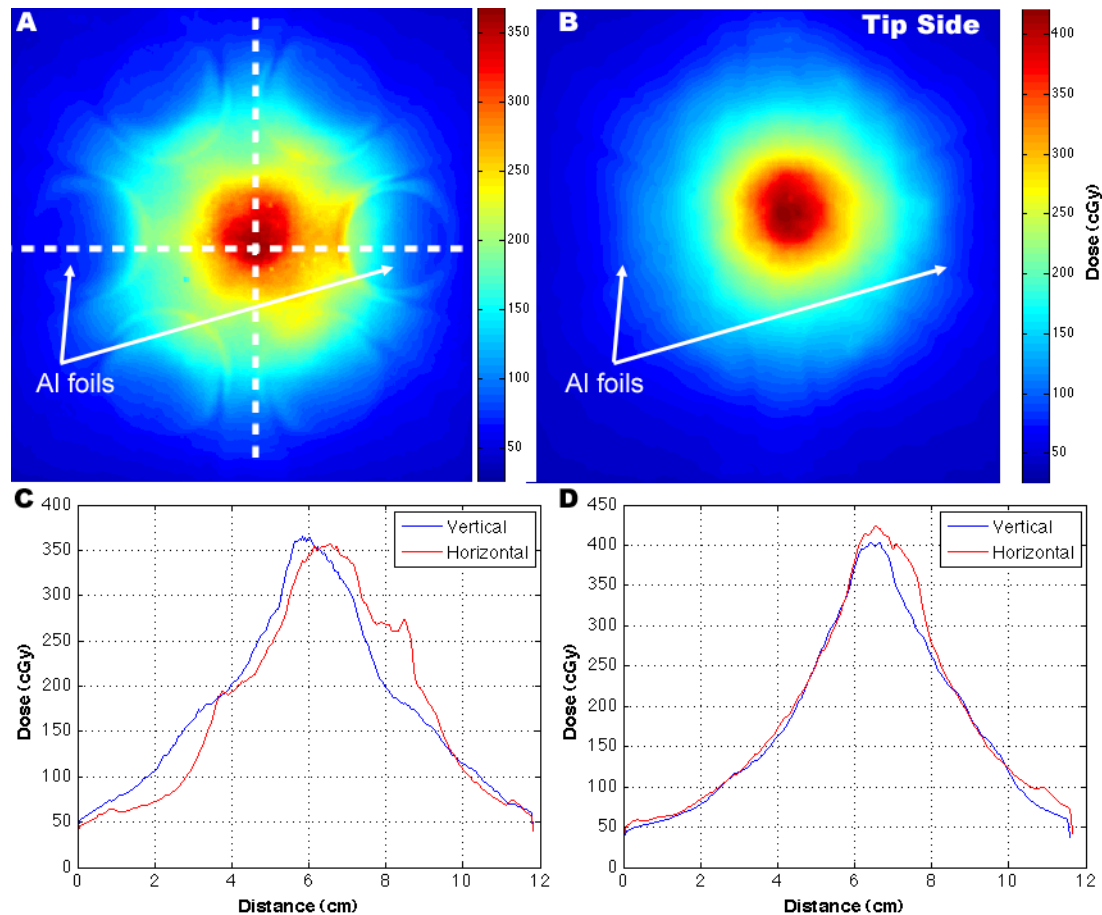


Figure 6.25 External dose distribution of live mouse exposure

XRQA film was placed in front and behind of the mouse stage and rotated with the stage. The first film was placed on the “cap side”, of the mouse stage and was closest to the neutron source for the first half of the mouse exposure (A). The mouse stage and films were then rotated 180°. The second film, placed on the “tip side” of the mouse stage, was exposed closest to the neutron source during the second half of the mouse exposure (B). Two Al foils were placed on top of the 50 ml vial caps (directly behind the film), and on the tips of the vials (directly in front of the film). One set of Al foils were placed at 3 O’clock and the other set at 9 O’clock. γ -ray contamination due to the Al foil activation de-excitation by ^{24}Na γ -ray emission (1368 keV) was investigated using dose profiles taken from the films through regions where Al foils overlapped, and would have exposed the films with γ -rays, and through regions where Al foils were not present to expose the films with γ -rays (C-D).

film was not centered horizontally on the neutron beam axis. Thus, when the mouse stage and film were rotated the film was offset slightly causing a slight shift in the horizontal line profile. The offset of the film is also manifested by the elongation of the central dose distribution in Figure 6.25(A), which measured an artificially increased central dose along the horizontal line profile in Figure 6.25(C) around the (7 to 9) cm point as compared to Figure 6.25(D). The initial cap and tip side films measured dose responses of (116.2 ± 55.9) cGy and (112.5 ± 51.0) cGy, respectively, whereas the average Al foil response was 164.7 cGy with ± 3.4 cGy statistical error and ± 8 cGy (~5%) systemic error from the HPGe γ -ray spectroscopy; the results for the films and Al foil agreed within 1 standard deviation (SD).

6.3.2.4.3 *Immersed film measurement compared to externally mounted measurement*

The combined externally mounted film dose responses was (114.3 ± 75.9) cGy (an average of both peripheral measurements), and the measured dose in the film placed at the peripheral slot within the water target was 123.2 cGy. When comparing the results for the externally mounted film with those of the more robust measurements of the film in water, the externally mounted film predicted with an accuracy of 93% the estimated mouse exposure.

6.3.3 Discussion

The XRQA film dose response, at the peripheral locations of the external mounted films, measured relatively large deviations in response to neutron dose as seen by the reported SD values. The deviation in value quoted for the XRQA film was due to

the averaging of the values in areas of steep dose gradient. The dose gradient was a result of the rapid fall off of the neutron beam intensity moving away from the 0° axis. The external XRQA films did agree within 1 SD to the average Al foil response. The discrepancy in the doses at the peripheral location determined by the film and Al foil methods is attributed mainly to a systematic feature in the neutron foil activation technique. The film and foil dose values were measured over similar spatial areas. However, in the neutron activation measurements the Al foil was treated as a point source in calculating the flux from the counts in the γ -ray energy spectrum measured with the HPGe detector. As an indirect point dose dosimetry system, Al foils were incapable of measuring the effects of the dose gradient at the peripheral location and subsequently its quoted error was predominantly a measure of the systemic error in the γ -ray spectroscopy measurement and not a measure of the spatial deviation of γ -rays. The effect is smaller at the center location because the activation distribution in the foil better approximates a point due to the shape of neutron flux distribution.

The XRQA film measured a greater sensitivity to neutron dosimetry than EBT film. The greater sensitivity to neutron-induced signal comes from the larger effective Z of the XRQA film ($Z_{eff} = 24$) compared with EBT film ($Z_{eff} = 6.6$), see section 2.1. The larger Z_{eff} results in more efficient ionization of the recoil protons in the XRQA film. Both films have equal percent hydrogenous material, which is known to be the most effective at absorbing energy from fast neutrons with the elastic scattering reaction. A

hydrogen detector provides the greatest cross section for elastic scattering of incident neutrons thereby better preserving directional information from the initial fast neutrons along the main beam axis. Due to the greater sensitivity to neutron dosimetry, XRQA film was used in the development of the film calibration technique and the dosimetry method for the mouse irradiation experiments.

RCFs were developed to be sensitive to photon radiation, and therefore the signal readout from the films exposed to a mixed neutron and γ -ray field will be a measurement of neutron and γ -ray dose. The neutron beam was comprised of three distinct types of radiation: fast 10 MeV mono-energetic neutrons from the $^2\text{H}(\text{d},\text{n})^3\text{He}$ reaction; continuous energy neutrons from the breakup of deuterons in beam and in the deuterium gas cell; and γ -rays¹²⁸. The γ -ray radiation was comprised of the: neutron capture on hydrogen; the $^1\text{H}(\text{n},\gamma)^2\text{H}$ reaction (2.225 MeV), in the targets and the radiation shielding material, which were mostly water; de-excitation of excited nuclei in the beam stop (gold) and beam collimation apertures (tantalum); and from the de-excitation of the Al foil through ^{24}Na de-excitation by γ -ray (1368 keV).

The breakup neutrons were shown to have a wide spectrum of energies from ~1 MeV to ~6.5 MeV where the peaks of the measured continuum of flux were centered at 2.7 MeV and 4.4 MeV. The breakup flux was measured along the main axis of the neutron beam and measured ~6% of the monoenergetic neutron contribution; where the break-up neutrons contributed much less to the overall neutron beam when measured

10° from the main beam axis¹²⁸. The γ -ray components were analyzed to determine their impact on the overall film dose. First, the dose component to the XRQA film from the γ -rays emitted from the $^1\text{H}(n,\gamma)^2\text{H}$ reaction was calculated using Monte Carlo. The percent dose contribution from $^1\text{H}(n,\gamma)^2\text{H}$ γ -rays are shown in Table 6-2. The maximum contribution of the $^1\text{H}(n,\gamma)^2\text{H}$ reaction γ -rays to the dose measured by the films was shown to be < 2%. Second, the γ -ray contribution from the deuteron beam interactions with the materials in the beam collimation and beam stop materials were measured previously for 8 MeV neutrons. In the previous report¹²⁸, the γ -ray and neutron doses were separately measured at the same location along the beam axis and the γ -ray contribution was measured to be 5% of the neutron beam. Third, the γ -ray dose contribution from Al foil activation, through ^{24}Na de-excitation by γ -ray, was shown to have a negligible impact on measured film dose response. Dose profiles in Figure 6.25 demonstrated similar dose responses when taken from the films through regions where Al foils overlapped, and would have exposed the films with γ -rays, and through regions where Al foils were not present to expose the films with γ -rays. The contamination in the film due to γ -rays was minimal compared to the measured neutron doses for several different conditions. Overall, γ -ray and breakup neutron contamination accounted for ~13% of the total dose to the films along the central beam axis, but only ~3% when measured 10° off the central beam axis¹²⁸.

The XRQA films were also exposed to scattered neutrons and γ -rays. The geometrical isotropy of the γ -rays and the scattered neutrons contributed to a consistent baseline dose measured by the film. This baseline dose was evident from the overall exposure of the film in spite of the collimated neutron beam. The tails of the dose profile in Figure 6.25 approached a value of ~ 50 cGy when measured outside of the region of direct neutron beam involvement.

6.3.4 Conclusion

Two types of modern RCFs, XRQA and EBT film, were studied as potential 2D neutron dosimeters. XRQA film measured a greater sensitivity to neutron dose than EBT film by a factor of 1.39 when exposed to a neutron dose of 165 cGy. A netOD-to-dose calibration curve technique was presented. Monte Carlo simulations were used to calculate soft tissue dose to film for 10 MeV neutrons over a range of 0-10 Gy. The Monte Carlo and XRQA film responses were fit using a least-squares fit of a nonlinear function that measured a correlation of 0.9926 with the calibration data. Monte Carlo results were benchmarked against an Al foil activation technique with the results matching within 0.4%. XRQA films were employed to measure a 2D dose distribution of the neutron beam flux for an experimental setup and used to make dose measurements on mouse targets. XRQA films placed in front of the experimental setup and within a water bottle, to simulate a mouse target, agreed within 7%. The good agreement of the external film with that of the *in vitro* film measurement demonstrated the ability of

XRQA film to be used in an uncomplicated passive manner to measure dose by placing a piece of film in front of a target. The XRQA film measurements within the water bottle were compared to the results from Monte Carlo simulations to test the accuracy of the film in neutron dosimetry measurements. The comparison of the film and Monte Carlo responses gave a correlation of 0.9982. To this end, we have demonstrated the potential application of RCF for accurate fast neutron dosimetry.

7 Conclusion

The purpose of this work was to expand the current limits of indirectly ionizing radiation dosimetry by using RCF as a spatially high-resolution, accurate dosimetry system. RCF is inherently 2D and can be extrapolated into the third dimension when considering volumetric dosimetry. This work was generalized into two aims. The first aim was the development of the RCF dosimetry system; it was accomplished by characterizing the film and the readout devices and developing a method to calibrate film response for absolute dose measurements. The second aim was to apply the RCF dosimetry system to three areas of dosimetry that were inherently volumetric and could benefit from multiple dimensional (2D or 3D) dose analysis. These areas were representative of a broad range of radiation energy levels and were: low-mammography, intermediate-computed tomography (CT), and high-radiobiological small animal irradiation and cancer patient treatment verification. The application of a single dosimeter over a broad range of energy levels is currently unavailable for most traditional dosimeters, and thus, was used to demonstrate the robustness and flexibility of the RCF dosimetry system.

The RCF dosimetry system was investigated for a full range of dosimetry characteristics to identify the limitations and optimal working parameters for two film types: EBT and XRQA film, and for two digitization devices. The investigation was thorough in its scope as it looked into eight separate factors affecting film response

accuracy and seven factors affecting accuracy for film readout digitization. Furthermore, a means to calibrate the film response to absolute dosimetry was defined. In each of the 15 investigations the RCF dosimetry system, was shown to be a robust and well suited for clinical and experimental laboratory environments.

Once a standard operational protocol for RCF dosimetry had been established, the dosimetry system was applied to the task of determining accurate 2D and 3D dosimetry in a wide range of applications. The applications spanned a wide range of radiation energies, namely: from the low mammotomography of 60 kV up to the very high 10 MeV neutron and 6 MV photon range. The films were applied to a total of six individual experiments and in each case the dosimetry system response was verified for accuracy and precision versus a golden standard device specific for the energy range tested. In all cases, and across all energy ranges, the RCF dosimetry system responded within better than 7% to the gold standard dosimeters. To date no dosimeter has been shown to be as robust and accurate over such a wide radiation energy range.

8 Future work

In the short history (~4 decades) of RCF research, improvements of the film have brought to pass approximately 13 different RCF types. In the short five years I have worked with the RCF at Duke University, EBT and XRQA film have been supplanted by EBT-2 and XRQA-2; each was presented with modified structures and improvements in response. The future work in RCF is bright. Continual verification and investigation into the dosimetric properties of an ever-improving dosimeter will be required. Better ways to digitize the film are also still being reported. But most importantly, different uses for RCF dosimetry are being investigated. As the intensity and scientific scrutiny continues for RCF, this dosimetry system will only become better.

Specific areas of future work include: the further development of 3D organ dosimetry for CT as was discussed in section 5.2.3. This will possibly open the door for better radiation risk assessment for patients being imaged or treated using radiological devices; further characterization of RCF energy and sensitivity response for neutron dosimetry; and the possible exploration of direct ionizing particle dosimetry like electrons or protons.

Additional verification of film response for dose distribution accuracy should be developed using Monte Carlo techniques. This work employed a purely empirical methodology for film verification using TLDs, MOSFETs, Al foils, and ion chambers. Each device is inherently 1D and provided a sampling of point dose measurements. The

sampling of the measured dose distributions using the point dose measurement techniques allowed for a comparison with film measured distributions, but not at a high dose resolution. To verify RCF over a point-by-point methodology throughout 2D and 3D dose distributions, future work will need to turn to Monte Carlo.

The most important consideration for future work for RCF dosimetry is the notion that 1D point dose measurements are limited in most current applications today, and must be expanded to include spatial information. We live in a modern medical world where planar imaging has been mostly replaced by volumetric imaging; so to, must go the way of radiation dosimetry!

A Appendix-Traditional Dosimeters

In this work there were three commonly cited dosimeters, the ion chamber, thermoluminescent dosimeter (TLD) and the metal-oxide semiconductor field-effect transistor (MOSFET). The following subsections of appendix A will provide more information on the operational handling and basic theory behind their use.

A.1 Ion Chamber

Ion chambers are the most ubiquitous detectors available for radiation detection, and are considered the gold standard. Ion chambers are: precise; tissue or air equivalent low Z_{eff} dosimeters; and can correlate absorbed dose to most any medium (D_{med}). Ion chambers are not absolute dosimeters by nature, but must be calibrated against an absolute standard, usually a free-in-air ionization chamber. The calibration process is performed at specific energy ranges and therefore may require multiple calibration point depending upon typical use. Standard intermediate energy calibration factors, e.g., 80 kV and 120 kV, can vary by as much as ~5%. Once established, the calibration factor (κ) will be used to modify the ion chamber response to absolute dosimetry. Other calibration factors are required to establish the ion chamber response as an absolute response as was shown in equation (3-7), (shown here for convenience):

$$D(cGy) = X(R) \cdot P_{TP} \cdot P_{ion} \cdot P_{pol} \cdot P_{elec} \cdot \kappa \cdot fFactor_{medium}^{energy} \left(\frac{cGy}{R} \right). \quad (A-1)$$

Task group 61 (TG-61), organized by the AAPM¹³², reported on the derivation of the various calibration factors shown in equation (A-1). The following is a brief description of the derivation of equation (A-1).

The following are various correction factors necessary to account for variations in the electronic readings:

(1) P_{TP} is the correction factor for temperature and pressure:

$$P_{TP} = \left(\frac{273.2 + T(^{\circ}C)}{295.2} \right) \left(\frac{101.33}{P(kPa)} \right) \quad (A-2)$$

where $T(^{\circ}C)$ is temperature measured in degrees Celsius and P is pressure measured in Pascals.

(2) P_{ion} accounts for the ion chambers collection inefficiency:

$$P_{ion} = \frac{1 - \left(\frac{V_H}{V_L} \right)^2}{\frac{M_{raw}^H}{M_{raw}^L} - \left(\frac{V_H}{V_L} \right)^2} \quad (A-3)$$

where V_H and V_L represent the high and low bias voltages (set on the electrometer) used to find their respective high and low raw readings M^H and M^L .

(3) P_{elec} is provided by a calibration lab, much like κ . Often times, the ion chamber and electrometer are calibrated together as a unit and therefore the ion chamber correction factor, κ , and P_{elec} will be one value.

(4) P_{pol} corrects for polarity effects due to beam quality and various other extraneous circumstances like cable position:

$$P_{pol} = \left| \frac{M_{raw}^+ - M_{raw}^-}{2 \cdot M_{raw}} \right| \quad (A-4)$$

where M^+ and M^- are the raw readings measured at \pm bias, and M_{raw} is the raw value of either the positive or negative bias measurement (note consistency is key, i.e., use the same M_{raw} , at either positive or negative bias, for all occurrences of M_{raw}).

(5) P_{stem} is not shown in equation (A-1) because it is often considered as unity for most energies discussed in TG-61¹³². The chamber stem correction factor accounts for the change in photon scatter, from the chamber stem, when the field size used during a field measurement differs from the one used during the calibration process, (P_{stem} is taken as unity for the same field size used in calibration and measurement, and is only necessary for measurements of dose with tube potentials $\leq 300\text{keV}$)

A.2 Thermoluminescent Dosimeter (TLD)

TLDs have 50+ years of experience in medical dosimetry, and are well accepted within the scientific community¹³³. A TLD is a small crystalline detector made from dielectric material with luminescence centers. The luminescence center is defined as a location where an electron and hole recombine causing light to be emitted. TLDs are

typically made from Lithium Fluoride (LiF) and are doped with various amounts of other elements that act as activators associated with the luminescence centers. The doped compounds are used in trace amounts making the LiF crystal structure the main elemental compound of the TLD when considering the interaction with the detector from the radiation field.

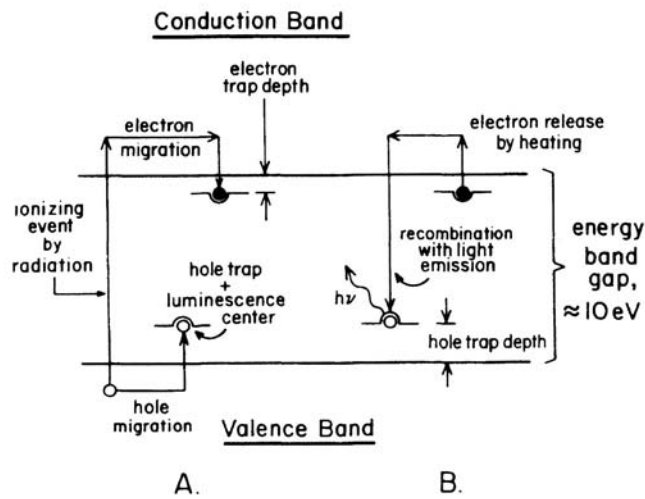


Figure A.1 TLD energy level diagram

Energy-level diagram of the thermoluminescence process: (A) ionization by radiation, and trapping of electrons and holes; (B) heating to release electrons, allowing luminescence production. This figure was reproduced from Figure 14.1 on page 396 from (Attix, 1986)³⁶.

The TLDs store their irradiated energy in the forms of electrons and holes. The electron is excited from its place in the valance band of the LiF structure, and is elevated into the conduction band (thus leaving behind a “hole”), see Figure A.1. Once separated the electron and hole become trapped within the energy band gap, and wait for

excitation in the form of external energy. To liberate the electron and hole, the detector is exposed to a controlled heating environment, which excites the electron, elevating it from the trap and allows it to de-excite down to the hole trap, or the luminescence center, where the electron and hole and electron to recombine and emit light. The heating process is called the readout used to convert the trapped electrons into light emissions.

The amount of light emissions from the trapped electrons is proportional to the detector exposure. Furthermore, the light emission is proportional to the rate of electron escape, which total light corresponds to a thermoluminescence (TL) brightness peak, or simply called a glow peak. There are various glow peaks, as a function of reading time, due to the varying depths of electron traps in the energy band gap. The summation of the light output is proportional to the radiation exposure from the radiation field surveyed.

Specific to this work are Harshaw TLD-100 detectors. TLD-100 chips consist of LiF doped with Mg and Ti (LiF:Mg:Ti) and are used in medical applications because of their tissue equivalent effective-atomic weight (Z_{eff}) of 8.2, (compared to tissue-7.4 and air-7.6). TLD-100 chips can measure energies > 5 keV; are dose rate independent; and have a linear dose response from $10 \mu\text{Gy}$ to 1 Gy and a supralinear response from 1 Gy to 20 Gy ³⁶. Additionally, TLD-100 chips are small in size, usually $(3 \times 3 \times 1)$ mm thick, which allows the radiation field to be measured with very minimal disturbance. All

TLDs were first tested for batch uniformity by being exposed to a cumulative exposure of 1 R. Chips that deviated more than 2 SD from the batch mean were discarded. All TLDs in this work were annealed using a TLD-annealing furnace (168-300, Radiation Products Design, Inc., Albertville, MN), and read using a TLD reader (Harshaw 5500, Thermo Fisher Scientific, Inc., Waltham, MA) with WinREMS software. Nitrogen gas was introduced during the readout cycle to reduce non-radiation-induced signals¹³⁴.

In general TLDs are passive detectors that require 24 hours to stabilize before reading, and when properly annealed before irradiation, the TLDs will maintain > 95% of the signal for up to 3 months¹³⁵. However, care must be taken to reduce nonradiation-induced signals. This is often accomplished by passing an inert gas, usually Nitrogen, through the readout chamber during the controlled heating cycle¹³⁴.

To use the TLD-100 as a dosimeter, they must be handled carefully, and undergo periodic batch assessments. Because TLDs can be easily contaminated (e.g., skin oil, dust, scratches, or chipping) and will affect the electron-hole trapping and recombination, TLDs are handled with vacuum tweezers and often irradiated in plastic bags. The batch assessment maintains the precision of a batch of TLDs to within 2 SD. This is accomplished by exposing the batch of TLDs to a given exposure level and then comparing the individual TLD responses to the mean batch response. All TLDs that lie outside of a confidence level of 2 SD are removed from the batch. Once the outlying TLDs are removed, the dosimeters must be annealed to liberate all remaining trapped

electrons returning the dosimeter to a baseline value. Annealing requires approximately 3 hours of baking time at specific temperature combinations, e.g., 2 hr at 400°C and 1 hr at 100°C. After annealing the TLDs are ready for exposure and then reading. The reading process applies a known amount of heat verses time to liberate the electrons for light emission and detection, see (Attix, 1986)³⁶ for an in depth treatment on glow curve heating.

A.3 Metal-Oxide-Semiconductor Field-Effect Transistor (MOSFET)

Metal-Oxide-Semiconductor Field-Effect Transistor (MOSFET) is a versatile field-effect transistor (FET) that has had a rich history in both digital and analog circuits going back to the 1950s; however, over the past decade and a half MOSFET technology has been applied to clinical dosimetry as a novel dosimeter capable of reading real-time dosages. The MOSFET dosimeter structure comes in several different design options, however, the following description is based only on the P-type semiconductor design, Figure A.2.

The MOSFET dosimeter can be understood by breaking up its colloquial name into its components: MOS and FET. The metal-oxide-semiconductor (MOS) is constructed of new, non-metal, technology called polycrystalline silicon layered on top of a silicon dioxide (SiO₂) layer. Since silicon is a dielectric, the MOS construct operates as a plain capacitor, but with the semiconductor as its top plate. The FET structure consists of two terminals, the Source and the Drain, each is connected to highly doped

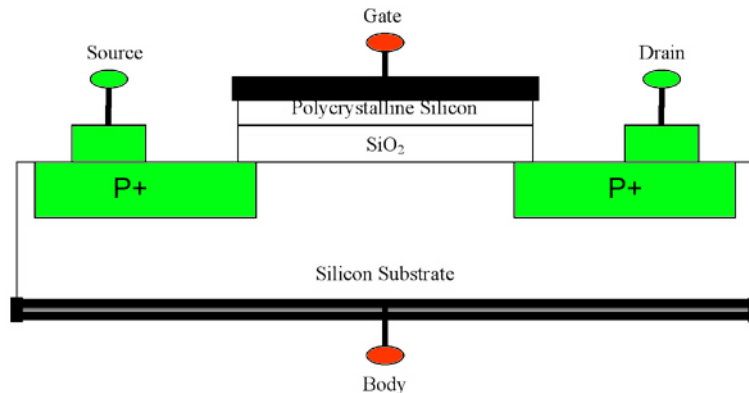


Figure A.2 P-Channel MOSFET diagram

(denoted by the “+”) P⁺ regions that are insulated from one another by a silicon substrate called the Body. The Body is an N-doped (or electron rich) region. The P and N regions denote relative amounts of one charge compared to the other, e.g., the P region contains more positively charged electron holes (referred to only as holes) than negatively charged electrons. The detector chip, shown in Figure A.1, measures approximately (1 x 1) mm with the SiO₂ region only measuring (0.2 x 0.2) mm.

The MOSFET detector is used as a dosimeter by allowing ionizing radiation to produce hole-electron pairs in the silicon substrate. When a high voltage is applied across the gate electrode, the positive holes migrate towards the negative Gate electrode, but stop at the SiO₂/silicon substrate interface, creating a concentration of positive charge carriers between the P⁺ doped Source and Drain terminals. The positive concentration of holes at the SiO₂/silicon substrate interface is called an inversion layer. The inversion layer allows current to flow from the Source to the Drain when a minimum voltage, defined as the threshold voltage (V_{th}), is applied to the Gate. A positive channel is

created allowing for current to flow; thus, a simple switch model is used to describe the MOSFET detector: when V_{GB} (voltage applied across the Gate and Body electrodes) $< V_{th}$ the MOSFET is “off” and $V_{GB} > V_{th}$ the MOSFET is “on.”

To operate the MOSFEET, a negative voltage bias is applied to the dosimeter before irradiation to increase sensitivity to the ionizing radiation. The Gate voltage is directly proportional to the sensitivity of the MOSFET during electron-hole collection. Once irradiated, the holes will then migrate towards the SiO₂/silicon substrate interface. The migrant holes become trapped, indefinitely, at the interface causing a negative threshold voltage shift (ΔV_{th}). The measured ΔV_{th} is directly proportional to the absorbed dose in the silicon substrate active region, i.e., the V_{th} is measured before irradiation and after and the ΔV_{th} is directly proportional to absorbed dose. One consequence of using silicon as a material in the MOSFET detector is that there is a non-linear dependence of absorbed dose to energy at lower photon energies. The non-linearity effect comes from the increased mass energy attenuation coefficient ratio due to the increased photoelectric cross-section (τ):

$$\tau \propto \frac{Z^4}{(h\nu)^3} \tag{A-5}$$

where Z is the atomic mass of the material and $h\nu$ is the energy of the ionizing radiation; thus, the difference in the atomic masses of the silicon substrate and the SiO₂ layer causes an increase in sensitivity to absorbed dose at orthovoltage energies. Because of the

increased sensitivity to absorbed dose at lower energies, the MOSFET dosimeters must be energy calibrated when first used.

B Appendix-Film Post Processing & Analysis Software

The following section is a technical document on how to use the film processing software tool described in section 5.2.1.5. Briefly, this software tool was developed in Matlab using a GUI interface. The tool was developed primarily to stream line RCF post processing, calibration, and analysis. The tool was also developed to provide comparison features with multiple batches of TLD and MOSFET dosimeters.

The first most important thing the user must understand is the file naming scheme! The software looks for specific sequences in the naming scheme, i.e., file number, file name, how many duplicates there are, etc. There is a built in mechanism to rename files that are not labeled how the software would like them. However, the loading process is speed up if at the time of scanning the films they are labeled consistently with what the software expects. The naming scheme should be as follows:

<film number><post or pre><duplicate number><file type suffix>

Examples are as follows:

1post001.tif
1pre001.tif
2post001.tif
2pre001.tif
Etc

The file names should not have any spaces. Also, the software is by nature CAPs sensitive, e.g., 1Post001.tif, verses 1post001.tif. Once again the software has been written to consider the difference and correct for it, but it is easier to maintain all letters in lower case font.

The software is launched by running the main script "filmCorrectionGUI_V_3_0.m". Once the main script is initialized, Figure B.1 will appear on the screen. The film processing tool is mostly self explanatory. Each "step" is labeled (1-5). The user is to proceed sequentially from step 1 to 5.

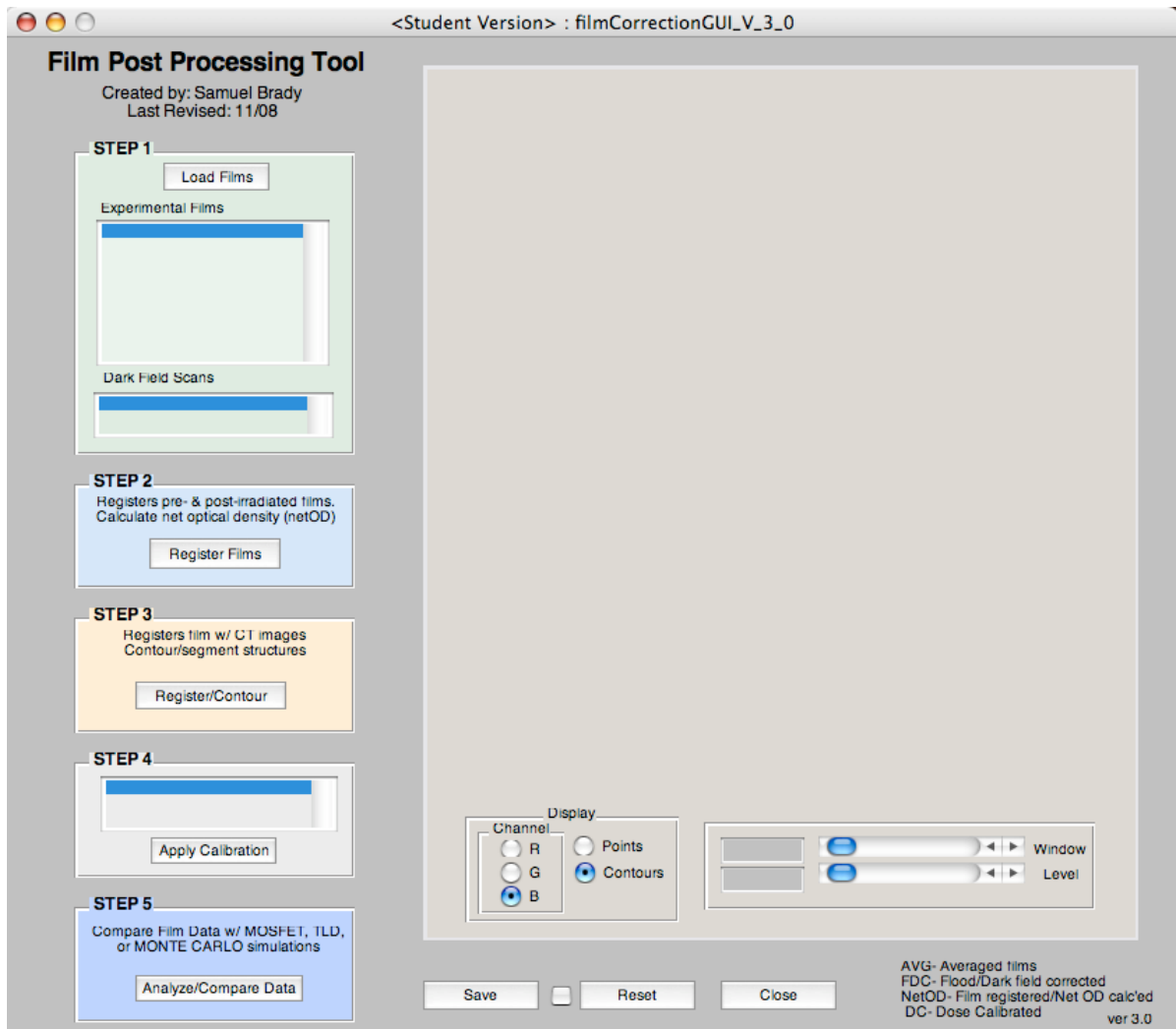


Figure B.1 Main window

STEP 1

To load the films click on the “load Films” button under the section labeled “step 1”. Figure B.2 will appear with empty load fields. Each field will be labeled with the

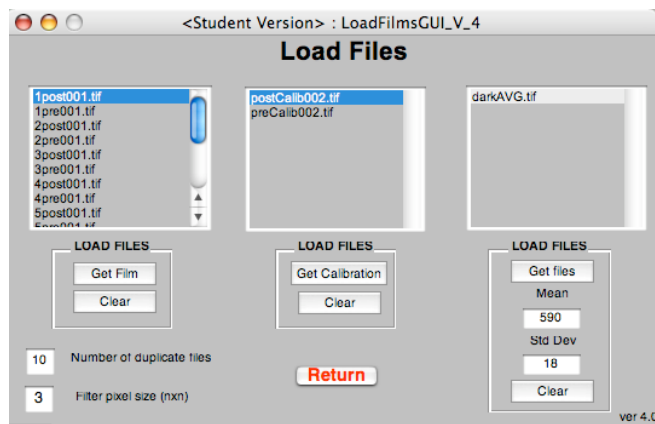


Figure B.2 Load film window

type of film that it will accept in the loading process. A red “Return” button is used to return to the main page after all of the Load Files fields are populated. Each Load Files field has a “Get XXX” and “Clear” buttons located below their respective fields. The “Get XXX” button will be specific to their respective fields, i.e., film, calibration or file. Also, on the bottom right there are two boxes that control how the software operates after the “Get Film” button has been selected and each field has been pre-established but can be changed for user preferences. The first field labeled “Number of duplicate files” tells the software how many of every film or file will be a duplicate. For example, if you scan each film five times such that you have 5 preFilm1.tif and 5postFilm1.tif files then you enter a 5 into this box and the software will search for 5 of every film uploaded. The files will be averaged into one file. It is crucial that the 5 files should be the same

physical dimension and resolution. It is all crucial that the pre and post scanned films are the same size for later in the post processing process. The recommended film digitization protocol is for only 1 scan per film, hence, the predefined value. The second field is labeled "Filter pixel size (nxn)". This field determines the smoothing kernel size. The software applies a 2D Wiener filter to each film. Traditionally, post exposed films are smoothed using a [3x3] kernel and the pre exposed films use a [7x7] kernel; the pre films are more aggressively smoothed to minimize the shoot noise inherent to the CCD detector devices used for digitization. One option is to simply leave the smoothing kernel size as [3x3], hence the predefined value.

The first load files field is labeled "Experimental films". All pre-irradiated and post-irradiated scanned films should be loaded into this field. To do so click on the "Get Film" button bellow the field and a navigation pane will appear and prompt you to select all PRE and POST films. Navigate to the director where those films are located and select all the films using either the SHIFT or CTRL (Apple key for a Mac) keyboard keys or simple click and drag the mouse over the files. Select "Ok". The software will process the film.

The second load files field is labeled "Calibration Films". Follow the same procedures as the "Experimental Films" loading.

The third load files field is labeled "Dark Field". This field requires the user to define how many dark films will be averaged in the "Number of duplicate files" field as

previously described. Before clicking on the “Get files” enter the number of dark fields to average in the “number of duplicates files” field. The software will average the loaded dark films and calculate a mean and standard deviation of the averaged dark field files.

To use the clear button, select any, or all, of the films in the specific field and click on the “Clear” button associated with that field. The name of the file(s) will be deleted from software memory.

When finished click “Return” The Load Files window will disappear and the main window will reappear and the loaded files will be placed within their respective fields, see Figure B.1. For example under “Step 1” there are two list boxes one labeled “Experimental Films” and the other “Dark Field Scans”. The loaded file names will populate these fields. If the user clicks on any one of the file names, the file image will appear on the right hand side. The image color scheme can be windowed and leveled using the sliding bars bellow the image. Note that the loaded calibration files were listed under “Step 4”. They can similarly be displayed on the right hand side of the software, but the files were listed in the order in which they will be needed.

STEP 2

The loaded files are displayed as intensities only. To calculate the netOD values of each film number, the user must proceed to “Step 2” by clicking on the “Register Films” button. Once the button has been selected the Film-to-Film Registration window

will appear, see Figure B.3. The experimental film names will appear in the upper right most field. The user may select any one of the film names and its accompanying image will display on the left hand side. The corresponding pre and post films must be spatially registered before a pixel-by-pixel netOD calculation can occur. By performing a pixel-by-pixel correction, the scanner non-uniformities are accounted for when the two images are divided. There are two ways to register the pre and post films: (1) manually, or (2) using fiducial markers. It should be noted that great care should always be taken during the digitization process to align the pre and post films in the same orientation at the same location on the scanner bed. The more careful the alignment the easier and more accurate the registration process will be.

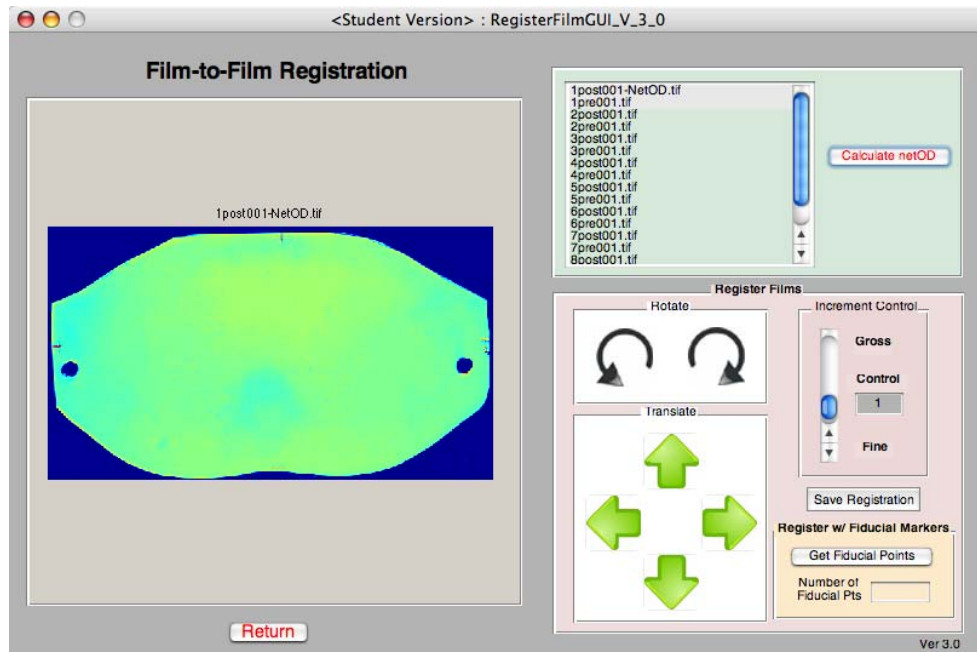


Figure B.3 Film-to-Film Registration window

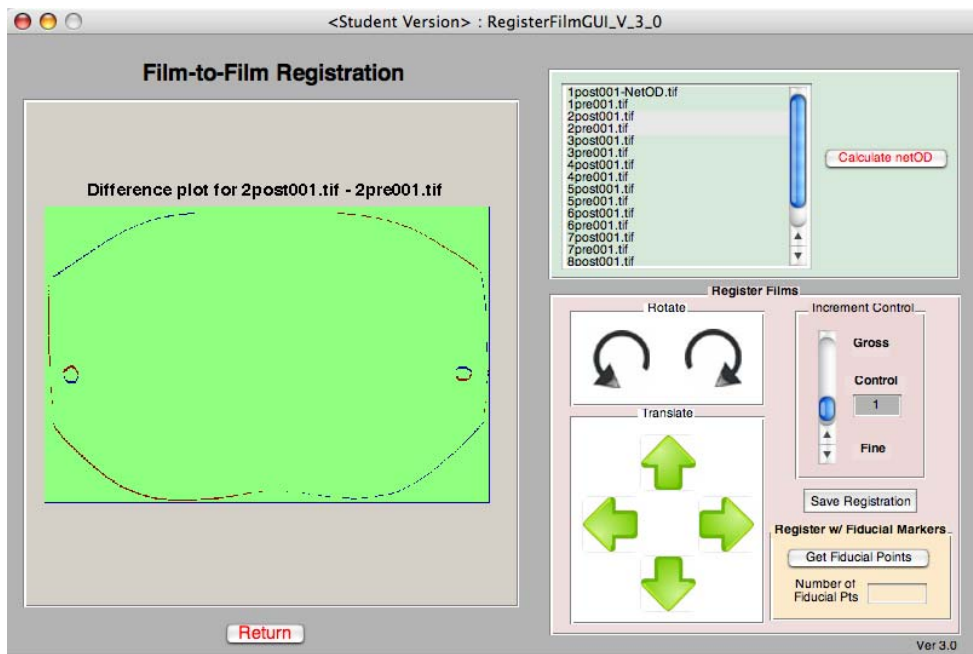


Figure B.4 Film-to-Film Registration window with difference plot demonstrated

First, the manual approach is described. When any two file names are selected the difference of the films will be shown to the left, see Figure B.4. If the two films were perfectly aligned nothing would appear in the image but a simple green screen. However, the film boundaries will most always appear due to minor setup inaccuracies. Boundaries will appear red and blue. The color red indicates areas of no overlap and conversely the blue indicates areas of overlap. Therefore, the user wants to translate the image in the direction of the red. This is performed by clicking on the arrows under the “Rotate” and or “Translate” boxes. All translation is performed by the pre film to preserve the post film accuracy. Every time the pre film is rotated a slight amount of blurring is introduced because of the bicubic interpolation that occurs when the image is rotated. For finer or grosser incremental movements of the film the slider to the right of

the buttons can be moved up or down or a number can be typed into the "Control" field. The film Left/right or up/down translations can only be performed with a fine/gross whole value, e.g., 1 or 2. However, the rotation controls will accept decimal values such as 0.5. Once the images appear well registered to the user, click on the "Save Registration" button and then the "calculate netOD" button. When the netOD calculation is finished the post film will have a "-NetOD" appended to the end of the film. Only the post films will show this appending.

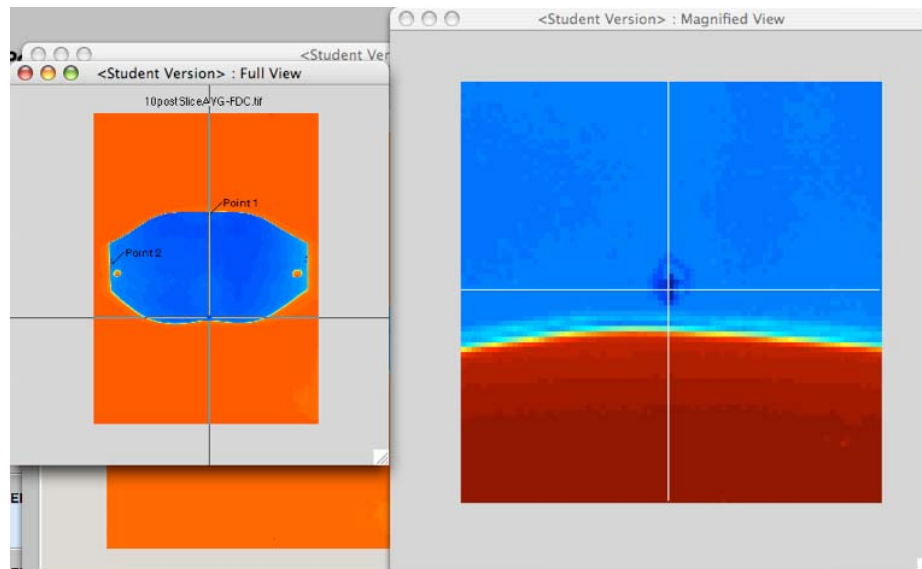


Figure B.5 Fiducial marker selection tool

Second, fiducial markers can be drawn onto the film and used to register the film. Care should be taken not to place fiducial markers in areas of sensitive data analysis. All writing on the films will corrupt the dosimetry at those pixel locations. The fiducial markers must be placed on the film prior to pre-irradiation scanning so that they appear on the pre and post scans. The fiducial markers should be added after the

film has been cut so no marker is lost. There is a minimum requirement of 4 fiducial markers to perform this task. To register with fiducial markers, enter the number of fiducial markers in the corresponding field and click "Get Fiducial Points". Figure B.5 will appear. The window on the left is the navigation window. As you move your mouse around that window a magnified (10x) view in the right window will follow the cursor. Move the mouse over each of the fiducial markers and click once. Once selected, the fiducial marker will be labeled in the navigation window. Be sure to click firmly when selecting the fiducial point. If the label doesn't appear in the navigation window click again. If the user moves the mouse at the same time as he/she clicks, depending on which command was executed first in the software, a marker may appear in the navigation window, but when the user moves to the next fiducial marker and clicks on it a duplicate of the last label may appear. If this happens the first marker was not stored in the software memory and should be reselected. The user must pay attention as he/she clicks to make sure the right labels are in the right place. It is ABSOLUTELY IMPORTANT that the pre and post films are labeled in the same sequence. The software uses the coordinates of the pre and post fiducial markers to calculate the matrix transforms to rotate or shift the images. If the films have miss-aligned fiducial markers, the resulting image will appear very distorted or warped and must be redone. Currently the only way to redo any step is to close the window before selecting "Return" and re-launching the window to start afresh. Once the "Return" button has

been selected the results are taken from temporary memory and stored in the permanent software memory and can not be deleted (at least in this current software version). To restart would mean to close out the software and start all over.

Once all the images have been registered and their netOD values calculated click on "Return" to go back to the main page. Once on the main page, the file names will have their new appended endings. The file names can be selected and the netOD image will be shown to the right, see Figure B.6.

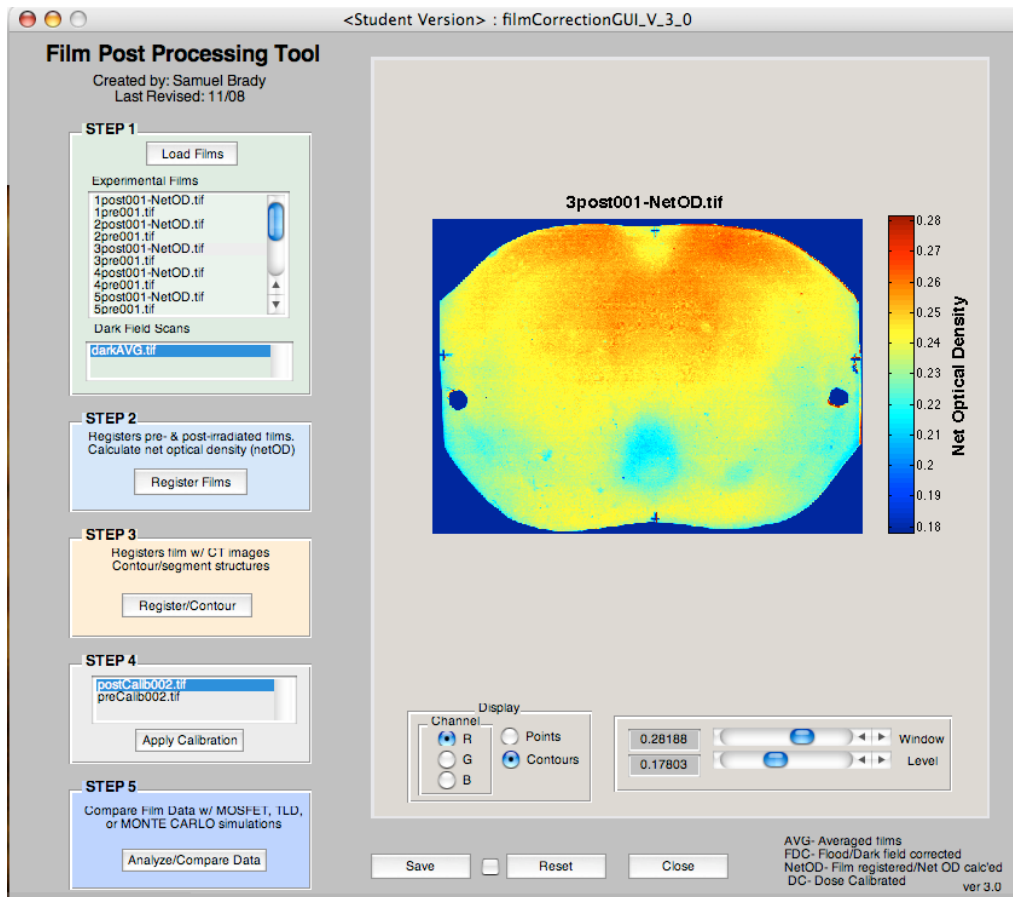


Figure B.6 Main window displaying film after film registration and netOD calculation has been completed

STEP 3

Once the films have been co-registered, in order to compare the film with any other dosimeter placed within a phantom, the reconstructed CT image of the phantom must be registered with the films before they can be registered with the other dosimeters. Step 3 also acts as a contouring tool to contour organ volumes in a reconstructed CT image for film response extraction. Launch the CT registration and contouring module by clicking on “Register/Contour” button under “Step 3”. The Contouring & Organ Extraction Tool window will appear, see Figure B.7. The film file

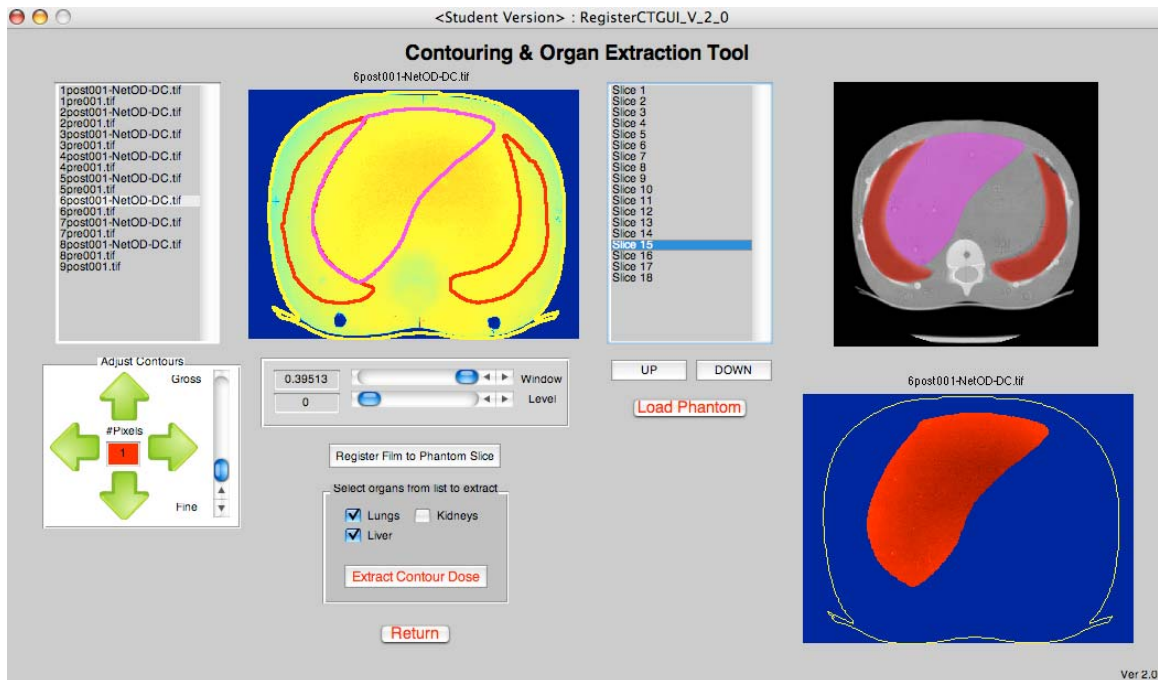


Figure B.7 Contouring & Organ Extraction Tool window

names will appear in the left most field. The file names can be selected and their corresponding image will appear to their right. To load the reconstructed CT images

with organ masks click on “Load Phantom”. Navigate to the *.mat file and click ok. The phantom *.mat file is created offline using Matlab. The CT images of the phantom and their corresponding structures are loaded into Matlab and a structure (see “help struct” for more information on how to create a structure file) file is created and saved as a *.mat file, e.g., ped5yrPhant.mat. In the case of Figure B.7, a pediatric phantom was developed in Matlab with each slice appropriately labeled and the DICOM image and organ mathematical mask saved in individual fields, e.g., ped5yrPhant.slice1.image for the DICOM image or ped5yrPhant.slice1.lungMask, for the lung mathematical mask. As the user clicks on the corresponding name of each structure field in Figure B.7 the image will appear with the organ masks overlaid.

Once the phantom is loaded, the user will select the film and the phantom section that correspond. Once both are highlighted in their respective fields, click on the “Register Film to Phantom Slice” button. The user must correlate the correct film number with the phantom section. The software contours the exterior boundary of the CT image and overlays the contour on the film image to the right. If the film and DICOM image are incorrectly associated, then the software will have a difficult time matching the contour with the film boundaries. The match may not be perfect even if the film and DICOM image were appropriately associated. To adjust the contour to better match the film boundary may use the “Adjust Contour” tool below the field box

listing the film names. This tool is used in the same manner as the one in the Film-to-Film registration module.

Once the contour is properly positioned, the organs/object that the user wants extracted for calibration must be checked in the field "Select organs from list to extract". Currently there are only three listed. The list can be populated over time as the need arises. After checking the organs click on the "Extract Contour Dose" button. The software will remove the film values corresponding to the organs selected and display them to the right below the DICOM image; the letters "-DC" will also be appended to the end of the file name. Also, a contour of the object mask will be displayed overlaid the film. This process is continued until all objects are contoured and the corresponding film responses are extracted. Note, if the user selects a file name that has been contoured, the corresponding DICOM image to the right will be changed to match with the registered image. This feature will allow the user to verify if the right film data was associated with the correct CT image. If all data collected is verifiably correct, click on "Return" to close the Contouring & Organ Extraction Tool window and return to the main window. Once back at the main window. The file names will show the "-DC" appending but if the file name is selected only the netOD image of the file will be displayed. The specific organ values are not visible until after they have been calibrated and displayed in "Step 5".

STEP 4

To calibrate the organ data extracted in Step 3 click on the “Apply Calibration” button under the “Step 4” field. The Film Calibration Tool window will launch, see Figure B.8. The list of film and calibration names are shown in their appropriate fields. By clicking on any of the names their image will appear to the right. Before selecting the

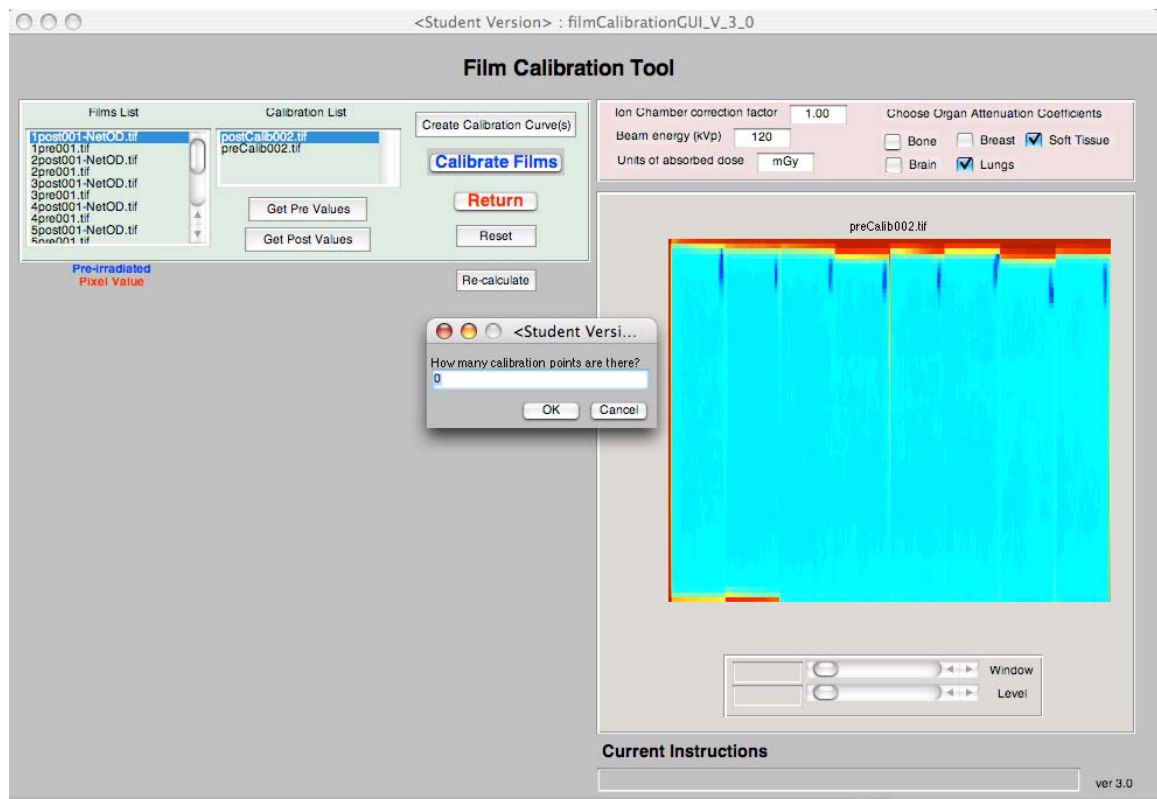


Figure B.8 Film Calibration Tool window with pre calibration file shown

calibration data, some dosimetry constants must be entered. Above the image pane and to the right of the film list pane (the red box) values for the “Ion chamber correction factor”, “Beam energy (kVp)”, and “Units of absorbed dose” need to be correctly entered. In-correctly entered values will affect the calibration curve results and the dosimetry analysis in the proceeding section. Also, the number of calibration curves

must be specified. This is done by selecting the types of tissues for which attenuation coefficients are used to calculate the f -Factors. Under “Choose Organ Attenuation Coefficients” in the red box click all pertinent tissue types.

Once the dosimetry factors are set, click on the “Get Pre Values” button. The pre-calibration image will appear to the right and a separate box will appear and prompt the user to enter the number of calibration points that will be used to form the calibration fitting function. Entering the number and clicking on the “OK” button will make that window disappear and make the cursor change from an arrow to small cross hairs. This indicates that the user will be able to create an ROI box in the image pane for the number of points indicated previously, see Figure B.9.

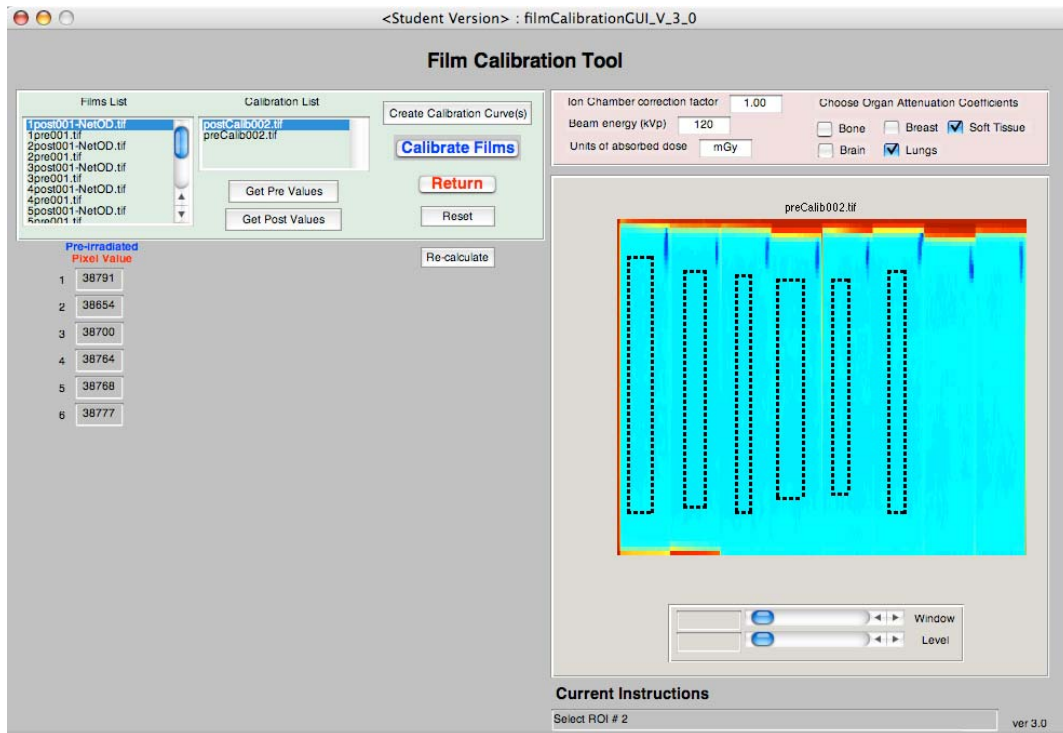


Figure B.9 Film Calibration Tool with pre calibration ROIs shown.

To draw an ROI on the image click and hold the mouse over the film strip from which the data will be taken. Continue holding the mouse and drag the ROI box to the appropriate size. Once the ROI position and size has been satisfied by the user, release the mouse button. The ROI box will remain where it was created by the user and a box displaying the average ROI pixel value will appear to the far left of the Film Calibration Tool window directly under the "Films List" field. Note, every pixel within the ROI is used for the average; therefore, when creating the ROI make sure not to overlap the ROI boundaries with the edges of the film or over writing on the film to preserve the highest accuracy for the ROI average. Once the "Get Pre Values" button is selected instructions will appear underneath the "Current Instructions" field at the bottom right of the window; in general, if there is ever confusion what to do during this process, see this field.

After drawing the appropriate amount of ROIs in the pre-calibration film the cursor will change from a small cross-hair back to the traditional black arrow. Now click on the "Get Post Values" button below the "Get Pre Values" button. Similarly, the post-irradiated films will be displayed in the display pane and the small window prompting the user to enter the number of calibration points will appear. This window will be pre-filled with the number entered for the pre-calibration film. The numbers must be identical. By clicking yes, the window will disappear and similarly the user will be prompted to create a number of ROIs as specified. When the user creates the first ROI

the “Current Instructions” field will prompt the user to “Enter exposure #1 then click outside the text box and press ‘Enter’”, see Figure B.10. Three boxes were also created when the ROI was drawn. The first was the mean pixel value of the ROI. The second is the calculated netOD of the pre and post pixel values. The third is blank and is waiting for the user to enter the exposure in (R). The user will then create ROIs and enter their corresponding measured exposure values for the number of post film as previously indicated.

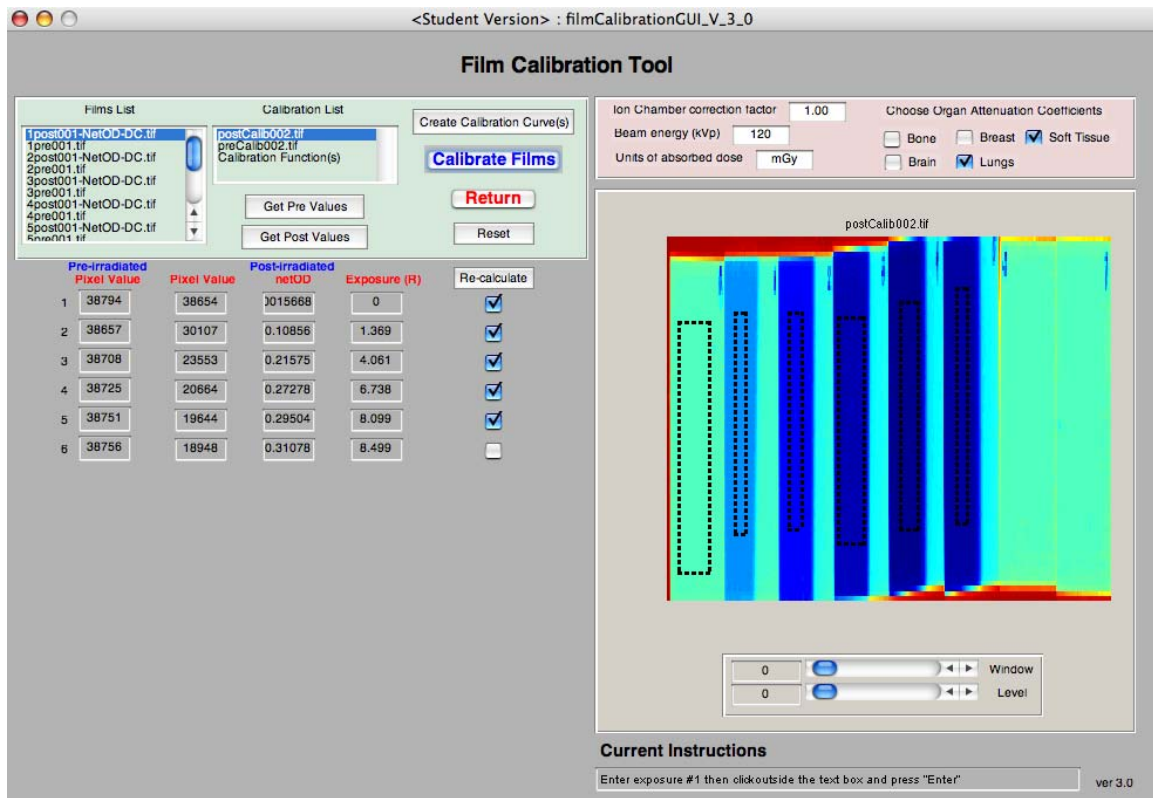


Figure B.10 Film Calibration Tool with post-calibration film image shown

Once the pre and post films have been measured, the user needs to click on the “Create Calibration Curve(s)”. The exposure values will be converted to dose using the

calibration factors entered into this window and equation (3-7) and plotted as a function of the calculated netOD. The calibration data will be fit using a modified exponential curve shown in equation (3-10) and plotted in the viewing pane *in lieu* of the post calibration film image. Also, the name "Calibration Function(s)" will appear under the "Calibration List" field for future viewing of the fitting function when the fitting function plot is replaced with a different image. Also note, that only one of the fitting functions is plotted from the list of fitting functions you generated by choosing different organ attenuation coefficients in the red pane above.

A separate plotting window will appear outside of the Film Calibration Tool window with the fitting error plotted. This plot can be analyzed for data points that caused the fitting function to fail in any specific area; remember the goal here is keep fitting function errors to below 2%, see section 3.3.3. The user can regenerate a fitting function with any of the calibration points removed from consideration by un-checking the box under the button "Re-calculate" corresponding to the offending calibration datum point, see Figure B.10. Once unchecked, click on the "Re-calculate" button and another fitting curve and fitting error plot will be displayed. Any number of data points can be removed or re-checked to find the best fitting function with the lowest overall fitting error.

Having created the fitting function, click on the "Calibrate Films" button. Every one of the post images will have their corresponding organs calibrated by their

corresponding organ attenuation types, i.e., the extracted lung organ data will be calibrated with the lungs fitting function, and the liver organ data by the soft tissue fitting function, etc. Once all of the films are calibrated, click on “Return” to close the Film Calibration Tool and return to the main window. Once back at the main window under “Step 4” film list field the name “Calibration function(s)” will appear. The user can click on the file name and see the fitting functions plotted in the viewing pane.

STEP 5

At this point the films have been post processed, and calibrated for a phantom of heterogeneous tissue type. The final step will prompt the user to load TLD and/or MOSFET data for comparison with film data. To launch the analysis module click on the “Analyze/Compare Data” button under “Step 5”. The “Data Reduction Tool” will appear with the file names listed in the bottom left pane (tan colored).

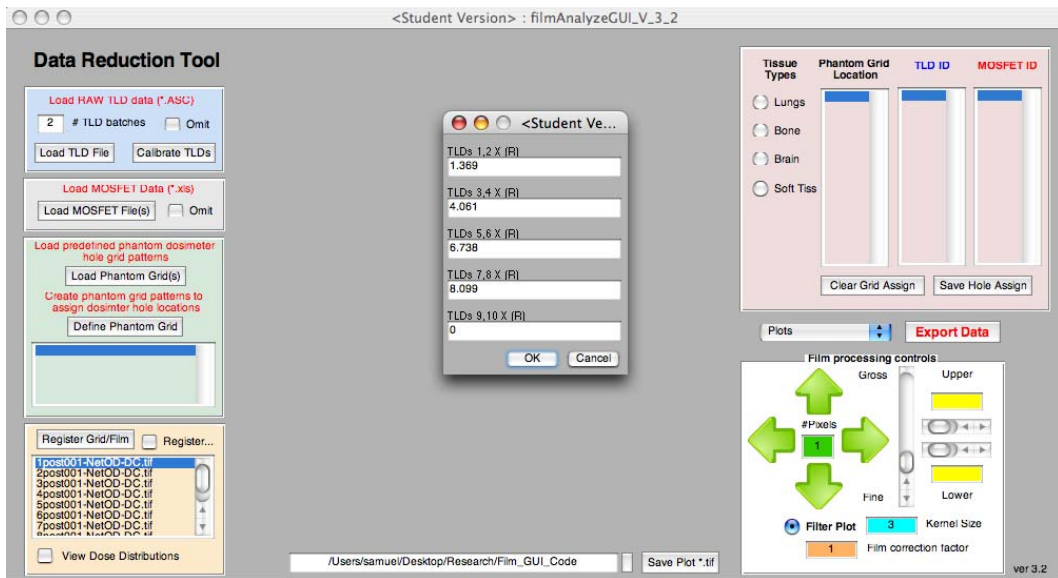


Figure B.11 Data Reduction tool

First, load the TLD data if there are TLD results to compare; if not click on the “Omit” box within the blue TLD pane. The user must tell the software how many batches of TLDs were used for comparison. Do so by entering the appropriate number in the field labeled “# TLD batches”. Then click on the “Load TLD File” button. A window will appear and prompt the user to enter the corresponding exposure level in (R) for the appropriate calibration TLDs, see Figure B.11. Note, the software explicitly assumes the first ten TLDs in all of the *.ASC file(s) are calibration data. The software also explicitly assumes that the sets of TLDs in each batch were exposed to the same exposure, e.g., TLDs 1 and 2 for batch 1 and 2 were exposed to 1.369 (R). After the user clicks “OK” a navigation window will appear and prompt the user to select the batch(es) of TLD. The files must be in *.ASC format, which is a simple comma sperated value (CSV) text file. The Harshaw TLD reader at Duke University uses this format. If this format is not universal, then the user needs to configure their TLD results to appear as similar to Figure B.12 in CSV format. The only pertinent information for the TLD calibration is found in columns 3 and 11 the rest can be filled with dumby text. It is important to include “PMT Noise” and “Test Light” rows at the beginning and after every 20 TLD data points. The software looks for those two rows of specific titles and the nine other columns of dumby text to remove them. Therefore, it is important to format the *.ASC file similarly to Figure B.12. Once the TLD data has been loaded, the software will parse the data into working form and the TLD IDs, i.e., row 3 of Figure

B.12, will be listed under the field titled "TLD ID" in the upper right of the Data Reduction Tool (in the red pane). A number and a hyphen will appear before the TLD IDs indicating which batch the ID comes from.

After the *.ASC files have been loaded, click on the "Calibrate TLDs" button and a number of calibration curves will be generated to match the number and type of RCF curves generated in the previous step.

5500, "	", "PMT Noise	", 20080916, 140819, 0, 1, 1, 0.000, 0.000, 0.120, "nC"
5500, "	", "Test Light	", 20080916, 140834, 0, 1, 1, 0.000, 0.000, 571.858, "nC"
5500, "	", "1	", 20080916, 140846, 4, 1, 4097, 0.000, 0.000, 1082.957, "nC"
5500, "	", "2	", 20080916, 141011, 4, 1, 4097, 0.000, 0.000, 1038.619, "nC"
5500, "	", "3	", 20080916, 141139, 4, 1, 4097, 0.000, 0.000, 152.108, "nC"
5500, "	", "4	", 20080916, 141309, 4, 1, 4097, 0.000, 0.000, 155.045, "nC"
5500, "	", "5	", 20080916, 141439, 4, 1, 4097, 0.000, 0.000, 435.980, "nC"
5500, "	", "6	", 20080916, 141611, 4, 1, 4097, 0.000, 0.000, 451.654, "nC"
5500, "	", "7	", 20080916, 141744, 4, 1, 4097, 0.000, 0.000, 704.780, "nC"
5500, "	", "8	", 20080916, 141919, 4, 1, 4097, 0.000, 0.000, 765.369, "nC"
5500, "	", "9	", 20080916, 142055, 4, 1, 4097, 0.000, 0.000, 0.770, "nC"
5500, "	", "10	", 20080916, 142231, 4, 1, 4097, 0.000, 0.000, 0.971, "nC"
5500, "	", "11	", 20080916, 142409, 4, 1, 4097, 0.000, 0.000, 857.143, "nC"
5500, "	", "12	", 20080916, 142546, 4, 1, 4097, 0.000, 0.000, 815.735, "nC"
5500, "	", "13	", 20080916, 142727, 4, 1, 4097, 0.000, 0.000, 700.806, "nC"
5500, "	", "14	", 20080916, 142905, 4, 1, 4097, 0.000, 0.000, 689.807, "nC"
5500, "	", "15	", 20080916, 143044, 4, 1, 4097, 0.000, 0.000, 849.661, "nC"
5500, "	", "16	", 20080916, 143225, 4, 1, 4097, 0.000, 0.000, 898.181, "nC"
5500, "	", "17	", 20080916, 143407, 4, 1, 4097, 0.000, 0.000, 824.181, "nC"
5500, "	", "18	", 20080916, 143549, 4, 1, 4097, 0.000, 0.000, 795.504, "nC"
5500, "	", "19	", 20080916, 143730, 4, 1, 4097, 0.000, 0.000, 762.062, "nC"
5500, "	", "20	", 20080916, 143912, 4, 1, 4097, 0.000, 0.000, 739.080, "nC"
5500, "	", "PMT Noise	", 20080916, 144057, 0, 1, 1, 0.000, 0.000, 0.046, "nC"
5500, "	", "Test Light	", 20080916, 144113, 0, 1, 1, 0.000, 0.000, 561.991, "nC"
5500, "	", "21	", 20080916, 144126, 4, 1, 4097, 0.000, 0.000, 768.423, "nC"
5500, "	", "22	", 20080916, 144308, 4, 1, 4097, 0.000, 0.000, 805.559, "nC"

Figure B.12 TLD *.ASC file format

To load the MOSFET data, click on the “Load MOSFET File(s)” button in the pane under the load TLD pane. The software will prompt the user to navigate to the MOSFET data sheet(s). Select all data sheets necessary for comparison with the TLD and RCF data. The data sheets will come in *.xls format, which is the standard format for Best Medical Canada. If the MOSFET data comes in any other format then the data must be placed into an excel spreadsheet (*.xls) and formatted identically to Figure B.13. The software looks for the data and text names in the correct columns. The number of Dosimeters is not limited to four as seen in Figure B.13. Once the MOSFET data is loaded and parsed properly, the MOSFET IDs will be listed to the right of the TLD IDs in the upper right pane. If no MOSFET data is needed, remember to click on the “Omit”.

DOSIMETER ASSIGNMENT:							
<u>Dosimeter</u>			<u>Target Dose</u>		<u>CF</u>		<u>CR</u>
A1:					29	mV/cGy	1
A2:					23	mV/cGy	1
A3:					28	mV/cGy	1
A4:					24	mV/cGy	1
MEASUREMENT RESULT:							
<u>Dosimeter</u>			<u>Voltage (mV)</u>		<u>Dose</u>		<u>Deviation</u>
A1:			191	mV	6.59	cGy	
A2:			132	mV	5.74	cGy	
A3:			191	mV	6.82	cGy	
A4:			181	mV	7.54	cGy	

Figure B.13 MOSFET *.xls file format

After the dosimeters are loaded, load the phantom grid data. This is accomplished by clicking on the “Load Phantom Grid(s)” button in the phantom pane (green color). A navigation window will appear and prompt the user to load all phantom grids of *.mat file format. In the case of the anthropomorphic phantoms, the each phantom grid corresponds to a phantom slice slab that had the film placed on top of it during the dosimetry experiment. If the phantom grids have not been digitized, the phantom section(s) need to be scanned on the flatbed scanner at the resolution that the films are traditionally digitized (i.e., 72 dpi). Then the user needs to click on the “Define Phantom Grid” button in the phantom panel. This launches the Phantom Grid Assignment Tool, see Figure B.14.

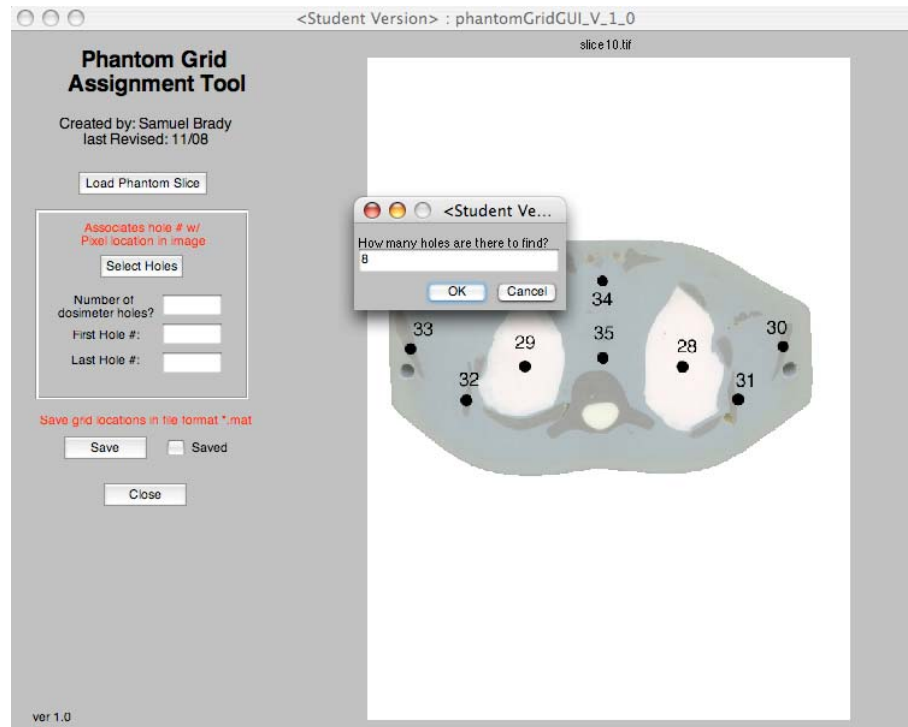


Figure B.14 Phantom Grid Assignment Tool

To load the phantom slice click on the “Load Phantom Slice” button and navigate to the directory and select one of the digitized images of the phantom. This tool only operates on one phantom slice/slab at a time. An image of the phantom slice will appear to the right. The user can manually enter in the “Number of dosimeter holes?”, “First Hole #:”, and the “Last Hole #:” in their respective fields, or when the user can clicks on the button “Select Holes” the software will step through the process automatically, see Figure B.14. Once the software knows how many holes to label, a labeling tool will launch that is similar to the one used in the Film-to-Film Registration module when selecting fiducial markers, see Figure B.15. Once each dosimeter hole is labeled, the software will prompt the user to associate the label number (“Point #”) with the actual number seen on the phantom slice/slab, see Figure B.16. Save the assignments and load another phantom

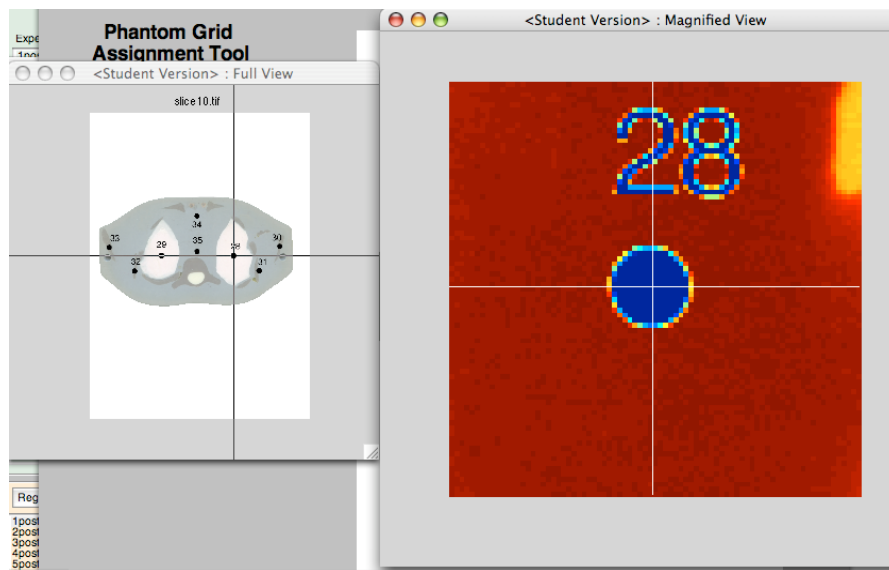


Figure B.15 Phantom Grid Assignment Tool grid number assigning feature

Slice or close the window by clicking on the “Close” button. When closing this window, the software will take you back to the Data Reduction Tool window.

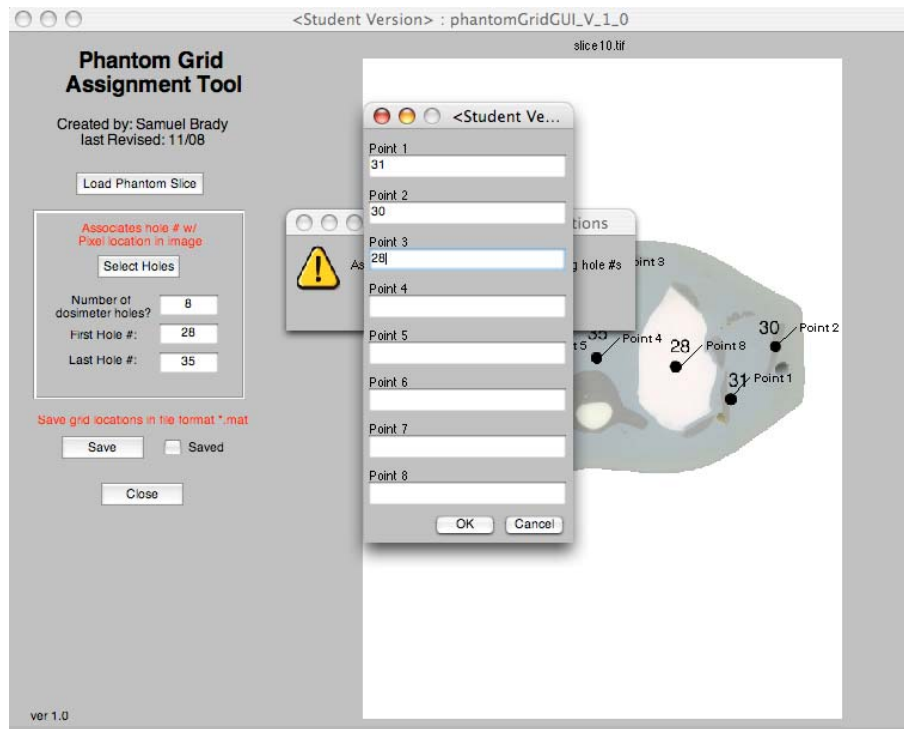


Figure B.16. Phantom Grid Assignment Tool dosimeter hole assignment

The MOSFET and TLD locations correspond to the phantom spatial coordinate system. By defining the phantom grid now the user must register the film with the phantom to correlate the dosimeters within the same spatial coordinate system. Once the phantoms are loaded and displayed in the phantom pane, select the phantom slice and its corresponding film number to register them spatially. Next click on the “Register Grid/Film” button; this will overlay the film and corresponding film organ contours on the phantom, see Figure B.17. The user may need to reposition the contour line set by using the translation arrows and fine/gross controls located in the lower right

corner (white box). The lung contours will not always line up well with the phantom defined boundaries; this is because the lungs were contoured from the reconstructed CT images and may not be perfect due to partial volume effects and other CT reconstruction artifacts. Once the film and phantom slice are registered a check will be placed in the “Registered” box.

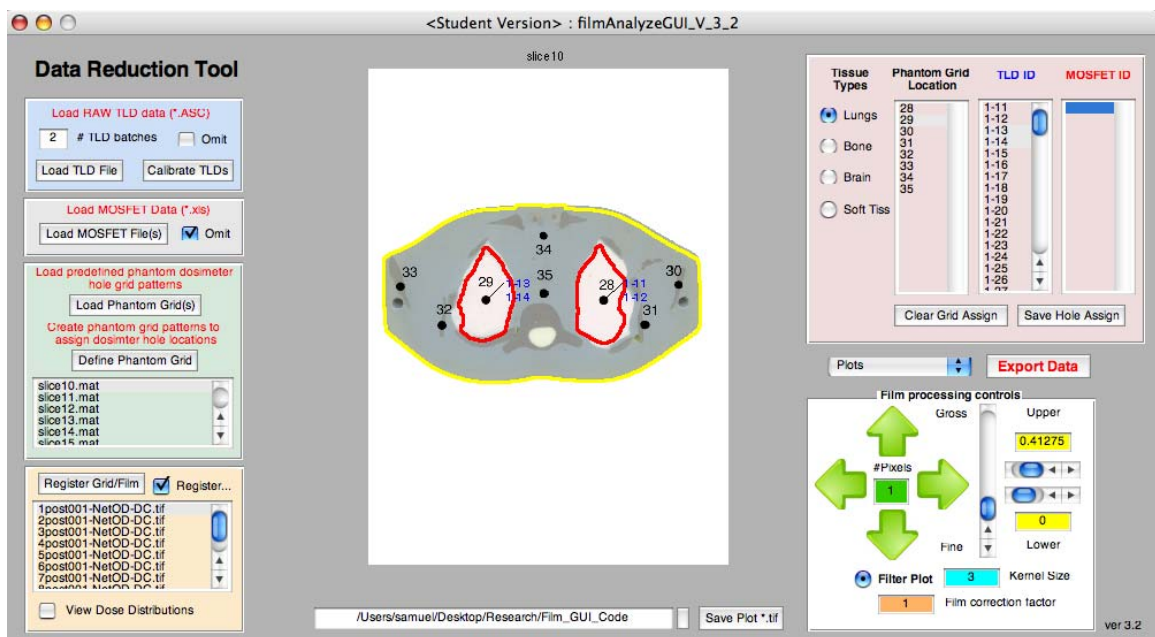


Figure B.17 Data Reduction Tool RCF and phantom registration

To compare the film results with TLD and MOSFET data select the organ tissue type you will be working with located at the upper right side in the identification pane (red box). If the “Phantom Grid Location” field is empty click on the phantom grid listed in the phantom pane field; the corresponding dosimeter holes will appear. To associate the film with the other dosimeters select the dosimeter hole number in the “Phantom Grid Location” field and the TLDs and MOSFETs that were placed in that

hole. The TLDs and MOSFETS are selected by likewise highlighting the corresponding TLD IDs in the “TLD ID” field and the MOSFET IDs in the “MOSFET ID” field; then click the “Save Hole Assign” button. Once saved, the corresponding TLD and MOSFET ID(s) are labeled in the hole of the phantom image seen in the middle of the window, see Figure B.17. This action can be undone by selecting the dosimeter hole number under “Phantom Grid Location” field and clicking “Clear Grid Assign”, which will remove the label from the phantom image. Once saved, the software will go to the specific location in the film organ data corresponding to the space coordinates of the phantom and extract an ROI eight pixels in radius. The ROI will be associated with the TLD and MOSFET data. To see the film organ dose distributions and the TLD and MOSFET IDs assigned in that organ image, check the “View Dose Distribution” box and then select the film, see Figure B.18. Note, the organ dose distribution will not appear unless the film has been first registered with the phantom. If the two have not been registered an image of the entire film will appear and it will be shown as netOD response not dose.

After all of the dosimeters have been associated with their correct dosimeter holes throughout the entire phantom volume (i.e., all slices) then the data can be exported by clicking on the “Export Data”. Select the data to export on the subsequent popup window. The data will be saved in a spreadsheet as a CSV file, or the Matlab Workspace will be saved in a *.mat file.

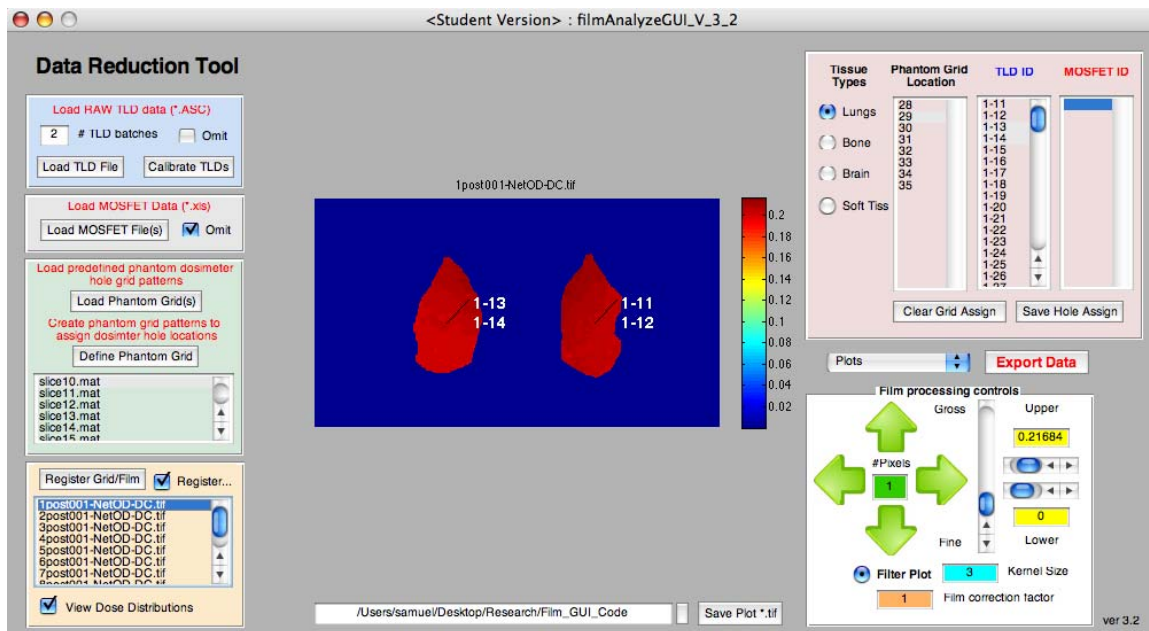


Figure B.18 Data Reduction Tool Dose distribution feature activated

To plot the data that was just assigned to the phantom’s dosimeter holes, click on the “Plot” pull down menu and select the type of plotting format desired. The plots, corresponding to the phantom file name, will be shown in the center viewing area of the Data Reduction window. To change data sets for a different plot analysis, select a different phantom file name.

To save the images in the viewing area (be they: data plots or dose distributions) first change the directory location where the file(s) will be saved. The current directory is listed in the bottom center of the Data Reduction Tool. To change the directory click on the small, unlabeled box to the right of the directory field. A navigation window will popup and allow the user to select a new directory. To save the image currently displayed in the center viewing pane click on the “Save Plot *.tif” button. A new

window will appear with the image and prompt the user to type a name for the file, see Figure B.19; the image shown in this window will be saved once the user clicks “OK”.

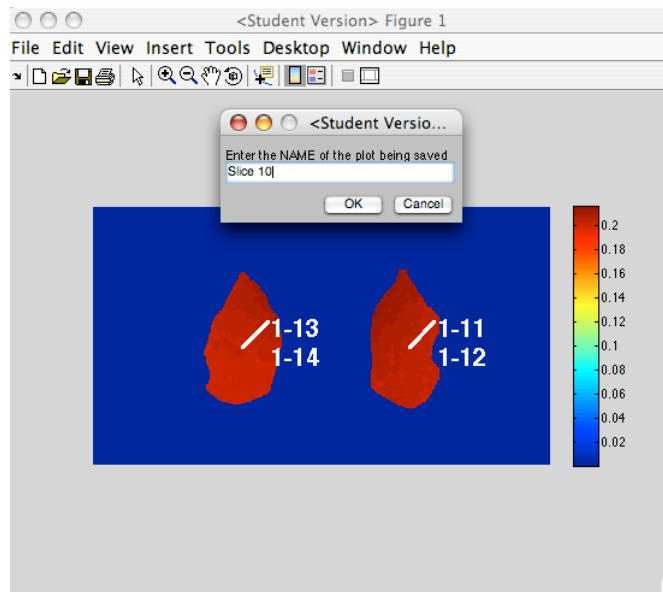


Figure B.19 plot saving tool

Other features of the Data Reduction Tool that are useful is the filtering and dose correction fields under the translation fine/gross controls. If additional filtration is necessary, select the radio dial labeled “Filter Plot” and a 2D Wiener filter will be applied to the data using the displayed kernel size. The film dose response may need to be offset by a certain percent. To change the film dose magnitude type in a percent value in integer form, e.g., for 10% type 1.10, in the field labeled “Film correction factor”.

To close the Data Reduction tool click on the “X” button at the top of the window frame (for PC users the look to the right for MAC users look to the left). This will close the window, and delete all the analysis data, and take you back to the main window. At

this point the main window can be closed by clicking on the “close” button or the Matlab Workspace can be saved by clicking on the “Save” button.

References

1. A. Rink, I. A. Vitkin and D. A. Jaffray, "Suitability of radiochromic medium for real-time optical measurements of ionizing radiation dose," *Med Phys* **32**, 1140-1155 (2005).
2. A. Niroomand-Rad, et al., "Radiochromic film dosimetry: recommendations of AAPM Radiation Therapy Committee Task Group 55. American Association of Physicists in Medicine," *Med Phys* **25**, 2093-2115 (1998).
3. C. D. Hillyer, Hall, J.M., Lackey, D.A., Wazer, D.E., "Development of colorimetric dosimeter for quality control of blood unit and irradiators," *Transfusion* **33** (1993).
4. K. C. Humpherys, Wilde, W.O., Kantz, A.D., "An opti-chromic dosimetry system for radiation processing of food," *Radiat. Phys. Chem.* **22**, 291-294 (1985).
5. High-Dose Dosimetry Proceedings of a symposium, IAEA, Vienna, "Measurement of high doses near metal and ceramic interfaces," 1985.
6. W. L. McLaughlin, et al., "Sensitometry of the response of a new radiochromic film dosimeter to gamma radiation and electron beams," *Nucl. Instrum. Methods Phys. Res. A* **302**, 165-176 (1991).
7. *Radiat. Prot. Dosim.*, "Novel radiochromic films for clinical dosimetry," in *Proceedings of the 11th International conference on solid state dosimetry, II, Vol. 66*, edited by A. a. U. Peto, G. Budapest, 1996, pp. 263-268.
8. A. S. Meigooni, M. F. Sanders, G. S. Ibbott and S. R. Szeglin, "Dosimetric characteristics of an improved radiochromic film," *Med Phys* **23**, 1883-1888 (1996).
9. P. J. Muench, A. S. Meigooni, R. Nath and W. L. McLaughlin, "Photon energy dependence of the sensitivity of radiochromic film and comparison with silver halide film and LiF TLDs used for brachytherapy dosimetry," *Med Phys* **18**, 769-775 (1991).
10. Y. Zhu, et al., "Quantitative evaluation of radiochromic film response for two-dimensional dosimetry," *Med Phys* **24**, 223-231 (1997).

11. M. J. Butson, T. Cheung and P. K. Yu, "Corresponding dose response of radiographic film with layered gafchromic film," *Phys Med Biol* **47**, N285-289 (2002).
12. M. J. Butson, P. K. Yu, T. Cheung and D. Inwood, "Polarization effects on a high-sensitivity radiochromic film," *Phys Med Biol* **48**, N207-N211 (2003).
13. M. J. Butson, P. K. Yu, T. Cheung and P. Metcalfe, "High sensitivity radiochromic film dose comparisons," *Phys Med Biol* **47**, N291-295 (2002).
14. M. J. Butson, P. K. Yu, T. Cheung and P. Metcalfe, "Radiochromic film for medical radiation dosimetry," *Materials Science and Engineering R* **41**, 61-120 (2003).
15. T. Cheung, M. J. Butson and P. K. Yu, "Experimental energy response verification of XR type T radiochromic film," *Phys Med Biol* **49**, N371-N376 (2004).
16. S. A. Dini, R. A. Koona, J. R. Ashburn and A. S. Meigooni, "Dosimetric evaluation of Gafchromic XR type T and XR type R films," *Journal of applied clinical medical physics* **6** (2005).
17. C. G. Soares, "New developments in radiochromic film dosimetry," *Radiation Protection Dosimetry* **120**, 100-106 (2006).
18. G. Thomas, R. Y. L. Chu and F. Rabe, "A study of GafChromic XR type R film response with reflective-type densitometers and economical flatbed scanners," *Journal of applied clinical medical physics* **4**, 307-314 (2003).
19. M. Todorovic, et al., "Evaluation of GafChromic EBT prototype B for external beam dose verification," *Med Phys* **33**, 1321-1328 (2006).
20. "Characteristics of XR-QA film," 2008.
21. A. Rink, I. A. Vitkin and D. A. Jaffray, "Characterization and real-time optical measurements of the ionizing radiation dose response for a new radiochromic medium," *Med Phys* **32**, 2510-2516 (2005).
22. E. C. McCollough and T. W. Holmes, "Acceptance testing computerized radiation therapy treatment planning systems: Direct utilization of CT scan data," *Med Phys* **12** (1984).

23. International Specialty Products, "Gafchromic EBT self-developing film for radiotherapy dosimetry (white paper)," August 2007.
24. S. Devic, et al., "Absorption spectroscopy of EBT model Gafchromic™ film," *Med Phys* **34**, 112-118 (2007).
25. S. Devic, N. Tomic, C. G. Soares and E. B. Podgorsak, "Optimizing the dynamic range extension of a radiochromic film dosimetry system," *Med Phys* **36**, 429-437 (2009).
26. A. Rink, I. A. Vitkin and D. A. Jaffray, "Energy dependence (75 kVp to 18 MV) of radiochromic films assessed using a real-time optical dosimeter," *Med Phys* **34**, 458-463 (2007).
27. International Specialty Products, "GafChromic(R) HD-810 radiochromic dosimetry film and D-200 pre-formatted dosimeters for high-energy photons (white paper)."
28. International Specialty Products "GafChromic(R) XR radiochromic dosimetry films for low energy photons (white paper)."
29. "Personal communication," 16 May 2008.
30. M. C. Saylor, et al., "A thin film recroding medium for use in food irradiation," *Radiat. Phys. Chem.* **31**, 529-536 (1988).
31. A. Rink, I. A. Vitkin and D. A. Jaffray, "Intra-irradiation changes in the signal of polymer-based dosimeter (GAFCHROMIC EBT) due to dose rate variations," *Phys Med Biol* **52**, N523-N529 (2007).
32. M. J. Butson, P. K. Yu and P. E. Metcalfe, "Effects of read-out light sources and ambient light on radiochromic film," *Phys Med Biol* **43**, 2407-2412 (1998).
33. O. Rampado, E. Garelli, S. Deagostini and R. Ropolo, "Dose and energy dependence of response of Gafchromic(R) XR-QA film for kilovoltage x-ray beams," *Phys Med Biol* **51**, 2871-2881 (2006).
34. T. Cheung, M. J. Butson and P. K. Yu, "Post-irradiation colouration of Gafchromic EBT radiochromic film," *Phys Med Biol* **50**, N281-N285 (2005).

35. National Institute of Standards and Technology, Gaithersburg, MD, "Tables of x-ray mass attenuation coefficients and mass energy-absorption coefficients (Version 1.4)," 2004.
36. F. Attix, *Introduction to Radiological Physics and Radiation Dosimetry*. (WILEY-VCH, 1986).
37. M. J. Butson, T. Cheung and P. K. Yu, "Absorption spectra variations of EBT radiochromic film from radiation exposure," *Phys Med Biol* **50**, N135-N140 (2005).
38. M. J. Butson, T. Cheung and P. K. Yu, "Absorption spectra of irradiated XRCT radiochromic film," *Phys Med Biol* **51**, 3099-3103 (2006).
39. C. Fiandra, et al., "Clinical use of EBT model Gafchromic™ film in radiotherapy," *33* **11** (2006).
40. M. Fuss, E. Sturtewagen, C. D. Wagter and D. Georg, "Dosimetric characterization of GafChromic EBT film and its implication on film dosimetry quality assurance," *Phys Med Biol* **52**, 4211-4225 (2007).
41. M. J. Butson, T. Cheung and P. K. Yu, "Measurement of energy dependence for XRCT radiochromic film," *Med Phys* **33**, 2923-2925 (2006).
42. L. E. Reinstein, G. R. Gluckman and A. G. Meek, "A rapid colour stabilization technique for radiochromic film dosimetry," *Phys Med Biol* **43**, 2703-2708 (1998).
43. I. Janovsky and K. Mehta, "The effects of humidity on the response of radiochromic dosimeters FWT-60-00 and GafChromic DM-1260," *Radiation Physics Chemistry* **43** (1994).
44. L. Rill, W. Huda and N. Gkanatsios, "View box luminance measurements and their effect on reader performance," *Acad Radiol* **6**, 521-529 (1999).
45. I. Ali, J. F. Williamson, C. Costescu and J. F. Dempsey, "Dependence of radiochromic film response kinetics on fractionated doses," *Appl Radiat Isot* **62**, 609-617 (2005).

46. M. K. Ranade, et al., "A prototype quantitative film scanner for radiochromic film dosimetry," *Med Phys* **35**, 473-479 (2008).
47. G. R. Gluckman and L. E. Reinstein, "Comparison of three high-resolution digitizers for radiochromic film dosimetry," *Med Phys* **29**, 1839-1846 (2002).
48. E. Wilcox, G. Daskalov and L. Nedialkova, "Comparison of the Epson Expression 1680 flatbed and the Vidar VXR-16 dosimetry PRO film scanners for use in IMRT dosimetry using Gafchromic and radiographic film," *Med Phys* **34**, 41-48 (2007).
49. S. Devic, et al., "Precise radiochromic film dosimetry using a flat-bed document scanner," *Med Phys* **32**, 2245-2253 (2005).
50. B. D. Lynch, et al., "Important considerations for radiochromic film dosimetry with flatbed CCD scanners and EBT GAFCHROMIC film," *Med Phys* **33**, 4551-4556 (2006).
51. M. J. Butson, T. Cheung and P. K. Yu, "Scanning orientation effects on Gafchromic EBT film dosimetry," *Aust. Phys. Eng. Sci. Med.* **29**, 281-284 (2006).
52. S. Devic, et al., "Dosimetric properties of improved GafChromic films for seven different digitizers," *Med Phys* **31**, 2392-2401 (2004).
53. B. C. Ferreira, M. C. Lopes and M. Capela, "Evaluation of an Epson flatbed scanner to read Gafchromic EBT films for radiation dosimetry," *Phys Med Biol* **54**, 1073-1085 (2009).
54. L. Menegotti, A. Delana and A. Martignano, "Radiochromic film dosimetry with flatbed scanners: a fast and accurate method for dose calibration and uniformity correction with single film exposure," *Med Phys* **35**, 3078-3085 (2008).
55. L. Paelinck, W. De Neve and C. De Wagter, "Precautions and strategies in using a commercial flatbed scanner for radiochromic film dosimetry," *Phys Med Biol* **52**, 231-242 (2007).
56. S. Saur and J. Frengen, "GafChromic EBT film dosimetry with flatbed CCD scanner: a novel background correction method and full dose uncertainty analysis," *Med Phys* **35**, 3094-3101 (2008).

57. H. Alva, H. Mercado-Uribe, M. Rodriguez-Villafuerte and M. E. Brandan, "The use of a reflective scanner to study radiochromic film response," *Phys Med Biol* **47**, 2925-2933 (2002).
58. J. Kalef-Ezra and K. Karava, "Radiochromic film dosimetry: reflection vs transmission scanning," *Med Phys* **35**, 2308-2311 (2008).
59. M. J. Butson, T. Cheung and P. K. Yu, "Evaluation of the magnitude of EBT gafchromic film polarization effects " *Australas Phys Eng Sci Med* **32**, 21-25 (2009).
60. K. R. Gorny, et al., "The calibration of experimental self-developing GafChromic(R) HXR film for the measurement of radiation dose in computed tomography," *Med Phys* **32**, 1010-1016 (2005).
61. P. R. Bevington and D. K. Robinson, *Data reduction and error analysis for the physical sciences*, 3 ed. (McGraw Hill, 2003).
62. L. J. van Battum, D. Hoffmans, H. Piersma and S. Heukelom, "Accurate dosimetry with GafChromic™ EBT film of a 6 MV photon beam in water: What level is achievable?," *Med Phys* **35**, 704-716 (2008).
63. W. Hendee, *Medical Radiation Physics*. (Yearbook Medical Publishers, 1970).
64. K. Levenberg, "A method for the solution of certain problems in least squares," *Quart Appl Math* **2**, 164-168 (1944).
65. D. Marquardt, "An Algorithm for least squared estimatin of nonlinear parameters," *SIAM J. Appl. Math* **11**, 431-441 (1963).
66. L. Bassett, et al., "Practice guidelines for the performance of screening and diagnostic mammography," (2008).
67. H. M. Warren-Forward and L. Duggan, "Towards in vivo TLD dosimetry in mammography," *Br J Radiol* **77**, 426-432 (2004).
68. X. Wu, G. T. Barnes and T. D. M, "Spectral dependence of glandular tissue dose in screen-film mammography," *Radiology* **179**, 143-148 (1991).

69. D. R. Dance, "Monte Carlo calculation of conversion factors for the estimation of mean glandular breast dose," *Phys Med Biol* **35**, 1211 (1990).
70. D. R. Dance, et al., "Influence of anode/filter material and tube potential on contrast signal-to-noise ratio and average absorbed dose in mammography: a monte carlo study," *Br J Radiol* **73**, 1056-1067 (2000).
71. D. R. Dance, et al., "Breast dosimetry using high-resolution voxel phantoms," *Radiat Prot Dosimetry* **114**, 359-363 (2005).
72. J. M. Boone, N. Shah and T. R. Nelson, "A comprehensive analysis of DGNCT coefficients for pendant-geometry cone-beam breast computed tomography," *Med Phys* **31**, 226-235 (2004).
73. J. M. Boone, T. R. Nelson, K. K. Lindfors and J. A. Siebert, "Dedicated breast CT: radiation dose and image quality evaluation," *Radiology* **221** (2001).
74. S. C. Thacker and S. J. Glick, "Normalized glandular dose (DgN) coefficients for flat-panel CT breast imaging," *Phys Med Biol* **49**, 5433 (2004).
75. M. J. Yaffe, et al., "The myth of the 50-50 breast," *Med Phys* **36**, 5437-5443 (2009).
76. M. P. Tornai, et al., "Design and development of a fully-3D dedicated x-ray computed mammatomography system," *Proc SPIE: Phys Med Imag* **5745**, 189-197 (2005).
77. D. J. Crotty, R. L. McKinley and M. P. Tornai, "Experimental spectral measurements of heavy K-edge filtered beams for x-ray computed mammatomography," *phys Med Biol* **52**, 603-616 (2007).
78. S. J. Cutler, D. J. Crotty and M. P. Tornai, presented at the Nuclear Science Symposium Conference Record, 2008 (unpublished).
79. A. L. C. Kwan, J. M. Boone and N. Shah, "Evaluation of X-ray scatter properties in a dedicated cone-beam breast CT scanner," *Med Phys* **32**, 2967-2975 (2005).
80. P. Russo, et al., presented at the IEEE Nuclear Science Symposium and medical Imaging, Orlando, FL, 2009 (unpublished).

81. NCRP Report No. 160, "Ionizing radiation exposure of the population of the United States," national Council on Radiation Protection and Measurements, Bethesda, MD, 2009.
82. T. B. Shope, R. M. Gagne and G. C. Johnson, "A method for describing the doses delivered by transmission x-ray computed tomography," *Med Phys* **8**, 488-495 (1980).
83. C. McCollough, et al., "The measurement, reporting, and management of radiation dose in CT," Report of AAPM Task Group 23 (2008).
84. L. M. Hurwitz, et al., "Effective dose determination using an anthropomorphic phantom and metal oxide semiconductor field effect transistor technology for clinical adult body multidetector array computed tomography protocols," *J Comput Assist Tomogr* **31**, 544-549 (2007).
85. T. T. Yoshizumi, et al., "Validation of metal oxide semiconductor field effect transistor technology for organ dose assessment during CT: comparison with thermoluminescent dosimetry," *AJR AM J Roentgenol* **188**, 1332-1336 (2007).
86. W. Kalender, B. Schmidt, M. Zankl and M. Schmidt, "A PC program for estimating organ dose and effective dose values in computed tomography," *Eur Radiol* **9**, 555-562 (1999).
87. W. C. a. A. Roesch, F.H., "Basic concepts of dosimetry," in *Radiation Dosimetry, Vol. I*, edited by W. C. a. A. Roesch, F.H. (Academic Press, New York, 1968).
88. "Personal communication," JL Shepherd Inc, Jan 26th, 2010.
89. "Email communication," JL Shephard Inc. 18 December 2009.
90. S. B. Jiang, J. Wolfgang and G. S. Mageras, "Quality assurance challenges for motion-adaptive radiation therapy: Gating, breath holding, and four-dimensional computed tomography," *Int J Radiat Oncol Biol Phys* **71**, S103-S107 four-dimensional (2007).
91. B. Nelms, E. Ehler, H. Bragg and W. Tome, "Quality assurance device for four-dimensional IMRT or SBRT and respiratory gating using patient-specific intrafraction motion kernels," *J App Clin Med Phys* **8**, 152-168 (2007).

92. H. Nakayama, et al., "Development of a three-dimensionally movable phantom system for dosimetric verifications," *Med Phys* **35**, 1643-1650 (2008).
93. E. Nioutsikou, N. S.-T. J. Richard, J. L. Bedford and S. Webb, "Quantifying the effect of respiratory motion on lung tumour dosimetry with the aid of a breathing phantom with deforming lungs," *Phys Med Biol* **51**, 3359-3374 (2006).
94. R. I. Berbeco, et al., "A technique for respiratory-gated radiotherapy treatment verification with an EPID in cine mode," *Phys Med Biol* **50**, 3669-3679 (2005).
95. P. J. Keall, et al., "The clinical implementation of respiratory-gated intensity-modulated radiotherapy," *Med Dosim* **31**, 152-162 (2006).
96. C. B. Saw, et al., "A review on the clinical implementation of respiratory-gated therapy," *Biomed Imaging Interv J* **3**, 1-8 (2007).
97. P. Ravindran, A. Mahata and E. S. Babu, "Phantom for moving organ dosimetry with gel," *J. Phys.: Conf. Ser.* **164**, 1-3 (2009).
98. S. Mansson, et al., "Dosimetric verification of breathing adapted radiotherapy using polymer gel," *J. Phys.: Conf. Ser.* **56**, 300-303 (2006).
99. S. Ceberg, et al., "Verification of dynamic radiotherapy: the potential for 3D dosimetry under respiratory-like motion using polymer gel," *Phys Med Biol* **53**, N387-396 (2008).
100. C. Baldock, "Historical overview of the development of gel dosimetry: another personal perspective," *J. Phys.: Conf. Ser.* **164**, 1-8 (2009).
101. P. Y. Guo, J. A. Adamovics and M. Oldham, "Characterization of a new radiochromic three-dimensional dosimeter," *Med Phys* **33**, 1338-1345 (2006).
102. P. Guo, J. Adamovics and M. Oldham, "A practical three-dimensional dosimetry system for radiation therapy," *Med Phys* **33**, 3962-3972 (2006).
103. H. S. Sakhalkar and M. Oldham, "Fast, high-resolution 3D dosimetry utilizing a novel optical-CT scanner incorporating tertiary telecentric collimation," *Med Phys* **35**, 101-111 (2008).

104. M. Oldham, P. Guo, G. Gluckman and J. Adamovics, "IMRT verification using a radiochromic/optical-CT dosimetry system," *J Phys* **56**, 221-224 (2006).
105. M. Oldham, H. Sakhalkar, P. Guo and J. Adamovics, "An investigation of the accuracy of an IMRT dose distribution using two- and three-dimensional dosimetry techniques," *Med Phys* **35**, 2072-2080 (2008).
106. J. Adamovics, J. Dietrich and K. Jordan, "Enhanced performance of PRESAGE - Sensitivity, and post-irradiation stability," *Med Phys* **32**, 1 (2005).
107. J. Adamovics and M. Maryanski, "New 3D radiochromic solid polymer dosimeter from leuco dyes and a transparent polymeric matrix," *Med Phys* **30**, 1 (2003).
108. J. Adamovics and M. Maryanski, "OCT scanning properties of PRESAGE - A 3D radiochromic solid polymer dosimeter," *Med Phys* **31**, 1 (2004).
109. J. Adamovics and M. J. Maryanski, "Characterisation of PRESAGE: A new 3-D radiochromic solid polymer dosemeter for ionising radiation," *Radiat Prot Dosimetry* **120**, 107-112 (2006).
110. H. Sakhalkar, J. Adamovics, G. S. Ibbott and M. Oldham, "A comprehensive evaluation of the PRESAGE/optical-CT 3D dosimetry system," *Med Phys* **36**, 71-82 (2009).
111. S. J. Doran, et al., "A CCD-based optical CT scanner for high-resolution 3D imaging of radiation dose distributions: equipment specifications, optical simulations and preliminary results," *Phys Med Biol* **46**, 3191-3213 (2001).
112. N. Krstajic and S. J. Doran, "Focusing optics of a parallel beam CCD optical tomography apparatus for 3D radiation gel dosimetry," *Phys Med Biol* **51**, 2055-2075 (2006).
113. N. Krstajic and S. J. Doran, "Characterization of a parallel-beam CCD optical-CT apparatus for 3D radiation dosimetry," *Phys Med Biol* **52**, 3693-3713 (2007).
114. P. J. Keall, et al., "The management of respiratory motion in radiation oncology report of AAPM Task Group 76," *Med Phys* **33**, 3874-3900 (2006).

115. H. Shirato, et al., "Four-dimensional treatment planning and fluoroscopic real-time tumor tracking radiotherapy for moving tumor," *Int J Radiat Oncol Biol Phys* **48**, 435-442 (2000).
116. L. Dietrich, T. Tucking, S. Nill and U. Oelfke, "Compensation for respiratory motion by gated radiotherapy: an experimental study," *Phys Med Biol* **50**, 2405-2414 (2005).
117. E. Rietzel, T. Pan and G. T. Chen, "Four-dimensional computed tomography: image formation and clinical protocol," *Med Phys* **32**, 874-889 (2005).
118. S. Babic, J. Battista and K. Jordan, "Three-dimensional dose verification for intensity-modulated radiation therapy in the Radiological Physics Centre head-and-neck phantom using optical computed tomography scans of Ferrous Xylenol-Orange gel dosimeters," *Int. J. Radiation Oncology Biol. Phys.* **70**, 1281-1291 (2008).
119. D. A. Low and J. F. Dempsey, "Evaluation of the gamma dose distribution comparison method," *Med Phys* **30**, 2455-2464 (2003).
120. D. A. Low, W. B. Harms, S. Mutic and J. A. Purdy, "A technique for the quantitative evaluation of dose distributions," *Med Phys* **25**, 656-661 (1998).
121. G. S. Ibbott, A. Molineu and D. S. Followill, "Independent evaluations of IMRT through the use of an anthropomorphic phantom," *Technol Cancer Res Treat* **5**, 481-487 (2006).
122. M. J. Butson, P. K. Yu and T. Cheung, "Rounded end multi-leaf penumbral measurements with radiochromic film," *Phys Med Biol* **48**, N247-252 (2003).
123. N. D. MacDougall, M. E. Miquel and S. F. Keevil, "Effects of phantom volume and shape on the accuracy of MRI BANG gel dosimetry using BANG3," *Br J Radiol* **81**, 46-50 (2008).
124. M. Bazioglou and J. Kalef-Ezra, "Dosimetry with radiochromic films: a document scanner technique, neutron response, applications," *Appl Rad Iso* **55**, 339-345 (2001).
125. International Specialty Products, "Gafchromic EBT self-developing film for radiotherapy dosimetry (white paper)," August 2007.

126. A. Hutcheson, et al., "Pulsed and monoenergetic beams for neutron cross-section measurements using activation and scattering techniques at Triangle Universities Nuclear Laboratory " Nucl. Instr. and Meth. in Phys. Res. B **261**, 369-372 (2007).
127. Pedroni, R.S., "Cross sections and analyzing powers in the 8- to 17-MeV range for neutron scattering from [Fe-54,56], [Ni-58,60], and [Sn-120]." in *The Department of Physics Duke University, Ph.D. Dissertation*, 1986.
128. Swartz, B., "Characterization of neutron beams produced using the $2\text{H}(d,n)$ reaction for determining dose to small animals," in *The Medical Physics Program, Duke University, M.S. Thesis* 2007.
129. "The physics models of FLUKA: status and recent developments. In: Computing in High Energy and Nuclear Physics," La Jolla, CA, USA, 2003.
130. F. G. Perey, T. A. Love and W. E. Kenney, A test of neutron total cross section evaluations from 0.2 eV to 20 MeV for C, O, Al, Si, Fe and SiO₂, ORNL-4823, ENDF-81972.
131. International Commission on Radiation Units and Measurements., "Neutron dosimetry for biology medicine. Report 26," Bethesda, MD: ICRU, 1977.
132. C. M. Ma, et al., "AAPM protocol for 40-300 kV x-ray beam dosimetry in radiotherapy and radiobiology," *Medical Physics* **28**, 868-893 (2001).
133. L. Duggan, et al., "Variations in dose response with x-ray energy of LiF:Mg,Cu,P thermoluminescence dosimeters: implications for clinical dosimetry.[erratum appears in Phys Med Biol. 2004 Sep 21;49(18):4445]," *Physics in Medicine & Biology* **49**, 3831-3845 (2004).
134. Y. S. Horwitz, *Thermoluminescence and Thermoluminescent Dosimetry*. (CRC Press, 1984).
135. F. Attix, *Introduction to Radiological Physics and Radiation Dosimetry*, 1st ed. (Wiley-VCH, 2004).

Biography

Personal

Name: Samuel Loren Brady
Date of birth: December 7th, 1979
Place of birth: Provo, Utah

Education

Duke University, Durham NC

Ph.D. in Medical Physics, 2010

- Dissertation: "Development of RCF for spatially quantitative dosimetric analysis of indirect ionizing radiation fields" Committee: Terry Yoshizumi, Ph.D., Eshan Samei, Ph.D., Rathnayaka Gunasingha, Ph.D., Donald Frush, M.D., Robert Reiman, Jr, M.D.

M.S. in Medical Physics, 2007

- Thesis: "Dose characterization of ¹³⁷Cs and orthovoltage x-ray irradiators" Committee: Mark Oldham, Ph.D., Terry Yoshizumi, Ph.D., Mark Dewhirst, D.V.M., Ph.D.

Utah Valley University, Orem UT

B.S. in Physics, 2005

- Thesis: "Acoustical tensile damage to epithelial tissue in the cornea from CO₂ laser radiation" Advisors: C. Brent Barger, Ph.D. and Alvin Benson, Ph.D.

Provo High School, Provo UT, 1998

Scholarships, Scholastic honors

Duke University, Durham NC,

Scholarship, Medical Physics program (2005-2007)

Utah Valley University, Orem UT

Scholarship, Physics Department (2001-2005)

National Deans List recipient (2005)

Deans List, Physics Departments (2004-2005)

Deans List, Computer Science (2001-2002)

Grants and External support

- National Institute of Health (NIH) and National Institute of Biomedical Imaging and Bioengineering (NIBIB) T32 EB007185
- National Institute of Allergy and Infectious Diseases (DIAID) 5U19 A1067798-03
- US Nuclear Regulatory Commission Nuclear Education (NRC) 38-07-494
- General Electric CT Research Grant

Refereed Journal Publications

Brady, S.L., Toncheva, G., Dewhurst, M., Yoshizumi, T., A Characterization of a ¹³⁷Cs irradiator from a new perspective with modern dosimetric tools, *Health Phys.* 97(3):195-205 (2009)

Brady, S.L., Brown, W., Clift, C., Yoo, S., Oldham, M., Investigation into the feasibility of using PRESAGE/optical-CT dosimetry for the verification of gating treatments, *Phys Med Biol* 55(2010) 2187-2201

Crotty, D.J., **Brady, S.L.,** Jackson, D.C., Toncheva, G.I., Anderson-Evans, C., Yoshizumi, T.T., Tornai, M.P., Investigating the dose distribution in the uncompressed breast with a dedicated CT mamotomography system, *Med Phys*, (In Review)

Brady, S.L., Gunasingha, R., Yoshizumi, T.T., Howell, C.R., Crowell, A.S., Fallin, B., A feasibility study using RCFs for passive fast neutron 2D dosimetry, *Phys Med Biol* (In Review)

Brady, S.L., Toncheva, G., Frush, D., Yoshizumi, T.T., A novel two-dimensional dosimetry in a pediatric anthropomorphic phantom using XRQA RCF, *Med Phys*, (In review)

Selected Abstracts and Conference Presentations

Brady, S.L., Gunasingha, R., Yoshizumi, T.T., Howell, C.R., Crowell, A.S., Fallin, B., Tonchev, A.P., Dewhurst, M.W., Radiation Dosimetry for 10 MeV Neutrons Using XRQA Radiochromic Film (Oral Presentation) *Health Physics Society, Annual Meeting* 2010.

Brady, S.L., Development of GafChromic™ film for spatially quantitative dosimetric analysis of indirect ionizing radiation fields. (Poster Presentation), *NIBIB Training Grantees Meeting*, 2010

Jackson, D.C., Crotty, D.J., **Brady, S.L.,** Toncheva, G.I., Anderson-Evans, C., Yoshizumi, T.T., Tornai, M.P., An investigation of 3D dose distribution in the breast with a

dedicated CT mammothography system. (Oral Presentation) *SPIE*, Annual meeting 2010.

Brady, S.L., Gunasingha, R., Yoshizumi, T., Howell, C., Crowell, A., Fallin, B., Song, H., Tonchev, A., Novel neutron dosimetry using RCFs for 10 MeV neutrons. (Poster) *AAPM*, Annual Meeting 2009.

Jackson, D.C., Crotty, D.J., **Brady, S.L.**, Toncheva, G.I., Anderson-Evans, C., Yoshizumi, T.T., Tornai, M.P., Empirical measurement of the 3D dose distribution in the uncompressed breast using a dedicated CT mammothography system. (Poster Presentation) Duke Comprehensive *Cancer Center*, Annual Meeting, 2009.

Gunasingha, R., Howell, C., Crowell, A., Fallin, B., Yoshizumi, T., Song, H., Tonchev, A., **Brady, S.L.**, Comparison of Neutron Doses to a Water Target Exposed to a 10 MeV Neutron Beam: Foil Activation Method vs. Monte Carlo Simulations. (Poster) *AAPM*, Annual Meeting 2009.

Brady, S.L., Toncheva, G., Dewhirst, M., Yoshizumi, T., A characterization of a ^{137}Cs irradiator from a new perspective with modern dosimetric tools. (Oral Presentation) *Health Physics Society*, Annual Meeting 2008

Brady, S.L., Sakhalkar, H., Maurer, J., Yoo, S., Adamovics, J., Gluckman, G., Oldham, M., The verification of respiratory-gated radiation treatments using 3D dosimetry techniques. (Moderated Poster) *AAPM*, Annual Meeting 2008.

Brady, S.L., Toncheva, G., Dewhirst, M., Yoshizumi, T., A characterization of a ^{137}Cs irradiator from a new perspective with modern dosimetric tools. (Oral Presentation) *North Carolina Health Physics Society*, Spring Meeting 2008

Brady, S.L., Muromotto, G., Toncheva, T., Diagle, L., Nguyen, G., Chute, J., Dewhirst, M., Yoshizumi, T., A novel mouse dosimetry with MOSFET technology in orthovoltage x-ray irradiator. (Oral Presentation) *Health Physics Society*, Annual Meeting 2007.

Brady, S.L., Yoshizumi, T., Frush, D., Toncheva, G., Nguyen, G., Oldham, M., Novel 2D dose distribution study in 5-Yr old pediatric phantom. (Poster) *Health Physics Society*, Annual Meeting 2007.

Brady, S.L., Muromotto, G., Changhong, Ke., Toncheva, T., Diagle, L., Nguyen, G., Chute, J., Marslek, P., Dewhirst, M., Yoshizumi, T., How accurate is the dose look-up

table in small animal cesium irradiator: a comparison between direct TLD measurement and dose look-up table. (Poster) *Health Physics Society, Annual Meeting 2007*.

Brady, S.L., Muromotto, G., Toncheva, T., Diagle, L., Nguyen, G., Chute, J., Dewhirst, M., Yoshizumi, T., A novel mouse dosimetry with MOSFET technology in orthovoltage x-ray irradiator. (Oral Presentation) *North Carolina Health Physics, Spring Meeting 2007*.

Benson, A., **Brady, S.L.**, Denning, A., Page, L., Utah Valley State College, McCally, R., Barger C., Johns Hopkins University, Thermoacoustical wave generation and propagation in the cornea. (Oral Presentation) *SPIE Photonics West, Annual Meeting 2007*

Manzoor, A, **Brady, S.L.**, Guo, P., Adamovics, J, Oldham, M, An exploration of new formulations for PRESAGE™ 3D dosimetry. (Poster) *AAPM Annual Meeting 2006*

Goss, M., **Brady, S.L.**, Guo, P., Oldham, M., Evaluation of a practical GafChromic® EBT film/flat-bed scanner combination for use in planar clinical dosimetry. (Poster) *AAPM, Annual Meeting 2006*